Search for a gravitational-wave background using a global interferometer network

Kamiel Janssens

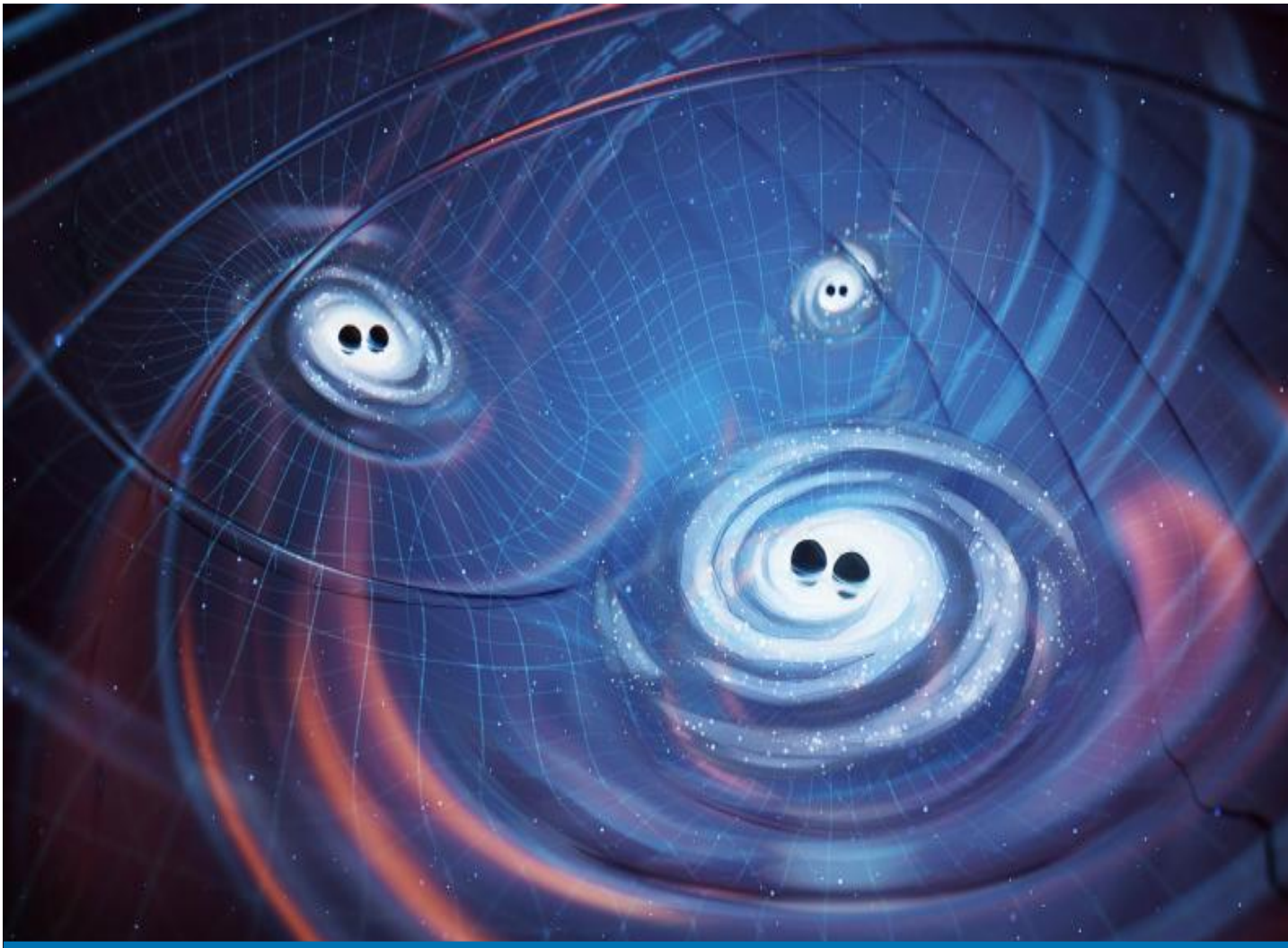

Supervisors: **Nick van Remortel | Nelson Christensen**

Thesis submitted for the degree of Doctor in Sciences: Physics
Faculty of Sciences | Department of Physics | Antwerp 2023

Universiteit Antwerpen
Research Foundation Flanders
Opening new horizons
UNIVERSITÉ CÔTE D'AZUR

Cover picture:

Artist impression of a gravitational wave background from the superposition of supermassive black hole binaries. *Illustration: Olena Shmahalo, reused under the Creative Commons Licence.*

Universiteit Antwerpen

UNIVERSITÉ CÔTE D'AZUR | ÉCOLE DOCTORALE SCIENCES FONDAMENTALE ET APPLIQUÉES

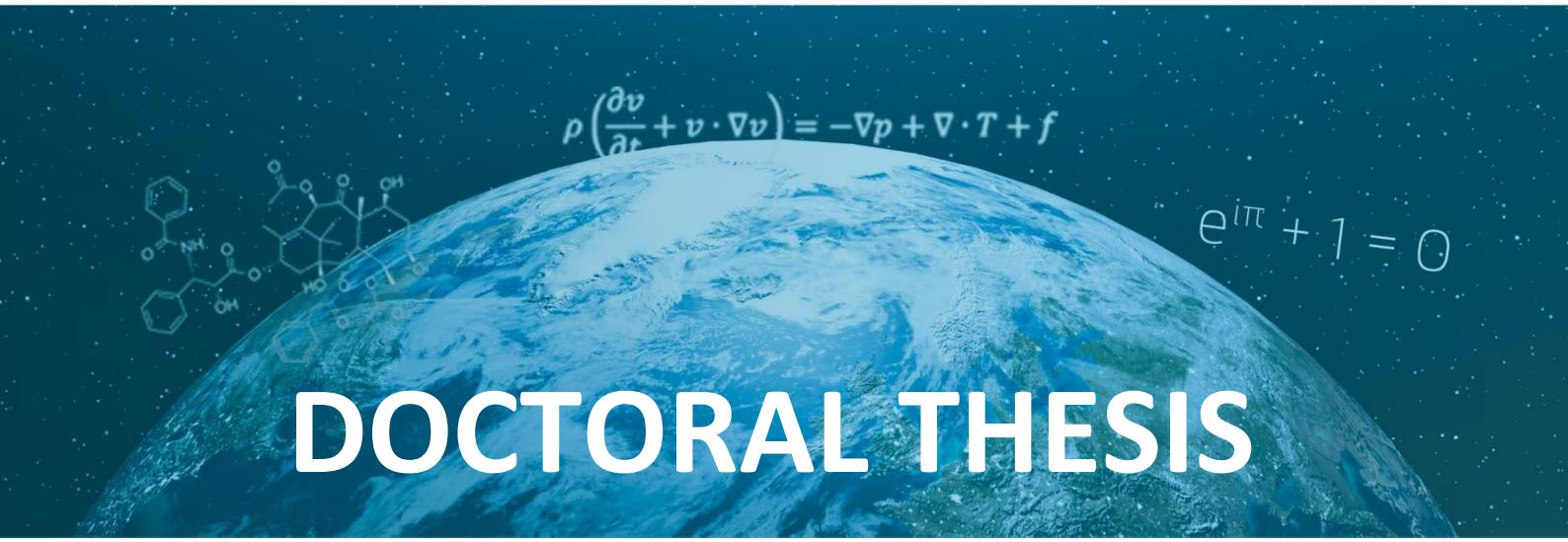

DOCTORAL THESIS

Search for a stochastic gravitational-wave background using a global interferometer network

Kamiel Janssens

Faculty of science – Department of physics

Thesis submitted for the degree of doctor in physics at Université Côte d'Azur
and doctor in sciences: physics at Universiteit Antwerpen
to be defended by Kamiel Janssens
Supervised by : Nick van Remortel / Nelson Christensen
Defended on : 24 Oct. 2023 in Antwerp

In front of the jury, composed of :
Marie-Anne Bizouard, Dr., Université Côte d'Azur
Thomas Callister, Dr., University of Chicago
Sofie Cambré, Professor, Universiteit Antwerpen
(President of the jury)
Nelson Christensen, Professor, Université Côte d'Azur
Joseph Romano, Professor, Texas Tech University
Alexander Sevrin, Professor, Vrije Universiteit Brussel
Nick van Remortel, Professor, Universiteit Antwerpen

fwo Research Foundation Flanders
Opening new horizons

Universiteit Antwerpen

UNIVERSITÉ CÔTE D'AZUR | ÉCOLE DOCTORALE SCIENCES FONDAMENTALE ET APPLIQUÉES

Proefschrift

Onderzoek naar een stochastische achtergrond van gravitatiegolven, gebruikmakende van een wereldwijd interferometer netwerk

Kamiel Janssens

Faculteit wetenschappen – Departement fysica

Gepresenteerd voor het behalen van de graad van doctor in de fysica aan Université Côte d'Azur
en doctor in de wetenschappen: fysica aan Universiteit Antwerpen
Onder supervisie van: Nick van Remortel / Nelson Christensen
Verdedigd op : 24 Okt. 2023 te Antwerpen

Voor de jury, samengesteld uit :
Marie-Anne Bizouard, Dr., Université Côte d'Azur
Thomas Callister, Dr., University of Chicago
Sofie Cambré, Professor, Universiteit Antwerpen
(Voorzitter van de jury)
Nelson Christensen, Professor, Université Côte d'Azur
Joseph Romano, Professor, Texas Tech University
Alexander Sevrin, Professor, Vrije Universiteit Brussel
Nick van Remortel, Professor, Universiteit Antwerpen

fwo Research Foundation Flanders
Opening new horizons

UNIVERSITÉ CÔTE D'AZUR | ÉCOLE DOCTORALE SCIENCES FONDAMENTALE ET APPLIQUÉES

Universiteit Antwerpen

Recherche d'un fond stochastique d'ondes gravitationnelles à l'aide d'un réseau d'interféromètres mondial

Kamiel Janssens

Faculté des sciences

Présentée en vue de l'obtention du grade de docteur en physique d'Université Côte d'Azur
et de docteur en sciences: physique d' Universiteit Antwerpen
Dirigée par : Nelson Christensen / Nick van Remortel
Soutenue le : 24 Oct. 2023 à Anvers

Devant le jury, composé de :
Marie-Anne Bizouard, Dr., Université Côte d'Azur (Examinatrice)
Thomas Callister, Dr., University of Chicago (Examinateur)
Sofie Cambré, Professeur, Universiteit Antwerpen (Président du jury)
Nelson Christensen, Professeur, Université Côte d'Azur (Directeur de these)
Joseph Romano, Professeur, Texas Tech University (Rapporteur)
Alexander Sevrin, Professeur, Vrije Universiteit Brussel (Rapporteur)
Nick van Remortel, Professeur, Universiteit Antwerpen (Directeur de these)

fwo Research Foundation Flanders
Opening new horizons

Abstract (English)

Search for a stochastic gravitational-wave background using a global interferometer network.

Observing the (stochastic) gravitational-wave background ((S)GWB) with Earth-based interferometric detectors will provide insights into astrophysical and/or cosmological processes in the early Universe. To confidently claim a detection in the future, a profound knowledge of the data quality and potential contamination by (environmental) noise sources is of utmost importance. In this work a comprehensive study is presented on a wide variety of potential data quality issues that may arise in the search for an isotropic GWB, both with current as well as next generation Earth-based gravitational-wave (GW) interferometric detectors.

To ensure reliable analysis results, non-stationary features as well as spectral artefacts have to be addressed first. The problematic spectral artefacts during the third observing run (O3) by the Laser Interferometer Gravitational-wave Observatory (LIGO) and Virgo were identified and removed from the analyses by applying notches. Furthermore, improvements to the followed procedures for the fourth observing run (O4) are presented.
Secondly, one needs to understand the effect of noise sources which are correlated between the observing detectors. When not properly accounted for, these noise sources could bias, or in the worst case even prevent, future detections of a GWB in the Hz to kHz frequency band. Observations of Earth-scale correlations in magnetic field fluctuations are described between 1Hz and 1kHz. By using measurements of the coupling strength of magnetic fields to GW detectors, the effect of correlated magnetic noise on GW searches is predicted. Searches for an isotropic GWB could become contaminated by correlated magnetic noise when the detectors reach their design sensitivity in the second half of the 2020 decade. Future projects such as the Einstein Telescope (ET) and Cosmic Explorer (CE), which are now in their design phase, should seriously consider the threat of (correlated) magnetic noise. If not addressed, environmental magnetic noise will dominate the detectors' sensitivity below $\sim$15Hz. The equilateral triangular configuration of three nested GW detectors of the ET brings certain advantages such as the sky independent null channel, which is insensitive to GW signals from any direction. This would prove useful for the

estimation of the detector noise, as the ET will have many overlapping signals at any given time. Within this context, this work includes a description how to take the effect of non-identical and correlated noise sources into account in the null channel framework. However, the triangular detector configuration comes at a cost. The (nearly) co-located placement of different detectors results in additional noise sources coupling coherently to multiple detectors. This could have a detrimental impact on the ET's capabilities in observing a GWB. The possibility of correlated seismic and Newtonian noise is investigated and shown to be problematic. More specifically, correlated Newtonian noise from seismic body waves has the potential to overwhelm a GWB signal up to $\sim$40Hz by many orders of magnitude. Expected levels of noise subtraction will be inadequate to properly deal with this correlated noise source for GWB searches.
Finally, this work presents the construction of a false alarm probability to differentiate between a correlated noise signal and a GWB signal relying on GW-geodesy. This framework will be useful to validate and build confidence in future detections of a Hz-kHz GWB.

In addition to the pursuit of a more profound understanding of the Universe through the observation of GWs, this work also pays attention to the mental well-being of the scientists pursuing this scientific endeavour. The results of the first survey focusing on large, international collaborations in the field of GW and high energy astrophysics are discussed.

Keywords: stochastic gravitational wave background, correlated noise, gravitational waves, interferometric detector, magnetic noise, seismic noise, Newtonian noise

Samenvatting (Nederlands)

Onderzoek naar een stochastische achtergrond van gravitatiegolven, gebruikmakende van een wereldwijd interferometer netwerk.

De observatie van een (stochastische) achtergrond van zwaartekrachtgolven ((S)AZG) met interferometrische detectoren op Aarde zal ons inzicht geven in astrofysische en kosmologische processen in het jonge Universum. Een diepgaande kennis van de datakwaliteit en potentiële ruisbronnen is vereist om vertrouwen te hebben in toekomstige observaties. Dit werk presenteert een uitgebreide studie van een grote verscheidenheid aan problemen met datakwaliteit voor de analyse van een isotrope AZG met zowel de huidige als ook de volgende generatie interferometrische zwaartekrachtgolf (ZG) detectoren op Aarde.

Om betrouwbare resultaten te garanderen, moeten eerst niet-stationaire data en spectrale artefacten aangepakt worden. De problematische spectrale artefacten tijdens de derde observatie periode (O3) van de 'Laser Interferometer Gravitational-wave Observatory' (LIGO) en Virgo werden geïdentificeerd en verwijderd uit de analyse. Verder werden verbeteringen aan de te volgen procedures voor de vierde observatie periode (O4) gepresenteerd.
Nadien moet het effect van gecorreleerde ruis op de detectoren begrepen worden. Indien dit niet goed in rekening wordt gebracht, kunnen deze ruisbronnen een afwijking introduceren in toekomstige analyses, of in het slechtste geval zelfs een detectie van een AZG in de Hz tot kHz frequentieband verhinderen. Correlaties in magnetische veld-fluctuaties over afstanden van duizenden kilometers worden in dit werk beschreven tussen 1Hz en 1kHz. Door gebruik te maken van metingen van de koppelingssterkte van magnetische velden naar de ZG detectoren worden er voorspellingen gemaakt van het effect van gecorreleerde magnetische ruis op de zoektocht naar ZG signalen. De analyse voor een isotrope AZG kan aangetast worden wanneer de detectoren hun geplande sensitiviteit bereiken in de tweede helft van het 2020 decennium. Volgende generatie detectoren zoals de 'Einstein Telescope' (ET) en 'Cosmic Explorer' (CE), die momenteel in hun ontwerpfase zijn, moeten de dreiging van (gecorreleerde) magnetische ruis ernstig nemen. Indien dit niet aangepakt wordt, dan zal environmentele magnetische ruis de sensitiviteit van de detectoren domineren onder $\sim$15Hz. De gelijkzijdige driehoeksconfiguratie

van de ET, bestaande uit drie in elkaar passende detectoren, heeft enkele voordelen zoals een nul kanaal dat ongevoelig is voor ZGen vanuit eender welke richting. Dit kan gebruikt worden om ET's detector ruis af te schatten aangezien dit niet triviaal zal zijn door de vele overlappende signalen op elk gegeven moment. Dit werk introduceert een beschrijving om niet-identieke en gecorreleerde ruis in rekening te brengen in de context van het nul kanaal. De driehoeksconfiguratie komt echter ook met een nadeel. De gecolokaliseerde plaatsing van de detectoren zorgt dat ruis op een coherente wijze kan koppelen aan de verschillende detectoren. Dit kan een schadelijke impact hebben op ETs vermogen om een AZG te observeren. De mogelijkheid van gecoreleerde seismische en Newtoniaanse ruis is bestudeerd en problematisch bevonden. In het bijzonder Newtoniaanse ruis van seismische ruimtegolven heeft het potentieel om een AZG signaal tot $\sim$40Hz met verschillende grootteordes te bedelven. De verwachtte niveaus van ruisonderdrukking zijn ontoereikend om effectief af te rekenen met het effect van gecorreleerde ruis op de analyse voor een AZG.
Tenslotte, presenteert dit werk de constructie van een valse alarm waarschijnlijkheid om te differentiëren tussen een signaal van gecorreleerde ruis en een AZG signaal, gebaseerd op ZG geodesie. Deze methode zal nuttig zijn om toekomstige detecties van een Hz-kHz AZG te valideren.

Naast het streven naar een dieper begrip van het Universum door observatie van ZGen, besteedt dit werk ook aandacht aan het mentale welzijn van de wetenschappers. De resultaten van de eerste vragenlijst gericht op grote, internationale samenwerkingen in het vakgebied van ZGen en hoge energie astrofysica worden besproken.

Kernbegrippen: stochastische achtergrond van zwaartekrachtgolven, gecoreleerde ruis, zwaartekrachtgolven, interferometrische detector, magnetische ruis, seismische ruis, Newtoniaanse ruis

Résumé (Français)

Recherche d'un fond stochastique d'ondes gravitationnelles à l'aide d'un réseau d'interféromètres mondial.

L'observation du fond (stochastique) d'ondes gravitationnelles (F(S)OG) avec des détecteurs interférométriques terrestres fournira des informations sur les processus astrophysiques et/ou cosmologiques de l'Univers primordial. Il est essentiel d'acquérir une connaissance approfondie de la qualité des données et de la présence de bruits environnementaux pour pouvoir aborder les futures détections avec confiance. Dans ce travail, une étude complète est présentée sur une grande variété de problèmes potentiels de qualité des données pour la recherche d'un FOG isotrope, spécifiquement pour des détecteurs interférométriques terrestres.

Pour garantir des résultats d'analyse fiables, les caractéristiques non-stationnaires ainsi que les artefacts spectraux doivent être traités. Pendant la troisième période d'observation (O3) du 'Laser Interferometer Gravitational-wave Observatory' (LIGO) et de Virgo, des artefacts spectraux problématiques ont été détectés. Ils ont été identifiés et éliminés des analyses. De plus, des améliorations apportées aux procédures pour la quatrième campagne d'observation (O4) sont présentées.
Dans un second temps, il est nécessaire de comprendre l'effet des sources de bruit corrélé entre les détecteurs. Lorsqu'elles ne sont pas correctement prises en compte, ces sources de bruit peuvent biaiser ou même empêcher les détections futures d'un FOG dans la bande de fréquences de 1Hz à 1 kHz. Les observations de corrélations de fluctuations du champ magnétique sont comprises. En utilisant des mesures de couplage des champs magnétiques aux détecteurs, l'effet du bruit magnétique corrélé sur les analyses d'ondes gravitationnelles (OG) est prédit. Les analyses d'un FOG isotrope pourraient être contaminées par un bruit magnétique corrélé lorsque les détecteurs atteindront leur sensibilité finale dans la seconde moitié de la décennie 2020. Les projets tels que 'Einstein Telescope' (ET) et 'Cosmic Explorer' (CE), qui sont maintenant dans leur phase de conception, devraient sérieusement tenir compte de la menace du bruit magnétique (corrélé). S'il n'est pas traité, le bruit magnétique environnemental dominera la sensibilité des détecteurs en dessous de $\sim$15Hz. La configuration triangulaire équilatérale de trois détecteurs imbriqués d'ET apporte certains avantages tels que le canal nul. Ce canal est insensible aux

signaux d'OG de n'importe quelle direction. En effet, ceci serait utile pour estimer le bruit du détecteur, car ET recevra de nombreux signaux se chevauchant. Cette étude comporte une description pour tenir compte de l'effet des sources de bruit non identiques et corrélées dans le contexte du canal nul. Cependant, la configuration triangulaire du détecteur a aussi des désavantages. Le placement colocalisé de différents détecteurs permet à des sources de bruit supplémentaires de se coupler de manière cohérente à plusieurs détecteurs. Cela pourrait avoir un impact négatif sur les capacités d'ET à observer un FOG. La possibilité de bruit sismique et de bruit Newtonien corrélés est étudiée et démontrée comme étant problématique. Plus précisément, le bruit Newtonien corrélé des ondes sismiques de volume a le potentiel de submerger un signal FOG jusqu'à $\sim$40Hz. Les niveaux de soustraction de bruit attendus seront inadéquats pour traiter correctement cette source de bruit corrélée pour les recherches d'un FOG.
Enfin, ce travail présente la construction d'une probabilité de fausse alarme pour différencier un signal de bruit corrélé d'un signal FOG reposant sur la géodésie d'OG. Ce cadre sera utile pour valider et renforcer la confiance dans les futures détections d'un FOG entre 1 Hz et 1 kHz.

En plus de la poursuite d'une compréhension plus profonde de l'Univers à travers l'observation des OG, ce travail comporte également une étude portant sur le bien-être mental des chercheurs. Les résultats de la première enquête sur les grandes collaborations internationales dans le domaine de l'astrophysique des OG et des hautes énergies sont abordés.

Mots clés: fond stochastique d'ondes gravitationnelles, bruit corrélé, ondes gravitationnelles, détecteur interférométrique, bruit magnétique, bruit sismique, bruit Newtonien

Acknowledgements

Four years ago Nick asked me whether I was interested in pursuing a PhD in gravitational-wave physics. At first this seemed daunting as my main experience was in the field of high energy physics and data analysis with the CMS detector at CERN. I am very grateful Nick managed to get me excited and convinced me to change topic, as this allowed me to explore new topics and be more productive than ever before.
Secondly, I would like to thank Nelson. From the start you were very welcoming to us newcomers. You helped us finding our way in the collaboration and provided a wealth of information. I already miss our insightful discussions during my stays in Nice.
This leaves me to thank a never ending list of colleagues: Tom for being a very patient mentor during my first own project, Irene and Federico to submerge me in the art of noise hunting and data quality investigations at Virgo, Michael for being involved in many of my projects and sharing your expertise, Andrew and Pat for helping me out when I was getting started on O3 data quality investigations, Marie-Anne for sharing her insights in the collaboration life (and politics) and my (Belgian) stochastic colleagues for being this amazing group of enthusiastic and genuine people, in particular Kevin, Alba, Max, Guillaume, Jishnu, Federico, Hannah, Aaron, Stavros, Katarina, Philip and Arianna. I would also like to thank all the co-authors of my publications and the people I have worked together with for helping me improve the work as well as my understanding of the matter at hand.
Furthermore, I am extremely grateful for everyone who helped make the mental well-being survey what it is now. In particular a big shout-out to Michiko for very patiently teaching me how to perform sociological analyses and to the LVK management, Patrick Brady and Giovanni Losurdo for their support of this effort. I also would like to thank the LVK diversity groups and in particular Ray and Tania for their contributions and never ending support. Finally, thank you to the diversity representatives of the Capra, CE, DESI, Fermi LAT and Fermi GBM, IceCube, IPTA, LISA and Vera Rubin collaborations to help me in spreading the survey to a larger audience.

This brings me to acknowledging the support I got from my family.
Laura, it has been a pleasure to have you along my side during this process. It is

strange to realize you were a total stranger at the start of my PhD and now you are (almost) my wife. Time with you went by so quickly that it already seems we have spent many more years together. Thank you for always being a support, cheer for every of my accomplishments and be there for me whenever I needed.
I want to thank my parents and sisters for raising me to be the person I am and support me in my curiosity of exploring the universe.

Finally, I would like to thank everyone, whom we might not always notice, but who make it possible to do our work. I would like to thank the cleaning, kitchen and administrative staff from Universiteit Antwerpen and Université Côte d'Azur and in particular Sarah, Angelique and Khaled.

Funding

I would like to thank 'Fonds wetenschappelijk onderzoek - Vlaanderen' (FWO) for funding my PhD (grant number 11C5720N). Furthermore, I would also like to acknowledge their support for my two half-year stays at the Observatoire Côte d'Azur (grant number V412921N and V433922N). I am grateful to Artemis and the 'Centre national de la recherche scientifique' (CNRS) for providing in my participation in several meetings and conferences and to the Antwerp doctoral school for providing in my participation to the LVK meeting in Cardiff, Sep. 2022.

List of acronyms

2G: Second generation (interferometric gravitational wave detector)
3G: Third generation (interferometric gravitational wave detector)
AION: Atom Interferometer Observatory and Network
ASD: Amplitude spectral density
B1: Photodide most sensitive to the differential armlength at Virgo (contains the gravitational wave signal)
BH: Black hole
BBH: Binary black hole (coalescence event)
BBN: Big bang nucleosynthesis
BNS: Binary neutron star (coalescence event)
BS: Beam splitter
CBC: Compact binary coalescence
CE: Cosmic Explorer
CEB: Central building (of Virgo)
CI: Confidence interval
CMB: Cosmic microwave background
CP: Compensation plate
CPTA: Chinese Pulsar Timing Array
CSD: Cross spectral density
CW: Continuous (gravitational) waves
ELF: Extremely low frequency (magnetic fields, i.e. $3\,\mathrm{Hz}-3\,\mathrm{kHz}$)
ELGAR: European Laboratory for Gravitation and Atom-interferometric Research
EM: End mirror
EMRI: Extreme mass ratio inspirals
EPTA: European Pulsar Timing Array
ET: Einstein Telescope
FAP: False alarm probability
FDP: False dismissal probability
GPS: Global positioning system
GR: General relativity
GRB: γ-ray burst

GWB: Gravitational wave background, sometimes also referred to as stochastic GWB

GW: Gravitational wave

H: LIGO Hanford observatory (also sometimes abbreviated as LHO)

HF: High frequency

hth: Horizontal to horizontal (seismic coupling)

IM: Input mirror

IMC: Input mode cleaner

InPTA: Indian Pulsar Timing Array

IPTA: International Pulsar Timing Array

ITGW: Inside-to-GW channel (magnetic coupling function)

KAGRA: Kamioka Gravitational Wave Detector

L: LIGO Livingston observatory (also sometimes abbreviated as LLO)

LF: Low frequency

LHO: LIGO Hanford observatory (also sometimes abbreviated as H)

LIGO: Laser Interferometer Gravitational-Wave Observatory

LLO: LIGO Livingston observatory (also sometimes abbreviated as L)

LVK: LIGO, Virgo and KAGRA (collaborations)

LSBB: Laboratoire Souterrain à Bas Bruit

$M_\odot$**:** Symbol to indicate 1 solar mass

MAGIS-100: Matter-wave Atomic Gradiometer Interferometric Sensor

MBH(B): Massive black hole (binary)

MCB: Mode cleaner building

MIGA: Matter-wave laser Interferometric Gravitation Antenna

MPTA: MeerTime Pulsar Timing Array

NANOGrav: North American Nanohertz Observatory of Gravitational Waves

NEB: North end building (of Virgo)

NN: Newtonian noise

NP: Noise projection

NSBH: Neutron star - black hole (coalescence event)

O3: LIGO, Virgo and Kagra's third observing run.

O*N*: LIGO, Virgo and Kagra's Nth observing run, with $N = 1;...;5$.

OMC: Ouput mode cleaner

OR: Odds ratio

ORF: Overlap reduction function

OTI: Outside-to-inside (magnetic coupling function)

PHQ-9: Patient Health Questionaire 9 item (question set probing depressive symptoms)

PI: Power-law integrated (sensitivity curve)

POP:	Pick of plate
PR(M):	Power recycling (mirror)
PSD:	Power spectral density
PPTA:	Parkes Pulsar Timing Array
PTA:	Pulsar timing array
SMBH(B):	Supermassive black hole (binary)
SNR:	Signal-to-noise ratio
SR(M):	Signal recycling (mirror)
SSI:	Stochastic search for an intermittent GWB
STEM:	Science, Technology, Engineering, and Mathematics
TBS:	The Bayesian Search
TDI:	Time-delay interferometry
TT:	Transverse-traceless (gauge)
tth:	Tilt to horizontal (seismic coupling)
V:	Virgo
vth:	Vertical to horizontal (seismic coupling)
WEB:	West end building (of Virgo)
ZAIGA:	Zhaoshan Long-baseline Atom Interferometer Gravitation Antenna

Contents

Introduction

After centuries of carefully performed experiments and groundbreaking theories validating and constructively building upon each other, physicists obtained a comprehensive understanding of the Universe. With quantum physics, the Standard Model of elementary particles and general relativity, we are able to describe phenomena from the smallest to the largest scales. So, does this mean there are no exciting discoveries left? The profound knowledge of the Universe pertains to only a tiny fraction of the entire Universe, i.e. barely 5%. This is all the matter we know around us, the planets, the stars, ... However, the Universe also contains about 25% of matter we cannot see, called dark matter, and an unknown form of energy driving the acceleration of the Universe, called dark energy. Even our knowledge of the 5% of the Universe is not perfect. Until today physicist have been unable to reconcile general relativity with quantum mechanics and the Standard Model. With the succession of more precise instruments testing these theories on the largest and smallest scales, we hope to find cracks in the current theories, which will provide us hints for a more fundamental, unified, theory.

In this dissertation I will use gravitational waves (GWs) as a probe of the Universe. More specifically, I searched for a (stochastic) gravitational wave background (GWB). What could be considered as one of the holy grails, is a GWB from fractions of seconds (on the order of 10^{-36} to 10^{-32} seconds) after the Big Bang. It would not only help us reveal the birth of the Universe, but also allow us to probe earlier in time then ever before. The oldest signal we have observed until today is the cosmic microwave background (CMB) coming from an era of 380.000 years after the Big Bang. The CMB originates from the time when light (photons) and matter decoupled, yielding us the oldest snapshot from the Universe accessible with light. Even though the CMB contributes only about 0,005% to the total energy density of the Universe, it revolutionized our knowledge of the early Universe. Penzias and Wilson were awarded a Nobel Prize for their discovery of the CMB.

Apart from a cosmological GWB which could give us profound insights in the early Universe, also a GWB from astrophysical origin is expected. This astrophysical GWB is composed of the incoherent superposition of numerous GW sources e.g. the merger of compact stellar objects such as black holes. Currently different experiments are probing the GWB at levels of 0,0000001% (i.e. 10^{-9}) of the density of the Universe.

That is, one part in one billion. However, do not be fooled. Even though the GWB carries a tiny fraction of the energy of the Universe it could give us critical insights to better understand our Universe, just as was the case for the CMB. Whereas the cosmological GWB will shed light on the birth of the Universe, the astrophysical GWB will elucidate stellar evolution. Maybe even more interesting, it could clarify whether a large population of (primordial) black holes contributes (in part) to the 25% of dark matter in the Universe. Furthermore, general relatively can be tested on an entirely different scale than ever before, allowing us to look for those cracks in the theory, hinting towards new physics.

After the first direct observation of gravitational waves in 2015, the field of GW physics has rapidly gained an impressive list of achievements including the recent announcement of strong evidence for a GWB in the nHz frequency band. Despite these spectacular accomplishments, the field of GW physics could be considered in its 'infancy'. Think of Galileo Galilei looking at stars in the 17th century with the first telescopes and the plethora of discoveries and observations made in the last centuries. Exciting times are ahead of us while exploring the universe through gravitational waves.

In Part I of this thesis I will introduce the different concepts which will be needed to understand the work I have performed. In Part II, I will describe the work I have performed during my PhD while searching for a GWB in the Hz to kHz frequency band. Chapter 6 describes the data quality validations I have performed and which were a critical part of the search for a GWB with data from the third observing run by LIGO and Virgo. In Chapters 7 and 8, the observation of correlated magnetic field fluctuations over Earth-scale distances are discussed as well as their impact on Earth-based GW detectors. This includes the work I performed indicating that next generation of Earth-based detectors such as the Einstein Telescope and Cosmic Explorer should have drastically lower coupling of magnetic fields to their instruments compared to present-day instruments. Otherwise these next generation detectors will not achieve their low frequency design sensitivity. In Chapter 9 we observe correlations in observed seismic velocities over distances of several hundreds of meters. In this chapter, I show how these correlations could have detrimental effects on the Einstein Telescope's capabilities for observing a GWB. Previously this source of correlated noise was not considered, but it is relevant for the Einstein Telescope given its equilateral triangular configuration of three co-located GW detectors. Chapter 10 focuses on a method enabling us to make statistical statements whether a future observation is likely to be of GW or correlated noise origin. Finally, Chapter 11 describes how the null channel will not only be a powerful tool for the estimation of the detector noise of a triangular configuration of GW

detectors, but also how the null channel can provide insights in correlations in noise sources between the detectors. All key conclusions from my work are summarized in Chapter 12. Moreover, I also provide my personal insights on possible future research.

Make sure to stick around till the end as in the appendix the researchers become the researched. I describe a mental well-being survey I conducted in the field of GW astronomy and discuss the results of the first edition which took place in 2021.

I hope you have as much fun reading as I did researching these different topics. Enjoy!

Part I

This thesis focuses on the search for an isotropic gravitational-wave background and the data quality for these searches with Earth-based interferometric detectors. The first part of this thesis introduces the different concepts to understand the work, i.e.: What are gravitational waves? How can one try to measure them directly? How does an interferometric gravitational-wave detector work? What is a gravitational-wave background? What are the most important noise sources that can bias or impede the search for a gravitational-wave background?

These questions will be answered in the next five chapters, to build the framework for my work as described in Part II and understand how it fits into the scientific landscape.

Chapter 1

In this first chapter we start by introducing Albert Einstein's theory of general relativity and how gravitational waves are predicted by this theory. We discuss the propagation of gravitational waves, their generation and how they interact with test masses.

Chapter 2

A short introduction is given of the different detector types one can use to directly observe gravitational waves. Afterwards a more detailed description of Earth-based interferometric gravitational-wave detectors is given, since they form the focus of this work.

This chapter contains content which is based on a review paper written in collaboration with N. van Remortel and K. Turbang published in [356].

Chapter 3

This chapter discusses the possible gravitational-wave sources across the frequency spectrum, both for individually resolvable signals as for the gravitational-wave background. We end the chapter with a short history of attempts to measure these gravitational waves and discuss the first direct observation of gravitational waves in 2015 by the LIGO and Virgo collaborations.

Chapter 4

We introduce the gravitational-wave background, a weak background of gravitational waves made up out of the superposition of a large number of individual sources. The (an)isotropy of the gravitational-wave background is discussed as well as analysis methods currently used and under development for Earth-based interferometric detectors.

Chapter 5

In this chapter we discuss the main categories of noise sources that can affect the search for a gravitational-wave background. The discussion in this chapter is relatively limited and focuses on the general concepts. More detailed discussions and discriptions will be given in Part II of this thesis since the study of these noise sources forms a substantial part of my work.

The content of this chapter is partially based on Sec. 5.1 of a review paper written in collaboration with N. van Remortel and K. Turbang [356].

1 General relativity and gravitational waves

> *Gravitational waves will bring us exquisitely accurate maps of black holes - maps of their spacetime. Those maps will make it crystal clear whether or not what we're dealing with are black holes as described by general relativity.*
>
> **— Kip Thorne**

In this chapter we will briefly describe how Albert Einstein's theory of general relativity (GR) [154–157] can describe gravitational waves (GW). We start by introducing gravity as spacetime curvature (Sec. 1.1). Afterwards we will discuss the so-called linearized theory of GR (Sec. 1.2). In Sec. 1.3-1.6 will discuss the propagation and creation of GWs in the linearized theory of Einstein's GR.

The mathematical component of this chapter is inspired on the derivations explained in the works by M. Maggiore [254] and S. Carroll [112]. The interested reader can turn to these works for a more detailed discussion of the topics which will be summarized in this chapter.

1.1 Gravity as spacetime curvature

The principal idea of Einstein's GR is that gravity is a part of the spacetime itself, in contrast to other forces which can be represented by fields on this spacetime [112]. Within GR, gravity can be understood as an effect from the curvature of spacetime. At its basis, a spacetime is defined by its metric $\mathrm{g}_{\mu\nu}$, which is a symetric two dimensional tensor (i.e. a matrix). The metric of flat spacetime (often also known as Minkowski space) is traditionally referred to by its own notation $\eta_{\mu\nu}$. We will use the convention $\eta_{\mu\nu} = diag(-1, +1, +1, +1)$. Furthermore we use the convention where Greek indices such as μ, ν,... run over 0,...,3. The zeroth index is

the time index and to refer to the spatial indices only, i.e. 1,2,3 Latin indices such as i,j,... are used.

The Riemann (curvature) tensor is given by

$$\mathrm{R}^{\rho}{}_{\sigma\mu\nu} = \partial_\mu \Gamma^{\rho}_{\nu\sigma} - \partial_\nu \Gamma^{\rho}_{\mu\sigma} + \Gamma^{\rho}_{\mu\lambda}\Gamma^{\lambda}_{\nu\sigma} - \Gamma^{\rho}_{\nu\lambda}\Gamma^{\lambda}_{\mu\sigma}, \tag{1.1}$$

where $\Gamma^{\rho}_{\mu\nu}$, also known as the 'Christoffel symbol', is related to the spacetime metric as follows,

$$\Gamma^{\rho}_{\mu\nu} = \frac{1}{2}\mathrm{g}^{\rho\sigma}(\partial_\mu \mathrm{g}_{\nu\sigma} + \partial_\nu \mathrm{g}_{\sigma\mu} - \partial_\sigma \mathrm{g}_{\mu\nu}). \tag{1.2}$$

The Riemann tensor gives us information on the curvature of the spacetime and only vanishes in the case of a flat spacetime. From the Riemann tensor one can also construct the Ricci tensor ($\mathrm{R}_{\mu\nu}$) by making a contraction as follows

$$\mathrm{R}_{\mu\nu} = \mathrm{R}^{\lambda}_{\mu\lambda\nu}. \tag{1.3}$$

The trace of the Ricci tensor is the Ricci (curvature) scalar,

$$\mathrm{R} = \mathrm{R}^{\mu}{}_{\mu} = \mathrm{g}^{\mu\nu}\mathrm{R}_{\mu\nu}. \tag{1.4}$$

Now that we can describe curvature, we still have to define the energy-momentum tensor $T^{\mu\nu}$. This tensor can be conceived as describing the flux of four-momentum p^μ across a surface of constant x^ν. The T^{00} component can be understood as the energy density, since it represents the energy flux (p^0) moving along the time (x^0) direction. Similarly, the momentum density is given by the terms $T^{0i} = T^{i0}$. The remaining (spatial) T^{ij} components describe the forces between neighboring infinitesimal elements and are often referred to as the 'stress'. The diagonal and off-diagonal components represent respectively the pressure and shear terms.

With all these definitions and nomenclature at hand we are ready to understand the Einstein equations. These equations are one of the central outcomes of Einstein's GR and they describe how the spacetime metric responds to energy and momentum and vice-versa. The Einstein equations are given by,

$$\mathrm{R}_{\mu\nu} - \frac{1}{2}\mathrm{g}_{\mu\nu}\mathrm{R} = 8\pi T_{\mu\nu} G, \tag{1.5}$$

where G is Newton's gravitational constant. Note, here we have implicitly assumed the speed of light to be $c = 1$. The Einstein equations describe how the curvature of spacetime changes in the presence of energy and momentum. Note that large

amounts of mass and or energy are needed to make a noticeable impact on the spacetime curvature due to the smallness of G, i.e. $G \approx 6.67 \cdot 10^{-11} \mathrm{m}^3\,\mathrm{kg}^{-1}\,\mathrm{s}^{-2}$

1.2 Linearized theory

The most straightforward approach to understand how GWs appear in GR is the so-called 'linearized theory', where the Einstein equations are expanded around the metric of flat spacetime. To this extent we can write

$$g_{\mu\nu} = \eta_{\mu\nu} + h_{\mu\nu}, \tag{1.6}$$

where we require $h_{\mu\nu}$ to be small, i.e. $|h_{\mu\nu}| \ll 1$. Here we imply that we can choose a reference frame such that this holds on a large enough region of space. However by choosing a reference frame we break the invariance of GR under all coordinate transformations $x^\mu \to x'^\mu(x)$, where x'^μ is a smooth function of x^μ, i.e. invertable, differentiable and with a differentiable inverse. This symmetry is referred to as GRs 'gauge symmetry'. Even though this symmetry is broken by choosing a reference frame in which Eq. 1.6 is valid, a residual gauge symmetry remains

$$x^\mu \to x'^\mu(x) = x^\mu + \xi^\mu(x), \tag{1.7}$$

with the derivatives $|\partial_\mu \xi_\nu|$ being small at the same order as $|h_{\mu\nu}|$. The change of the spacetime metric under a general coordinate transformation $x^\mu \to x'^\mu(x)$ is given by

$$g_{\mu\nu}(x) \to g'_{\mu\nu}(x') = \frac{\partial x^\rho}{\partial x'^\mu} \frac{\partial x^\sigma}{\partial x'^\nu} g_{\rho\sigma}(x). \tag{1.8}$$

Therefore the metric perturbation under the remaining gauge symmetry as introduced in Eq. 1.7, becomes

$$h_{\mu\nu}(x) \to h'_{\mu\nu}(x') = h_{\mu\nu}(x) - (\partial_\mu \xi_\nu + \partial_\nu \xi_\mu). \tag{1.9}$$

By merit of requiring $|\partial_\mu \xi_\nu|$ being small at the same order as $|h_{\mu\nu}|$, $|h_{\mu\nu}| \ll 1$ is preserved and the transformations defined by Eq. 1.7 are symmetries of linearized GR. Linearized GR is furthermore invariant under Lorentz transformations as well as under constant translations. Neither will be discussed here in more detail and we refer the interested reader to [254].

By combining Eq. 1.6 together with Eq. 1.1 and Eq. 1.2, one can show that up to first order in $h_{\mu\nu}$ the Riemann tensor becomes

$$\mathrm{R}_{\mu\nu\rho\sigma} = \frac{1}{2}(\partial_\nu\partial_\rho h_{\mu\sigma} + \partial_\mu\partial_\sigma h_{\nu\rho} - \partial_\mu\partial_\rho h_{\nu\sigma} - \partial_\nu\partial_\sigma h_{\mu\rho}). \tag{1.10}$$

To write the linearized version of the Einstein equations we will introduce h, the trace of the small metric perturbation $h_{\mu\nu}$, as well as the trace-reversed metric perturbation $\bar{h}_{\mu\nu}$. By using the convention to raise and lower indices in linearized theory by the flat metric $\eta_{\mu\nu}$ the trace and $\bar{h}_{\mu\nu}$ are respectively given by

$$h = \eta^{\mu\nu} h_{\mu\nu} \tag{1.11}$$

and

$$\bar{h}_{\mu\nu} = h_{\mu\nu} - \frac{1}{2}\eta_{\mu\nu} h. \tag{1.12}$$

Given that $\bar{h} = -h$, the inverted equation yields

$$h_{\mu\nu} = \bar{h}_{\mu\nu} - \frac{1}{2}\eta_{\mu\nu}\bar{h}. \tag{1.13}$$

By substituting Eq. 1.13 in Eq. 1.10 and subsequently computing the Ricci tensor and Ricci scalar the linearized Einstein equations are found:

$$\Box\bar{h}_{\mu\nu} + \eta_{\mu\nu}\partial^\rho\partial^\sigma\bar{h}_{\rho\sigma} - \partial^\rho\partial_\nu\bar{h}_{\mu\rho} - \partial^\rho\partial_\mu\bar{h}_{\nu\rho} = -\frac{16\pi G}{c^4}T_{\mu\nu} \tag{1.14}$$

Here we have introduced the d'Alembertian which is given by the d'Alembertian of flat space in linearized GR: $\Box = \eta_{\mu\nu}\partial^\mu\partial^\nu$. Given the definition of the partial derivative $\partial_\mu = \frac{\partial}{\partial x^\mu} = (1/c \cdot \partial_t, \partial_i)$, this also reduces to $\Box = -(1/c^2)\partial_t^2 + \nabla^2$.

Furthermore, we can use the remaining gauge freedom to choose

$$\partial^\nu\bar{h}_{\mu\nu} = 0. \tag{1.15}$$

This gauge is often also known as the Lorentz gauge. For a derivation why this gauge satisfies Eq. 1.7 we refer the interested reader to [254]. In this gauge the linearized Einstein equations simplify to a simple wave equation

$$\Box\bar{h}_{\mu\nu} = -\frac{16\pi G}{c^4}T_{\mu\nu}. \tag{1.16}$$

Note that the conservation of energy-momentum ($\partial^\nu T_{\mu\nu} = 0$) is implied by consistency among Eq. 1.15 and Eq. 1.16.

1.3 Gravitational waves in the transverse-traceless gauge

To study how gravitational waves propagate we are interested in the Einstein equations outside the source, i.e. where $T_{\mu\nu} = 0$,

$$\Box \bar{h}_{\mu\nu} = 0. \tag{1.17}$$

With the definition of the d'Alembertian (see previous section) this implies GW travel at the speed of light in GR.

The Lorentz gauge introduced in Eq. 1.15 does not fix the gauge freedom entirely. More specifically four degrees of freedom are left and an additional coordinate transformation $x^\mu \to x^\mu + \xi^\mu$ is allowed if

$$\Box \xi_\mu = 0. \tag{1.18}$$

ξ^0 can be chosen such that the trace of $\bar{h}$=0=h. This in turn implies $h_{\mu\nu} = \bar{h}_{\mu\nu}$. The remaining three degrees of freedom can be chosen to have vanishing terms $h^{0i}(x) = 0$. This is called the transverse-traceless gauge often also abbreviated by TT. This implies the $\mu = 0$ Lorentz condition (Eq. 1.15) yields

$$\begin{aligned} \partial^0 h_{00} + \partial^i h_{0i} &= 0 \\ \Downarrow\ h_{0i} &= 0 \\ \partial^0 h_{00} &= 0. \end{aligned} \tag{1.19}$$

Since we are interested in the GW, which is the time varying part of the metric, Eq. 1.19 implies $h_{00} = 0$. The remaining condition from the Lorentz gauge reads $\partial^j h_{ij} = 0$.

The solution to the Einstein equations become

$$h_{ij}^{TT}(t,z) = \begin{pmatrix} h_+ & h_\times & 0 \\ h_\times & -h_+ & 0 \\ 0 & 0 & 0 \end{pmatrix}_{ij} \cos[w(t - z/c)], \tag{1.20}$$

where we have assumed the plane wave traveling along the z-axis. h_+ and $h_\times$ are the amplitudes of respectively the 'plus' and 'cross' polarisation.

1.4 Observer frame and geodesic equation

In general relativity a specific gauge choice can be interpreted as being linked to a specific observer and their own reference frame. The frame linked to the TT gauge is called the TT frame. The frame naturally linked to the detector is called the detector proper frame [254]. To understand what it means to choose a certain frame we will introduce the geodesic equation as well as the geodesic deviation equation. For a derivation and more detailed discussion we refer to interested reader to [112, 254]. The geodesic equation is given by,

$$\frac{d^2x^\mu}{d\tau^2} + \Gamma^\mu_{\nu\rho}(x)\frac{dx^\nu}{d\tau}\frac{dx^\rho}{d\tau} = 0, \tag{1.21}$$

where τ is the proper time. The geodesic equation describes how test masses move in a curved spacetime described by the metric $g_{\mu\nu}$.

To understand the deviation of the geodesic one can parametrize two nearby geodesics by respectively $x^\mu(\tau)$ and $x^\mu(\tau) + \xi^\mu(\tau)$. If one chooses $|\xi^\mu|$ to be much smaller than the typical variations of the gravitational field, one can show the geodesic deviation equation is given by [112],

$$\frac{D^2\xi^\mu}{D\tau^2} = -R^\mu_{\nu\rho\sigma}\xi^\rho\frac{dx^\nu}{d\tau}\frac{dx^\sigma}{d\tau}. \tag{1.22}$$

Here $D\xi^\mu/D\tau$ is the covariant derivative defined as

$$\frac{D\xi^\mu}{D\tau} \equiv \frac{d\xi^\mu}{d\tau} + \Gamma^\mu_{\nu\rho}\xi^\nu\frac{dx^\rho}{d\tau}. \tag{1.23}$$

The geodesic deviation equation illustrate how nearby time-like geodesics are affected by curved spacetime as determined by the Riemann tensor.

1.5 Interaction of gravitational waves with test masses

1.5.1 Transverse-traceless frame

Even though the proper detector frame is the most natural frame to study the effect of a passing GW on a test mass, it is interesting to see its effect in the TT frame. In this work we restrict ourselves to a qualitative description and for more detailed derivation we refer the reader to [254].

Particles which are at rest in the TT frame before the arrival of a GW remain at rest afterwards as well (to linear order in h). This is true since the coordinates of the TT frame adapt themselves to the passing GW such that the positions of the test masses remain identical. This seems to suggest that there is no effect at all on a test mass due to the passing GW in the TT frame. However the physical effect is not described by the coordinate distance/time but rather by the proper distance/time. If we consider a GW traveling along the z-axis and two test masses given by (t,x_1,0,0) and (t,x_2,0,0), with $x_2 - x_1 = L$, the proper distance is given by

$$s \simeq L\left[1 + \frac{1}{2}h_+ \cos(\omega t)\right]. \tag{1.24}$$

Please note that here we have only kept terms up to linear order in h_+. The effect of the passing GW is an effect on the distance given by

$$\Delta L = \frac{1}{2}h_+ \cos(\omega t)L. \tag{1.25}$$

This equation yields several insights into how we can try to observe GWs by observing their effect on test masses. First we notice that to measure the effect from the GW, $h_+ \cos(\omega t)$, we should try to measure the induced length difference ΔL. Second, since ΔL is proportional to the length scale L of e.g. the detector, this will play an important role in increasing the detectors sensitivity. Possible detector designs and how they try to observe $\Delta L/L$, also known as the GW strain, will be discussed in Chapter 2.

1.5.2 Proper detector frame

When describing the proper distance in the proper detector frame one should distinguish between a space-based and an Earth-based detector. Consider a test mass on board of a drag-free satellite, the test mass is free falling in the gravitational field of both the Earth as well as the GW. An Earth-based detector on the other hand experiences an acceleration due to Earth's gravity. This leads to multiple effects such as Newtonian gravity and Coriolis forces, with which the GWs need to compete [254]. However one can choose a regime in which these additional terms are small and an Earth-based detector can be considered to have free falling test masses. A first condition is that the GWs have larger frequencies compared to the frequencies of the other effects. Given the natural frequencies of Newtonian noises on the Earth, this implies that the frequencies of the GWs have to be above several Hz. At lower frequencies other effects will be dominant. A suspensions system is needed to

mitigate the acceleration introduced by Earth's gravity and therefore the test mass can only be considered to be freely falling in the remaining degrees of freedom, not restricted by the suspensions. With these assumptions for Earth-based detectors one can write the geodesic deviation equation as follows [254]

$$\ddot{\xi}^i = \frac{1}{2}\ddot{h}^{TT}_{ij}\xi^j. \tag{1.26}$$

Here we have used a dot to indicate a time derivative, i.e. $\dot{f}(t) = \partial_t f = c\partial_0 f$, where the last equality holds based on the definition of ∂_μ introduced in Sec. 1.2. Eq. 1.26 shows that the effect from a GW in the proper detector frame on a freely falling pointlike test mass with mass m is a Newtonian force given by

$$F_i = \frac{m}{2}\ddot{h}^{TT}_{ij}\xi^j \tag{1.27}$$

In Eq. 1.26 and Eq. 1.27 the GW contribution from the TT gauge appears, even though we are in the proper detector frame. This is since the Riemann tensor is invariant and therefore can be computed in any frame, thus also the TT frame.

In the derivations leading to Eq. 1.26 the Christoffel symbols are calculated to linear order in ξ^μ. To satisfy this condition it implies the characteristic length-scale of the detector L is much smaller than the length-scale of the GWs, i.e. the reduced wavelength λ. This condition is met for bar detectors and to first approximation for Earth-based interferometric detectors. For space based interferometric detectors and spacecraft Doppler tracking the condition is not met and additional terms have to be taken into account. The different detector types will be introduced in more detail in Chapter 2.

To understand the effect of a passing GW on spacetime, we consider a ring of test masses and take the origin of the coordinate system in the center of the ring. This implies the distance from the origin is described by ξ^i. We assume the ring of test masses to lie within the x-y plane and the GW to travel along the $\hat{\mathbf{z}}$-direction. This choice is supported by the fact that the effect described in Eq. 1.26 depends on the GW in the TT frame. Therefore the physical effect of a GW traveling along the $\hat{\mathbf{z}}$-direction is fully in its transverse plane, i.e. the x-y plane. By using the definition of h^{TT} (Eq. 1.20) one can show the effect from the GW on the ring of test masses is as shown in Fig. 1.1.

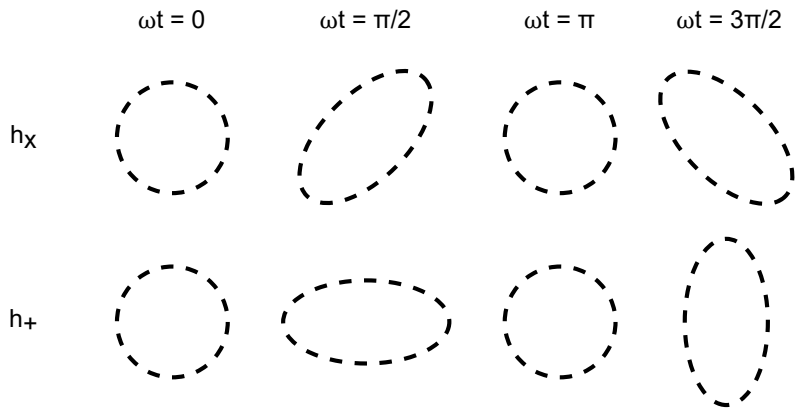

Fig. 1.1.: The effect of a gravitational wave traveling along the $\hat{\mathbf{z}}$-direction on a ring of test masses in the x-y plane.

1.6 Generation of gravitational waves in linearized general relativity

If we want to consider the generation of GWs in linearized GR, this implies we assume the spacetime to be sufficiently flat. In realistic sources of GWs this is not the case, however some insights can be gained from linearized GR which also hold in a more complete theory taking into account the effects of the curvature of the spacetime. Furthermore we will assume the velocity v of the source is small enough with respect to the speed of light c such that an expansion in terms of v/c is possible.

To perform the calculation of the generation of GW in linearized GR one needs to start from the linearized version of the Einstein equations, as given in Eq. 1.16. In Sec. 1.3 we looked at the propagation of GWs by putting the energy momentum tensor $T_{\mu\nu}$ to zero since we were interested in the solution outside the source. However to study the production of GWs one is interested in exactly the case where $T_{\mu\nu}$ is non-zero. In this work we will only summarize some of the most important insights and refer the interested reader to [254] for a derivation and more detailed description of the calculations. By working in the TT gauge one looks for h_{ij}^{TT} when solving Eq. 1.16. It is found that the lowest multipole contributing to h_{ij}^{TT} are time derivatives of the mass quadruple, where both the monopole and dipole terms vanish. In linearized theory the monopole and dipole, respectively depend on the

energy density moment M and the momentum density moment P^i. The energy and momentum density moments are respectively given by

$$\begin{aligned} M &= \frac{1}{c^2}\int d^3x\, T^{00}(t,\hat{\mathbf{x}}), \\ P^i &= \frac{1}{c}\int d^3x\, T^{0i}(t,\hat{\mathbf{x}}). \end{aligned} \tag{1.28}$$

However static sources do not produce GWs and h_{ij}^{TT} depends on the time derivatives of these quantities. In linearized theory both M and P are conserved and therefore no monopole or dipole contributions are present. Even though this is no longer true more generally, the monopole and dipole terms still vanish. For the derivation and discussion of this we refer the interested reader to [112, 254].

The quadrupole moment is defined as

$$Q^{ij} = \int d^3x \rho(t,\hat{\mathbf{x}}) \left(x^i x^j - \frac{1}{3} r^2 \delta^{ij} \right), \tag{1.29}$$

where $\rho(t,\hat{\mathbf{x}})$ is the mass density and $r = |\hat{\mathbf{x}}|$. The radiated power or GW luminosity is given by

$$\mathcal{L}_{\text{quadrupole}} = \frac{G}{5c^5} \langle \dddot{Q}_{ij} \dddot{Q}_{ij} \rangle. \tag{1.30}$$

We want to point out that the quadrupole moment has to be evaluated at the so called 'retarded time'. This is the time when the gravitational waves were emitted at the source. Eq. 1.30 and the definition of the quadropole moment in Eq. 1.29 teach us that the GW luminosity is only non-zero for time-varying, asymmetric mass densities. In next section we will give several examples of sources that produce gravitational waves and divide them in four categories based on their signal characteristics.

Gravitational-wave detectors

2

> *The most exciting science requires the most complex instruments.*
>
> **— Barry Barish**

There are several detection methods one can utilize to directly measure gravitational waves. In Sec. 2.1 we provide a short overview of the different methodologies. My PhD focuses on ground based gravitational-wave interferometric detectors, which will be discussed in more detail in Sec. 2.2.

2.1 Overview of different detection methods

A first method to observe GWs is to use resonant objects, as it was first conceived by Weber [362]. A massive object will be set into resonance upon the passage of a gravitational wave with a frequency equal to the natural frequency of the object. Human-made resonant mass detectors are typically sensitive to GWs in the kHz frequency band [306]. Planetary objects however, such as the Earth or the Moon are sensitive to GWs with frequencies between $\sim$ mHz-Hz [131, 193] (see Sec. 2.1.1).

Alternatively one can rely on electromagnetic radiation traveling between free falling test masses to study the distortion of spacetime caused by GWs. Namely, the beam of electromagnetic radiation can be used to study how the distance between the test masses changes when a GW passes by. Thus far, this has been the most successful method for GW detection, leading to the first direct detection of GWs in 2015 (see Chap. 3, Sec. 3.3). Earth- and space-based interferometric gravitational-wave detectors, pulsar timing arrays (PTAs) as well as spacecraft Doppler tracking belong to this category. In Sec. 2.1.2 PTAs are discussed, whereas in Sec. 2.1.3 we will discuss present day and future interferometric gravitational-wave detectors, which are often also referred to as 'laser interferometers'. We will not discuss spacecraft Doppler tracking, but refer the interested reader to [69, 304]. In Sec. 2.1.4 we will discuss the basic working principle of atom interferometers and highlight some of the current as well as proposed atom interferometers designed to search for GWs.

Finally, we would like to mention another technique which can be used to search for gravitational-wave backgrounds from cosmological origin[1], as these leave a polarization imprint on already measured quantities such as the Cosmic Microwave Background (CMB) [149, 285] measurements, as well as primordial deuterium abundance from Big Bang nucleosynthesis (BBN) [226]. Therefore one can use these experiments to place upper limits on a gravitational-wave background of cosmological origin.

2.1.1 Planetary bodies as resonant gravitational-wave detectors

In this section we will discuss how planetary bodies can be used as resonant objects to search for GWs, where we will use both the Earth and the Moon as examples.

GWs are expected to interact with elastic bodies and thus also with the Earth. Therefore, GWs can excite Earth's free oscillations, called normal modes. Using a network of gravimeters and seismometers, it is possible to monitor Earth's normal modes and excitations thereof by the passage of a GW [131]. By comparing these excitation's of the normal modes to the precise prediction for the Earth's response to the passage of a GW and the correlation across various gravimeters and seismometers, one can search for GWs.

More recently, the idea to use the Moon as a GW experiment was put forward [193]. At the core of this idea lies the same principle as the one used for the Earth's normal modes measurements described above. The Lunar Gravitational-Wave Antenna experiment entails the deployment of seismometers on the Moon to measure its normal modes and measure or constrain GWs. This experiment would be sensitive to the normal modes of the Moon within the 1mHz to 1Hz frequency band excited by GWs. An advantage compared to using the Earth as a GW observatory is the lower seismic activity of the Moon. Indeed, the absence of oceans and lower tidal activity increases the ability of seismometers on the Moon to detect GWs. The main seismic noise sources include Moonquakes and meteoroid impacts. The latter has been shown to be below the targeted sensitivity of the experiment [193], while the annual rate of seismic energy release has been shown to be up to 8 orders of magnitude smaller than on Earth [223].

[1] The different types of gravitational-wave backgrounds and their origin will be discussed in more detail in Chapter 3.

2.1.2 Pulsar timing and astrometry

Pulsars are highly magnetized, rapidly spinning neutron stars. Since their magnetic poles are misaligned with respect to the rotational poles, electromagnetic radiation, which is emitted at the magnetic poles, shows up as a pulse on Earth, assuming that the Earth is in the sweeping circle of the pulse. Due to their very stable conditions these pulsars (we will focus on millisecond pulsars) have very predictable arrival times for the pulses, often known with μs or even better precision [141, 248]. Therefore they can be used as clocks.

If a GW passes it will disturb spacetime and therefore introduce a disturbance in the time of arrival. The measurement depends both on a term describing the effect of the GW at the pulsar as well as at Earth, respectively referred to as the pulsar term and the Earth term. However, to reduce the effect of other non-GW processes introducing uncertainties, one typically wants to use a larger set of pulsars and look for a correlation in the disturbance of the time of arrival [248]. Furthermore GWs couple in a specific way to these pulsars. For an isotropic, all sky GW signal, i.e. an isotropic gravitational-wave background, this results in a unique spatial correlation between different pulsars if they are all affected by the same GW. This spatial correlation was derived by Hellings & Downs [198]. The 'Hellings & Downs curve' is given by,

$$C(\gamma) = \frac{3}{2}\left(\frac{1-\cos\gamma}{2}\ln\frac{1-\cos\gamma}{2} - \frac{1}{6}\frac{1-\cos\gamma}{2} + \frac{1}{3}\right), \tag{2.1}$$

where γ is the angular sky separation between any two pulsars. This specific spatial correlation between different pulsars is an important validation for the detection of GWs with PTA to bolster against different noise sources. Recent work looks into the variance in this correlation [53]. The Hellings & Downs curve is shown in black dashed on Fig. 3.2 in Chapter 3, where we discuss the latest PTA results. Several PTAs recently found strong evidence for a nHz GW signal.

Pulsars do not only have so called white noise but also red noise [248]. Since the latter mimics a GW signal one has to measure longer to average out the incoherent red noise of different pulsars to claim a detection. This also implies that observing a common red noise spectrum is not considered to be a 'smoking gun' evidence for detection, but one has to observe the Hellings & Downs spatial correlation.

To get a more accurate measurement of this Hellings & Downs curve one wants to have a large number of pulsars in each angular resolution bin. Namely, the pulsars each observe a different effect of the GWs and the phase of the pulsar term depends

on the distance to the pulsars which is known with limited accuracy. This limited accuracy will introduce incoherent noise with which the coherent signal from the effect of the GW on the Earth term has to compete. If one has multiple pulsars in a given angular resolution bin, one can average out the incoherent noise of the pulsar term as to reveal the coherent Earth term which follows the Hellings & Downs curve in the presence of a GW signal [248].

Other difficulties in PTA measurements are the fits of the timing models, which depend on pulsar parameters such as the rotationial period and its variation with time (the spindown) [248]. They are estimated from the pulsar signal since there is no independent method to determine them with sufficient precision. This implies that the model could already contain (and subtract) some GW contribution

Finally, over recent years the telescopes used for observation have broadened their frequency range. This drastically increases the signal-to-noise ratio (SNR) since it scales with the frequency band in which the pulsar is observed [248] and therefore reduces the time needed for detection. However, in PTA analyses the time of arrival is typically determined for the pulse averaged over the observed frequencies. Since the pulse shape of the pulsar depends on the frequency in which it is observed, the shape of the averaged pulse changes depending on which frequency range is used. In turn this introduces uncertainties in the time of arrival of this averaged pulse. Therefore different alternative schemes are investigated to reduce this uncertainty [248].

The frequencies to which PTAs are sensitive depend on the available data. Each pulsar is typically observed once every 1-2 week(s) [248] and therefore typically long data sets are used. The lowest frequencies that can be probed, are inversely proportional to the observing time. Given the latter is on the order of 10 years, PTA can probe down to $\sim$1nHz-10nHz. These are also the GW frequencies to which PTAs are most sensitive, however they can be sensitive to GWs with frequencies as large as $\sim 1\mu$Hz.

PTAs are mainly used to search for long duration GW signals, i.e. 'continuous GWs' or a gravitational-wave background signal[2]. However, this requires, extremely long data-sets ($\mathcal{O}(10\text{years})$) to get sufficient sensitivity. Additionally, these data sets typically contain many gaps in observing time. However PTA can observe GW bursts[3], i.e. signals which are short lived with respect to their observation time of $\mathcal{O}(10\text{years})$, e.g. a month long signal would be considered a burst for a PTA detection [105, 248]. In case these burst signals are significantly shorter compared to the

[2]Both types of GW signals will be introduced in Chapter 3
[3]This GW signal type will be introduced in Chapter 3.

timescale of the red noise processes in the pulsars, one just needs several pulsars to differentiate between the red noise processes and a GW signal.

There are multiple PTA collaborations active, namely the *North American Nanohertz Observatory of Gravitational Waves* (NANOGrav) [260], the *European Pulsar Timing Array* (EPTA) [238], the *Parkes Pulsar Timing Array* (PPTA) [205], the *Indian Pulsar Timing Array* (InPTA) [284], the *MeerTime Pulsar Timing Array* (MPTA) [333] and *Chinese Pulsar Timing Array* (CPTA) [236]. More recently NANOGrav, EPTA, PPTA and InPTA also joined forces in the overarching *International Pulsar Timing Array* (IPTA) consortium [206]. MPTA and CPTA are IPTA observers.

Despite all the challenges mentioned earlier, the different PTAs announced in June 2023 to have found strong evidence for a nHz gravitational-wave background [45, 65, 293, 367]. Their observations will be discussed in Chapter 3, Sec. 3.3.

Astrometry follows a similar principle as PTA [96, 289], where you rely on the precise astrometric measurement of a moderate number of stars. Note, these objects will not serve as clocks, but with very accurate measurement of their astrometric parameters one could observe changes induced by passing GWs. This field is considerably less developed compared to the PTA community, since there is a very large availability of highly precise pulsar timing measurements. However, as mentioned earlier, due to the observation cadence, PTAs are mainly sensitive to GWs with frequencies around 10nHz. By using high precision measurements of other stars, i.e. GW astrometry, one can select the sources such that the network is mainly sensitive to GWs between 10nHz and 1μHz. Therefore astrometry could be opening the window onto the Universe in a different frequency band. We want to mention that also other methods such as the use of asteroids [165] or a space-based interferometric detector for the 2050 decade [321] have been proposed to observe in the μHz frequency band. However, neither of these proposals will be discussed further.

2.1.3 Interferometric detectors

In this section we will discuss some of the basic concepts of GW interferometric detectors [303] and how they can be used for observing GWs. My PhD focusses on searches for a gravitational-wave background (see Chapters 3 and 4) and its data quality (see Chapter 5) with Earth-based interferometric detectors. Therefore in Sec. 2.2 we will give a more detailed description of the practical implementation of Earth-based interferometric GW detectors.

The response of an interferometer to GWs can be expressed as a 'strain' measured in the two arms of an interferometer: $h = \frac{\Delta L(t)}{L}$, where L is the arm length of the interferometer and ΔL is the change in length due to the passage of a GW. The strain signal $s(t)$ introduced in a laser intereferometric detector by GWs considering multiple polarization modes $h_A(t)$, is given by [151, 366]

$$s(t) = \sum_A d_{ij} e_A^{ij} h_A(t), \tag{2.2}$$

where we have used the long-wavelength approximation, i.e. when the wavelength of the GWs is large compared to the detector's geometry. Furthermore we assumed a sum over i,j and e_A^{ij} is the symmetric polarization tensor of mode A. The detector response d_{ij} is given by [297, 366]

$$\begin{aligned} \hat{\mathbf{d}} &= \frac{1}{2}(\hat{\mathbf{e}}^1 \otimes \hat{\mathbf{e}}^1 - \hat{\mathbf{e}}^2 \otimes \hat{\mathbf{e}}^2), \text{ with components} \\ d_{ij} &= \frac{1}{2}(e_i^1 e_j^1 - e_i^2 e_j^2), \end{aligned} \tag{2.3}$$

where $\hat{\mathbf{e}}^1$ and $\hat{\mathbf{e}}^2$ are the unit vectors along the interferometer's arms and $\otimes$ represent a tensorial product. For interferometer I we can define

$$F_I^A(\hat{\mathbf{n}}) = d_{I,ij} e_A^{ij}(\hat{\mathbf{n}}), \tag{2.4}$$

where we have explicitly introduced the dependence on the location of the GW source, with $\hat{\mathbf{n}}$ a vector pointing towards the source. F_I^A is called the antenna pattern function for detector I, with respect to GWs with polarisation A.

Earth-based interferometric gravitational-wave detectors have an arm length of several kilometers and are sensitive to GWs from a few Hz to a few kHz. To increase their sensitivity to passing GWs, they use a Fabry-Pérot cavity to increase the effective path length of the laser light [303], which will be discussed in more detail in Sec. 2.2.1.

Currently there are five operational Earth-based interferometric gravitational-wave detectors: Advanced LIGO[4] Hanford, Advanced LIGO Livingstonn [3], Advanced Virgo [37], KAGRA[5] [71] and GEO600 [250]. The first direct detection of GWs, made by Advanced LIGO in 2015, will be discussed in Chap. 3, Sec. 3.3. Both KAGRA and GEO600 did not reach the required sensitivity to observe the GW events observed by the LIGO and Virgo instruments during the most recent third observing run (O3)[6]

[4] Laser Interferometer Gravitational-Wave Observatory.
[5] Kamioka Gravitational-Wave Detector
[6] O3 started April 1st 2019 and ended March 27th 2020, where the month of October was used for further commissioning the detectors.

by the LIGO, Virgo and KAGRA (LVK) collaborations. KAGRA should reach a similar level of sensitivity over the coming years with the planned upgrades [52, 71, 271], whereas GEO600 will not. GEO600 focuses on researching technical challenges as well as taking data over long observation periods while other observatories (e.g. Advanced LIGO and Advanced Virgo) are being upgraded [58]. Advanced LIGO and Advanced Virgo undergo further upgrades to improve their sensitivity to the so-called A+ and AdV+ sensitivities for respectively LIGO and Virgo. These are planned to by reached during the fifth observing run (O5). Advanced LIGO and Advanced Virgo are often referred to as second generation (2G) detectors, since they have a significantly improved sensitivity compared to (initial) LIGO and (initial) Virgo. KAGRA is sometimes referred to as a 2.5G detector due to the implementation of some fundamentally new technologies, which will be more discussed in Sec. 2.2.1.

To extend the Earth-based LVK network, there are plans to have a third LIGO detector in India, which could become operational later this decade [74, 312]. At the same time, there are also plans to build interferometers that will be ten times more sensitive in their measured strain than LIGO and Virgo. Two such examples are the Einstein Telescope (ET) [56, 161, 201, 255, 288] and Cosmic Explorer (CE) [299], planned to become operational sometime in the next decade. ET and CE are referred to as third generation (3G) interferometric GW detectors, due to their drastic increase in sensitivity.

To reach larger distances between test masses in order to explore lower frequency ranges, one can build interferometers in space. Until today, there are no operational space-based laser interferometers. Nevertheless, the Laser Interferometer Space Antenna (LISA) is planned to launch somewhere in the 2030s [57, 138]. As of May 2022, the LISA mission design passed through Phase A, allowing to proceed for final design, opening up the path towards adoption of the mission by 2024. With its 2.5 million km long arms, LISA will be able to measure GWs in the 0.1mHz-1Hz frequency band. The proposed TianQin [251, 262] interferometer planned to start operating around 2035, will be sensitive to GWs in the same frequency region as LISA. Also in the 2030s, the launch of another space-based interferometer called B-DECIGO is planned, later followed by DECIGO [222]. B-DECIGO and DECIGO will be observing GWs in the frequency band from 0.1Hz to 10Hz, bridging the gap between the LISA and Earth-based detectors' frequency bands.

Since my PhD focuses on Earth-based interformetric GW detectors, their working principles will be discussed in more detail in Sec. 2.2. Since there will be some

synergies between LISA and ET, namely the 'null channel' (see Chapter 11), we will also briefly highlight the working principle of LISA below.

The Laser Interferometer Space Antenna

LISA is the European proposal for a a space-based GW interferometric detector sensitive to GWs in the 0.1mHz-1Hz frequency band. LISA consists of a triangular configuration with 2.5 million km long arms, trailing Earth at a distance of about 50 million km [57]. Just as with any other type of interferometric detector it tries to measure the induced difference in arm length due to the passage of a GW, by measuring the phase difference.

GW detectors are sensitive to GWs coming from every direction. This implies you do not need to point the detector to the direction of a source to observe it. However, this implies one is not able to determine the sky-position, without combining the data of multiple detectors allowing for triangulation. However, LISA will trail the Earth in orbit and therefore have a different relative position with respect to a source. For sources which are in LISA's sensitive band for about a week or longer, the sky position from the source can be determined based on the different response to the signal due to LISA's changed location.

LISA will consist of three satellites which form the corner stations, each equipped with two lasers and free-falling test masses. Of the 2W of emitted laser power, only $\sim$100pW arrives at the test mass on the other side of the arm. Therefore every satellite emits laser light in the arm, which is phase locked onto the weak incoming beam. The phase of this laser is compared with a reference laser present on the satellite. Laser frequency noise dominates possible measurements and would allow for a strain measurement of 10^{-13} in the relevant frequency region, whereas the goal is to reach a sensitivity of 10^{-20} or better. In the case of equal arm interferometers (e.g. Earth-based detectors), the frequency noise in both arms will be the same and therefore drastically reduced when the light is combined at the dark fringe[7]. This allows the Earth-based detectors to reach the desired accuracy on the phase measurement. Note that LISA directly measures the phase for each beam and does not rely on interference as is the case with Earth-based detectors.

However, in the case of space-based interferometric detectors, which have a non-negligible light travel time (e.g. $\sim$ 8s for LISA), the different arms will have non-equal lengths. These difference in arm-length are caused by deviations from the

[7] Dark fringe is used to refer to the result of destructive interference, i.e. when the waves are out of phase.

ideal orbit and imperfect clock measurement [351, 359]. Therefore one needs to rely on a different method to ensure sufficient reduction of the noise on the phase measurement. As an example, LISA would only be able to observe a strain of about 10^{-16} with its difference in arm-length of about 1%-10% [57]. The arm-length difference namely translates in different time of arrival of the frequency noise in the different arms. The proposed method to achieve the desired sensitivity is time-delay interferometry (TDI) [351].

In the context of TDI, LISA is considered as six one-way arm measurements between the test masses rather than three Michelson interferometers. In post-processing it is possible to combine the data products in such a way that the frequency noise gets suppressed and the desired strain sensitivity of 10^{-20} is achieved in the mHz frequency range. If we denote the first two one-way arm measurements as $y_1(t)$ and $y_2(t)$ and the laser frequency fluctations as $C(t)$ the following holds [351],

$$\begin{aligned} y_1(t) =& C(t-2L_1) - C(t) + h_1(t) + n_1(t), \\ y_2(t) =& C(t-2L_2) - C(t) + h_2(t) + n_2(t), \end{aligned} \tag{2.5}$$

where h_i and n_i are respectively the GW signal and noise signal entering in the measurement of the one-way arm i[8]. If one subtracts the two one-way arm measurements from each other and combines them with time-shifted data, one can observe that in the following combination the laser frequency noise cancels,

$$X = [y_1(t) - y_2(t-2L_1)] - [y_2(t) + y_1(t-2L_2)]\,. \tag{2.6}$$

This synthesized interfometer via TDI has an equal delay in each arm, i.e. $2L_1 + 2L_2$ [351].

Finally we want to point out that data from a triangular configuration such as LISA can be combined into two perpendicular equal arm interferometers and a third channel which is insensitive to GWs referred to as the null channel, null stream or Sagnac channel. The concept of a null channel will be further discussed in Chapter 11.

2.1.4 Atom interferometers

Atom interferometers could be considered to fall in the category of 'interferometric detectors' as they also use electromagnetic radiation traveling between free-falling test masses to study the effect of GWs on spacetime. However, the working principle

[8] Note that we have assumed the speed of light to be $c = 1$.

is very different compared to 'traditional' interferometry used for e.g. LIGO or LISA. In this section we will start by explaining how atom interferometers work and how they are sensitive to GWs. We will end by introducing several Earth- and space-based atom interferometers, both present and future.

The basic working principle of an atom interferometer

According to quantum mechanics atoms are also waves, which implies one can use them for interferometry similar to light. A (cloud of) cold atom(s) is launched on a ballistic trajectory after which it is split, deflected and finally recombined by atomic optics [109, 115, 144]. By letting the atom/atomic wave interact with an 'atomic beamsplitter' the atomic wave gets split and follows two different paths. Afterwards one can reflect the atomic wave using an 'atomic mirror' to recombine the waves with a second beamsplitter. This will result in an interference pattern similar to a traditional interferometer. Based on the observed distribution of the interference one can use an atom interferometer to measure the phase difference induced by the different paths. This makes atom interferometers good inertial sensors and they have a wide field of applications such as the measurement of fundamental constants [99, 172, 282, 307] or navigation [84].

The type of atomic optics we will discuss relies on the use of pulsed lasers. By tuning the pulse time one can create an atomic wave beamsplitter or mirror as illustrated in Fig. 1 and Fig. 2 of [108]. For more details we refer the interested reader to [108, 109].

How atom interferometers can measure gravitational waves

To measure GWs with atom interferometers one needs at least two atom interferometers, placed in a common laser beam, stored in a reflecting cavity as shown in Fig. 2.1 [109, 115, 144]. The phase difference of the two counter propagating beams leaves an imprint on the atomic interferometers. The phase difference between the two atom interferometers will contain a GW component, which one can observe assuming other contributions are properly dealt with. An important competing noise term contributing to this phase difference is gravity gradient or Newtonian noise, which will be further discussed in Chapters 5 and 9. The combination of two atom interferometers, which together are able to measure GWs is called an atom gradiometer.

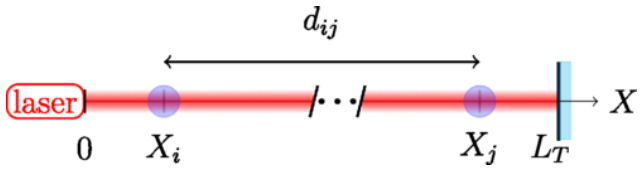

Fig. 2.1.: Gravity gradiometer schematic diagram. Two atom interferometers placed at X_i and X_j are separated by a distance L and coherently manipulated by a common laser retro-reflected by a mirror placed at position L_T. Figure taken from [108].

Whereas it is technically possible to measure gravitational waves with a single atom gradiometer, a so-called 'hybrid' design with atom interferometers in an L-shaped configuration offers multiple advantages. The atom interferometers in the different arms do not only benefit from laser frequency noise suppression, but the L-shape configuration also allows the atom gradiometer to be sensitive to GWs from different directions and improve sky localisation.

Current and proposed Earth- and space-based atom interferometers

A range of Earth- [108, 109] as well as space-based [144, 178, 207] atom interferometers have been proposed. They aim to observe GWs in the 0.1Hz to 10Hz band, respectively 1mHz to 10Hz, effectively filling in the gap between LISA and Earth-based interferometric detectors. The current generation of Earth-based atom gradiometers will consist of a limited number of atom interferometers with a separation on the order of hundred meter. The Matter-wave laser Interferometric Gravitation Antenna (MIGA) [109] will for instance have three atom interferometers with a total baseline distance of 200m. Whereas MIGA uses a horizontal baseline, several vertical $\mathcal{O}$(100m) long baselines are under construction, such as Matter-wave Atomic Gradiometer Interferometric Sensor (MAGIS-100) [33], Atom Interferometer Observatory and Network (AION) [78] and Zhaoshan Long-baseline Atom Interferometer Gravitation Antenna (ZAIGA) [369]. These experiments are planned to be followed-up with kilometer long successors in the next decades. An example of such a future multi-kilometer detector, using a horizontal baseline, is the European Laboratory for Gravitation and Atom-interferometric Research (ELGAR) [108]. ELGAR is planned to have 80 atom gradiometers, each with a baseline of 16.3km and a separation of 200m between the different gradiometers, leading to a total length of 32.1km [108]. One of the motivators to build such a large amount of nested atom gradiometers is to average out the effect of Newtonian noise, which otherwise will limit the sensitivity of each individual detector [115]. However, the gain in sensitivity could be more limited if the Newtonian noise is correlated between the gradiometers, as we will further discuss in Chapter 9

2.2 Earth-based interferometric detectors

In Sec. 2.2.1 we will discuss in more detail the layout and characteristics of Advanced Virgo [37, 344]. At the end we will highlight some differences concerning Advanced LIGO and KAGRA. Furthermore, in Sec. 2.2.2 we will briefly discuss how the next generation of detectors aim to improve the sensitivity by about one order of magnitude.

2.2.1 Second generation detectors

Fig. 2.2 shows a simplified optical layout of Advanced Virgo, where the arm length between input mirror (IM) and end mirror (EM) is 3km. In what follows we will give a simplified explanation of this already simplified model. For more details the interested reader can turn to the references in the respective paragraphs or more generally to [37, 344].

Whereas in this chapter we will explicitly use the names 'Advanced LIGO' and 'Advanced Virgo', in the next chapters we will use 'LIGO' and 'Virgo' to refer to the Advanced detectors. In case we want to refer to the initial detectors we will do this by refering to 'Initial LIGO/Virgo'.

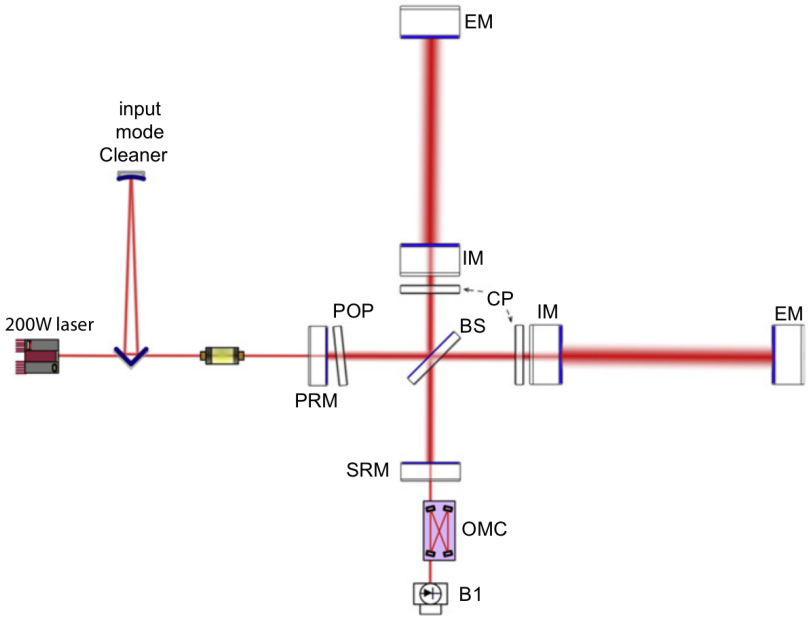

Fig. 2.2.: Basic optical layout of Advanced Virgo. Figure taken from [37]. The acronyms are defined in text as well as in the list of acronyms at the start of this thesis.

Michelson interferometer

The basic concept of Earth-based interformetric detectors, such as Advanced Virgo depicted in Fig. 2.2, is a Michelson interferometer. A standard Michelson interferometer consists of a laser, beamsplitter (BS), two EMs and a photodetector, here called B1. In this simplified set-up the power at B1 is [176],

$$P = P_0 \cos^2 (2\pi \Delta L/\lambda) \,. \tag{2.7}$$

P_0 is the input power, λ the laser wavelength and ΔL the differential arm-length between the two arms. In the case of a passing GW, the differential arm-length is related to the strength of the GW, see Eq. 1.25.

Current detectors are tuned such that the detection photodiode B1 operates near 'dark fringe'. The dark fringe is where the beams interfere destructively and the power equals zero. However, if the detector would be operating at exactly the dark fringe, the induced response of GWs on the observed power difference would scale as h^2. Namely, not only the power, but also the derivative of the power with respect to the observed phase is zero. Advanced Virgo operates with a differential offset of about $10^{-9} - 10^{-11}$m [344].

The set-up of the Michelson interferometer also naturally helps reducing laser frequency noise. Earlier we explained how overcoming laser frequency noise is a big hurdle for LISA. However, in case of Earth-based interferometeric detectors the time delay of light traveling through the two arms of the Michelson interferometer is, to first order, equal to zero. In this scenario the frequency noise in both arms will cancel when recombined, leading to a drastic frequency noise reduction at the dark fringe.

Fabry-Pérot cavity

A first additional complexity in the design of a more realistic interferometric GW detector is the Fabry-Pérot cavity. A Fabry-Pérot cavity is an optical cavity delimited by two (highly) reflective surfaces [254], i.e. the IM and EM in case of the Advanced Virgo design. One needs to tune the cavity to be resonant for the laser frequency to enable constructive interference inside the Fabry-Pérot cavity, leading to a larger circulating power in the cavity. Therefore the mirrors of the Fabry-Pérot cavity are curved with a radius of curvature approximately equal to half the arm-length [344]. The larger circulating power in the cavity will in turn yield a larger transmitted energy at the IM to recombine with the light from the second Fabry-Pérot cavity,

effectively increasing our sensitivity to GWs. Intuitively one can understand the gain of a Fabry-Pérot cavity as an effective increase in the arm-length of a Michelson interferometer, since the laser light does many round-trips in the highly reflective Fabry-Pérot cavity before being transmitted and recombined at the BS. The induced phase-change by a GW in a Michelson interferometer with Fabry-Pérot cavity is the same as in a standard Michelson interferometer with arm-length $\frac{2}{\pi}\mathcal{F}L$ [254]. $\mathcal{F} = \frac{\pi\sqrt{r_1 r_2}}{1-r_1 r_2}$ is called the finesse of the cavity, where r_1 and r_2 are the reflectivities of the two mirrors of the Fabry-Pérot cavity, in the case of Fig. 2.2 respectively the IM and EM. Advanced Virgo has a finesse of about 443 [176].

When the storage time of the laser light in the Fabry-Pérot cavity becomes comparable to the GW period, i.e. the long-wavelength approximation no longer holds, the sensitivity to those GWs decreases. Namely, in such a scenario the sign of the GW signal changes while the laser light is still making its round-trip, leading to a lower averaged sensitivity over the entire round-trip. This decreased sensitivity becomes significant for frequencies above the pole frequency $f_p = \frac{c}{4\mathcal{F}L}$ [254]. With a finesse of 443 and an arm-length of 3km, this implies the pole frequency for Advanced Virgo is about 56Hz. At higher frequencies the response decreases linearly with the frequency of the GWs, up to GW frequencies of about $\sim$ 15kHz for Virgo, after which the response decreases even more [254].

Pound-Drever-Hall locking scheme

The detector's cavities have to be controlled with very high precision, also often referred to as 'being locked'. In this conceptual explanation we will assume the laser frequency is assumed to be very stable and known with excellent precision. This will allow us to lock the cavity length to the laser frequency. Alternatively the Pound-Drever-Hall scheme could be used to improve the laser frequency stability, given a fixed cavity. For a more detailed explanation as well as mathematical calculation, we refer the interested reader to [90].
A first naive system relies on the transmitted light from the Fabry-Pérot cavity. If the arm length of the cavities changes such that the laser is no longer in perfect resonance, the transmitted power will decrease. This information could be used to correct the cavity length. However, there are two issues. First of all, this system is also sensitive to intrinsic fluctuations in laser intensity. Secondly, based on the change in intensity of the transmitted light, it is impossible to deduce the sign of the change in the cavity length. Both issues are addressed in the Pound-Drever-Hall locking scheme. To address the first issue, the reflected beam will be used rather than the transmitted. In an idealized situation the reflected power will be zero

if the laser is on resonance in the Fabry-Pérot cavity. This makes the error signal independent of any intrinsic laser intensity fluctuations. To determine the sign of the cavity length fluctuation, the laser light is modulated. In the case of GW interferometric detectors this are radio frequency modulations. By demodulating the reflecting beam, information is obtained on the sign of the variation of the arm length with respect to the laser frequency. This information can than be used as an error signal to control the cavity length [90].

Suspension system

A first objective of the suspension system is to ensure the test masses are free-falling in the degree of freedom along the laser beam. However, in order to reach the required sensitivity the effect of ambient seismic noise also has to be reduced by many orders of magnitude. The basic concept of Advanced Virgo's superattenuator is a chain of five pendulums, the true design is shown in Fig. 2.3. A pendulum is a mechanical filter above its resonant frequency f_0. Every movement at the top of a pendulum is damped by $\sim f_0^2/f^2$ at the bottom of the pendulum, for frequencies larger than the resonant frequency. By chaining N pendulums one can achieve a reduction by a factor of $\frac{f_0^2 \cdots f_N^2}{f^{2N}}$. The resonant frequency of the pendulums of Advanced Virgo's superattenuator are around several Hz. The true design is more complex, as shown in Fig. 2.3. The three-leg inverted pendulum, which has its resonance frequency around 30mHz - 40mHz, is able to provide significant seismic attenuation around the resonant frequency of the pendulum chain. The entire superattenuator has a length of 8m to 9m. For more information we refer the interested reader to [344].

Due to the 3km long arms of Advanced Virgo there is a small, but non-negligible effect from the curvature of the Earth. This facilitates the coupling of vertical seismic noise into a longitudinal noise sources along the laser beam. To this extent steel spring blades are installed at each pendulum stage. This turns the superattenuator in a multi-stage spring providing the required reduction of vertical noise sources [81].

Design sensitivity and key noise sources

The core concept enabling Advanced LIGO and Advanced Virgo to search for and detect GW signals is a Michelson interferometer with Fabry-Pérot cavity and suspended test masses. Before briefly highlighting the dominant mechanisms to increase the

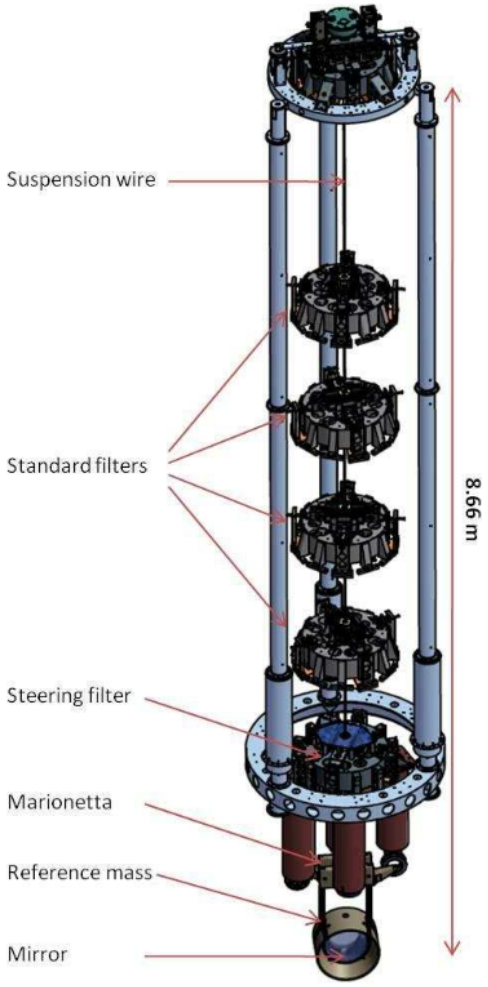

Fig. 2.3.: The Virgo superattenuator: the mechanical filter chain adopted to attenuate seismic vibration in the detection band, the three-leg inverted pendulum preisolator, the top filter of the chain and the mirror are well visible. Figure and caption taken from [344].

sensitivity of interferometric detectors, we will introduce Advanced Virgo's design sensitivity curve and break down the dominant noise contributions to enable a more intuitive understanding of the added value of certain systems and design choices.

Advanced Virgo's design sensitivity curve [37] is shown in Fig 2.4. This sensitivity curve is given by the detectors amplitude spectral density (ASD), which is the square root of the power spectral density (PSD) given by the auto-correlation of the detector's strain. The sensitivity curve shown in Fig. 2.4 [37] includes some additional work with respect to Advanced Virgo's technical design report [344] leading to a difference between the dashed budget of noise sources and the originally formulated solid black curve.

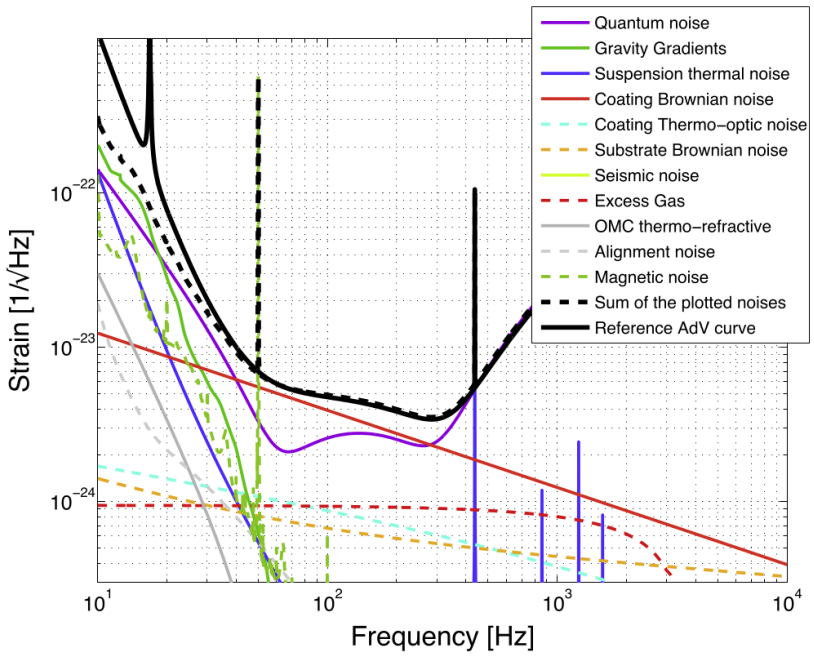

Fig. 2.4.: Principal noise contributions for Advanced Virgo with an input power of 125W. The black curve represents the design sensitivity curve proposed in Advanced Virgo's technical design report [344], whereas the dashed curve presents the sum of all the design sensitivity noise sources present in more recent work [37]. Figure taken from [37]. For more info on the principle noise sources, see in text or [37, 344].

At high frequencies seismic noise is sufficiently damped by the superattenuator, but closer to the pendulums resonant frequencies at several Hz, seismic noise becomes the dominant noise source. Whereas this happens below the lowest frequency represented in Fig. 2.4, one can see this for Advanced LIGO in Fig. 2 of [3]. Magnetic noise and gravity gradients will be discussed in more detail in Chapters 5, 7, 8 and 9, since both are studied in this PhD dissertation. The contribution shown here is the noise contribution of the respective ambient, environmental noise sources and not infrastructural, e.g. equipment generating magnetic noise.

Two types of quantum noise contribute significantly to the noise budget. Both find their origin in the fact that laser light is a beam consisting of discrete quanta, i.e. photons. The count of discrete and independent events is governed by the Poisson process, implying that the number of photons at a given time and location is fluctuating. At low frequencies the dominant quantum noise process is radiation pressure, where on impact momentum is transferred from the photons to the test mass. The amount of photons hitting the mirror fluctuates according to the Poisson process and these fluctuations introduce an intrinsic uncertainty. The noise in a

Michelson interferometer from radiation pressure is proportional to the square root of the laser power and inversely proportional to the mirror mass [254]. At high frequencies quantum noise is dominated by shot noise. Shot noise is caused by the fluctuating number of photons hitting the photodetector, inducing fluctuations in the current being readout by the photodetector. Shot noise in a Michelson interferometer is inversely proportional to the square root of the laser power [254]. To decrease both noise sources simultaneously Advanced Virgo increases the laser power, while also increasing the mass of the mirror to keep the level of radiation pressure under control [37, 344].

Another important noise source is the suspension thermal noise. Thermal excitation of the suspensions induces vibrational noise, introducing fluctuations of the mirror position. To decrease the contribution of suspension thermal noise Advanced Virgo uses monolithic suspensions and fused silica fibers, compared to steel suspensions in initial Virgo [36, 254, 345].

The dominant noise source in the mid-frequency ($\sim$ 50Hz-250Hz) is mirror-coating Brownian noise. This noise originates from the Brownian motion experienced by the atoms in the coating due to thermal excitation [114, 254]. New test masses with better coatings are part of the A+/AdV+ upgrades and are planned to be installed before O5 [173].

Observed sensitivity

Whereas Fig. 2.4 represented the predicted and idealized sensitivity, Fig. 2.5 presents observed sensitivities during O2 and O3. As a comparison the expected sensitivity for the O3 observing scenario is also displayed. This is a clear example of how the complexity of the instruments leads to a more 'messy' sensitivity than the predicted sensitivities. These include non-stationary transient effects (see also Sec. 5.1) and spectral artefacts (see also Sec. 5.2). Many of these spectral artefacts are visible in Fig. 2.5.

Understanding and mitigating these noise sources is a large data quality effort, to which I also participated during my PhD. Chapter 5 contains a more detailed discussion on the noise sources which could effect the search of a gravitational-wave background (see Chapters 3 and 4). In Part II my contributions to data quality investigations will be discussed.

It is interesting to point out that the noise contributions at low frequencies, below $\sim$ 11Hz, are currently not properly understood.

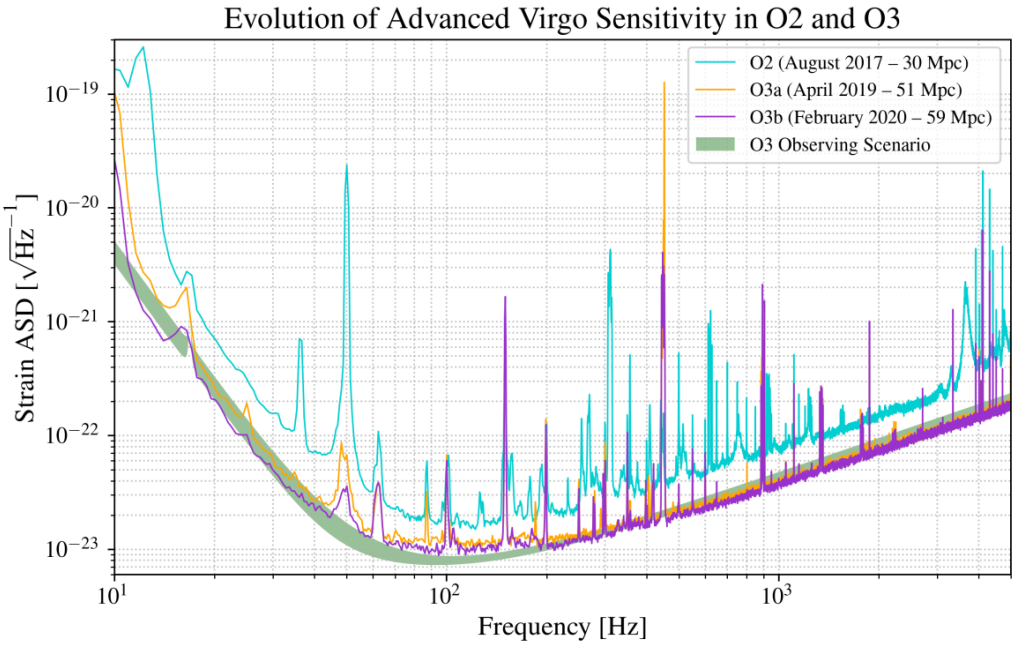

Fig. 2.5.: Virgo's sensitivity curves during O2 and O3 are shown in comparison to the Virgo O3 observing scenario (60-85Mpc) [20]. Figure taken from [88].

Recycling cavities

To help achieve the high laser power, Advanced Virgo has two recycling cavities for which two additional pieces of optics are added to the design, as illustrated in Fig. 2.2: a power recycling mirror (PRM) and a signal recycling mirror (SRM). The signal recycling cavity for Advanced Virgo was only installed between O3 and O4[9]. Both recycling cavities are about 12m long and are marginally stable, i.e. not only the fundamental mode, but also higher order modes can resonate at the same time. This makes the cavities extremely sensitive to optical aberrations and thermal effects [37, 185]. The choice for marginally stable cavities was mainly dictated by infrastructural and budgetary limitations. The marginally stable cavities have proven to make acquiring stable lock of the interferometer much more difficult in approach of O4.

The primary goal of the two recycling cavities is to increase the amplitude of the circulating laser power, but the length of the signal recycling cavity can also be used to tune the frequency dependent sensitivity [37, 185].

[9] O4 started May 24th 2023 [245] at which time both LIGO detectors and KAGRA joined the observing run. KAGRA only joined for one month, after which they again went into commissioning, to rejoin later with increased sensitivity. Due to sensitivity and commissioning issues at Virgo, Virgo will at the earliest join by the end of 2023.

Mode cleaner

Virgo has both an input and output mode cleaner, respectively abbreviated as IMC and OMC (Fig. 2.2). The mode cleaners are tuned such that the fundamental mode is resonant whereas higher order modes are not, leading to a transmitted beam with increased quality [3, 177]. The IMC provides both frequency stabilisation and spatial filtering for the input laser beam [3, 37]. In case of the latter the beam jitter is reduced. The OMC filters higher order modes as well as sidebands. By filtering out these beam components which do not contain information on the GW signal, the fraction of laser power containing information on GWs at the detection photodiode increases. The decrease of total power reduces the shot noise [3, 177]. We want to point out this is not in contradiction with the earlier statement that increasing the laser power decreases the shot-noise. The latter, namely assumes the entire signal received at the detection photodiode is sensitive to GWs. In such a scenario the signal to noise ratio of the received signal with respect to shot-noise is inversely proportional with the square root of the power. The absolute value of the shot-noise is however proportional with the square root of the power. This implies that if power, not containing any information on GWs, is deposited on the photodiode additional shot-noise is introduced. This additional noise can be reduced by reducing the power of the signals not sensitive to GWs on the detection photodiode, which is achieved by the OMC.
The sidebands mentioned earlier are radio-frequency sidebands used as error signals for controlling the different degrees of freedom of the interferometer, i.e. the Pound-Drever-Hall locking scheme as previously explained [161].

Thermal compensation and mirror coatings

As mentioned earlier, Advanced Virgo operates at high laser power to decrease the shot noise. More precisely Advanced Virgo is planned to have 700kW of circulating power in the Fabry-Pérot cavities [37, 344]. In such an extremely high power regime thermal effects become very important, such as the unequal deformation of the mirrors. To ensure the stability of the interferometer the radius of curvature of the optics should remain the same and one has to compensate the large deformation of the mirror in the central region where the laser beamspot is located. To this extent Advanced Virgo has ring heaters and compensation plates (CPs) [37, 344]. The pick-off-plate (POP) can also serve as a thermal compensation actuator, however its main purpose is to pick off a beam for controlling the interferometer [344].

Furthermore, coating design is important to ensure highly reflective coatings with low thermal noise properties. This also applies to the mirror substrate. Additionally, high levels of isotropy are required to prevent locally larger (or smaller) effects due to artefacts. An example of the latter are point absorbers, reported for Advanced LIGO in [103]. Also Virgo is affected by point absorbers [120].

Stray light and baffles

Advanced Virgo operates in a high vacuum ($\sim 10^{-6}$ mbar) to reduce the amount of stray light. However, remaining air molecules have a probability of deflecting a small fraction of the high intensity laser light. This light can afterwards scatter on surfaces which are not seismically isolated (e.g. the interior of the beam tube) and enter in the interferometer output, leading to increased levels of noise. To this extent baffles with high absorption are installed in critical locations to reduce the amount of scattered light [60, 253, 344]. Also at the level of the mirror stray light has to be small, requiring highly polished and flat mirror substrates and coatings.

Squeezing

The laser light has an amplitude and phase uncertainty, which are at the origin of the quantum noise (i.e. radiation pressure and shot-noise). One can create 'squeezed light' by decreasing one of the uncertainties. However, by merit of the Heisenberg principle the other uncertainty will increase. To this extend one could inject squeezed light in an interferometric GW detector with reduced phase uncertainty to decrease the level of shot-noise at high frequencies, but this will come at the cost of an increased level of radiation pressure noise at low frequencies [150, 261]. This approach is called frequency independent squeezing and was used successfully in Advanced Virgo and Advanced LIGO during O3 [150]. For O4 they both have implemented frequency dependent squeezing, where the squeezing angle is made frequency dependent such that the phase noise can be reduced at high frequencies and the amplitude uncertainty at low frequencies.

The main laser is not squeezed, but a squeezed ground state is injected at the dark fringe output port. The squeezed ground state enters the system and is supper-imposed with the laser light from the interferometer and replaces the unsqueezed ground state fluctuations. In this way, the quantum noise sources can be further reduced, increasing the detectors sensitivity to GWs [150, 261].

h(t) reconstruction and calibration

The final output from the interferometer, after reconstruction and calibration is often referred to as h(t) (read as 'h-of-t'), since this contains the (possible) GW signal. The first and most important step of this reconstruction is to remove the imprint of the detector controls on the measured output signal. To be able to understand how the control of the mirrors and test masses in the set-up influences the measured output, one has to calibrate their response. First of all, the response of the mirror actuators to the applied control signals has to be calibrated. Secondly, the relation between the output of the photodiode measuring h(t) and the input power of the signal on the photodiode should be understood [38]. For more details on Virgo's calibration methods we refer the interested reader to [38]. These effects are mainly important below 300Hz. In a second stage some noise sources are subtracted, based on witness signals from the many auxiliary monitoring channels. One example of a noise source subtracted from Virgo data during O3 is the effect of the power mains at 50Hz. After the reconstruction and noise subtraction of h(t), the data can be used by analysis pipelines. However the noise subtraction is very limited and a large effort is needed to further understand the data quality and, if needed, implement additional data cleaning methods.

Advanced LIGO and KAGRA

Earlier in this section we discussed the basic principles of the Advanced Virgo detector, now we will highlight the key fundamental differences for Advanced LIGO and KAGRA. Whereas Advanced Virgo (and KAGRA) have 3km long arm lengths, LIGO has an arm length of 4km. This leads to an increased sensitivity with a factor 4/3. Furthermore, Advanced LIGO uses a different suspension design. Virgo has a more performant passive seismic isolation with their superattenuator, whereas Advanced LIGO has additional active isolation to reach the desired level of seismic noise reduction [3]. Finally, a third crucial difference are the stable recycling cavities for Advanced LIGO [3, 68], instead of the marginally stable recycling cavities for Advanced Virgo. This facilitates the operation of the interferometer. As mentioned earlier, Virgo has struggled to lock the interferometer due to the marginally stable cavities in the commissioning period before O4.
The key conceptual differences in the KAGRA design, are the underground facility and a cyrogenic operating temperature [71]. Since these are fundamental technological changes, KAGRA is sometimes also called a 2.5G detector. During O3GK, KAGRA's first, month-long observing period at the end of O3, KAGRA operated at

room temperature due to difficulties operating the mirrors at cryogenic temperatures [123]. At the start of O4 KAGRA operated at room temperature, whereas they plan to have cryogenic temperatures after further commissioning later during O4.

2.2.2 Third generation detectors

Advanced Virgo, Advanced LIGO and KAGRA are still undergoing incremental upgrades to reach their design sensitivities later this decade [245]. At that time the sites will reach their 'infrastructural limits'. Any further improvement in sensitivity would have a decreased gain in sensitivity with respect to the technical (and budgetary) efforts needed to achieve such improvements. Therefore, plans are discussed to construct a next generation of gravitational-wave detectors with new infrastructure such as longer arm lengths, as well as being located in seismically quiet regions. These next generation detectors aim to have an overall improvement of strain sensitivity by one order of magnitude, and in some frequency regions even more. As mentioned earlier, there are two such efforts, the Einstein Telescope and Cosmic Explorer. These efforts are respectively European and US focused. The approach of CE is to scale up Advanced LIGO's latest technologies to a 20km and 40km L-shaped detector. In a second stage an additional gain in sensitivity might be achieved by using new technologies, especially to reduce quantum and thermal noise [189, 299]. ET on the other hand is planned to be a set of three 10km long interfererometers, nested in an equilateral triangular configuration [161], as illustrated in Fig. 2.6. Furthermore, the ET design plans to implement many technological advancements from the start in the detector. In 2021 the ET collaboration was created, which brings more than 1000 scientists in the field together and aims to finalize the detector design, prepare site selection and get the required funding to construct the ET.

As the work as part of this dissertation mainly took place in the European context there is a strong focus on the Einstein Telescope, of which we will discuss some key features in the next paragraphs.

As discussed in Sec. 2.2.1 and Fig. 2.4, some of the fundamental noise sources that have to be overcome to achieve a gain in sensitivity by an order of magnitude are: seismic noise (1Hz-10Hz), coating thermal (Brownian) noise (50Hz-250Hz) and quantum noise (radiation pressure: 10Hz-50Hz and shot noise $>$200Hz). Whereas gravity gradient noise does not form a problem for Advanced Virgo, Advanced LIGO and KAGRA, it will be one of the dominant noise sources (1Hz-10Hz) for the ET.

Since the methods to decrease these noise sources are often conflicting, in particular the trade off between radiation pressure noise and shot noise, a xylophone design is

proposed for the ET [124, 200], as shown in Fig. 2.6. This design consists of two different interferometers, one optimized for low frequencies (LF), the other for high frequencies (HF), of which the data is combined to achieve a broadband sensitivity to GWs in the range from few Hz to few kHz. To reduce seismic and gravity gradient noise the ET, will be constructed underground at a depth of ∼200m-300m. The low-frequency detector will operate at low power and cryogenic temperatures to decrease the contributions from the radiation pressure as well as the coating thermal noise. The high-frequency detector will operate at a high power to decrease the shot noise.

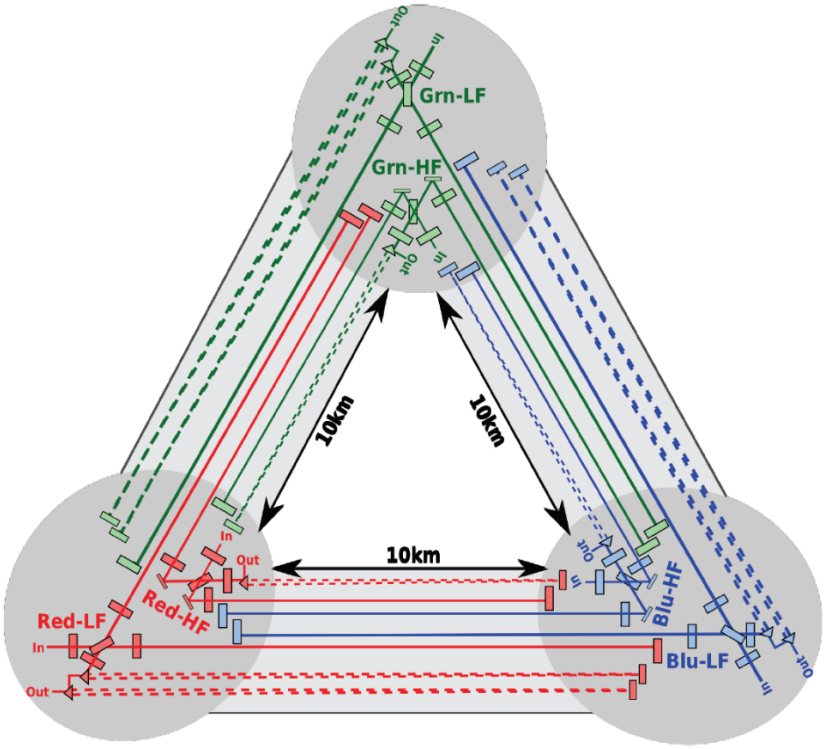

Fig. 2.6.: Conceptual configuration of the Einstein Telescope consisting of a Xylophone set-up and 3 Michelson interferometers with an opening angle of $\pi/3$ in a triangular configuration. Figure taken from [101].

Over the last decades several different sensitivity curves were used for the ET of which we plot the most relevant in Fig. 2.7. The most recent reference sensitivity curve was presented in [100]. There they refer to the xylophone sensitivity by 'HFLF-cryo' and they also consider the sensitivity of the ET without a cryogenic LF detector, referred to as 'HF-only'. We will follow their notation in view of a consistent use of notations in the scientific literature. An older and by now outdated xylophone sensitivity curve is referred to as 'ET-D' [200, 201]. The HFLF-cryo sensitivity is an updated version of the ET-D sensitivity curve, which is reflected in the similarity

of the two sensitivity curves in Fig. 2.7. Finally we also introduce the sensitivity curve of the 'ET-B' design, which does not use a xylophone design [200–202]. Even though this sensitivity curve is obsolete we introduce the sensitivity curve here since some studies we will discuss later make a comparison between ET-B and ET-D. Above 10Hz, the difference between the ET-B and HF-only design sensitivities is about a factor two or less. Therefore we can conclude that the statements on the effect of correlated noise with respect to ET-B we will make in Chapter 8 are also applicable to the HF-only design for frequencies above 10Hz. For lower frequencies the difference between the two designs becomes significant and even more than one order of magnitude below $\sim$ 3Hz.

Achieving the low frequency sensitivity target of the HFLF-cryo design might prove difficult due to several challenges. First of all, as mentioned earlier, Virgo and LIGO are dominated by unknown noise sources at low frequencies, below $\sim$ 11Hz. These noise sources are not captured in any of the fundamental noise contributions in the design sensitivity curves and have not yet been properly understood. Furthermore, the effect of gravity gradient noise on the detector will have to be reduced to achieve the sensitivity targets. However, also (environmental) magnetic noise could form an issue to achieve the low frequency sensitivity goals. Both gravity gradient noise and environmental magnetic noise will be further discussed in Chapter 5 as well as in Part II.

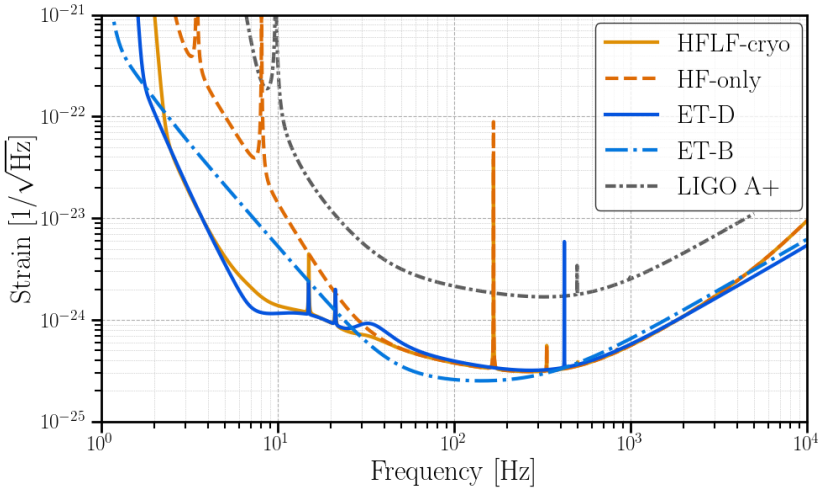

Fig. 2.7.: Sensitivity curves of the Einstein Telescope, according to the 'HFLF-cryo', 'HF-only', 'ET-D' and 'ET-B' designs. The latest HFLF-cryo, respectively HF-only designs can be compared with the outdated ET-D and ET-B designs. We also show LIGO's A+ design sensitivity as comparison. Figure created with data taken from [159, 160, 310]. The HFLF-cryo and HF-only sensitivities were first presented in [100], the ET-B sensitivity was first introduced in [202], whereas the ET-D sensitivity was first described in [200].

The baseline configuration of the ET consists of 3 (6 in the Xylophone set-up) Michelson interferometers with an opening angle of $\pi/3$ in a triangular configuration as illustrated in Fig. 2.6. This configuration was originally chosen for its benefits concerning sky-localisation and sensitivity to beyond-GR's polarisation of GWs. However in a recent study [100] a detailed investigation is performed to compare a triangular configuration with 2 L-shaped detectors within Europe and a separation on the scale of $\sim$ 1000km. They also consider different arm lengths of 10km (baseline), 15km and 20km [100]. Studies on correlated noise for the ET, performed in context of this PhD, are one of the inputs in this comparison of configuration designs. For more details see Chapters 8, 9 and 11.

One of the candidate sites to host the ET is near the former Sos Enattos mine in Sardinia, Italy [56]. A second candidate site is the Euro-Rhein-Maas region on the borders of the Netherlands, Belgium and Germany [56]. Recently there is also a third possible candidate site in Saxony, East Germany [342]. Since it would be very prestigious to host such a large and high-technological research facility in our region, there is an additional interest from Belgian (and Dutch) universities in the ET and the possibility to host the detector in our region. In this context, during my PhD I performed several analysis to investigate the impact of correlated noise on the ET of which the results can be found in Chapters 8, 9 and 11.

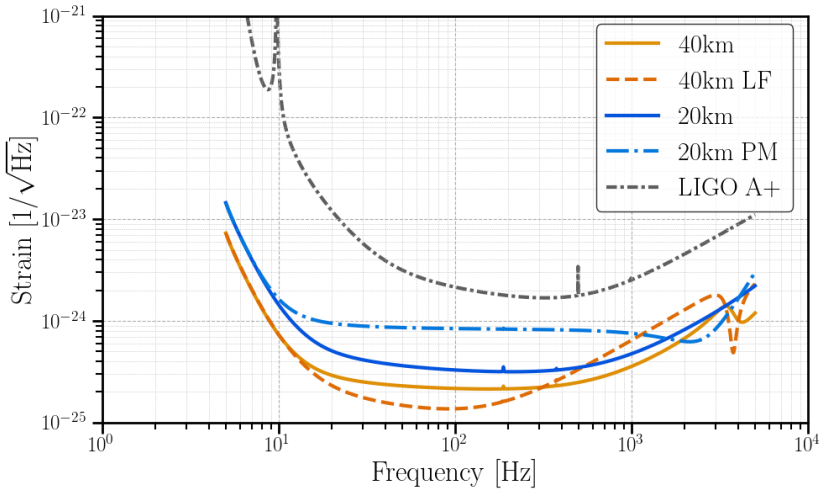

Fig. 2.8.: Sensitivity curves of Cosmic Explorer, according to the 20km and 40km baseline designs as well as the low frequency (LF) 40km and post-merger (PM) 20km tuned detector. We also show LIGO's A+ design sensitivity as comparison. Figure created with data taken from [233]. The sensitivity curves were first presented in [162, 335].

As mentioned earlier CE is planned to have two L-shaped detectors with respective arm-lengths of 20km and 40km. In contrast to ET, CE will not be built underground. This will allow for less reduction of seismic and Newtonian noise, however a detector at the Earth's surface is in line with CE's slightly less ambitious low frequency ($<$ 10Hz) design sensitivity. As highlighted in the previous paragraphs, achieving these low frequency sensitivity goals will be very challenging for the ET. Several different tuned interferometers are considered for CE in [162, 335]. In Fig. 2.8 we show the baseline design sensitivity for the 20km and 40km detectors. Furthermore we show the 40km detector tuned for low frequencies as well as the 20km detector tuned for observing the post-merger of binary neutron star coalescences. For more information on these different designs we refer the interested reader to [162, 335]

Gravitational-wave sources

3

> *Over and over in the history of astronomy, a new instrument finds things we never expected to see.*
>
> **— Rainer Weiss**

In Chapter 1 we have described how GWs are predicted by GR, how they propagate through spacetime, how they interact with test masses, as well as how they can be produced in GR. In this chapter we will discuss different sources of GWs and start by dividing the sources in four overarching categories based on their signal morphology in Sec. 3.1. In Sec. 3.2 some different key GW sources across the GW frequency spectrum will be discussed. Afterwards we briefly discuss some of the most important detections until July 2023 (Sec. 3.3). We will end this chapter with a short summary of the latest upper limits on the gravitational-wave background across the frequency spectrum (Sec. 3.4).

3.1 Different categories of gravitational-wave sources

An important characteristic by which signal types are often classified is the signal duration, i.e. the signal being a transient event or of continuous nature. However, this separation of signals is somewhat arbitrary since the duration of the signal can depend on the sensitivity of the detector to GWs as well as the frequencies to which the detector is sensitive. This implies that what might be a transient signal for a certain detector, might be a continuous signal for another detector. Furthermore the sources of gravitational waves which can be detected depend on the frequencies the detector is sensitive to.

A first type of GW sources are ‘compact binary coalescence’ (CBC) events. Two stellar bodies (e.g. neutron star, black hole) in a binary system orbiting around each other have a non-zero quadruple moment due to their time dependent mass distribution. Therefore this system will emit gravitational waves. Due to the emission of these gravitational waves, the two stellar bodies will inspiral and eventually coalesce with each other. The inspiral phase of the binary system is a long duration and almost

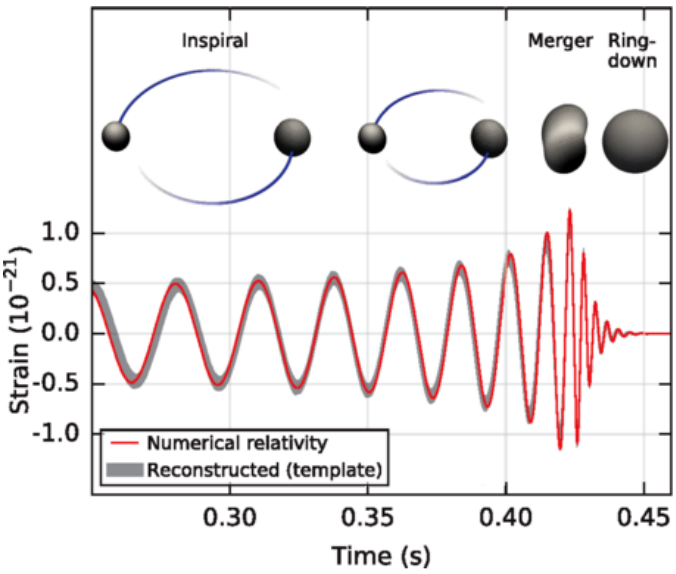

Fig. 3.1.: Estimated gravitational-wave strain amplitude from GW150914 projected onto the LIGO Hanford detector. The inset images show numerical relativity models of the black hole horizons as the black holes coalesce. Figure and caption taken and modified from [19], under the terms of the Creative Commons Attribution 3.0 License.

monochromatic signal. Such signals form another category of signals often called 'continuous waves' (CW) which we will discuss later in this section.
The final moments of the inspiral and the eventual coalescence of the two stellar bodies yields a transient signal, with a time-frequency behaviour well predicted by GR. This signal depends on the system parameters such as the masses and spins of the stellar bodies. After the merger of the two stellar bodies to a single stellar body, there will be a 'ringdown' and the emission of gravitational waves will end. This process is illustrated in Fig. 3.1.

Given the excellent description of these events by GR, one can rely on matched-filtering techniques to detect CBCs. With this technique one relies on the information available on a possible candidate signal and the matched-filter is the best linear filter one can use [357].

A second class of GW events are often referred to as 'bursts'. These are transient signals coming from violent processes such as core collapse supernova. In contrast to the well predicated waveforms for CBC events, the GW waveform for bursts are less understood due to uncertainties in the dynamics as well as initial stellar conditions [303]. This implies analysis pipelines have to rely on methods to identify excess power of gravitational-wave origin. These will be less optimal than matched-filtered methods that can be used for CBC events. Note that Burst pipelines could

also observe loud CBC events, but they intrinsically perform less well due to the non-optimal analysis method.

A third category of GW signals was already introduced earlier and are the 'continuous waves'. This definition is typically used for long duration signals wich are (almost) monochromatic. One possible example of GWs are, as mentioned earlier, the inspiral phases of a CBC event. However, the emission of GWs from the CBC merger and the inspiral occur at different frequencies and have to be observed with different detectors. Another possible source is a rotating non-axisymmetric stellar body (e.g. neutron star).

The fourth category is the gravitational-wave background (GWB), which consist of an incoherent superposition of many weak sources. Historically the GWB has been referred to as the stochastic GWB or SGWB, but more recently is often also referred to as GWB. In this thesis we will choose the latter convention. There are a large number of possible sources which could produce a GWB, both of astrophysical and cosmological origin. One example is the superposition of individually unresolved CBC events. The signal becomes Gaussian, by merit of the central limit theorem, in case the number of sources is large enough. On the largest scales of the entire Universe, one often can assume the signal to be isotropic, however on smaller scales the signal might exhibit anisotropies linked to e.g. the center of the Milky Way or the distribution of close-by galaxies. By definition the GWB consists of individualy unresolvable sources either by the weakness of their signal and or their large number. This implies that all loud and individually resolvable sources should first be subtracted or removed from the analysis for a GWB. Therefore in most cases, the GWB is much smaller than the detector noise and is operating in the so-called small signal-to-noise ratio limit[1]. Therefore long integration times are needed to enable a future detection as well as correlating data from two or more detectors. This however implies that a signal that is considered to be a GWB in a certain detector, might not be in another if for instance all the individual sources would be resolved. This will for example be the case for the GWB from CBC events in Earth-based detectors when comparing second generation detectors such as LIGO, Virgo and KAGRA with third generation detectors such as the Einstein Telescope. The different detectors were introduced and discussed in detail in Chapter 2. Some GWB signals are expected to be stationary, e.g. the GWB from unresolved BNS mergers, whereas other signals are expected to have an intermittent behaviour, e.g. the GWB from unresolved BBH mergers.

[1]LISA and ET are predicted to have a loud but unresolvable GWB due to the larger number of sources.

3.2 Overview of gravitational-wave sources probed by different detection methods

In the following subsections we will discuss GW sources in the nHz (Sec. 3.2.1), mHz (Sec. 3.2.2) and Hz-kHz (Sec. 3.2.3) regions. They can respectively be probed by PTAs, space-based interferometric detectors and Earth-based interferometric detectors, as discussed in Chapter 2. The GWB, and more specifically data quality for the search for an isotropic GWB, is the main topic of this thesis. Therefore a more extensive list of GWB sources will be given, compared to a limited number of examples for the other sources. More details on analysis methods for searching for an (isotropic) GWB with Earth-based interferometeric detectors will be discussed in Chapter 4. Chapter 5 contains a general discussion on possible noise sources for the search for an isotropic GWB, with Earth-based interferometric detectors.

3.2.1 nHz gravitational waves

The inspiral of supermassive black hole binaries (SMBHB), i.e. a pair of black holes (BHs), each with a mass $\gtrsim 10^7 M_\odot$ [2], will create continues waves which could be individually detectable in the nHz frequency region [105, 141, 248].

Apart from this GW signal in the nHz frequency region, cosmic strings could create burst of GWs [137, 141, 248]. Cosmic strings are topological defects which arise during phases of symmetry breaking in the early Universe [224]. Several mechanisms play a role in the production of GWs from cosmic strings for which we refer the interested reader to [354]. Depending on the energy at the time of the phase transition when the cosmic strings are created, they will yield GW signals in a different frequency range. Therefore different energies of cosmic strings can be probed with GWs in the nHz, mHz and Hz-kHz frequency regions. Cosmic strings producing nHz GWs were created during symmetry breaking at temperatures of $\sim 10^{-1}$GeV-10^{1}GeV [111].

nHz GWB

The superposition of inspiraling SMBHB is predicted to produce a GWB from astrophysical origin. This signal is even expected to be the first nHz GW signal to be observed [105]. Furthermore one could observe a GWB from the superposition

[2] $M_\odot$ is the symbol to indicate 1 solar mass, i.e. $\sim 1.99 \cdot 10^{30}$ kg

of cosmic string bursts. Finally a relic GWB from inflationary periods fractions of seconds after the Big Bang is another candidate signal [141, 248]. This GWB can in some sense be regarded as the GW equivalent of the CMB [149, 285] in the electromagnetic spectrum. Namely the CMB is the oldest electromagnetic radiation which can be observed and similarly the GWs from these inflationary periods would give us some of the oldest GW signals. Gravitational waves from this relic background could originate from initial tensor fluctuations or could be produced during the end of the inflationary period [111, 118]. The standard inflationary model yields levels of a GWB which are probably beyond reach of any of the detection methods in the next decade(s) both in the nHz and higher frequency bands [111, 118]. However alternative inflationary models could lead to amplified GW production, yielding a possibly detectable GWB [111, 118].

3.2.2 mHz gravitational waves

The mHz frequency band is very rich and has many different sources of GW signals [57, 303, 313]. A first category is the coalescence of massive black hole binaries (MBHB), i.e. BHs with masses between $10^3 M_\odot$ and $10^5 M_\odot$. These signals will have a transient signal nature with a duration of hours to months. The inspiral of binary systems with smaller masses (few solar masses to few tens of solar masses) will be observable in the mHz frequency band months to years before they coalesce in the Hz-kHz frequency region [321, 322]. The inspiral of even lighter compact galactic binaries, such as white dwarf binaries, also produces mHz GWs. Due to their sheer number only a limited fraction of these signals is expected to be individually resolvable. A fourth astrophysical GW signal comes from extreme mass ratio inspirals (EMRIs), where a BH with a mass of few tens of solar masses first inspirals and afterwards is engulfed by a massive BH.

Similarly to GWs in the nHz region, cosmic strings can produce mHz gravitational-wave bursts, which corresponds to symmetry breaking at temperatures of $\sim 10^3$GeV-10^6GeV [111].

mHz GWB

The superposition of the inspiral phases of many BHs with masses of few tens of solar mass can also produce a GWB, which will be mainly situated in the Hz-kHz frequency band, but might also be observable in the mHz frequency band. Furthermore a similar confusion background from compact galactic binaries is present in the mHz

frequency region, consisting of a large fraction of individually unresolvable galactic binary inspirals.

A GWB from cosmological origin could be produced by a first order phase transition at the electroweak phase transition at $\sim$ TeV energies. During a first order phase transition bubbles from the true vacuum state can nucleate in the meta-stable vacuum. The interaction of these true vacuum bubbles with each other can produce GWs through several mechanisms [111]. The incoherent supperposition of GW signals from cosmic strings also forms a possible GWB source. As was the case for the nHz region, a relic GWB from inflation produces a GWB, however the amplitude predicted by standard inflationary theory is probably undetectable [111, 118]. Alternative inflationary theories could yield detectable GWB signals [111, 118].

3.2.3 Hz-kHz gravitational waves

A first source of Hz-kHz GWs are CBC events where neutron stars and/or BHs with few to tens of solar masses merge i.e. binary black hole (BBH), binary neutron star (BNS) and neutron star black hole (NSBH) mergers. A priori those BHs are expected to be of astrophysical origin, however they could also be of priomoridal origin, i.e. they would have formed from scalar fluctuations in the early Universe. Even though these primordial BH could also have masses in the solar mass range, the observation of a sub-solar mass BH is considered as the 'smoking-gun' evidence for primordial BH, since they can not be formed from stellar collapse.

Apart from these CBC events there are several burst-type signals in the Hz-kHz frequency region. A first possible source for bursts of GWs are core collapse supernova. Furthermore, GW bursts could originate from violent events in magnetars, i.e. a highly magnetized neutron star. Bursts from cosmic strings generating Hz-kHz GWs originate from symmetry breaking at temperatures of $\sim 10^8$GeV-10^{10}GeV [111].

Spinning non-axisymmetric neutron stars produce continuous GWs at twice their rotational frequency. There are several hundreds known neutron stars with rotational frequencies which could yield observable GW signals in the Hz-kHz frequency range [32, 303].

Hz-kHz GWB

The superposition of a large population of distant and weak individual sources can create an astrophysical GWB. This applies for all the sources mentioned earlier,

i.e. CBC events from BBH, BNS and NSBH, but also GW bursts from core collapse supernova and CW from non-axisymmetric rotating neutron stars. The expected strength of the latter two is predicted to be beyond reach with the current generation of detectors. The GWB from rotating neutron stars could be observable with ET and CE, however the GWB of core collapse supernova might even be beyond the reach of ETs and CEs sensitivity targets [295]. The background of BBH and BNS mergers is not only expected to be observable with Advanced LIGO, Advanced Virgo and KAGRA, but it is expected to be the first GWB signal in the Hz-kHz frequency region to be observed [30]. Based on the measured merger rate of these events, it is predicted the signal would be observable after several years of data at the design sensitivity of LIGO A+, AdV+ and KAGRA [30].

Apart from these different astrophysical GWBs, there are a variety of cosmological sources that could create a GWB, such as cosmic strings [137, 354]. Upper limits on several cosmic string models were placed using the latest LVK results [23]. GWs in the Hz-kHz frequency region could originate from a first order phase transition at energy scales 10^7GeV-10^{10}GeV. As mentioned earlier, a GWB from 'standard' inflation is expected to be below the design sensitivities of current and (near) future detectors. However alternative inflationary models could yield amplified levels of GWs, also in the Hz-kHz frequency region [111, 118]. Finally the superposition of coalesence events of primordial BHs could also produce a GWB.

For a more detailed discussion the interested reader can have a look to several review papers for a discussion of the different sources [118, 295] as well as some implications for several of these sources based on the latest LVK results [301, 356].

The benefit of a $\sim$ Hz GW detector

One of the key goals of the ET is to push its low frequency sensitivity to a few Hz, compared to $\sim$ 10Hz-20Hz, for current generation Earth-based interferometric GW detectors. This comes with many technological (and budgetary) challenges such as operating a cryogenic interferometer and providing sufficient subtraction of seismic and Newtonian noise. However, achieving this low frequency sensitivity with the full ET HFLF-cryo xylophone design as introduced in Chap. 2 opens up several additional windows onto the GW Universe which might be hard to access with the HF-only design.

The HFLF-cryo sensitivity enables to obtain an excellent sky-localisation for a considerable larger number of BNS mergers compared to the HF-only sensitivity [100]. Furthermore, since the BNS mergers will enter the detectors sensitivity earlier, the

detectors can accumulate signal over a longer period. Due to this accumulation of SNR, an alert of the merging BNS system can be sent out with sufficient confidence before the merger even takes place [100]. Both elements are crucial to be more successful in observing optical counterparts of the BNS mergers. In addition, the distance at which BNS mergers can be observed is roughly doubled when one opts for the HFLF-cryo design compared to HF-only design [100]. Doing GW cosmology, e.g. measuring H_0 with HF-only becomes much more difficult since the uncertainty of luminosity distance and angular localisation increase significantly compared to the xylophone design [100]. For a more detailed discussion of these benefits as well as many other, less drastic, improvements achieved by the full ET HFLF-cryo xylophone design compared to HF-only, we refer the interested reader to [100].

Concerning the GWB, in [298] they show that the fraction of SNR below 30Hz drops from more than 95% to about 40% when one opts for the ET-B design instead of the ET-D design. As shown in Fig. 4.1 (see also [218]), the sensitivity for searches for an isotropic GWB is about an order of magnitude greater for power-law like signals in the 3Hz-10Hz frequency band if the ET(D) design is chosen over the ET-B design. More broadly speaking ET-D outporforms ET-B for frequencies up to $\sim$ 40Hz.
Note, as explained in Chap. 2 the ET-B design is more sensitive in the lowest frequency region compared to the HF-only design which is currently considered in case no low frequency detectors would be pursued. This implies that the loss of science case for the search for a GWB explained above will be even larger in case HF-only is constructed compared to the full HFLF-cryo design, which has a very similar sensitivity to ET-D. This is clearly illustrated in Fig. 4.1 in Chapter 4. Here the broadband sensitivity curves for an isotropic GWB are plotted in case of a baseline existing of two interferometers with both the same sensitivity, chosen to be either HFLF-cryo, HF-only, ET-D or ET-B, assuming a co-located triangular configuration. Whereas HFLF-cryo (and ET-D) is (are) the most sensitive to power-law GWB signals at $\sim$ 7Hz, a set-up with only two HF-only (ET-B) detectors has its peak sensitivity near 40Hz (50Hz). At 7Hz the sensitivity of HF-only to power-law signals with negative slopes is $\sim 200\times$ worse compared to HFLF-cryo. Similarly ET-B has a sensitivity $\sim 20\times$ worse compared to ET-D at 7Hz. For a GWB which has a frequency independent dimensionless energy density of GWs $\Omega_{\rm GW}$, which will be introduced in Chapter 4, HFLF-cryo/ET-D is 'only' about one order of magnitude more sensitive compared to HF-only/ET-B. Several cosmological GWBs are expected to have such a frequency independent behaviour.

We would like to note that CE does not aim to push to be sensitive to GWs with frequencies of $\sim$1Hz. However, their design sensitivity is planned to be similar to HFLF-cryo around 5Hz to 10Hz. Moreover, CE will even be more sensitive by up to a

factor of two, to GWs with frequencies between 9Hz and 100Hz. This is mainly due to different design choices, such as the 40km arm length compared to the 10km for the ET.

3.3 Detections of gravitational waves until July 2023

The first observation of evidence supporting the emission of GWs dates back to the Hulse-Taylor binary pulsar or PSR B1913+16 [209, 341]. This pulsar was first observed in 1974 and was found to be part of a binary system. As mentioned in previous section, binary systems have a time varying quadruple moment, leading to the emission of GWs. This emission of GWs in turn leads to a decay of the orbital period and the binary bodies inspiral towards each other. The decrease of the orbital period as observed in the Hulse-Taylor pulsar was found to be consistent with the emission of GWs as predicted by Einstein's theory of GR. Hulse and Taylor were awarded a Nobel prize in 1993 for the discovery of this pulsar system.

At the same time Joseph Weber pioneered the attempt to directly observe GWs by using a resonant bar detector [362]. He developed and build the first resonant bar detector in the 1960s. Even though over the next decades various other resonant bar detectors were constructed with significantly better sensitivity, they were unable to claim any convincing detection of a GW. Their sensitivity would have enabled them to see relatively loud events in our galaxy or close proximity. However, no such events were detected.

To be sensitive to GW signals from beyond our galaxy in the Hz-kHz frequency band, one has to rely on interferometric GW detectors [174]. The first GW interferometer was build by R. Forward [174]. This concept was also brought forward in the 1960s, first by M. Gersenshtein and V. I. Pustovoit. Later on it was pushed forward by R. Weiss and others in the end leading to the construction of the LIGO and Virgo instruments. These instruments were run in intermittent phases of observing mode and upgrading. In 2015 and 2017 the LIGO, respectively Virgo, instruments finished a more substantial upgrade which started the 'Advanced' detector era with the new and higher sensitivity detectors called Advanced LIGO and Advanced Virgo. This led to the first direct observation of GWs in 2015 [19] by the LIGO and Virgo collaborations. In 2017 R. Weiss, B. Barish and K. Thorne were awarded a Nobel prize "*for decisive contributions to the LIGO detector and the observation of gravitational waves*". In 2017 Alain Brillet of ARTEMIS, Université Côte d'Azur, was awarded a CNRS gold medal for his visionary contributions to Virgo. In the next section we

will discuss in more detail the first detection as well as some other important direct observations made afterwards.

3.3.1 First direct detections of gravitational waves

GW150914 - Binary black hole merger

On September 14, 2015 at 09:50:45 UTC the first direct detection of a GW was made [19]. The two LIGO detectors simultaneously observed a transient GW with a significance of over 5σ. The estimated signal from the binary merger was shown earlier in Fig. 3.1 as an illustration of a typical CBC event. The signal was consistent with the merger of two black holes with initial masses of $36^{+5}_{-4}\mathrm{M}_{\odot}$ and $29^{+4}_{-4}\mathrm{M}_{\odot}$ at a distance of 410^{+160}_{-180} Mpc [3] (redshift[4]: $z = 0.09^{+0.03}_{-0.04}$). The final black hole after the merger has a mass of $62^{+4}_{-4}\mathrm{M}_{\odot}$ with $3.0^{+0.5}_{-0.5}\mathrm{M}_{\odot}$ radiated away in the form of GWs.

This event, named GW150914 is not only the first direct observation of GWs but also implies that solar mass black holes and BBH systems exist.

GW170817 - Binary neutron star merger and the start of multi-messenger astronomy

Another remarkable detection was the observation of GW170817, the first GW signal coming from the merger of a BNS system [17]. The signal was observed by the Advanced LIGO and Advanced Virgo detectors on August 17, 2017. An excellent sky localisation was reached and the source was estimated to be within a sky region of 28 deg^2 with 90% probability. This excellent sky localisation was partially due to the addition of a third detector, Virgo, since this enabled a more precise triangulation of the signal. The binary system was inferred to have a luminosity distance[5] of 40^{+8}_{-14}Mpc. The event was even more extraordinary since 1.7 seconds after the coalescence of the BNS a γ-ray burst (GRB) GRB170817A was detected by the Fermi Gamma-ray Burst Monitor as well as the Anti-Coincidence Shield for the Spectrometer for the International Gamma-Ray Astrophysics Laboratory [15, 18]. This first joint detection of GWs and optical counterparts started the field of multi-messenger astronomy and proves BNS mergers can be progenitors of GRBs. Multiple

[3] Parsec is a unit of distance with 1 pc $\approx 3 \cdot 10^{16}$m

[4] Due to the expansion of the Universe signals are redshifted while traveling to us. Therefore redshift can be used as a measure of the distance traveled by the signal.

[5] The luminosity distance is the distance one can infer based on the relationship between the absolute magnitude and the apparent, observed magnitude of electromagnetic observation.

observations were made of this event in varying optical and radio bandwidths in the aftermath of the event [18].

Other observations until July 2023

Apart from these two high impact observations many other CBC events have been observed by the LIGO and Virgo detectors, reported by the LIGO, Virgo and KAGRA collaborations [13, 25, 27, 31, 343]. These observations include a wide variety of BBH mergers as well as several BNS [12, 17] and NSBH mergers [28]. With several tens of GW observations of CBC events one can start to look into the characteristics of the population of these binary systems [31]. Since the start of O4 on May 24th 2023 several tens of significant CBC candidates have been publicly announced [246].

Even though there are several other types of signals that could be observed by Earth-based GW detectors, such as bursts, CW and a GWB, at the moment Advanced LIGO and Advanced Virgo are only able to observe CBC events. Despite the large number of detections, the field of GW observations can be considered to still be in its infancy and the future might hold many more interesting observations of different GW sources.

Strong evidence for a nHz GWB signal

In 2020 multiple PTA observed a possible first hint of a GW signal. They observed correlations in disturbances of the time of arrival of the pulsars [62, 70, 117, 183]. However, at the time there was no statistically significant evidence to claim the process had the spatial correlation expected from a GW signal, as given by the Hellings & Downs curve. Therefore no robust detection of a GW signal could be claimed. In June 2023 the different PTA collaborations announced they found (strong) evidence for a nHz GWB. Note, at the moment they do not claim to have detected the nHz GWB, as for a first, 'gold-plated' detection a significance threshold of 5σ is typically used. At the moment the observed significance varies for the different collaborations[6], with a significance of 4.6σ (CPTA [367]), $\sim 3{-}4\sigma$ (NANOGrav [45]), $\gtrsim 3\sigma$ (EPTA/EPTA+InpTA [65]) and $\sim 2\sigma$ (PPTA [293]). When fixing the spectral behaviour to the one expected from a GWB from SMBHB, i.e. $f^{-2/3}$ in characteristic strain or $f^{-13/3}$ in the pulsar timing residuals, the characteristic strain amplitude A at the reference frequency $f_{\rm ref} = 1{\rm yr}^{-1}$ is $\log A = -14.7^{+0.9}_{-1.9}$ (CPTA [367]),

[6] In the remainder of this section we will order the results in decreasing order of significance as reported in the publications.

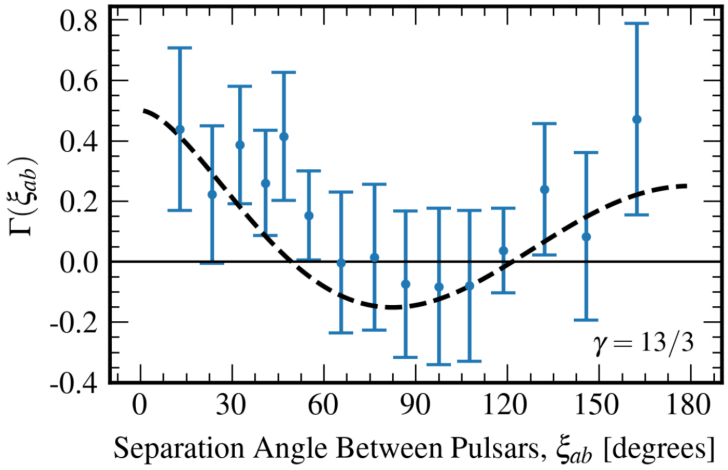

Fig. 3.2.: The inter-pulsar correlations (Γ) as a function of the angular separation between pulsars pairs (ξ_{ab}) for the 15yr NANOGrav data set, assuming maximum-a-posteriori pulsar noise parameters and a spectral behaviour of $f^{-13/3}$ in the pulsar timing residuals. The black dashed line shows the cross-correlated power predicted for Hellings & Downs correlations. For more information on the figure and data we refer the interested reader to [45]. Figure taken from [45].

$A = 2.4^{+0.7}_{-0.6} \times 10^{-15}$ (NANOGrav [45]), $A = 2.5 \pm 0.7 \times 10^{-15}$ (EPTA/EPTA+InpTA [65]) and $A = 2.04^{+0.25}_{-0.23} \times 10^{-15}$ (PPTA [293]). In Fig. 3.2 we show the observed spatial correlations between pulsars, as reported by the NANOGrav collaboration [45]. Even though the inferred spectral index is consistent with the one expected from a GWB from SMBHB, also other signals are compatible with the observed signal. As an example, the signal observed by NANOGrav is also consistent with e.g. cosmic inflation or first-order phase transitions [43]. Combining the already available data from the different PTAs in the IPTA analysis and/or the addition of more data in the future should lead to the claim of the detection of a nHz GWB with $\geq 5\sigma$ in the coming years. Over time this should also shed light on which is the most likely source of the signal. However, regardless of the source(s), the observation of the nHz GWB is another monumental achievement of GW astronomy and will help us gain more fundamental insights in various astrophysical and/or cosmological processes.

Apart from the main analysis in search for a nHz GW signal, the different PTA collaborations have also looked further into a range of different topics such as the astrophysical and cosmic implications of their signal, their data quality and the levels of anisotropy in the signal. We will not discuss any of these more detailed works, but refer the interested reader to the additional publications by the NANOGrav [43, 44, 46–49, 220], EPTA [63, 64, 66, 67, 330] and PPTA collaborations [292, 371].

3.4 Upper limits on the gravitational-wave background

In this section we will highlight some of the most stringent upper limits on the GWB across the different frequency bands. We will only focus on an isotropic GWB, since it is the main focus of this dissertation. Some of the mentioned sources and the upper limits discussed below, are represented in Fig. 3.3.

One can put upper limits on a relic GWB by requiring consistency with the imprint that would be left on the CMB and BBN [226] observations. Using data from the Planck experiment [39], the authors of [279] report 95% upper limits on the dimensionless energy density of GWs Ω_{GW}, which will be introduced in Chapter 4,: $h^2\Omega_{\text{GW}} < 1.2 \times 10^{-6}$ for frequencies $f > 10^{-15}$ Hz. h^2 parameterizes the value of the Hubble-Lemaître constant H_0, i.e. $H_0 = h \times 100$ km s^{-1} Mpc^{-1}. If we choose the value of $h = 0,679$ as inferred from the Planck 2015 observations [42] the upper limit reads $\Omega_{\text{GW}} < 2.61 \times 10^{-6}$.
The lack of an observation of an imprint of tensorial fluctuations in the CMB puts upper limits of about 10^{-14} on Ω_{GW} at 10^{-17}Hz. This can be extrapolated to an upper limit of about 10^{-15} on Ω_{GW} above 10^{-17}Hz for a GWB from standard inflation [234].

nHz GWB

The strength of the observed process by PTAs at reference frequency of 1 yr$^{-1} \approx 3.17 \cdot 10^{-8}$Hz has an amplitude of about $2 \cdot 10^{-15}$ in characteristic strain, when fixing the power-law slope of the signal to the one expected from SMBHB [62, 70, 117, 183]. The exact inferred value differs slightly for the results of the different PTAs. If we convert the characteristic strain[7] to the energy density of the GWB Ω_{GW}, this corresponds to $\sim 5.5 \cdot 10^{-9}$. For more information on the conversion from characteristic strain to the energy density Ω_{GW}, we refer the interested reader to [304].

mHz GWB

There are not many historical experiments trying to measure a GWB in the mHZ band and currently the best upper limits come from accurately measuring the Earth normal modes. The authors of [131] use 10 years worth of seismometer and gravimeter data monitoring Earth's seismic activity to constrain the SGWB, resulting in the

[7] The characteristic strain h_c is given by $h_c = \sqrt{f \cdot S_h}$, with S_h defined in Eq. 4.5 [304].

following constraints: $h^2\Omega_{\mathrm{GW}} < 0.035 - 0.15$ for the 0.3mHz - 5mHz band. Both LISA and the Lunar Gravitational-Wave Antenna will be able to drastically improve these upper limits by many orders of magnitude, or claim detections.

Hz-kHz GWB

In the Hz-kHz regime, upper limits have been placed on an isotropic GWB by searches using two bar detectors [72] as well as a bar detector and interferometric gravitational-wave detector [6]. However the most recent and best upper limits come from LIGO's and Virgo's third observing run, where they placed a 95% upper limit of $\Omega_{\mathrm{GW}} < 5.8 \cdot 10^{-9}$ for a flat GWB, i.e. frequency independent, in Ω_{GW} [30]. Previously upper limits were placed on a GWB with $\alpha = 3$ by using data of initial LIGO and initial Virgo ($\Omega_{\mathrm{GW},\alpha=3} < 0.32$ at 900Hz) [4] and the two co-located Hanford detectors ($\Omega_{\mathrm{GW},\alpha=3} < 7.7\,10^{-4}$ at 900Hz) [2].

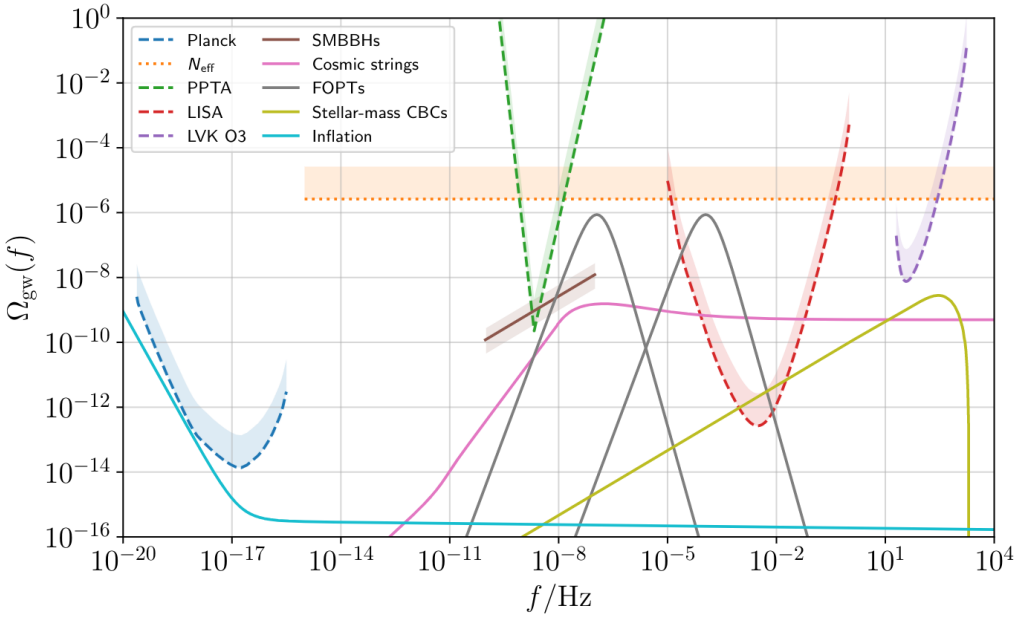

Fig. 3.3.: An overview of some of the GWB sources across the frequency spectrum. For more detail on the used parameters and models for the different sources, see [301]. Note that the upper limits denoted in this figure by N_{eff} (orange dotted) are the upper limits obtained by using information from BBN, as discussed in the text. Also the constraints from LVK's third observing run O3 are shown, as well as the PPTA results from 2021 [183], i.e. the data set where an excess was observed but without any evidence for the Hellings & Downs curve in the spatial correlation. However, the amplitude of the excess observed in 2021 is consistent with the more recent results as described earlier. Also the projected sensitivity for LISA is shown. Figure taken from [301].

4 The gravitational-wave background

> *The rule has been that when one opens a new channel to the Universe, there is usually a surprise in it. Why should the gravitational channel be deprived of this?*
>
> **— Rainer Weiss**

In this chapter we will discuss the gravitational-wave background and the analysis methods currently used by Earth-based interferometric detectors. Even though many of the concepts could more broadly be used, we only focus on Earth-based interferometric detectors. Furthermore, there is a strong focus on the search for an isotropic GWB, since this is the key subject of this dissertation.

Observing a Hz to kHz GWB would be another major achievement for the field of GW astrophysics, regardless of the origin of the background. In case of the astrophysical GWB coming from unresolved CBC events it would yield us additional information on the distant Universe inaccessible via direct observations with LVK. The most distant CBC events observed during the first three observing runs from LIGO and Virgo are located at a redshift $z \leq 1$. However, the observation of the GWB coming from the superposition of CBC events would give us valuable information on the population of CBC events on cosmological distances. Here we want to note that despite these distant CBC mergers $z \geq 1$ being too weak to be observed individually with LVK, CE and ET would be able to observe (almost) all CBC events in the observable Universe.

The search for a GWB from cosmological origin might be less certain, but in case of a detection it could revolutionize our knowledge of the processes in the early Universe. Even in case of non-detection, this can be used to place stringent upper limits on certain beyond Standard Model theories. These constraints are often complementary to constraints coming from particle physics experiments at accelerators, since both methods probe different regions of the parameter space.

4.1 Statistical properties of the gravitational-wave background

A GWB can be described in terms of the 'moments' of the metric perturbation [304]. In case the GWB is Gaussian, all statistical properties can be described in terms of the quadratic moment. For non-Gaussian GWB signals this simplification does not hold. We refer the interested reader for a more detailed discussion of the non-Gaussian scenario to [304]. The expectation value of the second moment in case of a Gaussian, stationary, unpolarized, spatially homogeneous and isotropic background is

$$\langle h_A(f,\hat{\mathbf{n}}) h^*_{A'}(f',\hat{\mathbf{n}'})\rangle = \frac{1}{16\pi} S_h(f)\delta(f-f')\delta_{AA'}\delta^2(\hat{\mathbf{n}},\hat{\mathbf{n}}'), \tag{4.1}$$

where $S_h(f)$ is the one-sided strain PSD. The stationarity assumption leads to $\delta(f-f')$, whereas $\delta_{AA'}$, with A the GW polarization, results from the assumption the GWB is unpolarized. $\delta^2(\hat{\mathbf{n}},\hat{\mathbf{n}'})$ comes from the spatial homogeneity and the isotropy, where $\hat{\mathbf{n}}$ is the vector indicating the sky location. If we abandon the assumption of spatial homogeneity and the isotropy, but require the anisotropies to be uncorrelated between different directions we get

$$\langle h_A(f,\hat{\mathbf{n}}) h^*_{A'}(f',\hat{\mathbf{n}'})\rangle = \frac{1}{4} \mathcal{P}(f,\hat{\mathbf{n}})\delta(f-f')\delta_{AA'}\delta^2(\hat{\mathbf{n}},\hat{\mathbf{n}'}), \tag{4.2}$$

where $\mathcal{P}(f,\hat{\mathbf{n}})$ quantifies the GW power as a function of the sky location and frequency. The isotropic power, $S_h(f)$, is simply the result of integrating the angular GW power, $\mathcal{P}(f,\hat{\mathbf{n}})$, across the entire sky,

$$S_h(f) = \int_{\text{sky}} \mathcal{P}(f,\hat{\mathbf{n}}) d\hat{\mathbf{n}}. \tag{4.3}$$

4.2 Analysis methods

4.2.1 Cross-correlation analysis for a Gaussian, stationary and isotropic gravitational-wave background

For an isotropic GWB we are interested in the dimensionless energy density $\Omega_{GW}(f)$ which is related to the energy density of GWs $\mathrm{d}\rho_{\mathrm{GW}}$ in a logarithmic frequency interval $\mathrm{d}\ln f$,

$$\Omega_{\mathrm{GW}}(f) = \frac{1}{\rho_{\mathrm{c}}} \frac{\mathrm{d}\rho_{\mathrm{GW}}}{\mathrm{d}\ln f}\,. \tag{4.4}$$

Here $\rho_c = 3H_0^2c^2/(8\pi G)$ is the critical energy density for a flat Universe. H_0 is the Hubble-Lemaître constant, c is the speed of light and G is Newton's constant. From hereon we will always use the 15-year Planck value of 67.9 km s^{-1} Mpc^{-1} for H_0 [42], unless explicitly stated otherwise.

The energy density of the GWB $\Omega_{GW}(f)$ and the strain PSD $S_h(f)$ are related to each other by the following equality,

$$S_h = \frac{3H_0^2}{2\pi^2}\frac{\Omega_{GW}(f)}{f^3}. \tag{4.5}$$

To understand how S_h relates to the output from our detector, we note that the strain signal, $s_I(f)$, observed by a GW interferometric detector I can be written as,

$$\begin{aligned} s_I(f) &= n_I(f) + h_I(f) \\ &= n_I(f) + \sum_A F_I^A(f)h^A(f), \end{aligned} \tag{4.6}$$

with F_I^A the antenna pattern function of detector I for a GW with polarization A, as introduced in Eq. 2.4. $n_I(f)$, $h_I(f)$ represent the noise, respectively the GW component in detector I. The correlation between two detectors can be written as,

$$\begin{aligned} \langle s_I s_J\rangle &= \langle h_I h_J\rangle + \langle h_I n_J\rangle + \langle h_J n_I\rangle + \langle n_I n_J\rangle \\ &= \langle h_I h_J\rangle + \langle n_I n_J\rangle, \end{aligned} \tag{4.7}$$

where we dropped the explicit frequency dependence. We have used $\langle h_I n_J\rangle = \langle h_J n_I\rangle = 0$ since the GW signal and infrastructural/environmental noise are uncorrelated. Generally one assumes $\langle n_I n_J\rangle = 0$, i.e. the noise in each detector is fully uncorrelated. Given the large separation between the current generation of Earth-based GW detectors this seems a good assumption. To first order this is true, however there are environmental and instrumental noise sources that can be correlated over these long distances. In this chapter we will assume $\langle n_I n_J\rangle = 0$ to formulate the mathematical formalism. However, the deviation of this assumption and the study of correlated noise sources is a key focus of this dissertation and an introduction to possible correlated noise sources as well as how this affects the formalism will be given in Chapter 5. A detailed discussion of the work performed in the context of this thesis is reserved for Part II.

One can show that in the case of a Gaussian, stationary, unpolarized, spatially homogeneous and isotropic background, $\langle h_I(f)h_J^*(f')\rangle$ reduces to [304],

$$\langle h_I(f)h_J^*(f')\rangle = \frac{1}{2}\delta(f-f')\Gamma_{IJ}(f)S_h(f), \tag{4.8}$$

with Γ_{IJ} the overlap reduction function. The overlap reduction function, given in Eq. 4.9, is related to the antenna pattern function $F_I^A(f)$, as defined in Eq. 2.4 and describes how the baseline, i.e. a pair of detectors, responds to an isotropic GW signal.

$$\Gamma_{IJ}(f) = \frac{1}{8\pi} \sum_A \int_{\text{sky}} F_I^A(f, \hat{\mathbf{n}}) F_J^A(f, \hat{\mathbf{n}}) e^{2\pi i f \Delta \mathbf{x} \cdot \hat{\mathbf{n}}/c} d\hat{\mathbf{n}} \tag{4.9}$$

One can define the normalized overlap reduction function (ORF)[1] $\gamma_{IJ}(f)$ by requiring that $\gamma_{IJ}(0) = 1$ for aligned and co-located detectors. This leads to the definition of the normalized overlap reduction function,

$$\begin{aligned} \gamma_{IJ}(f) &= \frac{5}{\sin^2\beta} \Gamma_{IJ}(f), \\ &= \frac{5}{8\pi \sin^2\beta} \sum_A \int_{\text{sky}} F_I^A(f, \hat{\mathbf{n}}) F_J^A(f, \hat{\mathbf{n}}) e^{2\pi i f \Delta \mathbf{x} \cdot \hat{\mathbf{n}}/c} d\hat{\mathbf{n}} \end{aligned} \tag{4.10}$$

where β is the opening angle between the two arms of an interforometric detector, i.e. $\pi/2$ for LIGO, Virgo and KAGRA and $\pi/3$ for ET and LISA. This leads to a pre-factor of respectively $\frac{5}{8\pi}$ and $\frac{5}{6\pi}$. Intuitively one can understand the ORF as follows: two co-located and co-aligned detectors have the same detector response and therefore see every signal in the same way, their ORF is unity. However by misaligning and/or separating the two detectors the signal they observe becomes different and therefore their coherent response decreases. One could argue the most optimal detector set-up is to have co-located detectors. However, having co-located detectors drastically increases the amount of correlated noise which forms a huge threat for performing the search for a GWB since this changes the observed correlation given that $\langle n_I n_J \rangle \neq 0$. This was a large problem for the search between the two co-located Hanford detectors during the fifth science run (S5) of initial LIGO [2, 175]. In Chapters 5 and 9 we will discuss how for instance correlated seismic noise might become important for the ET due to its co-located triangular design, whereas this is not a problem for the widely separated LIGO, Virgo and KAGRA detectors. Correlated magnetic noise can even be a problem for widely separated detectors and will be discussed in Chapters 5, 7 and 8.

In practice a cross-correlation statistic can be constructed which is an unbiased estimator of $\Omega_{GW}(f)$:

$$\hat{C}_{IJ}(f) = \frac{2}{T} \frac{\text{Re}[\tilde{s}_I^*(f) \tilde{s}_J(f)]}{\gamma_{IJ}(f) S_0(f)} , \tag{4.11}$$

[1] When using the abbreviation ORF, we refer to the normalized ORF, unless specifically stated otherwise.

where $\frac{2}{T}\mathrm{Re}[\tilde{s}_I^*(f)\tilde{s}_J(f)] = \mathrm{Re}[\mathrm{CSD}_{IJ}]$, the cross spectral density (CSD), with T the time over which the Fourrier transform is calculated. The normalisation factor $S_0(f)$ is given by $S_0(f) = \frac{3H_0^2 \sin^2\beta}{10\pi^2 f^3}$. In the small signal-to-noise ratio limit for the GWB, the uncertainty on $\hat{C}_{IJ}(f)$ is given by [55, 304],

$$\sigma_{IJ}(f) \approx \sqrt{\frac{1}{2T\Delta f}\frac{P_I(f)P_J(f)}{\gamma_{IJ}^2(f)S_0^2(f)}}, \tag{4.12}$$

where Δf is the frequency resolution and $P_I(f)$ the PSD of detector I.

An optimal estimator for $\Omega_{\mathrm{GW}}(f)$ does not only rely on the cross-correlation but also on the auto-correlation of detectors I and J [55, 304]. However they are not known with sufficient precision for the current detectors, in which case $\hat{C}_{IJ}(f)$ is approximately an optimal estimator.

The signals one expects to observe are often predicted to follow a power-law behaviour, in the relevant frequency region,

$$\Omega_{\mathrm{GW}}(f) = \Omega_{\mathrm{ref}}\left(\frac{f}{f_{\mathrm{ref}}}\right)^{\alpha}, \tag{4.13}$$

where $\Omega_{\mathrm{GW}}(f)$ is the spectral shape of the GWB and it is reported with respect to a reference frequency f_{ref}. This reference frequency can be arbitrarily chosen. As we saw earlier for PTA this is typically chosen to be 1 year^{-1}, whereas for Earth-based interferometric detectors it is typically chosen to be 25Hz, since this is around their most sensitive frequency region for a GWB. In general the spectral shape of $\Omega_{\mathrm{GW}}(f)$ can take other forms as well. For example, there are several cosmological GWBs, such as first order phase transitions, which are predicted to have a broken power-law behaviour [111, 327]. Some examples of GWBs which are expected to behave as power-laws in the relevant frequency range are the GWB from unresolved CBC events ($\alpha = 2/3$) [16, 254, 295] and the GWB from core collapse supernovae ($\alpha = 3$) [168]. Multiple cosmological GWBs, e.g. cosmic strings [23], predict a flat GWB ,i.e. $\alpha \approx 0$.

Optimal filter and parameter estimation

Given a model of the spectral shape of the GWB one can combine the different discrete frequency bins f_k optimally as follow [30],

$$\begin{aligned}\hat{C}_{IJ} =& \frac{\sum_k w(f_k)\hat{C}_{IJ}(f_k)\sigma_{IJ}^{-2}(f_k)}{\sum_k w(f_k)^2\sigma_{IJ}^{-2}(f_k)},\\ \sigma_{IJ}^{-2} =& \sum_k w(f_k)^2\sigma_{IJ}^{-2}(f_k).\end{aligned} \tag{4.14}$$

Here the optimal weights $w(f_k)$ are:

$$w(f_k) = \frac{\Omega_{\rm GW}(f_k)}{\Omega_{\rm GW}(f_{\rm ref})}, \tag{4.15}$$

Finally if one has more than two detectors in the observing network one can construct multiple baselines, for which a weighted average yields a network cross-correlation statistic,

$$\hat{C} = \frac{\sum_{IJ}\hat{C}_{IJ}\sigma_{IJ}^{-2}}{\sum_{IJ}\sigma_{IJ}^{-2}}, \quad \sigma^{-2} = \sum_{IJ}\sigma_{IJ}^{-2}. \tag{4.16}$$

This weighted cross-correlation statistic of multiple baselines is the preferred alternative for computing higher order correlations for the different detectors in the network [55, 83, 256, 269, 304].

To perform parameter estimation (or place upper limits), one can use the following likelihood

$$p(\hat{C}_{IJ}(f_k)|\mathbf{\Theta}) \propto \exp\left[-\frac{1}{2}\sum_{IJ}\sum_k\left(\frac{\left(\hat{C}_{IJ}(f_k) - \Omega_{\rm GW}(f_k|\mathbf{\Theta})\right)^2}{\sigma_{IJ}^2(f_k)}\right)\right]. \tag{4.17}$$

In more complex scenario's one could model multiple signals simultaneously [258] or model a signal and e.g. correlated noise [267]. The latter will be further discussed in Chapter 5.

Power-law integrated sensitivity curve

Earlier we mentioned that many signals are expected to follow a power-law behaviour (Eq. 4.13). Therefore the uncertainty on the cross-correlation statistic, $\sigma_{IJ}(f)$ (Eq. 4.12), is not the optimal metric to judge the sensitivity of a certain detector to a GWB signal. The power-law integrated (PI) sensitivity curve [350], $\Omega_{IJ}^{\rm PI}(f)$, does take the expected broadband character of the GWB into account. The

PI-curve is constructed using $\sigma_{IJ}(f)$ so that its tangent at any frequency represents the sensitivity at which one could detect this tangent power-law $\Omega_{GW}(f)$. One can define the PI-curve for any signal-to-noise ratio.

As an illustration, Fig. 4.1 shows the PI-curve for the ET, equivalent to the sensitivity curves in Fig. 2.7. We use a co-located, triangular configuration for the three ET-interferometers and calculate the PI curve for one pair of interferometers. Furthermore we assume 1yr of continuous observation or equivalent two years of observation at 50% duty-cycle and use a SNR of 1. Fig. 4.1 shows HFLF-cryo/ET-D could be sensitive to a GWB at the $\Omega_{\mathrm{GW}}(f) \sim 10^{-12}$ range, with an SNR=1 after 1 year of observation. This seems to be consistent with earlier investigations stating a GWB with strength $\Omega_{\mathrm{GW}}(f) = 2 \cdot 10^{-12}$ would be detected with an SNR=5 after 1.3 years of observation time [324].
Apart from the different PI-curves, we also show the GWB expected from CBC events in Fig. 4.1. This illustrates the possible detection of this signal by Advanced LIGO and Advanced Virgo at their design A+, respectively AdV+ sensitivities. Note that with the ET many of the individual BBH mergers contributing to the GWB for LIGO and Virgo will be resolvable. This is also true for individual BNS mergers, however they might be more difficult to disentangle due to their larger signal overlap.

For ET we can calculate the PI-curve as the location and orientation of one detector is known with respect to another due to ET's triangular configuration of detectors. However, for CE we do not know the possible locations nor the detectors' orientation. Therefore we are unable to calculate the ORF, which is needed to construct a baseline's sensitivity to a GWB. Future work could aim to probe different configurations of two CE detectors as well as combinations between CE and ET to provide statements on their capabilities to observe a GWB.

4.2.2 Analysis techniques for an isotropic gravitational-wave background of intermittent nature

For a GWB of intermittent nature but still isotropically distributed on the sky, one could imagine improving upon the cross-correlation statistic defined in Eq. 4.11. An example of an intermittent GWB is the background from unresolved BBH events. These signals have a typical duration of ∼1 sec, whereas the time between two signals in the observable Universe is on average about 5-10 minutes based on the merger rates from the direct BBH observations [9, 31]. During most of the time no signal is present, therefore the sensitivity of the cross-correlation statistic (Eq. 4.11) to such a signal is drastically reduced since it averages over both times with and

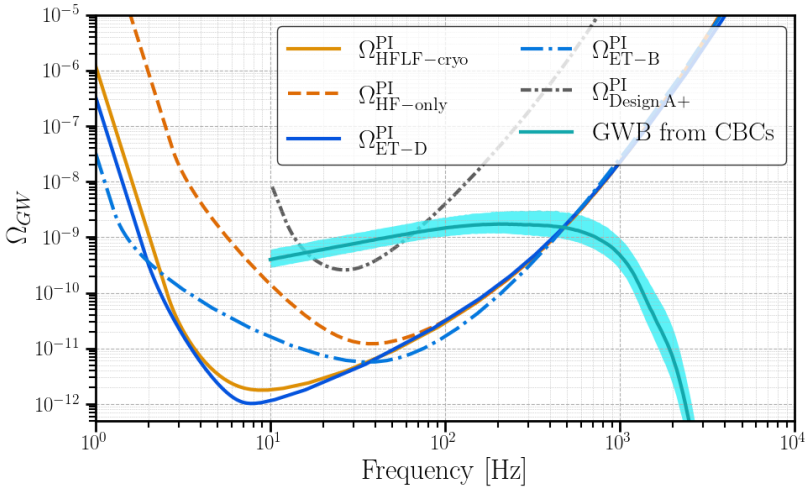

Fig. 4.1.: Power-law integrated sensitivity curves of the Einstein Telescope, according to the 'HFLF-cryo', 'HF-only', 'ET-D' and 'ET-B' designs. We assume a co-located, triangular configuration for the ET-interferometers and construct the PI curve for 1yr of observation time and SNR of 1 for one pair of ET-interferometers. For comparison we also show the PI curve for LIGO Hanford and LIGO Livingston at design A+ sensitivity.
The GWB expected from CBC mergers (BBH, BNS and NSBH combined) based on the population observed during LVKs third observing run [31] is shown, where the curves are obtained from the public dataset [242]. The 5% to 95% percentiles are delimited by the teal band, whereas the median is indicated in dark teal.

without signal present in the data. To this extent two approaches have been proposed to increase the sensitivity to such an intermittent signal and possibly enabling a detection much earlier.

A first discussion on how to account for the intermittent nature of such a background was discussed in [145], on which later [331, 339] and [235] build. We will briefly highlight the philosophy of the two methods currently being investigated, but refer the interested reader to the relevant literature for a more detailed discussion.

A first method is called 'Stochastic Search for an Intermittent GWB' (SSI) [235]. The key concept is to have a likelihood such that it contains one part with signal present and one part without signal and only noise. The ratio between both is governed by the duty-cycle which is a measure for intermittence. A duty cycle of 1 equals to a fully Gaussian background and the closer to zero the duty cycle is, the larger the intermittent nature of the signal becomes. In this way the signal-likelihood is not diluted by averaging over segments where no signal is present.

A second method tries to apply match-filtering techniques used to observe CBC events. This method is computational very expensive and will be more strongly

driven by sub-threshold, but individually resolvable BBH events. This search method is called 'The Bayesian Search' (TBS) [331, 339].

The advantage of TBS is that by using more information on the type of signal, a detection could be made sooner, however it comes at a computational cost. The advantage of SSI is that it is a more agnostic approach and is also sensitive to other intermittent backgrounds. However, both of them could achieve a detection of the GWB from BBH significantly earlier compared to the standard cross-correlation analysis explained in Sec. 4.2.1

Although both methods are very promising and have made great progress over the last years, they still have to mature further before they can be used on real data. As an example, for now the methods only have been tested on idealized Gaussian detector noise. Also the effect of correlated noise as well as correlated glitches on these methods will have to be understood.

4.2.3 Analysis techniques for an anisotropic gravitational-wave background

In Eq. 4.2 we introduced $\mathcal{P}(f, \hat{\mathbf{n}})$,which quantifies the GW power across the sky. Searches looking for anisotropic GWBs assume this angular GW-power distribution factorizes in a directional power $\mathcal{P}(\hat{\mathbf{n}})$ and a direction independent spectral shape $H(f)$ [304], i.e.

$$\mathcal{P}(f, \hat{\mathbf{n}}) = \mathcal{P}(\hat{\mathbf{n}})H(f). \tag{4.18}$$

Similar to the isotropic analysis one often assumes a power-law spectral shape, i.e. $H(f) = \left(\frac{f}{f_{\rm ref}}\right)^{\alpha}$, where $H(f)$ is normalized to equal 1 at $f = f_{\rm ref}$.

The anisotropic cross-correlation statistic, i.e. the equivalent of Eq. 4.11 for isotropic searches, is given by [304]

$$\hat{C}_{IJ}(t, f) = \frac{2}{T}\tilde{s}_I^*(t, f)\tilde{s}_J(t, f) \tag{4.19}$$

and its expectation value equals

$$\langle \hat{C}_{IJ}(t, f)\rangle = H(f) \int d\hat{\mathbf{n}}\, \gamma_{IJ}(t, f, \hat{\mathbf{n}})\mathcal{P}(\hat{\mathbf{n}}). \tag{4.20}$$

Here $\hat{C}_{IJ}(t,f)$ is evaluated at time segment t and frequency f and the anisotropic ORF $\gamma_{IJ}(t,f,\hat{\mathbf{n}})$ is given by

$$\gamma_{IJ}(t,f,\hat{\mathbf{n}}) = \frac{1}{2}\sum_{A} F_I^A(t,f,\hat{\mathbf{n}}) F_J^A(t,f,\hat{\mathbf{n}}) e^{2\pi i f \Delta\mathbf{x}\cdot\hat{\mathbf{n}}/c}. \tag{4.21}$$

Up to a factor of $1/(4\pi)$, $\gamma_{IJ}(t,f,\hat{\mathbf{n}})$ equals the integrand of $\Gamma_{IJ}(f)$, as introduced in Eq. 4.9. Interesting to point out is that both $\hat{C}_{IJ}(t,f)$ and $\gamma_{IJ}(t,f,\hat{\mathbf{n}})$ can have non-zero real and imaginary parts, whereas for the isotropic search only the real part contributes as seen in Eq. 4.11.

Even though an isotropic search is also sensitive to an anisotropic GWB, it is sub-optimal for several reasons. First of all it does not enable to use the information present in the angular power distribution $\mathcal{P}(\hat{\mathbf{n}})$. This angular power distribution can entail a large amount of information on the source, such as is the case with the CMB. Secondly, an isotropic analysis is typically less sensitive to an anisotropic GWB. If one considers a point source from direction $\hat{\mathbf{n}}$, the SNR ratio between an isotropic and anisotropic analysis is [82]

$$\frac{(\mathrm{SNR})_{\mathrm{iso}}}{(\mathrm{SNR})_{\hat{\mathbf{n}}}} = \frac{[\gamma_{\mathrm{iso}},\gamma_{\hat{\mathbf{n}}}]}{\sqrt{[\gamma_{\mathrm{iso}},\gamma_{\mathrm{iso}}][\gamma_{\hat{\mathbf{n}}},\gamma_{\hat{\mathbf{n}}}]}}, \tag{4.22}$$

where we have used the shorthand notation γ_{iso} and $\gamma_{\hat{\mathbf{n}}}$ to refer respectively to the isotropic ORF (Eq. 4.10) and anisotropic ORF (Eq. 4.21). We used the notation $[A,B] = \sum_i \int df A_i^* B_i(f) H^2(f)/(P_{I,i}P_{J,i})$, where I,J refers to the interferometer and i is the index for summing over sidereal time[2]. The SNR between an isotropic and anisotropic analysis for a point source can take values between -1 and 1 depending on the sky-location [82]. This implies that the anisotropic analysis typically outperforms an isotropic analysis, unless the source is located at a very specific location. This is in line with your intuition that an anisotropic search should outperform an isotropic search in the case of a localized source. Maybe less intuitive is that point sources at certain sky positions will yield negative SNR when searched for with an isotropic analysis.

There are several types of anisotropic searches which use different methods to search for a GWB, based on the physical properties of the angular GW power distribution, $\mathcal{P}(f,\hat{\mathbf{n}})$. A first method decomposes $\mathcal{P}(f,\hat{\mathbf{n}})$ into a basis of spherical harmonics. This method, called spherical harmonic decomposition, targets extended GW sources on the sky, which could for instance follow the luminous matter distribution of the galaxy, such as the binary white dwarf GWB for LISA. To look for widely separated

[2]Time calculated from the motion of the Earth with respect to the distant stars, in contrast to solar time where the time is calculate with respect to the sun.

point sources on the sky, several analysis methods are being pursued. The broadband radiometer search looks for point sources on the entire sky, but does this by looking for an excess power in a wide frequency band. Narrowband radiometer searches on the other hand look for excess correlated power in narrow frequency bins, but only for specific sky localisations. This trade-off between the broadband and narrowband radiometer searches in all-sky/all-frequency coverage is due to the large computational cost to perform an all-sky-all-frequency search [184, 349]. However, recently the computational limitations where overcome due to higher computational efficiency and the folding of data [22]. The temporal symmetry of the directional ORF allows folding to reduce the data-set to one sidereal day, leading to a reduction factor equal to the number of observing days. The latter is of the order of $\mathcal{O}(100)$ for the most recent observing run of LIGO and Virgo. As the name suggests, the all-sky-all-frequency search looks for any point source on the entire sky in narrow frequency bins.

Since anisotropic searches for a GWB are not the focus of this dissertation, we refer the interested reader to the relevant literature for a more detailed discussion [8, 54, 82, 126, 270, 304, 347].

5

Noise sources for gravitational-wave background searches and methods to address them

> *If you torture the data long enough, it will confess to anything.*
>
> **— Ronald H. Coase**

In this chapter we will focus on noise sources that might affect the search for a GWB with Earth-based interferometric detectors. Typically we can divide these noise sources in three large categories. The first category consist of short duration, but high amplitude noise transients which breaks the non-stationary character of the noise spectrum. These features are often also called 'glitches' and will be discussed in Sec. 5.1. Afterwards, in Sec. 5.2, we will discuss narrowband spectral artefacts, often called 'noise lines' and how they can affect the search for a GWB. Whereas glitches are short duration and broadband in frequency, the noise lines are narrowband in frequency but are present on a long duration of days to even months or years. Finally, in Sec. 5.3, we will discuss how correlated (broadband) noise sources can bias the search for a GWB.

This chapter will mainly focus on the introduction of the different noise sources and how they can bias the search for a GWB. More information on a number of these noise sources and the investigations performed as part of this thesis will be discussed in Part II.

Furthermore, we want to point out that we assume in this chapter some initial data quality vetoes are already applied to the data. These vetoes are produced by the detector characterisation groups of the individual instruments and indicate times which should be excluded from analysis due to known instrumental effects causing transient and/or broadband noise in the detector. More discussion on this data quality veto's can be found in Sec. 4 of [5].

5.1 Non-stationary noise features

As mentioned in Sec. 4.2.1, one assumes the detector noise is stationary in the standard cross-correlation analysis. This assumption can break down for several reasons. First of all, the background noise slowly varies over the course of hundreds of seconds or more due to slowly varying sensitivity conditions. To this extent one breaks down the data in smaller segments typically on the order of $\mathcal{O}(100s)$ which ensures the slow variation of the detectors noise level is minimal.

Secondly, the data can contain short duration, high amplitude transient noise events, called glitches. These loud transient events can affect stochastic analyses by introducing a bias in the PSD and CSD estimation as is illustrated in Fig 5.1. These glitches can be particularly harmful for GWB searches looking for intermittent signals as introduced in Sec. 4.2.2, since they might mimic the intermittent behaviour of the signal. However also the standard search for an isotropic GWB will be affected by these glitches as they introduce a bias in the PSD estimation.

For pairs of detectors with a large separation e.g. LIGO, Virgo and KAGRA, these glitches are typically uncorrelated since they are of instrumental origin. However a recent study shows that lightning strikes can introduce correlated glitches over Earth-scale distances [214, 229]. This work will be discussed in more detail in Chapter 7.

$\Delta\sigma$-cut

A first method to address glitches and more generally all forms of non-stationarity in the data is to apply a cut removing all times where the standard deviation on the coherent map, σ_{IJ}, introduced in Eq. 4.12, varies too much between adjacent segments. This cut was introduced in [7] and is often refereed to as the '$\Delta\sigma$-cut'. Conceptually this cut can be conceived as [7, 300]

$$\frac{|\sigma_i - \sigma_{i+1}| + |\sigma_i - \sigma_{i-1}|}{2\sigma_i} > \text{threshold}\,, \tag{5.1}$$

where the index i refers to segment index. However, in practice a slightly different calculation is performed as discussed in [300]. This calculation entails the use of σ_i, averaged over frequency bins for a given power-law signal, i.e. as in Eq. 4.14. To be able to cover the entire frequency range, different power-law signals are considered and the final $\Delta\sigma$-cut is the union of all the different $\Delta\sigma$-cuts. In their analysis of

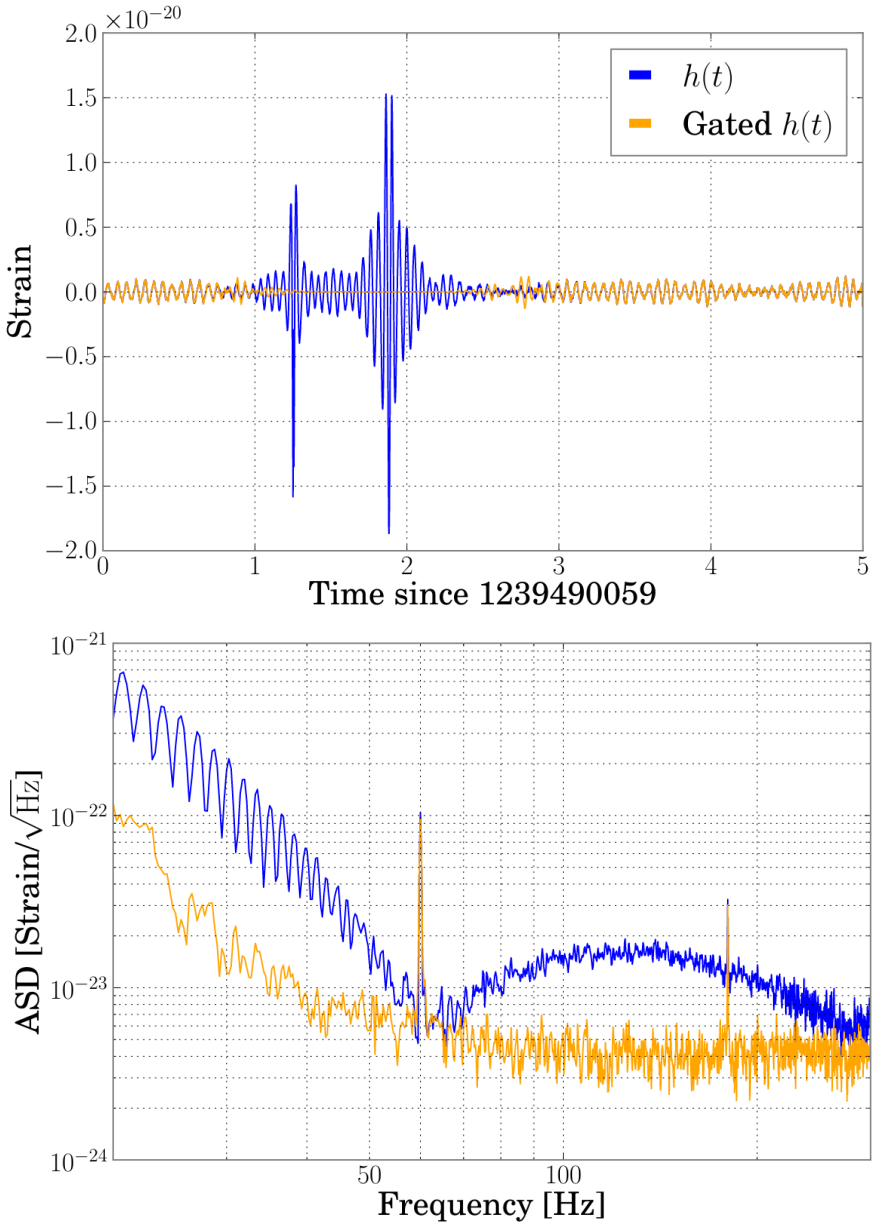

Fig. 5.1.: Example of gating. Top panel: time series of 5s of LIGO Livingston data with and without gating applied, starting at April 16, 2019 22:47:21 UTC. Bottom panel: the ASD for a 16s segment containing the data on the top panel, with and without gating applied. We see that even though the glitch is short compared to the duration of the segment, it leads to a large, broadband increase in the ASD. Figure taken from [259].

O3 data [30], the LVK collaborations have chosen to limit this variation between segments to maximally 20%.

With the current implementation segments with an drastically improved sensitivity are aslo removed by the $\Delta\sigma$-cut. This might be a sub-optimal decision of which the impact in future work should be further understood. However, typically this only concerns a (very) small fraction of the entire data-set as this mainly applies to data segments right after recovering from a drop in sensitivity due to e.g. a glitch.

Gating

Due to the high rate of glitches during O3 in the LIGO detectors, more than 50% of the data was lost after applying the $\Delta\sigma$-cut. Therefore a method called gating [221, 259] was implemented. The procedure can be understood as zeroing out the times of the glitch by using an inverse Tukey window [221]. A regular Tukey window preserves the amplitude in the central part of the window, whereas it tapers of to zero at the edges of the window. Its shape is governed by a parameter α taking values between 0 and 1. If $\alpha = 0$ ($\alpha = 1$) the Tukey window becomes a rectangular (Hann) window.
Gating applied to O3 data effectively removed glitches by zeroing out a small amount of data $\lesssim 1\%$, while preventing a much larger fraction ($\gtrsim$30%) of data being rejected by the $\Delta\sigma$-cut [30]. The effect of gating on both the time and frequency domain data is illustrated in Fig. 5.1

The effect of gating on the search for an isotropic GWB was investigated using mock data [259]. No significant bias from gating for stochastic searches was observed. However, for anisotropic searches some additional artefacts around noise lines were introduced due to gating [29], see also Sec. 5.2. Furthermore, known GW events were not removed and introduced spectral artefacts were found to be minimal [259].

5.2 Narrowband spectral artefacts

When analyzing long stretches of data, as is done for the search for a GWB, spectral lines or artefacts can have a significant impact on the search. These are (very) narrow spectral features that often need to be studied with long duration time segments ($\geq$ 100s - 1000s) and over a long time period ($\geq$ 1 day) to be able to observe them. Although both the search for an isotropic as well as anisotropic GWB are affected by

these spectral lines, the anisotropic narrowband radiometer search [29] as well as the all-sky all-frequency search (Sec. 4.2.3) can be affected more since one looks in detail at the frequency spectrum of a specific sky location/the entire sky. Therefore, one needs to understand which features are from experimental/environmental origin and which could be from a GW signal. In addition to individual narrow spectral lines, spectral artefacts can also appear in a set of lines with equal spacing which is called a comb of lines.

Individual spectral lines can have various origins of which we present the most important categories below.

- **Calibration lines:** A set of lines that are purposely injected into the detector to control and calibrate the detector [1, 35, 139].
- **Mechanical resonances:** Detector components have intrinsic resonances and their spectral artefacts are therefore an intrinsic part of detector design and cannot be completely removed [1, 35, 139].
- **Instrumental lines:** Another part of the lines originates from operating instruments (e.g. air conditioning, vacuum equipment, ...). Often they operate at a certain frequency, inducing spectral lines matching that frequency. The coupling mechanism (e.g. vibrational, magnetic, ...) depends on the type of noise and equipment [1, 35, 139]. Combs most often fall under this last category.

Whereas these narrowband noise sources are often not correlated among detectors, this is not always the case. An example is a 1Hz comb caused by blinking LEDs which are synchronised to the same time, i.e. Global positioning system (GPS) [135].

The frequencies of calibration lines and mechanical resonances are typically always excluded from the analysis. Instrumental lines are often only removed from the analysis if they show up significantly in the searches [29, 30]. These noise lines are eliminated from the analysis by notching them [29, 30].

More concrete examples of lines and combs are discussed for the LIGO detectors in [139] and for the Virgo detector in [1, 35]. The full list of lines for O3 for both LIGO and Virgo can be found in [241]. The list of spectral lines that was identified for the search for a GWB using data from LIGO's and Virgo's third observing run can be found in [30, 243] for an isotropic GWB and in [29, 244] for an anisotropic GWB. As explained in [29] the search for an anisotropic GWB includes some additional frequency bins with respect to the isotropic search. More specifically, the anisotropic analysis has wider notches around (already notched) loud lines e.g. calibration lines.

These wider notches aim to remove small spectral artefacts which are caused by gating [29]. In Chapter 6 the work done as part of this thesis to identify the spectral artefacts and apply the notches will be described.

5.3 Correlated noise sources

Apart from narrow spectral features, there are also noise sources which can affect a broader frequency range. The example best studied in the context of the search for a GWB are the Schumann resonances [318, 319], which can couple magnetically to the detectors and induce a correlated signal from terrestrial origin. The origin and properties of Schumann resonances will be discussed in Sec. 5.3.1. To a lesser extent the effect of correlations between individual lightning strikes has been investigated [214, 229]. In Chapters 7 and 8 we will discuss the observed correlations in magnetic field fluctuations and their impact on GWB searches.

In the context of this PhD also seismic and Newtonian noise were considered as possible correlated environmental noise source for (almost) co-located detectors, such as will be the case for the 3G detector ET. Seismic and Newtonian noise will be discussed in Sec. 5.3.2, whereas Chapter 9 is dedicated to discussing the observed correlations and their possible impact on interferometric GW detectors.

5.3.1 Schumann resonances

Schumann resonances are electromagnetic excitations in the cavity formed by the Earth's surface and the ionosphere, sourced by lightning discharges across the globe [318, 319]. The dominant contribution originates from cloud-to-ground lightning discharges [320]. The electromagnetic fields radiated by these discharges can, at their lowest frequencies, travel multiple times around the Earth before they degrade. The addition and cancellation of the waves create a resonant spectrum, the Schumann resonances, of which the properties are linked to the normal modes of the Earth-ionosphere cavity.

There are several key conditions on which the propagation of magnetic fields in the extremely low frequency (ELF) band (3Hz - 3kHz) depend. First of all, the attenuation increases with frequency and can be 1dB/1000km or less below 100Hz

[181]. Secondly, further attenuation of the magnetic fields is observed for a day-night[1] as well as night-day transition, respectively 1dB and up to 3dB [358], due to changes in the ionospheric height. Some other effects are discussed in Sec. II of [214].

Both the spatial as well as the temporal variations in the Schumann resonances are consistent with the distribution of lightning strikes [320]. These lightning strikes occur mainly in three regions: South-East Asia, sub-Saharan Africa and the Americas. In each region the peak in thunderstorm activity occurs around late afternoon, which corresponds respectively to 10 UTC, 16 UTC and 22 UTC for the different regions. Since the Schumann resonances mainly peak at 22 UTC (followed by 16 UTC), the Americas seem to be the dominant region for the Schumann resonances [320].

The first four Schumann resonances have a resonance frequency of about 7.8Hz, 14Hz, 21Hz and 27Hz, where the fundamental mode has a magnetic strength of the order of 0.5pT - 1pT. Both the frequencies at which the peak amplitude is observed as well as the peak amplitude are subjected to a diurnal variation, respectively $\pm$ 0.5Hz and $\pm$0.25pT - $\pm$0.5pT [320]. Also seasonal variability has been observed [320, 370]. Studies at the site of the underground KAGRA detector have shown that local geographical factors can magnify the resonances [73].

In quiet locations the Schumann resonances are the dominant magnetic noise source between 6Hz and 60Hz [320]. Furthermore the resonances are highly coherent, even over distances on the order of $\mathcal{O}$(1000km), which makes them relevant as a potential correlated noise source for GW detectors on Earth.

As an example, Fig 5.2 shows the Schumann resonances as measured at multiple measurement stations around the world. The first four Schumann resonances are clearly visible.

5.3.2 Seismic waves and Newtonian noise

In this section we will discuss seismic and Newtonian noise on a conceptual level. We refer the interest reader to the following references for an in depth discussion in seismic noise [50, 309] and Newtonian noise [192].

[1] The propagating wave makes the transition from the side of the Earth facing the sun to the the side not facing the sun.

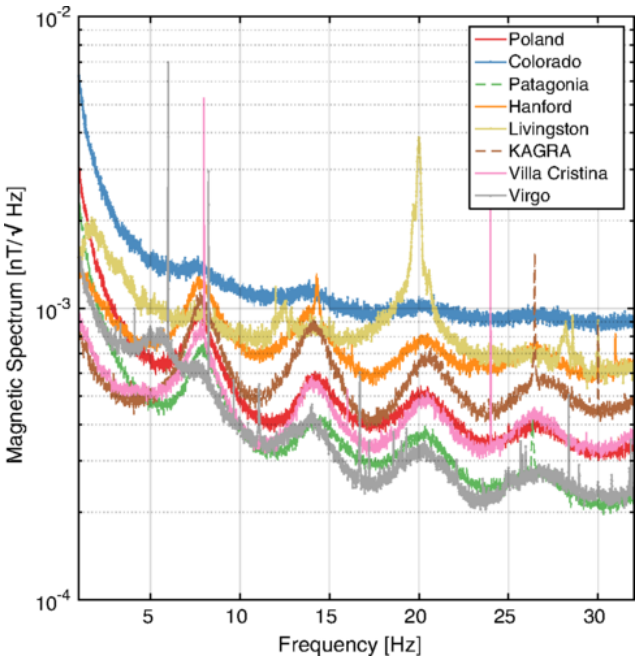

Fig. 5.2.: Median power spectral density of the North-South direction magnetometers deployed in Poland (in the Bieszczady Mountains), Colorado (in the Hugo Wildlife Area in Colorado, USA), Villa Cristina (near the Virgo detector) and Patagonia (Argentinia), as well as the KAGRA, LIGO Hanford and LIGO Livingston X-arm direction magnetometers, as described in [134]. These are computed using 128s segments. In addition to the sharp instrumental line features in the Villa Cristina magnetometer at 8 Hz and 24 Hz, the Schumann resonances are visible in all of the magnetometers. The 20 Hz line at LIGO Livingston is likely due to power lines which cross the site on the Y-arm. Figure taken from [134]. ©APS.

Seismic waves

There are two types of seismic waves which travel through a continuous medium, i.e. P-waves and S-waves [50, 309]. P-waves create compression and expansion along the travel direction of the seismic waves and travel faster than S-waves. S-waves on the other hand consist of two different polarisations, transverse to the traveling direction of the wave. The transverse horizontal and vertical S-wave are referred to as respectively S_H and S_V. P- and S-waves are also called 'body waves', in contrast to 'surface waves', which are the solutions to the equations of motion in the case of a free surface. The two types of surface waves are Love-waves (or L-waves) and Rayleigh-waves (or R-waves). Love-waves find their origin in constructive interference of S_H-waves and are only non-zero in the presences of a depth-dependent seismic wave velocity. Rayleigh-waves on the other hand originate from the interference between S_V- and P-waves. A particle affected by a passing Rayleigh-wave follows a retrograde elliptical path in the plane perpendicular to the

surface and parallel to the propagation direction. Surface waves have a frequency dependent, exponentially decreasing amplitude with depth [50, 302, 309]. However the geometric dispersion of their energy only occurs in a 2D-circle compared to a 3D-sphere for body waves [309]. The effect of these different types of seismic waves is illustrated in Fig. 5.3.

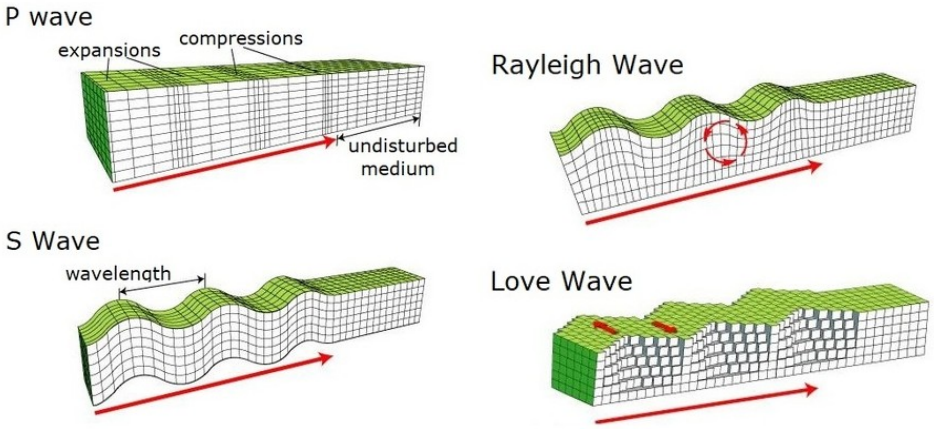

Fig. 5.3.: Illustration of P-, S_V-, Rayleigh- and Love-waves. Figure taken from [353]. ©Science Learning Hub – Pokapū Akoranga Pūtaiao, University of Waikato.

Newtonian noise

Density fluctuations in a medium lead to changes in the gravitational field which exerts a force on a GW test-mass and therefore is a noise source for GW interferometric detectors, as first introduced in Chapter 2. This type of noise is referred to as Newtonian noise (NN) or gravity(-gradient) noise [192, 208, 314]. As indicated earlier, NN is not yet a problem for current generation GW detectors, but will be the dominant noise source in the low frequency region for future Earth-based detectors, such as the ET. The direct nature of the force from NN is analogous to the effect of a passing GW in the sense that both change the local gravitational field. Therefore one cannot shield the GW detector from NN without also shielding from the effect of a passing GW. Therefore the method under investigation to address NN is to use witness sensors to make an accurate prediction of the NN such that it can be subtracted from the output of the GW detector [127, 129, 147, 148, 192, 194] (See also Sec. 5.4.3).

Here we will only discuss NN from density fluctuations induced by seismic waves and not NN from atmospheric density fluctuations. We refer the interested reader to the relevant literature on atmospheric NN in the context of GW detectors [56,

136, 171, 192, 314]. A more detailed discussion on seismic NN in the context of GW detectors can be found in [85–87, 192, 195, 208, 314].

P- and Rayleigh-waves introduce density fluctuations leading to NN, whereas S-waves only induce density fluctuations when interacting with a discontinuous medium. This could for instance happen in case of impact upon a cavern wall, or the passage through a boundary between two different rock types. Love-waves do not induce density fluctuations. The calculation of NN is complex due to its dependence on many factors such as geological structures and the shape of the caverns/buildings housing the detector. We will introduce the relation between NN and seismic noise in case of some general assumptions, which will be used later in Chapter 9 to compute the contribution of correlated NN. However, given the many assumptions one should consider these results as an order of magnitude estimate rather than very accurate calculations and the final results will depend on the exact geology and shape of the caverns/buildings housing the detector.

Newtonian noise from Rayleigh-waves

Rayleigh-waves can produce NN due to rock compression and the displacement of the cavern wall as well as the surface. The combined effect of these three contributions introduces the following effect in GW strain at one test mass [56, 192],

$$S_{h,\text{Rayleigh}}(f) = \left(\frac{2\pi}{\sqrt{2}} G\gamma\rho_{0,\text{Surface}}\right)^2 \frac{1}{L^2(2\pi f)^4}\mathcal{R}(h,f)S_{\xi_z}(f). \tag{5.2}$$

Here G is Newton's gravitational constant, $\rho_{0,\text{Surface}}$ the mass density of the medium at the surface and γ is a factor between 0.5 and 1 which describes the partial cancellation of NN from surface displacement and soil compression. The factor $\frac{1}{L^2(2\pi f)^4}$ converts the NN contribution from acceleration to strain for one test mass, where L is the arm-length of the GW interferometric detector under consideration. In [56] the equation equivalent to Eq. 5.2 is multiplied by an additional factor 4 under the assumption the four test masses experience incoherent NN contributions. $S_{\xi_z}(f)$ is the PSD of the vertical displacement ξ_z at the surface and $\mathcal{R}(h,f)$ describes the dependence with depth h and is given by [56, 192],

$$\mathcal{R}(h,f) = \left|\frac{-k_R(f)(1+\zeta(f))e^{-k_R(f)h} + \frac{2}{3}\left(2k_R(f)e^{-q_P(f)h} + \zeta(f)q_S(f)e^{-q_S(f)h}\right)}{k_R(f)(1-\zeta(f))}\right|^2. \tag{5.3}$$

$k_R = 2\pi f / v_R(f)$ is the Rayleigh wave number and $\zeta(f)$ is given by

$$\zeta(f) = \sqrt{\frac{q_P(f)}{q_S(f)}}, \tag{5.4}$$

with

$$\begin{aligned} q_P(f) &= 2\pi f \sqrt{\frac{1}{v_R(f)^2} - \frac{1}{v_P^2(f)}} \text{ and} \\ q_S(f) &= 2\pi f \sqrt{\frac{1}{v_R(f)^2} - \frac{1}{v_S^2(f)}}. \end{aligned} \tag{5.5}$$

$v_R(f)$, $v_P(f)$ and $v_S(f)$ are the frequency dependent seismic wave speeds for Rayleigh-, P- and S-waves. Having an accurate dispersion model $v_R(f)$ for Rayleigh-waves is important since it has an important impact on reduction of NN from Rayleigh waves with increasing depth. A simplified prediction of NN from Rayleigh waves is shown in Fig. 5.4. The top panel projects the effect of NN at the surface whereas the bottom panel projects the effect of NN at different depths. This illustrates the significant effect of the choice of the depth on the NN from surface waves. For a more detailed discussion we refer the interested reader to [75, 192].

Newtonian noise from body-waves

P-waves contribute to both cavern wall displacement as well as rock compression, whereas S-waves only contribute to the cavern wall displacement. This relies on the fact that in the frequency range relevant for Earth-based interferometric GW detectors, i.e. 3Hz-20Hz, surface displacement from body waves can be neglected since this is dominated by Rayleigh-waves. The combined NN from body-waves effects is given by [56, 192],

$$S_{\text{Body-wave}}(f) = \left(\frac{4\pi}{3} G \rho_{0,\text{Underground}}\right)^2 (3p+1) \frac{1}{L^2 (2\pi f)^4} S_{\xi_x}(f), \tag{5.6}$$

where $\rho_{0,\text{Underground}}$ is the mass density of the underground medium close to the cavern housing the underground detector and $S_{\xi_x}(f)$ is the PSD of the horizontal displacement ξ_x. Fig. 5.4, also shows a simplified prediction of the contribution of NN from body waves. For a more detailed discussion we refer the interested reader to [75, 192].

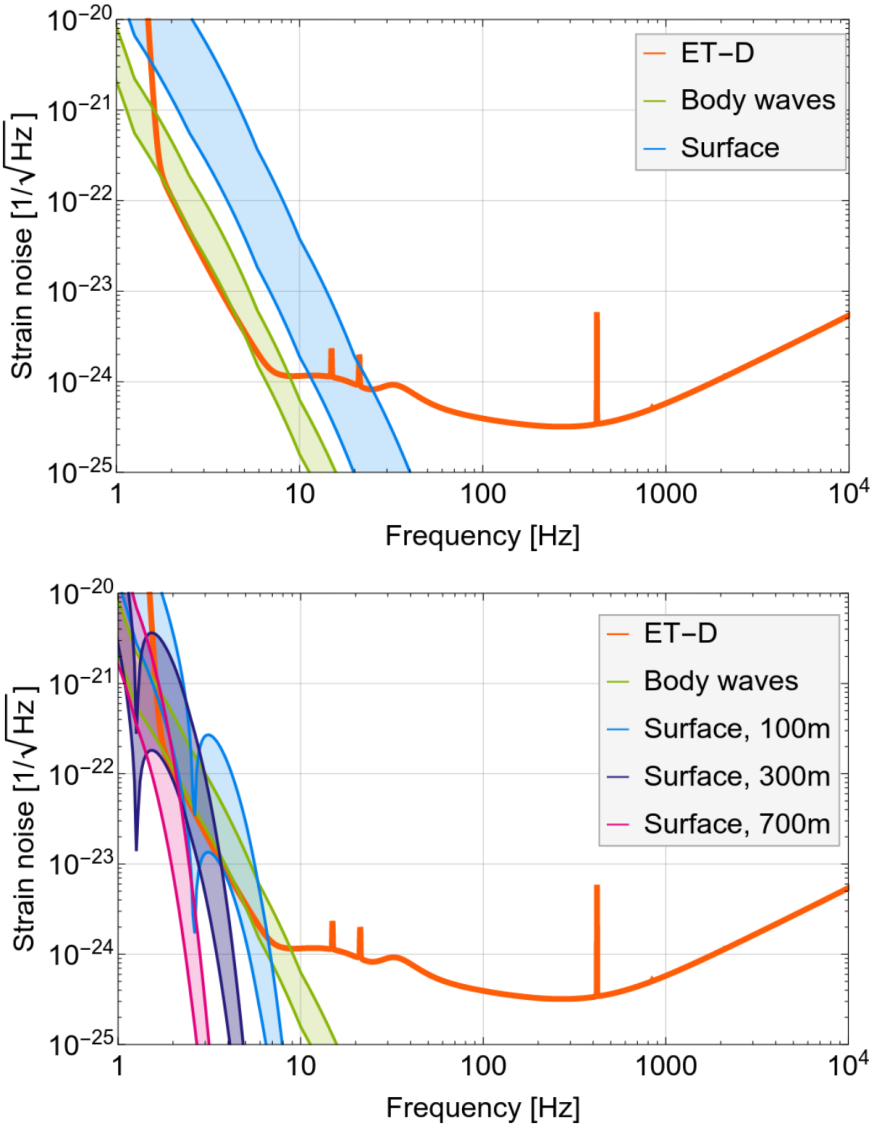

Fig. 5.4.: Top panel: Simplified predicted contribution from NN from seismic body waves (green) and Rayleigh waves (indicated by 'Surface', blue). The ET is expected to be located at the surface. Bottom panel: Predicted NN contribution for ET at a depth of 100m, 300m and 700m. The contribution of body waves remains unchanged, the contribution of Rayleigh waves (indicated by 'Surface') significantly decreases with increasing depth. NN contributions from Rayleigh waves shown for a depth of 100m (blue), 300m (dark purple), 700m (light pink). Figure taken from [75].

5.4 Methods to address (correlated) noise sources

In this section we will discuss several methods that have been used or suggested to investigate, estimate, and/or mitigate the effect of (correlated) noise on the search for an isotropic GWB[2]. In Sec. 5.4.1 and Sec. 5.4.2 we will discuss two methods which aim to answer the question whether the search is contaminated by correlated noise or not. In Chapter 11 we will introduce the null channel, which can also serve as a diagnostic method that could be used for a triangular configuration of GW detectors, as is planned to be the case for ET and LISA. Sec. 5.4.3 and Sec. 5.4.4 describe two methods that can be used to address correlated noise in case it couples significantly.

5.4.1 Instrumental and environmental monitoring

The LIGO, Virgo and KAGRA detectors have many witness-sensors installed to continuously monitor the instrumental and environmental conditions. The first check to complete when dealing with a possible detection is to look for indications the signal could be caused by instrumental or environmental transients or ambient noise.

Such studies are already performed by the LIGO, Virgo and KAGRA collaborations when searching for a GWB [29, 30]. When performing these analyses, spectral features are thoroughly investigated and if witness channels give proof that these spectral features are of environmental or instrumental origin, they are added to a list of known instrumental/environmental lines [241, 243, 244]. Based on this list, such lines can be excluded from the analysis, as will be further discussed in Chapter 6.

Another example of an additional study investigating environmental noise is the construction of the magnetic budget to investigate the impact of global magnetic fields, and more specifically the Schumann resonances that were introduced in the previous section. Given the broadband character of the Schumann resonances - as can be seen in Fig 5.2 - excluding these frequencies from the analysis would lead to a significant decrease in sensitivity. Therefore, this is not desirable and the magnetic budget informs us whether the amplitude is negligible compared to the sensitivity of the search for a GWB or not. If one finds that the Schumann resonances are

[2]Even though these methods mainly have been studied in the context of an isotropic GWB, some of them could be trivially extended to also work for anisotropic searches. However, in this discussion we will mainly focus on their use for the search for an isotropic GWB.

affecting the sensitivity, one needs to resort to other techniques such as subtraction (Sec. 5.4.3) or Bayesian parameter estimation (Sec. 5.4.4) to address them.

To construct this magnetic budget one needs to know how the magnetic fields couple to the detector. This is measured by injecting strong magnetic fields in the main buildings of the detector and observe the impact of these injections on the GW sensitive channel of the detector [121, 122, 170, 277]. The magnetic coupling function will be discussed in more detail in Chapter 7.

Fig 5.5 shows the magnetic budget constructed as part of the analysis searching for an isotropic GWB. It is concluded there is no effect from magnetic contamination, neither broadband, nor narrowband. Broadband features (the blue band) of the magnetic budget have to be below the PI-curve, which is a measure of the sensitivity of an isotopic GWB search to broadband signals (see Sec. 4.2.1,). The narrowband magnetic features on the other hand are well below the sensitivity to GWs in each frequency bin, σ_{GW}, as defined in Sec. 4.2.1, Eq. 4.12. Please note that because of an error in the code, the budget in Fig. 5.5 is underestimating the magnetic contributions by a factor of 10. An erratum to [30] is in preparation. Whereas this error has no effect on the conclusion of the effect on O3, it will play a role for future observing runs, as we will see in Chapter 8 when we present a correct and more accurate budget.

Whereas the broadband magnetic budget is about two to three orders of magnitude below the latest sensitivity of the third observing run by LIGO and Virgo, Schumann resonances might affect stochastic searches in the future. Current generation interferometric gravitational-wave detectors keep on increasing their sensitivity, and next generation detectors will do so even more. Due to changes in the detectors setup, the coupling function can sometimes unintentionally increase because of some new, additional coupling. Therefore it remains crucial to accurately measure this magnetic coupling during each observing run and assess the importance of the magnetic budget.

In Chapters 7 and 8 we will discuss the latest magnetic budget calculations and studies of the effect of magnetic noise on both 2G and 3G detectors, which were performed as part of this PhD.

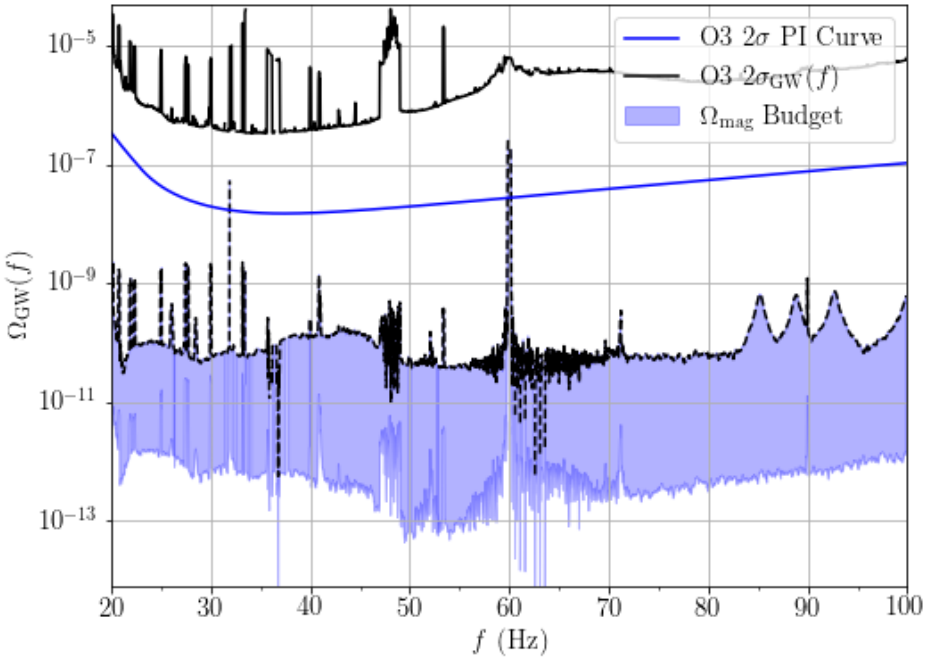

Fig. 5.5.: Correlated magnetic noise budget, as described in the main text of [30]. The blue band shows the expected range of magnetic contamination, using weekly measurements of the coupling function at each site, and accounting for the uncertainty in the coupling function measurements. We display the O3 sensitivity in two ways. The PI-curve is shown as a blue line. This indicates the sensitivity of the search to power-law GWBs and includes the effect of integrating over frequencies, and should be compared with the overall trend of the blue band. The square root of the variance σ_{GW}(f) – introduced as $\sigma(f)$ in Eq. 4.12 – is plotted as a black line, which gives the sensitivity of the search to narrowband features. This can be compared with narrow features in the upper range of the noise budget, shown as a black dashed line. The O3 sensitivity is well above the level of correlated magnetic noise estimated in O3. The original version of this plot was presented in [30]; the version shown here was obtained using open data published in [243]. Note: currently an erratum is in preparation to correct an error in this figure, the latest (correct) results are discussed in Chapter 8.

5.4.2 Gravitational-wave geodesy: a validation tool for the gravitational-wave background

As mentioned before, many external factors can affect the signal, and thus, the claim of a detection as well. Therefore, GW geodesy was proposed as an additional tool to validate the detection of an isotropic GWB [106]. This method is complementary to using instrumental and environmental monitoring as explained in Sec 5.4.1, as well as the methods that will be discussed in Sec. 5.4.3 and Sec. 5.4.4.

GWs couple in a specific way to each interferometric GW detector, as described by their detector response function, introduced in Sec. 2.1.3. When looking for an

isotropic GWB, these response functions enter via the ORF as defined in Eq. 4.10. This ORF uniquely depends on the distance between the two detectors, as well as their rotation angle around their respective vertex point.

When a GWB is observed, its signal has to be consistent with the ORF associated to the observing baseline. A priori, there is no reason for any non-GW signal to be consistent with this specific ORF or geometrical setup of the detectors. The GW geodesy tool uses this assumption to differentiate between GWB signals and other sources of correlation. To this end, two hypotheses are constructed:

- Hypothesis $\mathcal{H}_\gamma$: The observed cross-correlation is consistent with the ORF / geometry of the observing baseline.
- Hypothesis $\mathcal{H}_{\text{Free}}$: The observed cross-correlation is consistent with an ORF linked to a baseline model with unconstrained geometry on the Earth's surface. The orientation of the individual detectors and the distance between them are inferred for this model.

In order to compare these two hypotheses one constructs a Bayes factor,

$$\mathcal{B} = \frac{p(\hat{C}|\mathcal{H}_\gamma)}{p(\hat{C}|\mathcal{H}_{\text{Free}})}, \tag{5.7}$$

where $p(\hat{C}|\mathcal{H}_\gamma)$ and $p(\hat{C}|\mathcal{H}_{\text{Free}})$ are the probabilities of finding the observed cross-correlation given hypothesis $\mathcal{H}_\gamma$ and $\mathcal{H}_{\text{Free}}$, respectively. In a Bayesian analysis, the $\mathcal{H}_{\text{Free}}$ hypothesis will be penalized by the 'Occam's factor' given its more complex model, leading to a preference of the $\mathcal{H}_\gamma$ hypothesis for a GWB signal. Globally correlated signals from non-GW origin are expected to be consistent with $\mathcal{H}_{\text{Free}}$, due to the additional degrees of freedom in this model.

The GW geodesy tool was demonstrated to be effective in differentiating a correlated signal coming from a comb of lines as well as a signal from Schumann resonances with respect to a GWB as expected from unresolved CBC events, as shown in Fig 5.6 [106]. As reference, a negative ln$\mathcal{B}$-factor prefers model $\mathcal{H}_{\text{Free}}$, a factor between 0 and 1 has marginal evidence, a factor between 1 and 3 has positive evidence for $\mathcal{H}_\gamma$ and a factor between 3 and 5 or > 5, has strong, respectively very strong evidence for $\mathcal{H}_\gamma$ [304].

In general, this tool can be used for any correlated noise source that might affect the isotropic GWB search. The only requirement is to know the cross-correlation spectrum. As part of this PhD, the possibility of defining false alarm probabilities and detection probabilities in the framework of GW geodesy were studied. These could be used to make quantitative statements on the origin of a signal being correlated

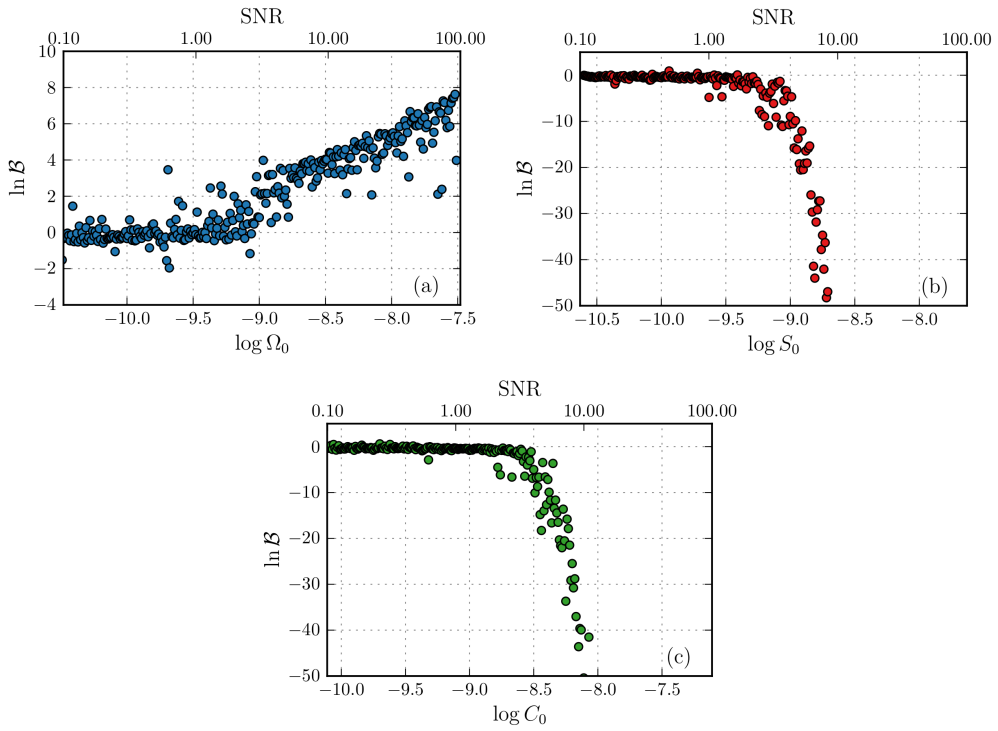

Fig. 5.6.: Log-Bayes factors between the physical and un-physical hypotheses $\mathcal{H}_\gamma$ and $\mathcal{H}_{\text{Free}}$ as a function of injection strength for an isotropic astrophysical background (top left panel; Ω_0), Schumann resonances(top right panel; S_0), and correlated combs (bottom panel; C_0) [Eqs. (11), (12), and (13) of [106]]. To enable a direct comparison between injection types, the upper horizontal axes show the signal-to-noise ratios of these injections. ln$\mathcal{B}$ increases linearly with the strength of an astrophysical GWB injection, indicating consistency with the correct (known) detector geometry. Meanwhile, ln$\mathcal{B}$ decreases exponentially for the terrestrial sources of correlation, disfavoring the correct geometry. In the considered cases, ln$\mathcal{B}$ therefore successfully discriminates between astrophysical and terrestrial sources of measured cross-correlation. Figure taken from [106]. ©AAS.

noise or a GW signal [217]. The results I obtained as part of my PhD were published in [217] and will be discussed in Chapter 10.

Although the tool is currently only able to validate an isotropic GWB, investigations are ongoing to explore if the same ideas can be used for validating an anisotropic GWB [217].

5.4.3 Subtraction of noise sources

If one is able to measure the noise sources that couple to the detector using dedicated sensors, it could be possible to subtract these noise sources. One needs two key ingredients: an accurate measurement of the noise source, as well as of the transfer function describing how this noise source couples to the channel that the subtraction needs to be applied to.

A first method to get the transfer function is to directly measure it. In Sec. 5.4.1, we explained briefly (see Chapter 7 for a more detailed discussion) how the magnetic coupling function or transfer function is measured on a regular basis by injecting known magnetic fields and studying the impact on the GW sensitive channel. However, if one wants to implement successful subtraction, this transfer function should be known accurately. Often this is not the case since the coupling mechanisms are complex and depend on many variables – such as directionality, homogeneity or phase of the noise source and coupling mechanism – which might be hard to control during the injections.

A second, more general technique is to use a Wiener-filter to construct the transfer function. First we will explain some general concepts of the Wiener filtering formalism. Afterwards, we will use the Schumann resonances as an example and discuss the investigations that were performed to apply Wiener filtering to reduce/mitigate the impact of Schumann resonances on the search for a GWB if they were to couple significantly.

Wiener filter

If the channel of interest does not only contain the target signal, but also a noise source, one could use witness sensors observing this same noise source to construct a transfer function using a Wiener filter [133, 134, 346, 348].

Let us assume we have a strain channel s, which contains a GW component h which we want to measure. However, assume s also contains the noise source we want to subtract m, whose coupling is described by the transfer function t. We allow for other noise source(s) n to be present in s as well. Furthermore, we have a witness channel w, which monitors the noise source m directly. The witness channel also contains a noise source η which is independent of the s channel. In such a scenario the following equations hold:

$$\begin{aligned} \tilde{s}(f) &= \tilde{h}(f) + t(f)\tilde{m}(f) + \tilde{n}(f) \\ \tilde{w}(f) &= \tilde{\eta}(f) + \tilde{m}(f), \end{aligned} \tag{5.8}$$

where the tildes denote Fourier transforms. The transfer function between the witness channel w and target channel s, can be estimated as [346]

$$\hat{t}(f) = \frac{\overline{\tilde{s}(f)\tilde{w}^*(f)}}{\overline{|\tilde{w}(f)|^2}}, \tag{5.9}$$

where $\hat{t}$ is the statistical estimator of the transfer function t, and the overline in Eq. 5.9 implies time-averaging. Please note that the denominator also contains a term related to $\tilde{\eta}(f)$. Therefore, $\tilde{\eta}(f)$ should be sufficiently small compared to $\tilde{m}(f)$ for this Wiener filter to be accurate, as we will discuss in more detail below.

Noise subtraction

Once one has an estimate for the transfer function $\hat{t}(f)$, either because one measured it, or because one constructed it using the Wiener filtering formalism as in Eq. 5.9, one can construct the subtracted data, s', [346]

$$\tilde{s}'(f) = \tilde{s}(f) - \hat{t}(f)\tilde{w}(f). \tag{5.10}$$

When the estimator $\hat{t}(f)$ equals the true value $t(f)$, the correlated noise between the target channel and witness channel m will be successfully subtracted. This limit is reached in the regime where m is the dominant component of the witness channel w, and η is negligible. If η dominates the witness channel w, Wiener filtering will fail.

If one defines $M(f) = \langle \tilde{m}^*(f)\tilde{m}(f) \rangle$ and $\mathcal{N}(f) = \langle \tilde{\eta}^*(f)\tilde{\eta}(f) \rangle$, one can define a 'witness signal-to-noise ratio' ρ_w,

$$\rho_w = \sqrt{\frac{M(f)}{\mathcal{N}(f)}}, \tag{5.11}$$

which plays an important role in determining whether Wiener filtering is successful or not [346]. Although partial subtraction might already take place when $\rho_w < 1$, the witness signal-to-noise ratio should be large enough ($\rho_w > 4$) to achieve more complete noise subtraction [346].

Case study of noise subtraction – Schumann resonances

Noise subtraction has been tested using simulated data in the context of Schumann resonances, both with measuring the transfer function as well as constructing it using a Wiener-filter. Furthermore a proof of concept analysis has shown Wiener filtering is effective in (partial) subtraction when applied to magnetometers [133, 134, 346, 348].

Fig 5.7 shows the effect of Wiener and Wiener-like filtering – that is the formalism where one estimates $\hat{t}(f)$ relying on other methods than the Wiener filter, e.g. direct measurement– on simulated strain data containing Schumann resonances. Both formalisms are able to subtract a part of the correlated Schumann noise, where the Wiener filter performs the best. However residual contamination remains [346].

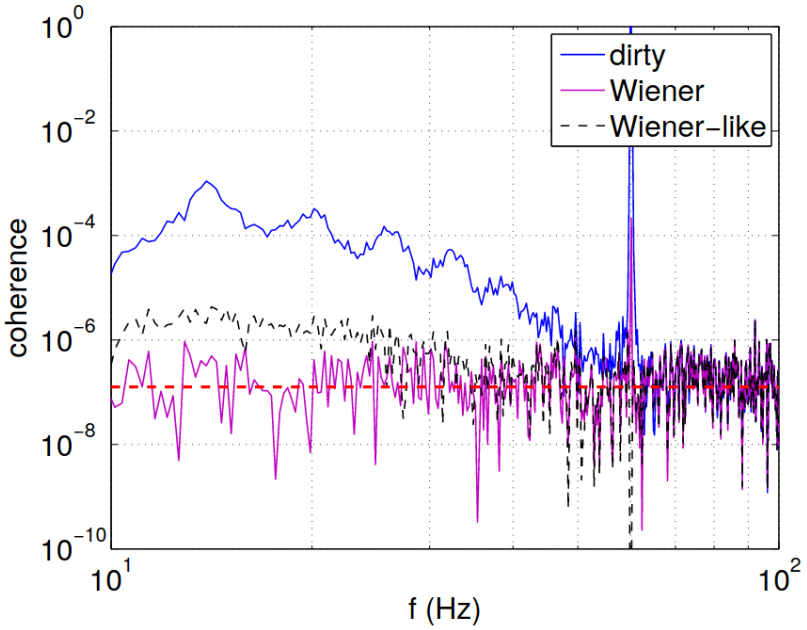

Fig. 5.7.: Coherence spectra showing the contaminated strain channels (blue), the somewhat cleaner spectrum obtained by Wiener-like filtering (black dashed), and the spectrum obtained with true Wiener filtering (magenta). The Wiener-filtered spectrum is significantly cleaned, but measurable residual contamination remains. 1 yr of integration time was assumed. Figure taken from [346]. ©APS.

It has been shown Wiener filtering could be used to significantly reduce the effect of Schumann resonances [133, 134, 346, 348]. Since the Schumann resonances are currently not coupling significantly to detectors, the method could not be applied to real GW data. However, the simulations combined with proof of concept applied to magnetometers illustrate Wiener filtering would be promising once Schumann resonances couple significantly to the interferometers [133, 134, 346, 348].

Another noise source for which Wiener filtering is investigated is Newtonian noise [75, 127, 148, 196]. Although Newtonian noise will mainly become an important issue for third generation interferometric gravitational-wave detectors such as the Einstein Telescope [61, 77, 142, 228], Newtonian noise subtraction has also been investigated for second generation detectors Advanced LIGO [128, 130] and Advanced Virgo [76, 352].

We want to end this section with a caveat on the use case for Wiener filtering. To be able to use Wiener filtering, one assumes the correlated noise is observable in the target channel, i.e. in our case the strain channel s, over the time one calculates the Wiener filter. This Wiener filter will have to be calculated on segments with a reasonable duration e.g. $\mathcal{O}$(100s-1000s), such that the data is sufficiently stationary. However, some of the lower coherence signal might not be significantly observable over this time-scale and has to be looked for with much longer integration time, e.g. weeks or months. Since Wiener-like filtering, i.e. using an independent measurement of the transfer function, is not affected by this one could argue this method might be more optimized in such a scenario. However, Fig. 5.7 shows this method is less effective. Furthermore, also in this case the question can be raised how to address the non-stationary character of the data as well as the stability of the transfer function or coupling function over (very) long durations. This suggest that, even though noise subtraction seems very promising and might even be necessary in the future, it is highly likely there will remain some effects from correlated noise in the data depending on the circumstances.

5.4.4 Joint Bayesian modeling of noise sources and a gravitational-wave background

Recently, a new method was proposed to take Schumann resonances into account using Bayesian model selection [267]. However, one could imagine using this technique for any known source of correlated noise.

In the context of taking Schumann resonances into account, one can construct a likelihood as follows[3] [267]

$$p(\hat{C}^{IJ}(f_k)|\mathbf{\Theta}_{\mathrm{GW}}, \mathbf{\Theta}_{\mathrm{Mag}}) \propto \exp\left[-\frac{1}{2}\sum_{IJ}\sum_{k}\left(\frac{\left(\hat{C}^{IJ}(f_k) - \Omega_{\mathrm{GW}}(f_k|\mathbf{\Theta}_{\mathrm{GW}}) - \Omega_{\mathrm{Mag}}(f_k|\mathbf{\Theta}_{\mathrm{Mag}})\right)^2}{\sigma^2_{IJ}(f_k)}\right)\right]. \tag{5.12}$$

Compared to Eq. 4.17, Eq. 5.12 takes the Schumann resonances $\Omega_{\mathrm{Mag}}(f_k|\mathbf{\Theta})$ into account in addition to the GWB model $\Omega_{\mathrm{GW}}(f_k|\mathbf{\Theta})$. This framework has been applied to a typical magnetic Schumann spectrum [267], where the magnetic coupling functions were approximated as a power-law and the coupling strength and the power-law slope were treated as nuisance parameters.

It was shown that the method is able to differentiate between an isotropic GWB and correlations arising from Schumann resonances [267]. However, strong magnetic coupling or noisy magnetic measurements can decrease the significance of the detection of a GWB. Furthermore, the simulations show that going from a two to a three detector network significantly increases the effectiveness of the method, regardless of whether the third detector contributes much to constraining the GWB power or not. This strongly supports using a larger detector network even though their contribution to observing a GWB might be small/negligible due to a lower sensitivity or effects of the ORF, as is the case for adding Virgo and KAGRA to the LIGO Hanford and Livingston network. Since correlated noise sources, e.g. Schumann resonances, couple differently to the network compared to a GWB, a larger network helps nevertheless in differentiating a GWB from correlated noise.

While this method can be used as an alternative for the subtraction of the Schumann resonances with Wiener filtering as explained in Sec. 5.4.3, both methods could also be used simultaneously. One could imagine first applying (partial) Wiener filtering and afterwards use this Bayesian parameter estimation model to allow for a remaining contribution coming from the Schumann resonances. Depending on the situation, one could use these two methods in parallel and cross check the two independent results with each other, or adopt this combined approach. This leads to a large flexibility in applying these methods and ensuring to efficiently take globally cross-correlated signals such as the Schumann resonances into account. However, note that in the end the accuracy of the observed magnetic spectrum and/or the magnetic coupling function will be a limiting factor for the potential gain.

[3] Note our Eq. 5.12 uses a slightly different notation compared to Eq. 25 of [267].

Part II

In Part I, I introduced the gravitational-wave background and the groundbreaking nature of a future observation of this signal. An astrophysical GWB would give us insights in the astrophysical evolution of our Universe. Even more important would be the observation of a cosmological GWB, which could revolutionize our knowledge of early Universe cosmology or high energy physics models. Given the importance of the first claim of a detection of a GWB, one wants to be very sure there is no other possible signal that could lead to an observed excess and avoid any backlash of a falsely claimed detection.

To this extent the goal of my PhD is to work on methods that enable future analysts with Earth-based interferometric detectors to bolster their confidence in a possible detection. During my PhD I worked on a broad range of projects to develop certain tools and frameworks as well as noise studies for both second as well as third generation detectors. All these projects have in common that they will facilitate the data quality procedures for a future GWB detection in the Hz to kHz frequency band.

Here in Part II I will present the analyses I have performed as part of my PhD. The different chapters are introduced below and I indicate how they fit in the overall scope of my PhD.

Chapter 6

This chapter focuses on the data quality procedures used to identify problematic spectral artefacts for the search for an isotropic gravitational-wave background. We start with a discussion of the methods and procedures used during O3. Afterwards we show some of the O3 results. We end this chapter with a brief introduction of the methods implemented for O4 and how they plan to improve upon earlier work.

The investigations explained in detail in this chapter were performed in context of the data quality of the LVK analysis searching for an isotropic gravitational-wave background published in [30]. Furthermore, this chapter contains content from [300] in collaboration with A. Renzini, et al.

Chapter 7

This chapter discusses investigations of correlations in the magnetic field fluctuations on Earth-scale distances. We present results of magnetic correlations observed between the LIGO and Virgo detectors, but also include other sensors in our discussions. Secondly, we describe the magnetic injections performed at Virgo, the hardware used for this and the plans for magnetic injections for O4.

This chapter is based on content in collaboration with M. Ball, R. M. S. Schofield, N. Christensen, R. Frey, N. van Remortel, S. Banagiri, M. W. Coughlin, A. Effler, M. Gołkowski, J. Kubisz and M. Ostrowski published in [214]. Furthermore also content from [218] in collaboration with K. Martinovic, N. Christensen, P. Meyers and M. Sakellariadou is presented. Finally, we also discuss material published in [170] from work in collaboration with I. Fiori, F. Paoletti, M. C. Tringali, C. Karathanasis, A. Menéndez-Vázquez, A. Romero-Rodríguez and et al.

Chapter 8

Using the observed magnetic correlations and magnetic coupling functions discussed in the previous chapter, we project the effect of magnetic noise on the detector sensitivity for Virgo. Furthermore we also provide upper limits on the maximally allowed magnetic coupling function such that the Einstein Telescope or Cosmic Explorer would not be affected. Afterwards we also predict the effect of correlated magnetic noise on the search for an isotropic GWB with second generation detectors at their design sensitivity, as well as for the third generation detector Einstein telescope.

This chapter includes material published in [170] from work in collaboration with I. Fiori, F. Paoletti, M. C. Tringali, C. Karathanasis, A. Menéndez-Vázquez, A. Romero-Rodríguez and et al. Furthermore, we present results published in [218] in collaboration with K. Martinovic, N. Christensen, P. Meyers and M. Sakellariadou. Finally, we also discuss the work published in [214] in collaboration with M. Ball, R. M. S. Schofield, N. Christensen, R. Frey, N. van Remortel, S. Banagiri, M. W. Coughlin, A. Effler, M. Gołkowski, J. Kubisz and M. Ostrowski.

Chapter 9

We start this chapter by highlighting how the Einstein Telescope and atom interferometers could be sensitive to other correlated noise sources than magnetic noise discussed in earlier chapters. Afterwards we investigate correlations in seismic measurements on horizontal separations of several hundreds of meters. Finally, we use these observed correlations to predict how correlated seismic and Newtonian noise could impact the sensitivity and science goals of the Einstein Telescope.

The content of this chapter is based on collaboration with G. Boileau, N. Christensen, F. Badaracco and N. van Remortel published in [216]. Furthermore we also discuss some updates made to this work as presented in [100] in collaboration with M. Branchesi and et al.

Chapter 10

In this chapter we focus on a tool, gravitational-wave geodesy, which can be used to validate a future isotropic GWB detection. Building on earlier work we introduce a false alarm probability to differentiate a GWB signal from a correlated terrestrial noise signal.

The content of this chapter is based on collaboration with T. A. Callister, N. Christensen, M. W. Coughlin, I. Michaloliakos, J. Suresh and N. van Remortel, published in [217].

Chapter 11

In this chapter we discuss how the null channel can be a useful tool for detector noise estimation with a triangular configuration of interferometric detectors such as the Einstein Telescope or LISA. We investigate how non-identical noise as well as correlated noise between the different interferometers might bias the null channel and how to account for this bias. After providing a proof of concept of the proposed formalism we highlight the next steps needed to build upon the work presented here to create a Bayesian parameter estimation framework.

The content of this chapter is based on collaboration with G. Boileau, M.-A. Bizouard, N. Christensen, T. Regimbau and N. van Remortel published in [215].

Chapter 12

In this final, concluding chapter I summarize some of the most important findings presented in this PhD dissertation. I frame it in the context of the state of the art and highlight what I consider to be interesting topics which currently aren't explored to the fullest. I discuss how these future research projects could help our understanding of how noise sources could affect second and third generation interferometric detectors and more specifically the search for an isotropic GWB.

Appendix A

I believe it is not only important to have attention for the science we are doing, but also for the people doing the science. At the start of my PhD I went through a difficult period after a break-up. These feelings were only strengthened by living alone at that time in Italy for a research stay at Virgo and the subsequent outbreak of the COVID-19 pandemic. During this period I developed a strong interest in mental health. This pushed me to create a survey, focusing on the mental well-being of scientists in the LIGO, Virgo and KAGRA collaborations. The idea was received positively by both LVK management and fellow collaborators. In the summer of 2021 we distributed the first edition of the survey in the LVK collaborations, to which

$\sim$400 people participated. In 2022 we expanded our target audience and more than ten collaborations in the field of high energy and gravitational-wave astrophysics participated, with $\sim$700 scientists responding to the survey. In this appendix we present the results of the first survey conducted in 2021. We investigate how, among others, career stage, job insecurity and minority status are associated with reported levels of depressive symptoms and the desire to leave.

The content of this chapter is based on collaboration with M. Ueda which is submitted for peer-review and available as preprint [219].

6 Identification and mitigation of spectral artefacts for the search for an isotropic gravitational-wave background

In this chapter we focus on how one can identify spectral artefacts and take them into account for the search for an isotropic GWB. In Sec. 6.1 we start with introducing how we identified these spectral artefacts during O3 and show some examples of the identified noise lines. Afterwards, in Sec. 6.2, we discuss how these noise lines are taken care of in the search for an isotropic GWB within the LVK collaborations during O3. We also highlight how the new code implemented before O4 plans to use a slightly modified method compared to what was used during O3. Finally, in Sec. 6.3 we introduce some of the changes to the general workflow which are implemented for data quality investigations during O4. The goal of this more pro-active method discussed here is to enable ourselves to react quicker in case problematic noise features are observed in the data.

The methods explained in this chapter assume the detector is noise dominated rather than signal dominated. This assumption will no longer hold for third generation detectors such as ET and CE, as well as for LISA. For the moment it is mainly an open question how to perform similar data quality studies at those future observatories and more research is needed to prepare ourselves for data quality studies in a signal dominated detector.

6.1 Identifying the origin of spectral artefacts

In Sec. 5.2 we introduced narrowband spectral artefacts and introduced the main categories they can belong to: calibration lines, mechanical resonances and instrumental lines. Here we will discuss in more detail how the spectral lines, which form

a potential problem for the search for an isotropic GWB, were identified during O3 (Sec. 6.1.1). Afterwards we present the identified spectral artefacts during O3 (Sec. 6.1.2). The search for an anisotropic GWB uses these identified artefacts as a starting point for their analysis. However, since they are more sensitive to these features they do additional vetting. This will not be discussed, but we refer the interested reader to [29, 244]. In next section (Sec. 6.2) we will briefly discuss how these identified noise lines result in a notch list, which is applied to the analysis.

6.1.1 Procedure during O3

When applying (data quality) selection criteria to data during an analysis, one always has to be very careful to not introduce a bias, consciously or unconsciously. To this extent, the procedures to identify the noise lines and to reject them from the analysis have several mechanisms in place to reduce the risk of introducing a bias. First of all we start by looking at baseline coherence to identify loud lines that might affect the analysis. The coherence[1], Γ, is given by,

$$\begin{aligned}\Gamma(f) &= \frac{\langle|\tilde{s}_I^*(f)\tilde{s}_J(f)|^2\rangle}{\langle|\tilde{s}_I(f)|^2|\rangle\langle|\tilde{s}_J(f)|^2\rangle} \\ &= \frac{\langle|\mathrm{CSD}_{IJ}|^2\rangle}{\langle|\mathrm{ASD}_I|^2|\rangle\langle|\mathrm{ASD}_J|^2\rangle},\end{aligned} \tag{6.1}$$

where $\tilde{s}_{I,J}(f)$ are the Fourier transforms of $s_{I,J}(t)$ and $\langle\cdot\rangle$ represent the average over N-segments. Furthermore, we have used the definitions of the CSD and ASD. Even though the coherence is related to the CSD, and therefore the isotropic cross-correlation statistic (Eq. 4.11), the relation is distant enough that the coherence is considered as a 'safe' variable, i.e. not directly impacting the search. In case both PSDs are stationary Gaussian random processes and the true coherence value equals zero, the observed coherence follows the following probability distribution [102, 268],

$$p(\Gamma, N|\Gamma = 0) = (N-1) * (1-\Gamma)^{N-2}, \tag{6.2}$$

where N is the number of independent segments averaged over. When performing the data quality checks during O3 we used an approximate distribution [139], namely

$$p(\Gamma) \propto e^{-\Gamma N}. \tag{6.3}$$

[1] Note that we use the same symbol for the coherence and for the non-normalized ORF in Eq. 4.9. In the remainder of this dissertation Γ will refer to coherence, unless specifically mentioned otherwise.

For realistic values of N we use during our data quality investigations both methods are (almost) identical. However, for future observing runs, as well as in the figures reported in this chapter we will use the probability distribution in Eq. 6.2, as this does not provide any evidence for coherence's above 1, whereas Eq. 6.3 does.

Secondly, when analysing the data and performing the search for an isotropic GWB, one first performs the analysis with a time-shift [360]. Here one purposefully applies a time offset to the data of one of the two detectors to break the signal coherence. Any GWB signal would be 'washed-out' by this time-shift and therefore this can give valuable information of the data quality. However, correlated noise could also be 'washed-out' by this method. Therefore further data quality checks have to be performed on the zero-lag data, i.e. the data without any time-shift applied.

Finally, an important safeguard against accidentally removing potential narrowband GWB signals is that significant noise lines are only added to the notch list in case we find sufficient evidence the spectral feature is of instrumental or environmental origin.

6.1.2 Spectral artefacts during O3

Identification of noise lines affecting the search for an isotropic GWB

When identifying spectral artefacts for O3 the coherence was investigated with four different frequency resolutions: 0.1Hz, 1/32Hz, 0.01Hz and 0.001Hz, where the different frequency resolutions might be more or less sensitive to broader or narrower spectral features. 1/32Hz was the frequency resolution used for the final analysis [30]. Coherences were calculated both on time-shifted and zero lag data, here we present the zero lag results. As mentioned earlier, the coherence is expected to follow the distribution in Eq. 6.2 for Gaussian data. This can be used to identify lines which are outliers of the distribution and are likely to be instrumental noise lines that should be rejected from the analysis.

To identify potential spectral lines, it is important to first deal with non-stationarities in the data. In Chapter 5, we explained how both the $\Delta\sigma$-cut and gating can be used to veto/remove time segments that contain non-stationary effects. In Fig. 6.1 and Fig. 6.2, we show the coherence as observed during O3a[2] for the LIGO Hanford-Livingston or HL baseline, with a frequency resolution of 0.1Hz and 0.001Hz, respectively. For both the figures, the top panel shows the coherence

[2]O3a is the first half of LIGO's and Virgo's third observing run which took place between Apr 1 2019 and Sep 30 2019.

when the $\Delta\sigma$-cut was applied, but gating was not. The bottom panel shows the reverse situation were gating was applied but the $\Delta\sigma$-cut was not applied. These figures show that during O3a the $\Delta\sigma$-cut was not able to remove all non-stationary effects from the data, even though it removed a very large fraction of the data ($\sim$ 50%), as mentioned in Chapter 5. Furthermore, they show that depending on the frequency resolution, non-stationary effects could manifest themselves in different ways. We would like to state that the only difference between Fig. 6.1 and Fig. 6.2 is the frequency resolution. The same non-stationarities that create a deficit of coherence when using a resolution of 0.1Hz, lead to an excess of coherence when using a frequency resolution of 0.001Hz. Finally, the $\Delta\sigma$-cut does remove an additional $\sim$ 18% of contaminated data segments in the gated data, as mentioned in the O3 isotropic results [30]. There are no clear data quality issues visible in the coherence after gating, see Fig. 6.2 bottom panel and Fig. 6.4, even if no $\Delta\sigma$-cut is applied. This indicates that the effect of these segments is less problematic than those which are targeted by gating. However, the segments rejected by the $\Delta\sigma$-cut could still introduce noise contamination in the analysis due to non-stationary features, even though maybe not directly obvious from looking at the integrated coherence spectrum in Fig. 6.1 and Fig. 6.2.

Once one has properly taken care of non-stationarities in the data one could identify outliers: frequency bins which have a coherence higher than expected from Gaussian data. A very convenient way to visualize this and at the same time check that, apart from the outliers, the coherence behaves as expected from Gaussian data is shown in Fig. 6.3. This figure shows the number of frequencies with a given coherence. The data used in Fig. 6.3 corresponds to the data shown in the top panel of Fig. 6.2, i.e. coherence data with a frequency resolution of 0.001Hz where only the $\Delta\sigma$-cut is applied to the time-domain data. In Fig. 6.4 we show the equivalent histogram for the scenario where only gating was applied to the time-domain data, i.e. representing the bottom panel of Fig. 6.2. The bottom panel of Fig. 6.4 zooms in on coherence values ≤ 0.005.

In both Fig. 6.3 and 6.4 the expected behavior for Gaussian data is indicated by the blue line, as calculated by Eq. 6.2. The orange dashed line is the threshold which was used to define coherence-outliers, i.e. the coherence value where only one event is expected from Gaussian data. Similarly to what we concluded from Fig. 6.1 and Fig. 6.2, we can clearly see that without gating the data behaves as highly non-Gaussian. However the gated data shown in Fig. 6.4 matches very well with Gaussian data apart from some outliers. The next step in the data quality process is to try and understand these outliers, i.e. find any infrastructural or environmental reason why there is a narrow spectral feature at those frequencies. We will use the

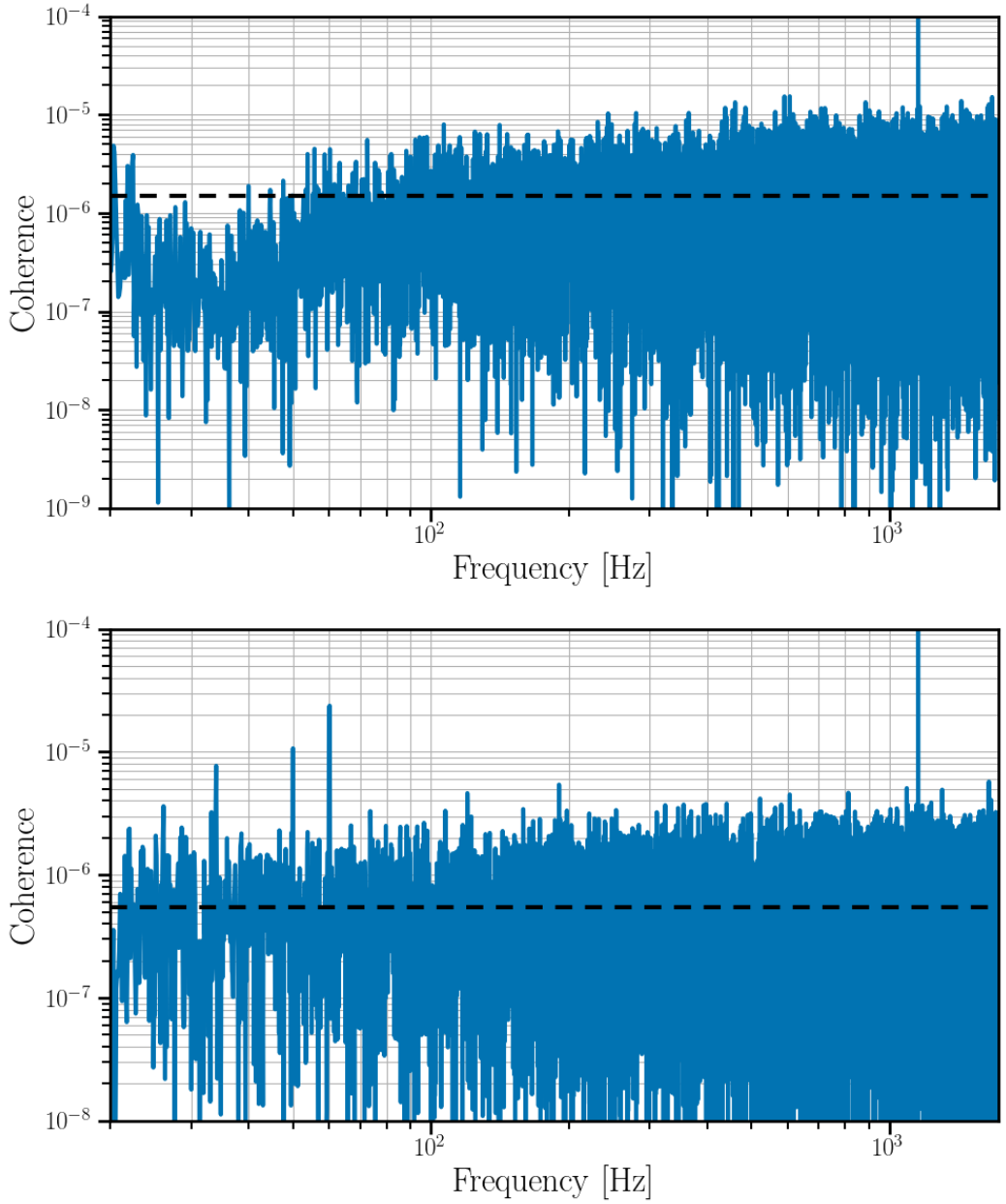

Fig. 6.1.: Observed coherence for the Hanford-Livingston baseline using a frequency resolution of 0.1Hz. Top panel: the $\Delta\sigma$-cut was applied, but gating not. Bottom panel: the $\Delta\sigma$-cut was not applied, but gating was. The black dashed line represents the expected level of coherence from Gaussian data, which equals to $1/N$, with N the number of segments averaged over. Note that the value of the black line in the bottom panel is lower, as more segments were averaged over due to not removing segments with the delta sigma cut.

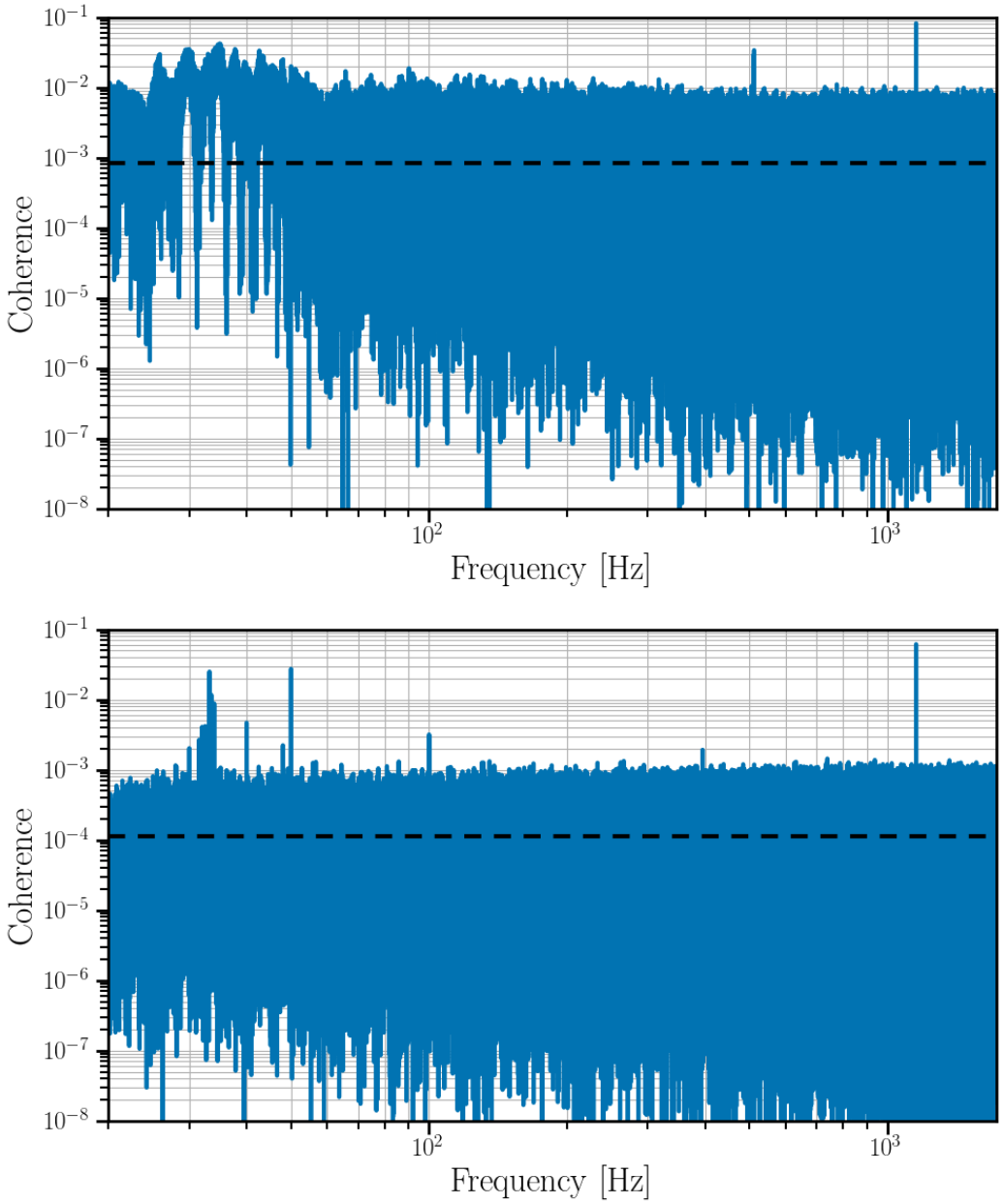

Fig. 6.2.: Observed coherence for the Hanford-Livingston baseline using a frequency resolution of 0.001Hz. Top panel: the $\Delta\sigma$-cut was applied, but gating not. Bottom panel: the $\Delta\sigma$-cut was not applied, but gating was. The black dashed line represents the expected level of coherence from Gaussian data, which equals to $1/N$, with N the number of segments averaged over. Note that the value of the black line in the bottom panel is lower, as more segments were averaged over due to not removing segments with the delta sigma cut.

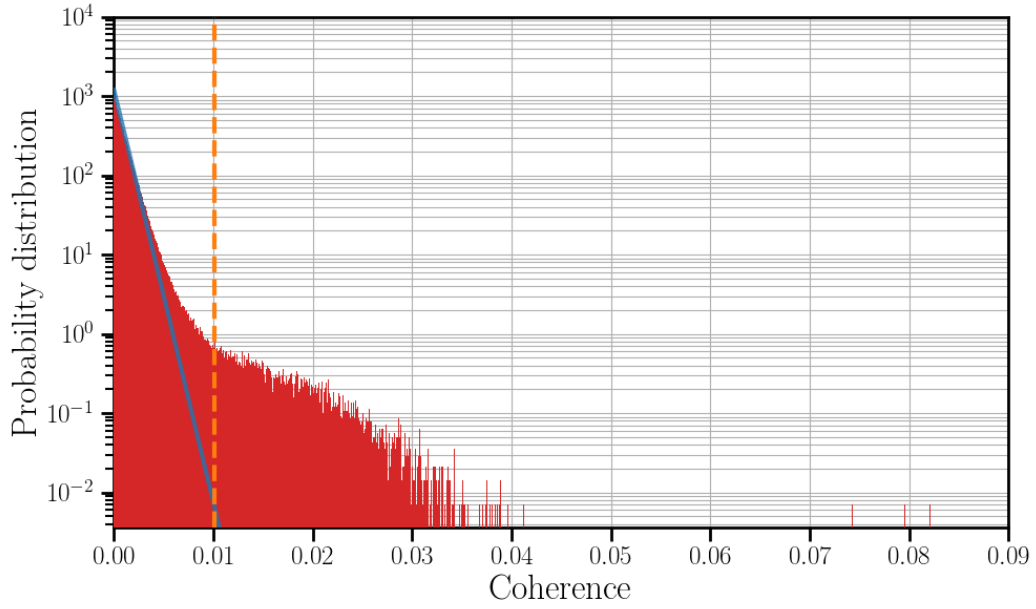

Fig. 6.3.: Histogram of the observed coherence in the frequency region considered for the analysis (20Hz-1726Hz), from data with applying the $\Delta\sigma$-cut, but without applying gating. The blue line is the expected behavior for Gaussian data. The orange dashed line is the threshold which was used to define coherence-outliers. The threshold used is set to the coherence value where only one event is expected from Gaussian data.

outliers in Fig. 6.4 as an example before we summarize the final outcomes from these studies.

Identification of the origin of loud noise lines

Tab. 6.1 summarizes the twenty coherence outliers from Fig. 6.4, the frequency they occur at as well as the identified origin of the spectral artefact. To identify these lines, typically three steps are followed. First of all we look if the lines are known spectral artefacts. For this we can rely on a number of internal web-pages summarising calibration lines, mechanical resonances, etc. Another resource is the online detector logbook in which, among others, noise features are discussed and identified when they are spotted by the relevant research teams. If the cause of the spectral artefact after this first step is not yet identified, we often reach out to different experts and research teams interested in spectral artefacts. This are for instance people working on detector characterisation or CW analysis, since the latter are very sensitive to spectral artefacts. After these first two options, the majority of the lines in Tab. 6.1 were identified. Only the line at 32Hz was not identified. In such a case a third method to identify the origin of spectral lines is to rely on tools

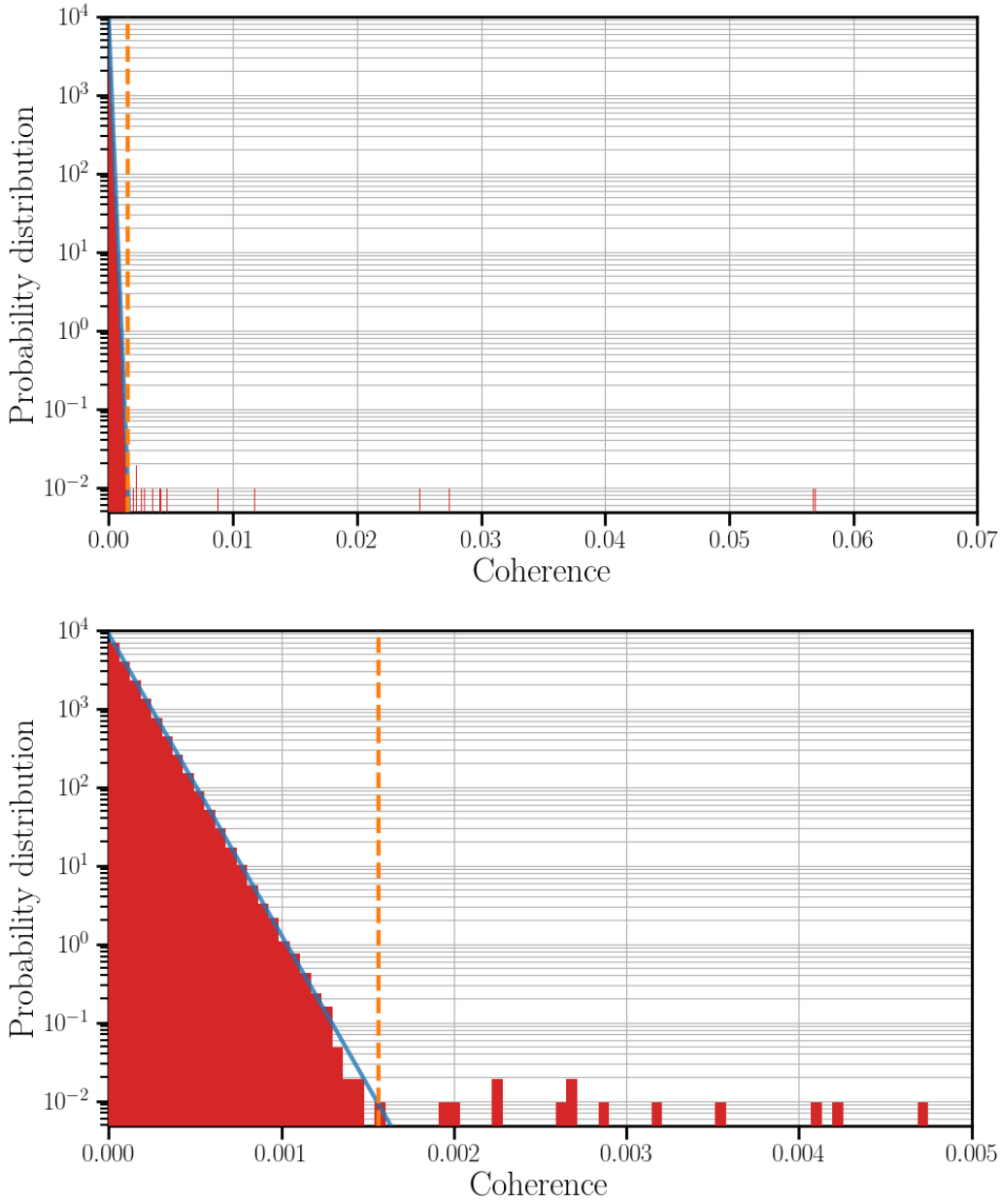

Fig. 6.4.: Histogram of the observed coherence in the frequency region considered for the analysis (20Hz-1726Hz), from data without applying the $\Delta\sigma$-cut, but with applying gating. The bottom panel zooms in on coherence values ≤ 0.005. The blue line is the expected behavior for Gaussian data. The orange dashed line is the threshold which was used to define coherence-outliers. The threshold used is set to the coherence value where only one event is expected from Gaussian data. The exact coherence values are expected to differ from the values in Fig. 6.3, as both figures have a different number of segments over which it is averaged.

that systematically compute the coherence between the GW-data, $h(t)$, and a large number of witness channels. The number of witness channels is typically several hundreds and consists of sensors which measure the environment of the detector and its behaviour without them containing any information on the GW signal e.g. seismometers, magnetometers, accelerometers. Two tools which are able to perform such calculations are Fscan [132] and STAMP-PEM [265]. With the use of these tools we found significant correlation between $h(t)$ and a number of accelerometers at the corner station of LIGO Hanford for the noise line at 32Hz. For the lines at 49.999Hz - 50.001Hz also significant correlation between $h(t)$ and a number of magnetometers as well as seismometers was identified. These lines could however already be explained by the known 1Hz spaced comb at Hanford and 10Hz spaced comb at Livingston.

During O3, Fscan and STAMP-PEM were only available for data from the two LIGO detectors and not for Virgo data. This implied that this third and final step to identify unknown lines was a bit lacking for Virgo. To this extent we set-up a manual effort to identify these lines. A tool that did run at Virgo was NoEMi [34] which identifies loud lines in $h(t)$ during the entire run. On our request NoEMi did run on about hundred witness channels for one day during O3a and one day during O3b. This day was somewhat arbitrarily chosen as a day with good sensitivity. For the unidentified noise lines, we identified all the witness channels that had also lines at the same frequencies. Whereas this is already a first indication there might be a common origin, this does not give irrefutable proof they share the same physical origin. Therefore, for the same day of data we computed the coherence between $h(t)$ and this subset of witness channels. By analysing these data we were able to identify a number of additional spectral artefacts. All the identified spectral artefacts for Virgo can be found in [241] and will be discussed in a bit more detail below.

Whereas this approach was the best we could do given available person-power as well as computing resources at that time, it is far from ideal. First of all, it required a tremendous cost of person power spent manually doing these computations and analysing the data. Secondly, it is far from a systematic method and easily could have missed a number of lines that otherwise would have been identified. To this extent STAMP-PEM was implemented for Virgo before O4.

The entire set of spectral artefacts identified for the search for an isotropic GWB can be found in the data release of the search [243].

Frequency [Hz]	Coherence	Identified origin
30.000	0.0018	Known combs: 1Hz comb in LHO, 10Hz comb in LLO
31.500	0.0026	Known combs: 1Hz comb with 0.5Hz offset in LHO and LLO
32.000	0.0041	Environmental witness channel: LHO corner station accelerometers
32.500	0.0042	Known combs: 1Hz comb with 0.5Hz offset in LHO and LLO
33.199	0.0037	Calibration line non-linearity
33.200	0.025	Calibration line non-linearity
33.201	0.0028	Calibration line non-linearity
33.500	0.012	Known combs: 1Hz comb with 0.5Hz offset in LHO and LLO
34.000	0.0086	Known combs: digital comb
34.001	0.0026	Known combs: digital comb
40.000	0.0044	Known combs: 1Hz comb in LHO, 10Hz comb in LLO
48.000	0.0022	Non-stationary, non-linear scattered light noise (LHO), fixed in Sep 2019
49.999	0.0023	Environmental witness channel: LLO magnetometers and seismometers
50.000	0.028	Environmental witness channel: LLO magnetometers and seismometers
50.001	0.0027	Environmental witness channel: LLO magnetometers and seismometers
100.000	0.0032	Known combs: 1Hz comb in LHO, 10Hz comb in LLO
394.661	0.0019	Calibration line non-linearity (LHO)
1153.099	0.057	Calibration line @ 1153.1Hz
1153.100	0.062	Calibration line @ 1153.1Hz
1153.101	0.057	Calibration line @ 1153.1Hz

Tab. 6.1.: The outliers of the HL coherence distribution when analysing O3a data, with gating applied. The $\Delta\sigma$-cut was not applied and the used frequency resolution was 0.001Hz. These correspond to the outliers in Fig. 6.4.

Identification of additional noise lines at Virgo

Apart from identification of noise lines affecting the search for a GWB we also try to identify noise lines observed in the individual interferometers. For Virgo during O3 I led the effort to put together a list of identified lines as well as performed the majority of the identifications.

Spectral artefacts in Virgo are characterized by two parameters called 'presence' and 'persistence'. The presence of a spectral artefact is the percentage of days it was observed in Virgo's strain. The persistence of a noise line is a measure how persistent the line was during a day, taking values between 0 and 1. Due to the large amount of noise lines $\sim$ 2000 it was unfeasible to follow up all the noise lines. To identify which noise lines are the most relevant we used the product of presence times persistence as a figure of merit, which can take values between 0 and 100. The majority of the lines ($\sim$ 87%) are very weak and/or are present only occasionally. This reflects in a low value of $\mathrm{presence} \times \mathrm{persistence} < 5$. We only followed up lines with $\mathrm{presence} \times \mathrm{persistence} \geq 5$ between 12Hz and 2500Hz, as these are the most likely to form potential data quality issues for long duration GW searches. This amounts to 245 lines flagged for follow-up. The majority of these lines are 'known' and can be found in line databases, i.e. calibration lines, mechanical resonances of the detector, power mains, etc. Another set of lines could be easily linked to a 1Hz electromagnetic comb which is known to be present at Virgo and has multiple magnetometers as witness channels. This left us with 43 (of 245) unidentified lines. In an attempt to identify these lines we used the manual effort as described above. We identified 84 environmental channels as high probability candidates to provide proof of coherence between $h(t)$ and these environmental channels and calculated the coherence between these 84 channels and $h(t)$ for one day during O3b. Afterwards we checked for each of the 43 unidentified spectral artefacts whether any of the 84 chosen witness channels had significant coherence with $h(t)$ indicating the noise line is caused by an environmental/instrumental effect[3]. This led to the identification of an additional 25 noise lines, leaving 18 lines unidentified. The resulting list of identified lines for Virgo can be found in [241].

[3]Due to the enormous size of the manual work (about $\sim$ 3500 combinations had to be checked) this work was not solely performed by me but in coordination with the Virgo detector characterisation group. This is a clear example why the implementation of STAMP-PEM for Virgo was crucial before O4.

6.2 Creating a notch list

As mentioned in Chapter 5, one wants to notch all known spectral artefacts, i.e. set the value of the cross-correlation statistic, $\hat{C}_{IJ}$, in the affected frequency bins to zero. This is equivalent to take the limit where the uncertainty, $\sigma(f) \to \infty$. This ensures the contaminated frequency bins do not bias the analysis results by excluding them. In this section we will start by mentioning how the notch list was created based on the list of known spectral artefacts during O3. Afterwards we will briefly introduce `pygwb`, the new analysis pipeline that will be used by the LVK collaborations during O4. Finally we will describe the updated method used to create the notch list in `pygwb`.

In the discussion below we will use the terms 'noise line' and 'notch'. With the former we refer to the physical noise line, whereas with the latter we refer to how we deal with the noise line in our analysis.

Creation of a notch list during O3

After identification of noise lines using the procedures discussed in last Section, one provides a central frequency of the noise line and its a width to create a notch list. In case the noise line is a known calibration line or mechanical resonance, the known width is used. Otherwise an estimate width is determined based on the observed spectral artefact. Given a certain frequency resolution, the central frequency of the notch would be the frequency bin center closest to the peak frequency of the noise line. The width of the notch was set to the noise line width rounded upwards to an odd number of frequency bins. A width of an even number of frequency bins was not allowed to ensure a symmetric notch width. Afterwards this list of notches was stored and applied to the analysis for a GWB. The official notch list for O3 are published as part of the public data release [243].

`pygwb`, a new isotropic analysis pipeline

`pygwb` [300] is the new LVK pipeline for the search for an isotropic GWB and replaces an old matlab code from 2004. Whereas the philosophy of the analysis in `pygwb` heavily builds upon the old code, `pygwb` is an open source, object-oriented and modular python package. Furthermore it unifies all the different aspects needed to perform the search for an isotropic GWB and includes a notch module which enables to deal with spectral artefacts. In the past the notch list was provided by a separate

piece of python code of which the output was passed on to the analysis pipeline in matlab. For more details on `pygwb`, all its features and performance, we refer the interested reader to [300]. My contribution to `pygwb` was the updated method to apply notches to the analysis, which will be discussed in more detail below.

Creation of a notch list in `pygwb`

The `notch` module of `pygwb` provides the framework to properly deal with the identified noise lines in the case of the search for an isotropic GWB. To this extent the `notch` module provides a frequency mask which may be applied to the spectra involved in the analysis. The key object of the `notch` module is the `StochNotchList`, which is a list of `StochNotch` objects. A `StochNotch` object represents a physical noise line which has been identified and needs to be removed from the analysis. The object has a minimum and maximum frequency indicating the contaminated frequency region. Furthermore, it also comes with a descriptive string which allows the user to keep track of the reason why the line was notched. All the different `StochNotch` objects for a certain analysis are then stored in the `StochNotchList` which contains the entire list of lines to be notched from the analysis.

The notch mask used to apply a set of notches within the analysis is constructed conservatively, such that any frequency that has overlapping frequency content with the noise lines defined in the `StochNotchList` will be removed when applying the notch mask. Concretely, the GWB estimator $\hat{C}_{IJ}(f_k)$ is calculated at the discrete frequency bin f_k. Its value at frequency f_k estimates $\Omega_{\mathrm{GW}}(f_k)$ at this discrete frequency. This value can be conceived as the average of $\hat{C}_{IJ}(f)$, i.e. with an infinite frequency resolution, over the frequency range of the bin with a width Δf centered around f_k, i.e. $[f_k - \Delta f/2, f_k + \Delta f/2]$[4]. If a noise line has any overlap with this interval, the kth frequency bin is excluded. This implies that a hypothetical delta-peak noise line at $f_k + \Delta f/2$, leads to notching both f_k as well as $f_{k+1} = f_k + \Delta f$.

We present the creation of a notch mask with an example in Fig. 6.5, which illustrates how our conservative notching strategy excludes frequency bins based on different scenarios of noise lines. The strategy implemented in `pygwb` improves upon the method used in O3 in several ways. In `pygwb` a more clear distinction is made between the list of noise lines and the list of notches, i.e. the notch mask which depends on the used frequency resolution. Whereas in O3 the stored output was the notch list for the frequency resolution used in the analysis, currently the key

[4]Typically the edge frequencies contribute half to each bin of which they form the edge frequency, rather than contributing entirely to e.g. the lower frequency bin and not to the higher frequency bin.

output stored, is the list of noise lines independent of the frequency resolution used in the analysis. When the list of noise lines is supplied to an analysis using `pygwb`, it can be used to create the notch mask for any given analysis. This improves the re-usability of the stored output. However, if needed also the applied list of notches or the notch mask can be saved for that specific analysis. Furthermore, `pygwb` has a more optimal notching scheme, while remaining conservative. Previously, both the center frequency and the number of bins were rounded upwards, which might have led to notching bins which were not affected by the spectral artefacts. This in turn leads to a (small) loss in sensitivity. The notching scheme implemented in `pygwb` is conservative, but not overly by notching all bins which should contain contaminated frequency content but not any additional bins.

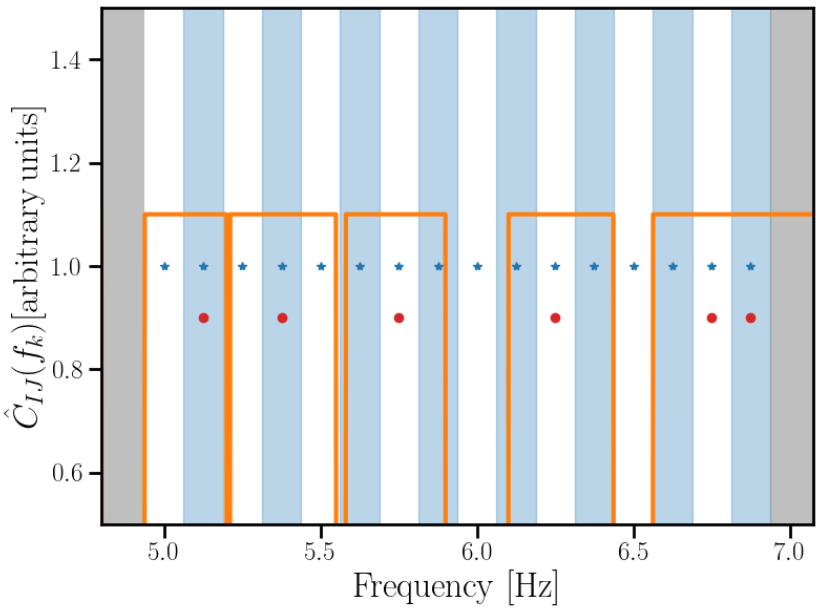

Fig. 6.5.: Example of how the notching of noise lines (orange curve) applied to the discrete measurements of the spectrum $\hat{C}_{IJ}(f_k)$ (blue stars) leads to a final set of measurements (red dots). The vertical shaded regions indicate the bins, where even bins are white and odd bins are light blue. The orange line traces out the noise lines such that a noise line is present where the orange curve is zero. The analyzed data spans $[5.0, 6.875]$Hz, in the un-shaded region. In this example there are five noise lines, from left to right: a noise line ending at the lowest frequency bin, a noise line entirely contained in one frequency bin, a noise line spread across two frequency bins, a noise line spread across multiple frequency bins, and a noise line from bin-edge to bin-edge. After our notching procedure (see text for more details), the data is reduced to the bins marked by the red dots. For visual convenience we have changed the amplitude in these remaining frequency bins by a factor 0.9.

The current code is set up to apply the same notches to an entire stretch of data, which can be considered as time-independent notching. To allow for time-dependent

notching we could either use the current `notch` module and split the analysis in different segments, e.g. a month long period, each having their own notch list. Afterwards the results of these multiple mid-duration segments could be combined. Alternatively, one could extend the current module with an additional parameter which keeps track of which times have to be notched. Since typically the majority of the notched lines in the search for an isotropic GWB with data from the LIGO and Virgo detectors are present during the entire dataset, the possible gain of implementing time-dependent notching is expected to be limited.

6.3 Procedure for data quality investigations during O4

During O3, virtually all data quality investigations for the GWB analysis were done at the end of the run. Even though there were certain tools to already follow-up the data quality for the GWB, they were underused. This lead to a very late identification of the issues caused by the large amount of loud glitches in the LIGO detectors. In the end this was solved by implementing gating. However, due to the late realisation of the problem this lead to large delays in achieving the deliverables of the analysis. Therefore we proposed a much more pro-active approach during O4, as summarized in the flowchart in Fig. 6.6. First of all, on a daily/weekly timescale we will be performing a number of tests on timeshifted data to identify potential data quality issues. Among others we will look at coherence spectra as well as coherence histograms, such as shown in Figs. 6.1-6.4. This will enable us to spot potential issues sooner. Broadband features in the coherence can point towards not properly dealing with non-stationary features such as glitches. Additionally, we will be able to follow-up noise lines with a lower latency, as well as a time-dependence. This allows more time to identify problematic spectral artefacts. More specifically, this also enables us to push for potential interventions and additional tests to identify lines at the different detectors. A scenario where this would be very valuable is in case an outlier is observed in the search for an anisotropic GWB. In the anisotropic GWB analysis of O2 data [10] an outlier at 36.06Hz was found with a SNR > 5 for O2 data only. When including O1 data the significance dropped to below a SNR of 5. Since no excess was observed when analyzing O3 data, it was concluded that this outlier is not a persistent GW source [29]. No similar outlier was found in an all-sky CW search, which even put more stringent upper limits on this frequency and sky position [11]. This seems to support the noise hypothesis. With the noise investigation approach planned during O4, we will be aware of a similar outlier well before the end of the data taking period. This will allow more thorough follow-up

of the spectral artefact to identify a potential instrumental and/or environmental origin. In case no such evidence can be found for a high significance, potential signal candidate, one can think of doing more dedicated tests at the detectors with e.g. noise injections. This can either still reveal a potential pathway for the coupling of instrumental noise or otherwise further increase our confidence in its potential to be a GW signal. Such additional verification would not have been possible with the approach followed during O3.

An additional benefit of this proactive approach is that it is also in line with the prospects for longer observing runs. O4 is scheduled to be 18 months, plus two months of commissioning and O5 will be even longer. The approach we are planning to deploy during O4, enables us to have a faster turnover of the results at the end of the run. Whereas this was not mandatory in the past, it will be needed more and more with longer runs and the tighter plans for releasing the data to the public.

Fig. 6.6 represents the workflow we will follow and the checks we plan to make on a weekly basis on time-shifted data to determine the data quality for the search for an isotropic GWB. Issues with broadband coherence and the follow-up investigations could for instance lead to additional times marked for removal if they have too high levels of non-stationarity even though they passed the checks currently in place. The list of outliers we identify when performing narrowband checks will form the start of our list of noise lines to be notched from the analysis, given that we have identified their origin. In case we do not know their origin we plan to do follow-up investigations with tools such as STAMP-PEM or discuss this with noise line experts from CW analyses.

Furthermore, at the end of every 1-2 months we plan to 'open the box', and analyse the data without time-shift. That is, we basically perform a full analysis on this month-long segment. Before opening the box we will fix a temporary list of segments marked for removal based on the $\Delta\sigma$-cut and potentially additional segments flagged by manual investigations. We will also fix a list of noise lines to be notched, based on the weekly investigations. This monthly unboxing enables us to quickly identify potential additional data quality issues which were not found before. This will also help to drastically reduce the analysis turn over time at the end of the run as the entire analysis was already run in month-long subsections.

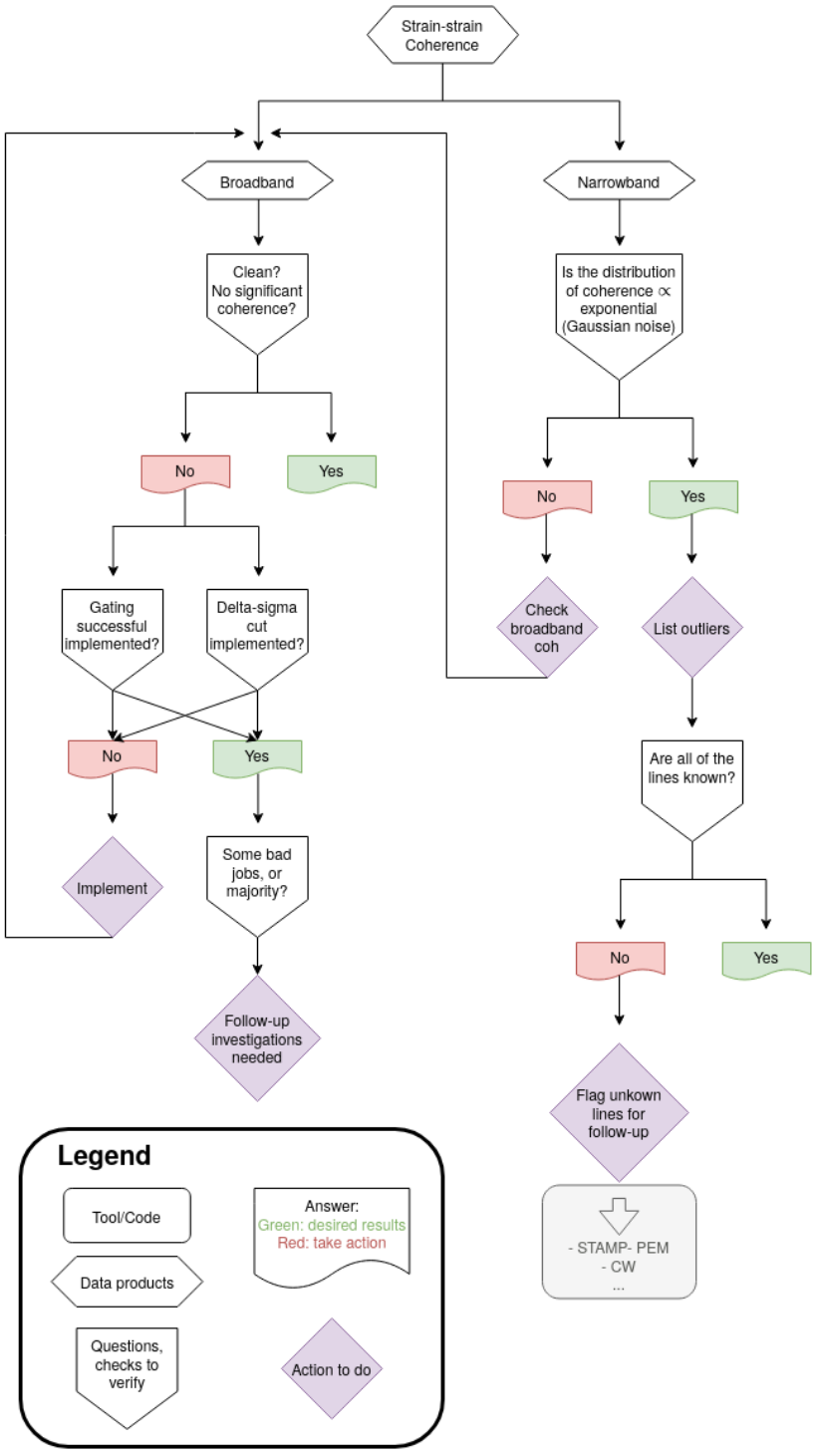

Fig. 6.6.: Workflow to perform data quality checks for the search for an isotropic GWB on a weekly basis on time-shifted data.

6.3.1 Preliminary O4 data quality

In this subsection, we will present some of the preliminary data quality features based on the first two months of O4 data (i.e. from 24 May 2023, 15:00 UTC up to 1 Aug 2023 00:00 UTC). Any statements made here rely on the use of time shifted data, where a time-shift of 1 second is applied to the LIGO Livingston data. Based on the daily data quality checks performed we find that there is about 55% to 60% of coincident time between LIGO Hanford and LIGO Livingston. Note, during these first two months of data the percentage of coincident time during the weekend is about 10% higher compared to the entire dataset. Of the total coincident time, about 10% to 15% is discarded due to data quality veto's similar to veto's used during the analysis of O3 data [30]. However, based on the preliminary results form the last two months, only about 1% of the coincident data is lost due to the $\Delta\sigma$-cut. The amount of data gated in each interferometer is less than 0.16%. When comparing the amount of data lost due to gating as well as due to the $\Delta\sigma$-cut with the O3 analysis, we observe the current loss in data is about a factor ten smaller compared to O3. This seems to be an indication the first two months of O4 have exquisite data quality.

Based on daily as well as weekly coherence spectra and histograms, no major new spectral artefacts are found. As illustration we show in Fig 6.7 the observed coherence spectrum and histogram for the timeshifted HL data during the week of Tue 26 July 2023 to Tue 1 Aug 2023. In this week we find one noise line which has a very low probability ($\sim 10^{-5}$) to be consistent with Gaussian noise and is not yet included in the notchlist. This line occurs at a frequency of 24.5Hz. However, at this frequency an additional calibration line was injected during this specific week as stated in [225]. Otherwise no noise lines were found in any of the weeks during the first two months of O4 data. More detailed data quality investigations with longer integration times are needed and will be performed over the coming weeks. However, the preliminary data quality investigations for the search for an isotropic GWB seem to indicate O4 promises to be an observing run with plenty of high quality data to analyse.

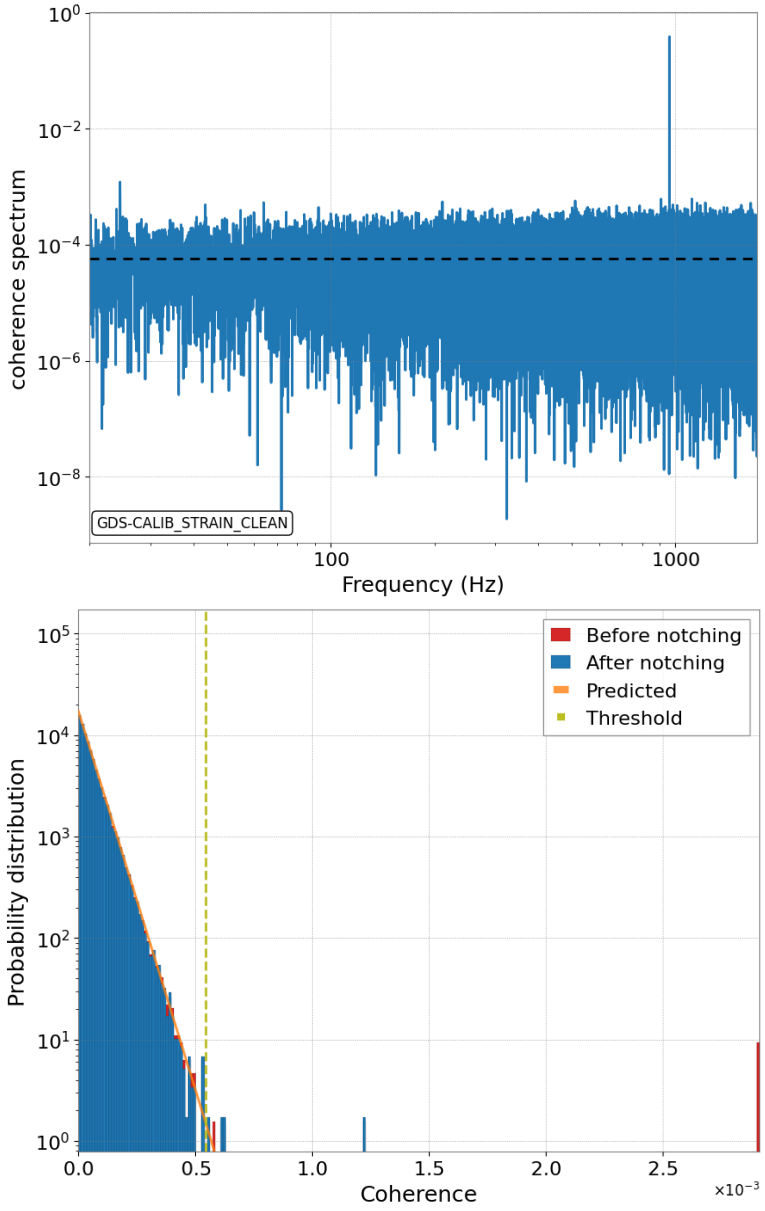

Fig. 6.7.: Coherence of the timeshifted strain between LHO and LLO during the week of Tue 26 July 2023 to Tue 1 Aug 2023. A frequency resolution of 1/32Hz is used. Top panel: coherence spectrum. Bottom panel: coherence histogram, where the last bin contains all the frequencies with a coherence larger than $3 \cdot 10^{-3}$. The red histogram contains all noise lines with frequencies between 20Hz and 1726Hz, whereas the blue histogram shows only the data which is not removed by the notch list. The orange line is the expected behavior for Gaussian data. The light green dashed line is the threshold which was used to define coherence-outliers. The threshold used is set to the coherence value where only one event is expected from Gaussian data. The only significant noise line outlier which is not yet included in the notch list is 24.5Hz (coherence ∼0.0012), which is known to be a temporary calibration line at LHO [225]. The other noise lines above the set threshold all have a probability of more than 20% to be from Gaussian noise.

6.4 Conclusion

In this chapter we discussed the procedures used in the LIGO, Virgo and KAGRA collaborations to identify spectral artefacts which impact the search for an isotropic GWB. We used the results and analysis of O3 data as an example and showed how the initial investigations were impeded by the effect of loud glitches. After the implementation of gating to deal with these glitches, the effect of these non-stationary effects was small on the coherence spectrum and problematic noise lines could be flagged. We used the HL baseline as an example and showed the subsequent identification of the flagged spectral artefacts. Afterwards, we discussed how these spectral artefacts are dealt with in the search pipeline by using a notch list. We also highlighted the new approach of notching that is implemented in the new isotropic analysis pipeline `pygwb`. This updated approach allows to have more precise notches for very narrow spectral artefacts. Finally, we ended the chapter with a discussion of the pro-active data quality procedure followed during O4. This also included a short discussion on some of the preliminary data quality features for the search for an isotropic GWB with the first two months of O4 data. Based on these preliminary investigations, O4 data quality seems to be very good and promises to become an interesting observing run.

7 Correlations in magnetic field fluctuations and their coupling to Earth-based gravitational-wave detectors

In Chapter 5 we introduced the Schumann resonances and some details of the propagation of electromagnetic fields in the atmosphere. In this chapter we will start by highlighting, in Sec. 7.1, some studies of the cross-correlation between LIGO Hanford (H or LHO), LIGO Livingston (L or LLO) and Virgo (V) performed as part of this PhD. Afterwards in Sec 7.2 we will introduce the so called 'magnetic-coupling function' which describes how magnetic fields couple to the detectors. In Chapter 8 this information is combined to predict the impact of these correlations from magnetic field fluctuations both on current and future generation Earth-based GW detectors.

7.1 Schumann resonances and individual lightning strikes

As part of data quality checks for the search for an isotropic GWB during O3, the correlations of the magnetic field fluctuations were studied between the LIGO and Virgo observatories. The impact of these magnetic correlations during O3 was reported up to 100Hz by the LVK collaborations [30]; however, this was not done for frequencies above 100Hz.

In Fig. 7.1, the coherences of the magnetic field fluctuations between LHO-LLO, LHO-Virgo and LLO-Virgo are shown (the Hylaty data will be introduced later in this section). The spectra are calculated using data taken between Apr 2 2019 00:00:00 UTC and Mar 27 2020 00:00:00 UTC, consistent with O3 (but also including the data during the commissioning break during October 2019). Furthermore, the coherence represented in Fig. 7.1 is, at each frequency, the maximal value from the

four possible coherence pairs using the two orthogonal magnetometers at each site (along the x- and y-arms for LHO, LLO and along geographical North-South and East-West for Virgo).

Some of the Schumann resonances are more coherent in one pair or another. Typically the difference between the minimal and the maximal observed coherence at the different magnetometer pairs for a given baseline is about one order of magnitude or less at a given frequency. In some limited number of cases the difference is two orders of magnitude.

There is a non-zero magnetic coherence above 60Hz, where one might expect the strength of the Schumann resonances to be small. This higher frequency coherence has not been previously reported in the context of gravitational-wave detectors. The observation of this high-frequency inter-site correlation was facilitated by the acquisition, for O3, of magnetometers placed far from the magnetically noisy buildings.

It is interesting to note that earlier investigations of magnetic correlations between LHO and LLO during the initial detector era reported some excess coherence between 50Hz - 100Hz [348]. The magnetic coherence during the fifth science run (S5) was rather minimal above 50Hz and did not extend above 100Hz. Since the integration time used in the S5 analysis is quite similar to the time used for O3 (Fig. 7.1), the difference is likely due to the use of sensitive magnetometers located far from the buildings during O3. During the earlier S5 run, all magnetometers were inside the buildings in a magnetically noisy environment.

Fig. 7.2 reports the CSD between the different magnetometers for the HL, HV and LV baselines – pairs of the GW detectors – of data taken between Apr 2 2019 00:00:00 UTC and Mar 27 2020 00:00:00 UTC. Here, we show the quadratic sum of the four different individual CSD combinations, as represented in Eq. 7.1. Furthermore we use the modulus of the individual magnetic CSD instead of only the real part. This choice is made since it is the most conservative option we can choose:

$$\begin{aligned} CSD_{IJ} = & \frac{2}{T} [\, |\tilde{m}^*_{I_1}(f)\tilde{m}_{J_1}(f)|^2 + |\tilde{m}^*_{I_1}(f)\tilde{m}_{J_2}(f)|^2 \\ & + |\tilde{m}^*_{I_2}(f)\tilde{m}_{J_1}(f)|^2 + |\tilde{m}^*_{I_2}(f)\tilde{m}_{J_2}(f)|^2 \,]^{1/2} , \end{aligned} \tag{7.1}$$

with $\tilde{m}^*_{I_1}(f)$ the Fourier transform of the magnetic data $m_{I_1}(t)$ measured by sensor 1 located at GW detector I. The factor of $2/T$ is a normalisation constant of the Fourier transform, where T is the time duration of the data segment when applying the Fourier transform. In the remainder of this PhD dissertation we will use this conservative estimate of the CSD when discussing the magnetic CSD, unless specifically mentioned otherwise.

In [214] we argue that the magnetic coherence above 50Hz is likely due to the superposition from individually correlated lightning strikes. M. Ball of the University of Oregon performed a study where he links glitches in the magnetometers to lightning strikes. Afterwards he showed that by gating away these glitches, the magnetic coherence at frequencies above $\sim$ 100Hz, reduces significantly, see Fig. 7 of [214]. In addition, in [203] the authors investigated the impact of a non-uniform lightning distribution on the observed Schumann resonances.

Both the magnetic coherence (Fig. 7.1) and the CSD (Fig. 7.2), fall off more rapidly with increasing frequency in the case of HV and LV compared to HL. The fast decline in magnetic CSD for the HV and LV baselines can be explained by the increased attenuation of magnetic field fluctuations caused by lightnings at larger distances. Namely the distance between LHO and LLO is about 3000 km, whereas the distances between Virgo and LHO, LLO are respectively $\sim$ 8800 km and $\sim$ 8500 km. This is also in line with the elevated thunderstorm activity in the Americas compared to Europe. The rate of lightning near LLO tends to be greater than the rate in Europe, and the rate around LHO is lower than around Virgo [355].

To further test this hypothesis, we include data from another magnetometer station in Fig. 7.1 and Fig. 7.2. The station we use is part of the World ELF Radiolocation Array (WERA) [231]: the Hylaty station located in the Bieszczady Mountains in Poland [232]. The distance between the Hylaty station LHO, LLO and Virgo is respectively $\sim$ 8800 km, $\sim$ 9000 km and $\sim$ 1100 km. The station is equipped with two magnetometers, oriented along North-South and East-West and is located in a very quiet location to measure ELF magnetic fields. The rate of lightning strikes in Poland is about the same as at LHO [355]. The magnetometer response, as a function of frequency, is quite flat up to 250Hz, but declines rapidly above with only 50% response at 262Hz. Therefore we will focus in the following analysis on the frequency region 1Hz - 250Hz.

The coherence and CSD between the magnetometers located at Hylaty and GW detectors are shown in respectively Fig. 7.1 and Fig. 7.2. We notice the coherences between different baselines span several orders of magnitude, even at the Schumann frequencies. Above 100Hz, the HL-baseline has the highest coherence followed by the Hylaty-Virgo baseline. HV and LV have the lowest coherence of all. When looking at the CSD, we notice the amplitude of the CSD at the fundamental Schumann mode (7.8Hz) ranges from 0.4 $\mathrm{pT}^2/\mathrm{Hz}$ to 1 $\mathrm{pT}^2/\mathrm{Hz}$. Above 100Hz the CSD of HL is the largest by one order of magnitude. The baseline CSDs in descending order are (above 100Hz): $\mathrm{CSD}_{\mathrm{HL}} > \mathrm{CSD}_{\mathrm{Hylaty-V}} > \mathrm{CSD}_{\mathrm{HV}} \approx \mathrm{CSD}_{\mathrm{LV}} > \mathrm{CSD}_{\mathrm{Hylaty-H}} \approx \mathrm{CSD}_{\mathrm{Hylaty-L}}$.

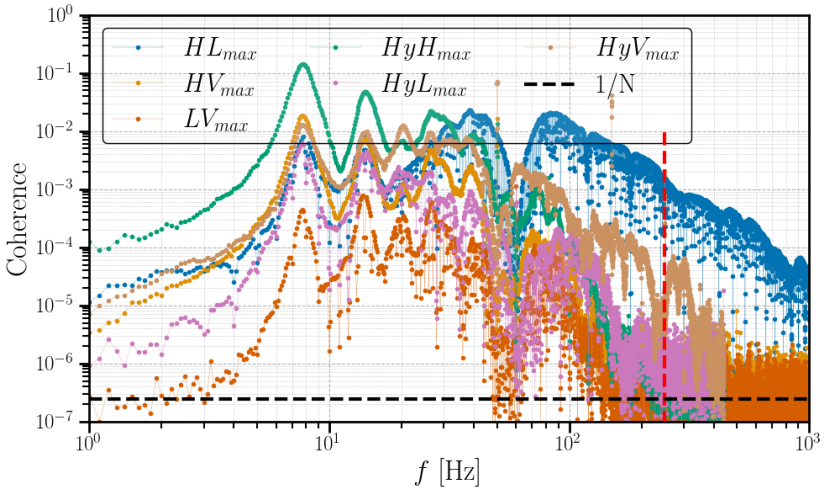

Fig. 7.1.: Coherence spectrum between HL (blue), HV (orange), LV (red), Hylaty-LHO (green), Hylaty-LLO (purple) and Hylaty-Virgo (brown). At each frequency the maximal coherence of the four magnetometer pairs is plotted for a given baseline. In the absence of correlated noise, one expects this to be consistent with Gaussian noise given by the inverse of the number of averages (N) used to make the coherence spectrum, indicated by the black dashed line. Data spans April 2 2019 00:00:00 UTC to March 27 2020 00:00:00 UTC, consistent with the overlap between LIGO's and Virgo's third observing run (also including data from the commissioning break during October 2019). Above 250Hz, the magnetometers at the Hylaty experience significant loss in sensitivity.

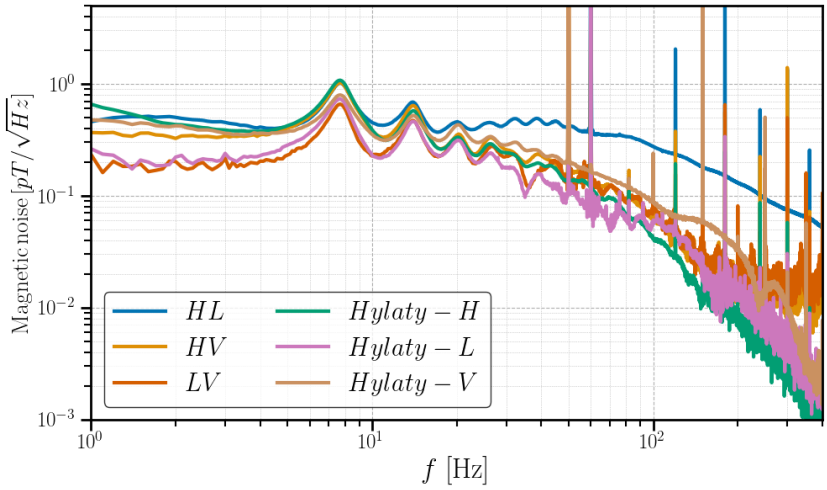

Fig. 7.2.: CSD$^{1/2}$ (as given by Eq. 7.1) of HL, HV, LV, Hylaty-LHO, Hylaty-LLO and Hylaty-Virgo. Data is used from April 2 2019 00:00:00 UTC to March 27 2020 00:00:00 UTC, consistent with the overlap between LIGO's and Virgo's third observing run (also including the data from the commissioning break during October 2019).Above 250Hz (red dashed line) the magnetometers at the Hylaty experience significant loss in sensitivity. The broad peaks below 60Hz are associated with the Schumann resonances.

This can be explained by the characteristics of the propagation of electromagnetic waves in the Earth's atmosphere and the location of the main thunderstorm regions, as explained in Chapter 5. The magnetometers located at LHO-LLO and Hylaty-Virgo have the highest CSDs. The distance between the magnetometers for other baselines is 2.5 to 9 times larger, leading to larger attenuation of the electromagnetic waves. The significantly higher coherence and CSD in the HL baseline compared to the Hylaty-Virgo baseline can be explained by the main thunderstorm regions. Whereas LHO and LLO are located in a (very) active thunderstorm region, Hylaty and Virgo are further away from the main thunderstorm regions, located in America, Africa and Asia.

The observed behaviour discussed in this section is consistent with what is expected from our hypothesis postulated in [214], i.e. the superposition of individual lightnings is the likely source to explain the observed coherence and cross-correlation above 100Hz between the magnetometers at the GW detectors during O3.

Schumann resonances measured at Sos Enattos

As a part of site characterisation of the Sos Enattos mine for the ET [275, 305], magnetic field measurements were taken from 5Hz to 100Hz in the exceptionally quiet environment inside the unused mine. We use 48 days of data taken from Nov 14 2019 to Dec 31 2019, using a single-axis Metronix MFS-06e magnetometer positioned inside the Sos Enattos mine about 200 m below ground level. The magnetometer is sampled at 250Hz. We show in Fig. 7.3 percentiles of the magnetic ASD. In some later studies, see Chapters 8 and 11, we will use the shape of the 10% magnetic percentile curve, since it captures the peaks of the Schumann spectrum very well. We then scale the amplitude to match the amplitude of the 95%-percentile curve at 7.8Hz, the first Schumann mode. This gives a good prediction for the Schumann resonance spectrum at Sos Enattos, while being conservative.

7.2 Magnetic coupling function

In the previous section, correlations of magnetic field fluctuations on Earth-scale distances were introduced. Here we will discuss how magnetic fields can couple to the GW sensitive strain channel. We consider two different components. In Sec. 7.2.1 we will discuss the coupling of magnetic fields to the GW sensitive channel based on the magnetic field measured inside the experimental building(s), i.e. the

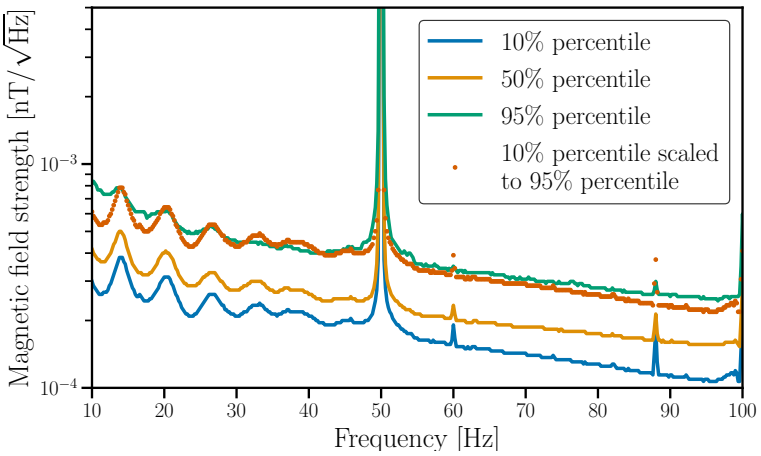

Fig. 7.3.: Sos Enattos magnetic ASD constructed using 48 days of data from Nov 14 2019 to Dec 31 2019. A one-directional magnetometer was employed to collect the data in the mine approximately 200 m below ground level. The line at 50Hz is coming from the power mains.

'inside-to-GW channel' (ITGW) coupling. Afterwards in Sec. 7.2.2, we will focus on the additional effect to project the strength inside the experimental building(s) based on the magnetic fields observed outside. This effect is described by the so called 'outside-to-inside' (OTI) magnetic coupling function which takes into account the shielding or amplification effect caused by the building's structure. As the OTI coupling only describes the effect of the buildings structure, this can be considered as a second order effect. It is represented as a multiplicative factor and has a value close to one, whereas the dominant effect of the magnetic coupling is described by the ITGW coupling. Finally, in Sec. 7.2.3 we will discuss some of the plans for magnetic injections during LIGO, Virgo and KAGRA's fourth observing run.

7.2.1 'Inside-to-GW channel' magnetic coupling function

Magnetic fields can couple to a GW interferometric detector by acting on the permanent magnets of electromagnetic actuators located on the test masses and/or their suspensions [121, 122, 170, 277]. This is typically the dominant effect at low frequencies, where additional coupling might enter by magnetic fields acting on optical components such as suspended benches. The external magnetic field can couple to magnets or other magnetically sensitive components mounted on the bench, leading to an exerted force on the bench. This force results in a movement of the bench which in turn can enhance other noise sources such as scattered light coupling to the detector and affecting the sensitivity [170]. At higher frequencies other mechanisms

(sometimes also specific to a certain interferometer) induce magnetic coupling to the interferometer, such as interaction with signal cables [121, 170].

To measure the coupling of magnetic fields to the interferometer, large magnetic fields are generated during a program of environmental noise injections at the beginning and end of observing runs [277], as well as on a weekly basis [170]. The weekly injections are typically performed at one (fixed) location and aim to measure the time variability of the magnetic coupling, assuming this far-field injection is representative. The pre- and post-run injections probe multiple locations and should give a more accurate understanding of the magnetic coupling, but would be too time consuming to perform every week. A composite or "sitewide" coupling function can be created for these pre- and post-run injections, which uses the largest local coupling for every frequency bin. The magnetic coupling function (κ) is given in Eq. 7.2, with Y and X being respectively the ASD of the GW sensitive channel and the witness sensor during the injection (inj) and an adjacent time without injection (bkg).

$$\kappa(f)_{\text{measured}} = \sqrt{\frac{Y^2_{\text{inj}}(f) - Y^2_{\text{bkg}}(f)}{X^2_{\text{inj}}(f) - X^2_{\text{bkg}}(f)}}, \tag{7.2}$$

The witness sensor of the total magnetic field is the modulus of the magnetic field observed by the three perpendicularly orientated magnetometers. The magnetic coupling of Virgo is shown in Fig. 7.4, for several months observed in the central building (CEB). Also a single injection was performed at the end stations, i.e. the West end building (WEB) and the North end building (NEB), also shown in Fig. 7.4. If the injected field results in an increase of the strain ASD of at least a factor 2 we claim to have measured the coupling, see dots in Fig. 7.4. Otherwise we place an upper-limit on the coupling function, see Eq. 7.3, under the additional condition that the witness sensor detects an effect of at least a factor of 10, as pointed out by stars in Fig. 7.4.

$$\kappa(f)_{\text{upper limit}} = \frac{Y_{\text{bkg}}(f)}{\sqrt{X^2_{\text{inj}}(f) - X^2_{\text{bkg}}(f)}}. \tag{7.3}$$

An in-depth discussion on magnetic injections can be found in [121]. Here we comment on the most important features of the measured coupling function in Fig. 7.4: the low frequency part (up to 100Hz) with a declining slope and the high frequency part (above 100Hz) with a rising slope. The low frequency part is dominated by the coupling of the ambient magnetic field to the small magnets that

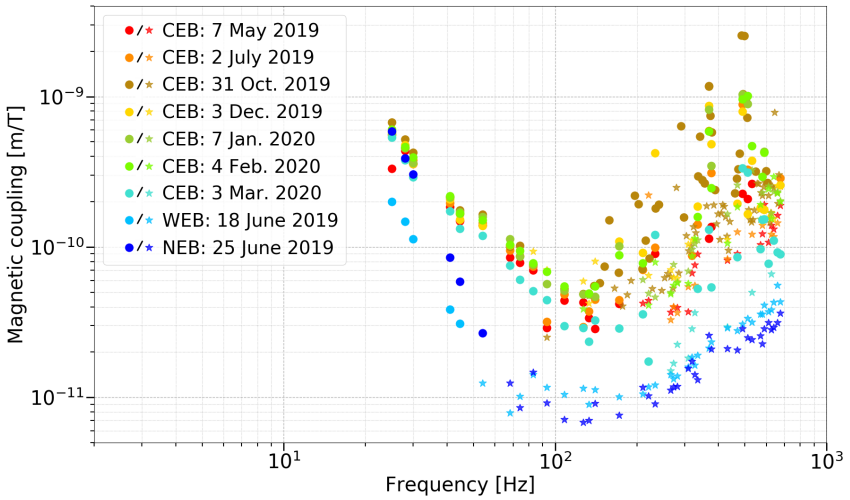

Fig. 7.4.: Magnetic coupling functions for CEB, WEB and NEB. For CEB multiple injections over the time of O3 are shown to illustrate the time variations. Dots are measured values of the magnetic coupling, while stars are upper-limits, calculated using Eq. 7.2.

are attached to the back of each test mass and are used to control the mirror position. The coupling to these magnets is known to decay as the third power of frequency [121]. The measurements at NEB and WEB confirmed the expected behavior, while the magnetic coupling measured in CEB does not follow the same slope. Even if we do not have an exhaustive explanation for this result, it is reasonable to ascribe the enhanced low frequency coupling to other noise sources triggered by the magnetic injection (e.g. scattered light). This mechanism is very likely in the complex environment of the central building, as is discussed in more detail in [170]. This resulted in a significantly stronger coupling from magnetic fields in the Virgo CEB during O3, compared to the WEB and NEB.

At frequencies above several hundreds of Hz, the effect from the injected fields is often not strong enough to be observed in the GW sensitive strain channel. In that case an upper limit of the magnetic coupling function is provided. Note that the upper limits increase as a function of frequency due to the lower amplitude of injected magnetic fields. Namely, the delivered current decreases as a function of frequency, due to the increase of resistance, for a fixed voltage supplied by the amplifier, i.e. near the maximal voltage of the amplifier. While at the LIGO detectors, only upper limits were placed above $\sim$ 200Hz-300Hz, at Virgo it was possible to measure the high frequency coupling during some weeks in the CEB as seen in Fig. 7.4. At these higher frequencies a possible coupling mechanism is the interaction of

the magnetic fields with signal cables [121, 170]. In the WEB and NEB only upper limits were placed. Fig. 7.4 also illustrates the large weekly variations in the central building with a variation of about an order of magnitude depending on the time of the injection.

It is assumed that the injection coil is distant so that the field at a magnetic coupling site is about the same as it is at the magnetometers nearest to the coupling site. The ideal condition would be that of generating a uniform field across the whole interferometer and the witness sensors. The best practical approximation that could be realized at Virgo consisted in one injection coil placed in one corner of the experimental halls and witness magnetometers centrally located with respect to the potentially sensitive components. This places the coil at an approximate distance of $\sim$ 20m from the majority of the sensitive detector components. Deviations from this assumption led to an intrinsic uncertainty of about a factor 2 [277] and will form the dominant uncertainty when making a noise projection in Chapter 8.

7.2.2 'Outside-to-inside' magnetic coupling function

The coupling function discussed above is for magnetic fields measured by magnetometers in the buildings and is referred to as the inside-to-GW channel coupling. The sensitive magnetometers for measuring intersite coherence are located far from the magnetically noisy buildings and the coupling of outside fields to inside fields, is termed the outside-to-inside coupling function.

Previous estimates of this outside-to-inside magnetic coupling function were made using a coil generating magnetic fields outside the central building at LHO [30]. However, the fields generated by the injection coils differ from lightning-generated fields in that the lightning fields are transient on shorter time scales and more uniform over a site. Therefore the outside-to-inside magnetic coupling was measured using the magnetic fields generated by distant lightning strokes[1]. This method is explained in more detail in Appendix A of [214]. A scalar outside-to-inside magnetic coupling function was calculated by M. Ball of the University of Oregon for magnetic fields from lightning for LLO [214]. The distribution was found to be log-normal with a mean of $0.7^{+0.4}_{-0.3}$ nT/nT. Future studies should aim to measure the outside-to-inside magnetic coupling function for lightning fields at the different sites.

[1]The term 'strike' is colloquially used for lightning. However, in the technical literature, 'stroke' describes both cloud-to-cloud and cloud-to-ground lightning. 'Strike' only refers to cloud-to-ground. In the analysis mentioned here both cloud-to-cloud and cloud-to-ground 'strokes' were used [214].

7.2.3 O4 magnetic injection plans

Lessons learned form O3

During O3 a ∼1m diameter magnetic coil was used at Virgo to perform the magnetic injections. To ensure loud enough magnetic injections, a set of sinusoidal magnetic fields were created. This set of lines gives a good overall sense of the magnetic coupling function, but might miss some important, more narrow features. This became clear after the installation of several multi-meter coils at LIGO Hanford during O3 [316, 317]. With these large coils it was possible to perform a broadband injection and several resonant features were observed in the magnetic coupling function, some of which moved in frequency over consecutive weeks [278, 315, 317]. This highlighted the need of similar, improved injection coils at LIGO Livingston and Virgo to gain a more profound understanding of the magnetic coupling at the different sites.

Installation of a 4m-coil at the Virgo central building

The lessons learned from the more detailed magnetic injections at LIGO Hanford lead to the construction of large coils at the key buildings at both the LIGO Livingston [153] and Virgo [211, 212] sites. For Virgo, I was involved in deciding the dimensions and characteristics of the coil in the CEB. The parameters were chosen, such that the new coil – driven with a more powerfull amplifier – would be able to outperform the previously used coil by at least one order of magnitude, enabling more detailed broadband injections.

The 'theoretical' parameters as well as the final parameters are shown in Tab. 7.1. As a comparison the small coil, used during O3, is also shown. As you can see, the predicted magnetic field strength at a distance of 20m is ∼41.5 larger for the new coil compared to the old coil. To calculate the predicted magnetic field we assume that our coil will have a negligible width and our observer to be located at a distance d from the coil, where the connecting line between the observer and the center of the coil is perpendicular to the plane of the coil, i.e. the observer has a 'central' placement with respect to the coil. In this case the magnetic field is given by[2] [186],

$$B(I,d) = \frac{\mu_0 N I}{2} \frac{r^2}{(r^2+d^2)^{3/2}}, \tag{7.4}$$

[2]Please note that in Eq. 5.38 of [186] they only consider one loop. However by using a zero-width coil the net effect is a magnetic field amplification by a factor N, the number of turns.

where μ_0 is the magnetic permeability of the vacuum, N the number of turns of the coil, r the radius of the coil and I the current flowing through the coil.

	Small coil	Large coil	
		Theoretical parameters	Real parameters
Wire area [mm^2]	0.7854	4	4
Wire length [m]	154.88	1366.12	1496.4
Wire material	Copper	Copper	Copper
Number of turns	50	80	86
Shape	Circle	Circle	Rectangle
Height [m]	-	-	4.2
Width [m]	-	-	4.5
(Effective) radius [m]	0.493	2.54	2.45
B(I=1A;d=20m) [T]	$9.54\ 10^{-10}$	$3.96\ 10^{-8}$	$3.96\ 10^{-8}$

Tab. 7.1.: Table summarizing the dimensions of the coils used for magnetic injections in the CEB of Virgo. The last row shows the predicted magnetic field at a distance of 20m from the coil for a current of 1A. In case of the rectangular shaped coil, the effective radius is determined based on the total area of the coil.

At the end of July 2020, this ∼4m large coil was installed at the CEB in Virgo and several test were performed. A first test was to investigate the loss in the strength of the magnetic fields due to the more distant placement of the coil. To this extent we injected a set of magnetic noise lines with the 1m-diameter coil in its original location, used during O3, and just in front of the large 4m-coil. For this injection we used the amplifier used during O3, which is able to deliver ±20V at the output. Based on this test we found that for frequencies below ∼50Hz a factor 4 reduction is observed due to the larger distance. Between 50Hz and 700Hz the reduction is about a factor 2. However we want to note that not only the strength of the magnetic fields, but also their homogeneity matter for the injections. Even though no detailed magnetic map was produced, one could expect the magnetic field to be more homogeneous at the most important coupling locations in the CEB due to the larger separation from the coil.

Afterwards a set of three injections were performed. The first used the 1m-diameter coil with the amplifier used during O3. To make a fair comparison the coil was placed just in front of the new 4m-coil. Secondly, the same amplifier was used to drive the large coil. Even though this amplifier is unable to drive the coil with similar currents as the maximal voltage is fixed, it is a fair comparison of the increased capabilities of the new coil itself. Third and finally we performed an injection with the new coil using a more performant amplifier able to deliver ±40V. During O4 it is foreseen to use an even better amplifier able to deliver ±72V, thus achieving even

Fig. 7.5.: Top: the 1m-diameter, circular coil used for magnetic injections during O3. Bottom: the new coil in Virgo's CEB, planned to be used during O4. Note the wall to which this coil is attached is the same as the wall in the back of the top photo.

stronger magnetic injections. In all three cases we injected broadband noise between 1Hz and 201Hz, above which a slow decrease of injected amplitude occurs.

In Fig. 7.6 we compare the observed magnetic fields in the CEB magnetometers during the times of the injections, as well as a reference time without injection. The distance between the magnetometers and the coil is about 20m-30m. The reference measurement without magnetic fields injected is shown in brown, the magnetic injection with the small coil is shown in green, the one with the large coil and original amplifier in olive green and the injection with the large coil and stronger amplifier in blue. For all three injections we observe an excess in magnetic noise up to $\sim$ 250Hz, which is the most visible in the west-orientated magnetometer due to its lower noise levels. When the large coil is driven with the more powerful amplifier, we even observe increased magnetic noise from the injection up to $\sim$ 350Hz. The peak in injected magnetic field is reached around $\sim$4Hz. At this frequency the large coil outperforms the small coil by an order of magnitude and about a factor 20 when using the stronger amplifier. Around $\sim$60Hz the large coil produces magnetic fields twice as strong as the small coil, when using the same amplifier. For higher frequencies the gain in injection strength with the new coil decreases even further.

Similar, multi-meter coils were constructed in the WEB [180] and the NEB [169].

Measurement of outside-to-inside magnetic coupling

The goal is to make a measurement of the outside-to-inside coupling during O4 at LHO, LLO and Virgo, similar to the measurement at LLO during O3 [214]. Currently discussions are ongoing with Vaisala [140, 273, 311, 355] to get access to their lightning database for this purpose. In case we would have data for the entire O4-run, we could imagine having more detailed studies such as investigating whether there is a direction dependence for the OTI magnetic coupling.

Proposal for the first correlated magnetic injection between LIGO and Virgo

Up to now, the effect of correlated magnetic fields has been studied indirectly by measuring the magnetic coupling at individual detectors. Furthermore, the magnetic fields at the different interferometers are monitored continuously using dedicated magnetometers, located in a magnetically quiet location. By cross-correlating the magnetometer's data and using the coupling measurements from weekly magnetic injections, one can project the expected level of magnetic noise that would show up in the search for an (isotropic) GWB, as we will discuss in detail in Chapter 8.

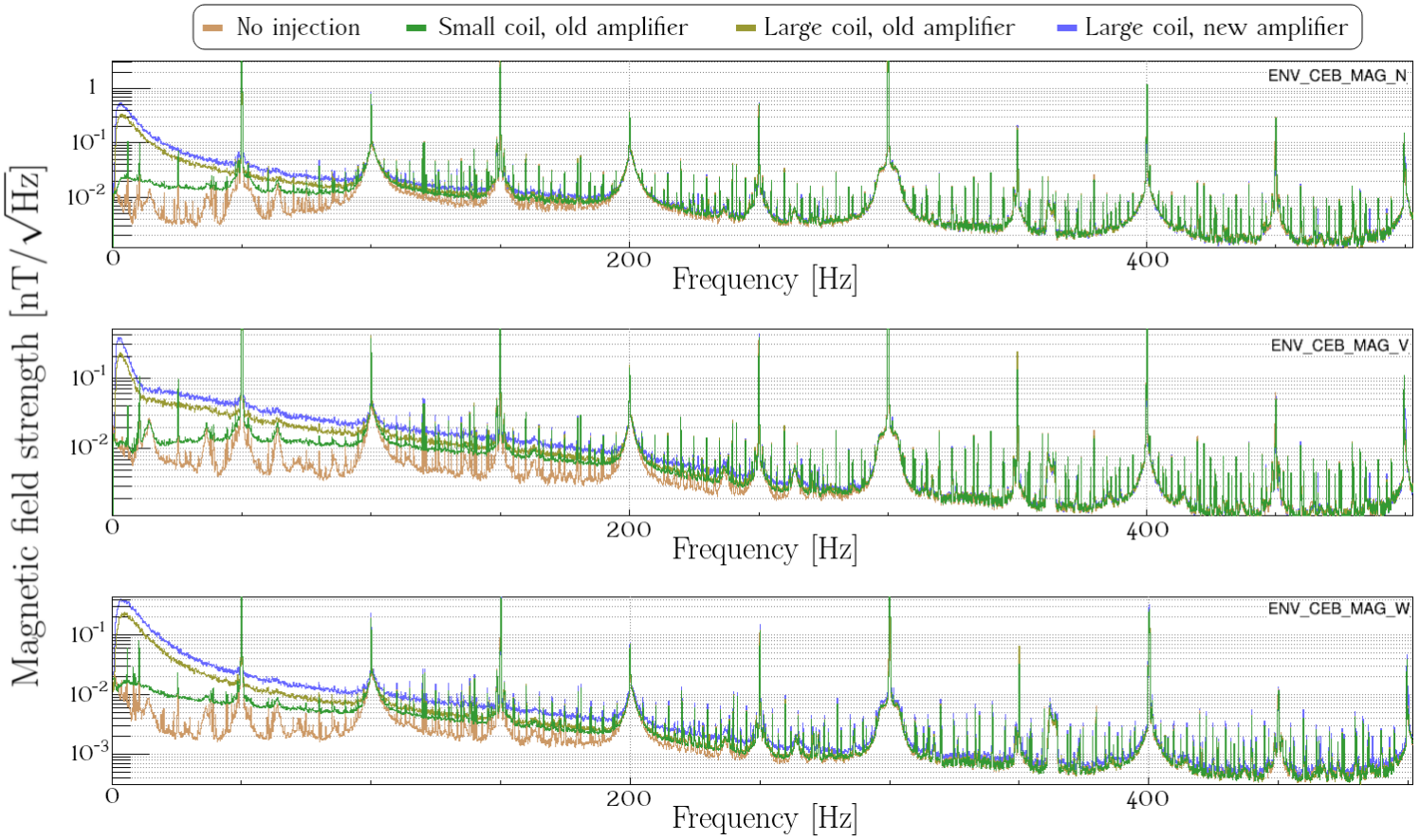

Fig. 7.6.: Observed magnetic field during no injection (brown), a magnetic injection with the small coil, original amplifier (green), large coil, original amplifier (olive green) and large coil and new amplifier (blue). The different panels show the observed magnetic field in the magnetometers with different measurement direction in the CEB, top: North-South (N), middle: vertical (V), bottom: East-West (W)

As proposed within the LVK collaboration [213], we would like to go one step further in understanding how globally correlated magnetic noise can/will impact the search for an isotropic GWB. For O4, we propose to perform a correlated magnetic injection across LIGO/Virgo detectors to directly study the effect of correlated magnetic fields. Over the last decade many methods have been proposed to understand/deal with the impact of correlated magnetic noise, as introduced in Chapter 5, e.g. Wiener filtering, joint Bayesian parameter estimation of the GW signal and magnetic noise and GW Geodesy.

We propose to conduct a correlated magnetic noise injection across LIGO/Virgo observatories, with the following main objectives:

- Gain understanding how correlated magnetic noise would show up in the search for an isotropic GWB.
- Provide the possibility to test the tools created to target correlated noise in a situation where we can use actual data from the interferometers.
- Gain a more fundamental understanding of magnetic coupling. With this injection, we would be able to answer, at least partially, the efficiency of the current set of magnetometers at the observatories in identifying and reducing the effect of globally correlated magnetic fields. This is usually hard to do with just software injections.

Recently, multiple bugs were found in the code to produce the magnetic noise projection for the O3 isotropic search [11]. Despite the thorough review of code and results, this error went unnoticed and currently the stochastic group is in the process of creating a corrected version of the code and an erratum of Fig. 2 of the O3 isotropic collaboration paper [30], i.e. Fig 5.5. The correlated injections proposed here will be an additional method to verify these results and to prevent similar errors during O4 and the future.

Many of the true parameters in the highly complex problem of global magnetic fields and their coupling to the interferometers are known only to a limited precision. The injection proposed here will not try to capture all the complexity of the true problem but rather suggest a minimal set of parameters which we believe can yield the first correlated magnetic injection between the LIGO Hanford, LIGO Livingston and Virgo detectors. Based on the experience and knowledge gained from this injection more elaborate correlated magnetic injections could be envisioned for future observing runs.

A proof of concept injection was performed at LHO and LLO at the end of June 2023 [89, 146]. At both detectors, an identical injection of a 5 minute long, white noise spectrum between 10Hz and 40Hz, was started at a synchronised gps-time. This simultaneous injection was able to successfully inject magnetic fields in a coherent way between the two detectors. Fig. 7.7 and Fig. 7.8 show the coherence, respectively cross spectral density between the magnetic noise observed at each detector. For these spectra we used a single magnetometer at each site, pointing along the x-arm direction and not the quadratic sum, as introduced in Eq. 7.1. The sensor was located in the central building, close to beamsplitter. We observe a fully coherent magnetic injection, with a peak amplitude of $\sim$ 100pT between 10Hz and 20Hz. The injection was also strong enough to be visible in the detector's GW-strain measurement. In the cross-detector strain we observe significant coherence during the magnetic injection as illustrated by Fig. 7.9 and Fig. 7.10. Between 10Hz and 40Hz we observe coherence up to 0.8. No coherence between the strain measurements at LHO and LLO is observed below 10Hz, whereas significant magnetic coherence is observed. The resonant feature in the suspension thermal noise at 10Hz [3] is the likely culprit for the sharp decrease in coherence. At lower frequencies, the injected strength is not strong enough to couple significantly to the measured strain.
Over a large fraction of the frequency band targeted by the injection, we also observe a strain cross spectrum larger by up to factor $\sim$5 compared to times adjacent to the injection. This first, successful attempt at injecting magnetic noise in a coherent way between two GW detectors, separated by thousands of kilometers, illustrates we have the needed infrastructure, both hardware and software.

With the current experience we plan to inject a physically motivated magnetic noise spectrum to test our pipelines for the effect of correlated magnetic noise. More specifically, we aim to conduct one successful correlated magnetic injection during O4, with a duration of around 30 minutes. At least 2 detectors need to be in low noise state at the same time. For this injection we will focus on the frequency band between $\sim$20Hz and $\sim$40Hz, i.e. the third to sixth order Schumann resonances. This frequency band is chosen for its relevance for GWB searches. They typically start their analysis at 20Hz and above 40Hz the expected effect of correlated magnetic noise becomes small due to the lower magnetic coupling at these frequencies. The injected spectrum will be based on the one observed at the Sos Enattos mine, presented in Fig. 7.3. We will use the 10% percentile spectrum scaled to the 95% percentile amplitude as presented in the dark orange. To not overburden the magnetic injection system, the injected spectrum will be tapered off outside the target frequency band, i.e. below 20Hz and above 40Hz. The search for an isotropic GWB typically starts

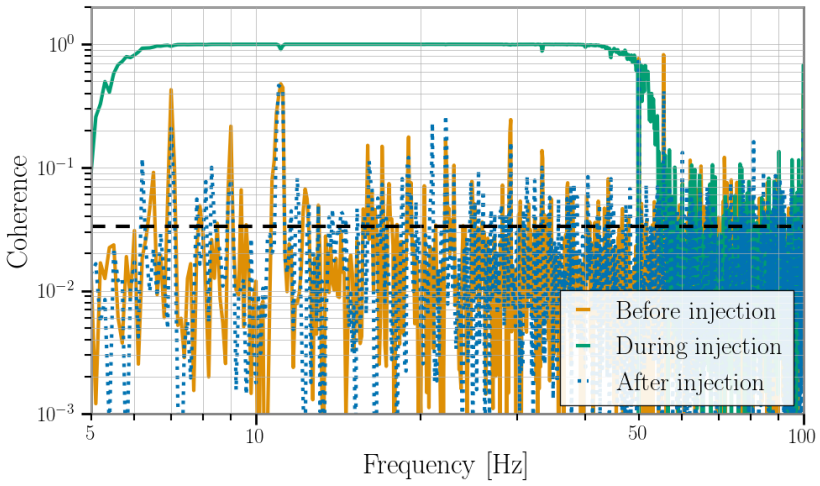

Fig. 7.7.: Coherence spectrum between magnetometers at LHO and LLO. At both sites a single magnetometer was used, pointing along the x-arm of the respective detector. More specifically the used sensors are: H1:PEM-CS_MAG_LVEA_VERTEX_X_DQ and L1:PEM-CS_MAG_LVEA_VERTEX_X_DQ. The coherence is calculated during a five minute window before (orange), during (green) and after (blue, dotted) the magnetic injection. In the absence of correlated noise, one expects this to be consistent with Gaussian noise given by the inverse of the number of averages used to make the coherence spectrum, indicated by the black dashed line.

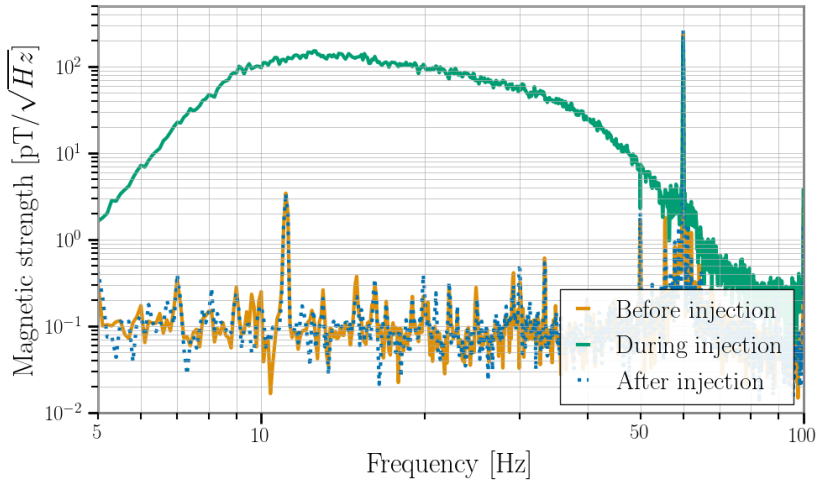

Fig. 7.8.: CSD$^{1/2}$ between a magnetometers at LHO and LLO. At both sites a single magnetometer was used, pointing along the x-arm of the respective detector. More specifically the used sensors are: H1:PEM-CS_MAG_LVEA_VERTEX_X_DQ and L1:PEM-CS_MAG_LVEA_VERTEX_X_DQ. The CSD is calculated during a five minute window before (orange), during (green) and after (blue, dotted) the magnetic injection.

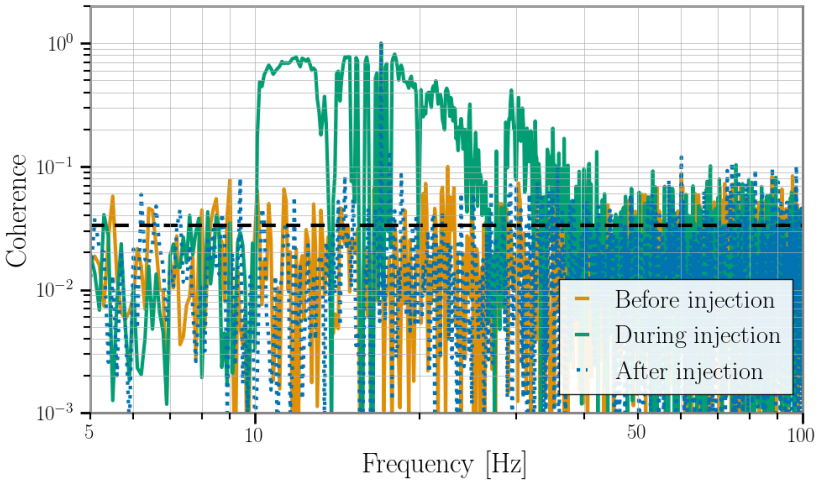

Fig. 7.9.: Coherence spectrum between the observed strain at LHO and LLO. The coherence is calculated during a five minute window before (orange), during (green) and after (blue, dotted) the magnetic injection. In the absence of correlated noise, one expects this to be consistent with Gaussian noise given by the inverse of the number of averages used to make the coherence spectrum, indicated by the black dashed line.

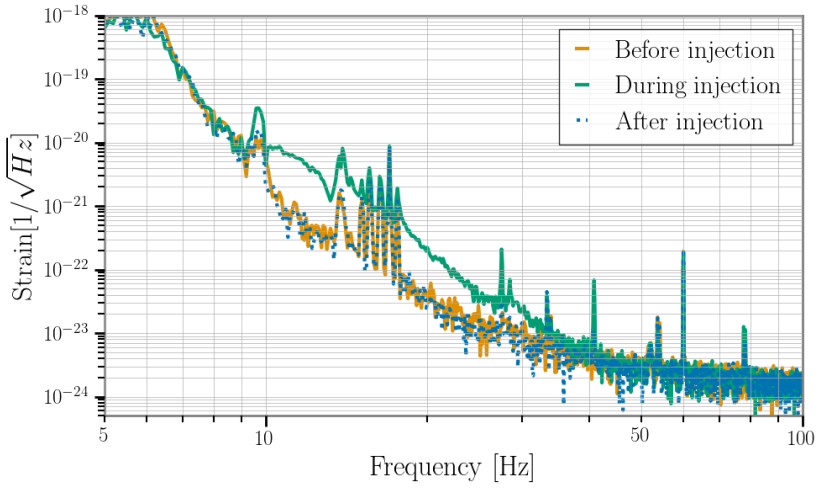

Fig. 7.10.: CSD$^{1/2}$ between the observed strain at LHO and LLO. The CSD is calculated during a five minute window before (orange), during (green) and after (blue, dotted) the magnetic injection.

analyzing data above 20Hz, thus there is no interest from the analysis point of view to also inject magnetic fields at lower frequencies. Above 40Hz, the magnetic coupling will have decreased significantly such that no to minimal effect from the injection is expected, given a realistic injection amplitude. This was also the case for the test injection demonstrated above. Therefore we want to focus the available power of the amplifier in the most relevant frequency region, without diluting the injection by spreading over too large of a frequency band. More concretely, the injected magnetic m_{inj} spectrum will have the following frequency content:

$$\begin{aligned} f < 18\mathrm{Hz} \quad &: \quad m_{\mathrm{inj}} = m_{\mathrm{Schumann}}(18\mathrm{Hz}) * \left(\frac{f}{18\mathrm{Hz}}\right)^{3} \\ 18\mathrm{Hz} < f < 42\mathrm{Hz} \quad &: \quad m_{\mathrm{inj}} = m_{\mathrm{Schumann}}(f) \\ 42\mathrm{Hz} < f \quad &: \quad m_{\mathrm{inj}} = m_{\mathrm{Schumann}}(42\mathrm{Hz}) * \left(\frac{f}{42\mathrm{Hz}}\right)^{-2.5}, \end{aligned} \tag{7.5}$$

where m_{Schumann} is the magnetic spectrum observed at Sos Enattos. Afterwards this spectrum is multiplied by a 32nd order high-pass Butterworth filter with a critical frequency of 16Hz and a 32nd order low-pass Butterworth filter with a critical frequency of 45Hz. In Eq. 7.6 the definition of the Butterworth filter is given with N the order of the filter. If N is positive the produced filter is a low-pass filter, if N is negative $G(f)$ is a high-pass filter. f_{cutoff} is the cutoff frequency of the filter.

$$G(f) = \frac{1}{\sqrt{1 + \left(\frac{f}{f_{\mathrm{cutoff}}}\right)^{2N}}} \tag{7.6}$$

The power law behaviour of the injected spectrum below 18Hz and above 42Hz creates a more smooth transition between the Schumann resonances regime of the injection and the tapering by the Butterworth filters. This spectrum is shown in Fig. 7.11.

Based on this test injection, the amplitude of the final injection was chosen to be 150 times the ambient magnetic spectrum observed. This is about a factor 10 smaller compared to the test injection. This strength was chosen to be as small as possible to cause the least amount of contamination, while still ensuring the signal will be properly recovered by a cross-correlation analysis.

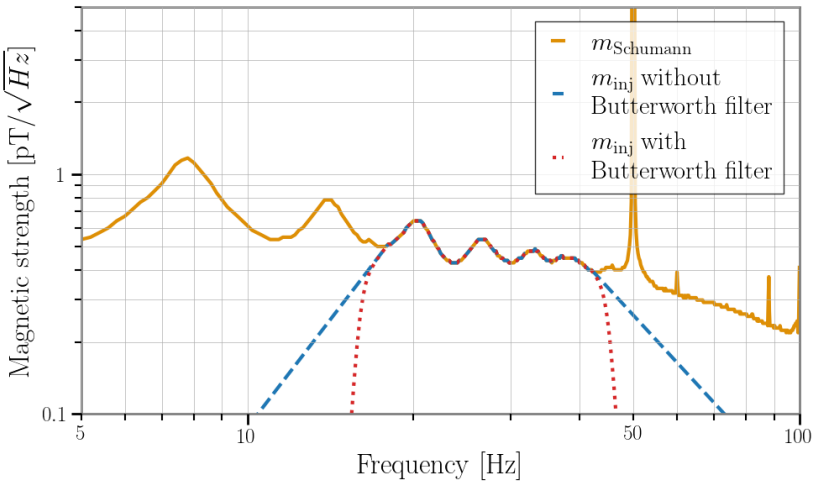

Fig. 7.11.: The magnetic spectrum, m_{inj}, that will be used to inject coherently between multiple GW detectors to test how correlated noise affects GWB pipelines. The spectrum is compared to the Schumann resonance spectrum observed at Sos Enattos (10% scaled to 95% amplitude, see Fig. 7.3). Furthermore m_{inj} is shown both before as well as after applying the 32nd order low- and high-pass Butterworth filters.

7.3 Conclusion

In this chapter we have presented the observed correlations in magnetic field fluctuations on Earth-scale distances ranging from ∼1100km to ∼9000km. This also includes sensors in regions with different levels of lightning activity. We observed significant coherence around the Schumann resonances and also for frequencies above 100Hz. In [214] we show how these observed magnetic correlations are linked to the superposition of individually correlated lightning strikes and in this chapter we illustrated how this hypothesis is supported by the observed coherence spectra. Furthermore we also present observations of the Schumann resonances at the Sos Enattos mine in Sardinia, Italy. The data presented here will be used in the next chapter to understand what the effect of these correlations in the magnetic field fluctuations are on the search for an isotropic GWB.

Afterwards we discussed how magnetic fields can couple to GW interferometric detectors. We present the observed 'inside-to-GW channel' magnetic coupling at Virgo during O3 and briefly highlight the measurement of the 'outside-to-inside' magnetic coupling at LIGO Livingston. These measurements are crucial to understand at which level magnetic fields couple to our detectors and our analysis, which we will calculate in next chapter.

We ended the chapter with a more in-depth discussion of the measurement technique of the inside-to-GW channel magnetic coupling function. To enable more performant injections during future observing runs, we built a larger injection coil at Virgo. We demonstrated how this $\sim$ 4m square coil is able to significantly outperform the previously used coil and facilitates more detailed investigations of the magnetic coupling at Virgo during future observing runs. Finally, we presented results of the first, successful magnetic injection coherent between LIGO Hanford and LIGO Livingston. We also describe the preparation of a physically motivated spectrum to validate the effect of correlated magnetic noise, and more specifically the Schumann resonances, on GWB searches.

8 Impact of magnetic noise on Earth-based interferometric gravitational-wave detectors

Before discussing the effect of (correlated) magnetic noise on Earth-based GW interferometric detectors in this chapter, I briefly highlight the potential interest of future work in the context of atom interferometers. In the past the effect of magnetic noise on atom interferometers was investigated [110, 116, 237]. However, these analyses assumed uncorrelated magnetic field fluctuations. Therefore future work could aim to probe the correlations for magnetic field fluctuations between 0.01Hz and 10Hz and project their impact on atom interferometers.

In this chapter we will combine the information of the last chapter and make predictions at which level the observed correlations of the magnetic field fluctuations can affect the search for an (isotropic) GWB. However, first we will discuss the effect on the detector ASD for Virgo as well as the ET and CE in Sec. 8.1. Afterwards in Sec. 8.2 we will discuss the formalism to project the effect of correlated noise on the search for an isotropic GWB. In Sec. 8.3 we will discuss the impact on the second generation interferometric gravitational-wave detectors LIGO and Virgo. We will also predict the impact of correlated magnetic noise on the ET and derive upper limits on its magnetic coupling function such that search for an isotropic GWB is not affected by it.

8.1 Effect on individual detector amplitude spectral density

The projection of a certain noise source onto the sensitivity of a GW analysis is typically called a noise budget or noise projection. By constructing this noise budget we make predictions at which level these noise disturbances couple to our interferometric detectors. In Sec. 8.1.1 we will discus the magnetic (noise) budget for Virgo's instantaneous sensitivity, i.e. the ASD. In Sec. 8.1.2 we will perform

similar calculations for the ET, however for the ET we will provide upper limits on the coupling function such that the magnetic budget is below the ET's design sensitivity. Finally we will perform the same analysis for CE in Sec. 8.1.3.

8.1.1 Virgo

The noise budget of ambient magnetic noise in the Virgo central area is reported in Figure 8.1. In order to visualize the variability of the ambient fields, projections are computed using the 10%, 50% and 90% percentile ASD of the ambient magnetic noise. We used one week of magnetic data recorded from Feb 10 2020 to Feb 16 2020, i.e. during the second half of the third observing run. The noise budget provides information on the relevance of the ambient noise: if the projected noise is close to the strain ASD it requires immediate attention, otherwise it might become relevant as the detector sensitivity improves. If the noise is at least a factor ten below the target sensitivity it is expected not to contribute significantly and can be given little attention. Examining Figure 8.1, we notice the noise estimate is quite low across most of the frequency band, except for some frequencies where the 90% percentile (or even 50% percentile) has a predicted noise level which is less than a factor of ten below the O3b[1] strain noise. Many of these peaks are located around the mains frequency (50Hz) and harmonics. The effect at 50Hz is however mitigated by an active subtraction. The two peaks at approximately 49.5Hz and 50.5Hz are linked to the mode cleaner building (MCB) electric heater and limits the O3b sensitivity at those frequencies, see top panel of Figure 8.1. A likely pathway for this magnetic noise from the MCB to the CEB is the observed electric current flowing in the mode cleaner pipe.

If no actions are taken, magnetic noise will be limiting the Virgo detector sensitivity at several frequencies in O4 and even more in O5, as visible in Figure 8.1. To minimize the impact of magnetic noise on future observing runs four main activities were planned between O3 and O4. A first intervention was able to succesfully mitigate the noise coming from the current traveling in the mode cleaner pipe [281]. Additional interventions were also planned, as discussed in [170]. This also includes the construction of larger injection coils, as discussed in Chapter 7.

[1] O3b refers to the second half of LIGO's and Virgo's third observing run, O3.

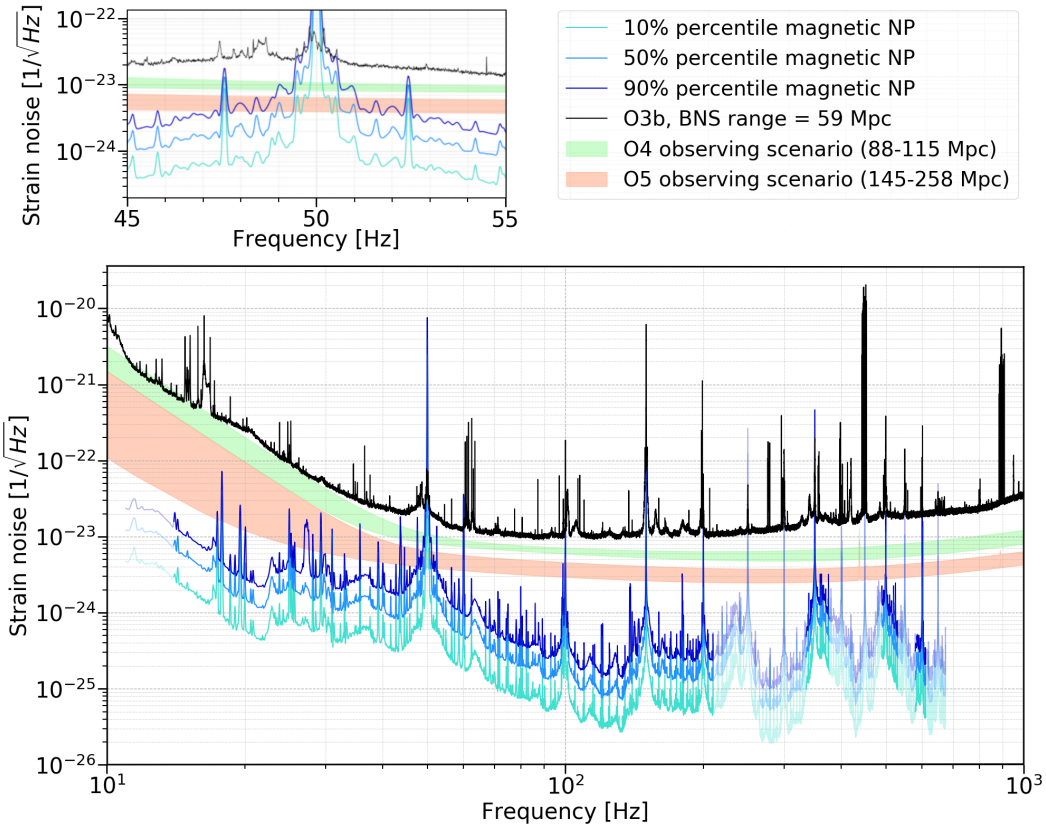

Fig. 8.1.: Noise projection (NP) of ambient magnetic fields in the Virgo central building. The strength of the ambient magnetic field is visualized in the form of percentiles computed over a 1 week period (Feb 10 2020 to Feb 16 2020) with frequency resolution of 0.05Hz. For each frequency at which we determined the coupling function we took the maximal measured value within all injections in the CEB during O3. To produce a continuous noise projection we applied a linear interpolation between frequencies at which magnetic injections were performed. In regions with a partially transparent color, the coupling function only gives an upper-limit. The projected noise (blue shaded curves) is compared with the O3b measured sensitivity (black curve) and with Virgo future observing scenarios, O4 and O5.

8.1.2 Einstein Telescope

We are also interested in the effect of magnetic noise on the ET. Since the ET is still in its design phase, this is a unique opportiunity to provide upper limits on the maximally allowed magnetic coupling κ. To investigate the impact of magnetic noise sources on the ASD of an individual interferometer, we construct what we refer to as the 'ASD upper limit':

$$\kappa_{\mathrm{ET}}^{\mathrm{ASD}}(f) \equiv k \, \frac{P_{\mathrm{ET}}(f)}{P_{\mathrm{mag}}(f)} \, , \tag{8.1}$$

where k is set to be $1/10$ to require any single technical noise contribution to be a factor of 10 lower[2] than ET's ASD, $P_{\mathrm{ET}}(f)$. $P_{\mathrm{mag}}(f)$ is the one-sided ASD of the magnetometers witnessing the local noise of ET, assuming the magnetic noise to be the same for the three individual ET interferometers ET_1, ET_2 and ET_3. If magnetic fields couple significantly at this level, they will limit the expected sensitivity of the interferometer. The 'ASD' upper limit should be investigated to prevent magnetic noise from drastically impacting *all* science goals of the planned GW interferometric detector.
When constructing this upper limit it is placed on the entire magnetic coupling, i.e. the product of the OTI and ITGW magnetic coupling. However, as indicated in Chapter 7, the OTI is described by a multiplicative factor which has a value of $\sim \mathcal{O}(1)$. Therefore, the OTI can be understood as a second order effect and the provided upper limits predominantly concern the ITGW magnetic coupling.

Data

In this analysis we use observed magnetic data. However, since the location and exact positioning of ET is unknown we will estimate $P_{\mathrm{mag}}(f)$ using a variety of observed magnetic spectra that we describe below.

For an estimate of fundamental correlated magnetic noise $\leq$ 100Hz for closely located detectors, we use the magnetic spectrum measured at Sos Enattos, presented in Chapter 7 Fig. 7.3. We use a factor 2 to allow for higher magnetic fields at the final site and to be more conservative, i.e. $P_{\mathrm{mag,ET}}(f) = 2P_{\mathrm{mag,SosEnattos}}(f)$. Here we use the 10% percentile scaled to the 95% percentile curve for $P_{\mathrm{mag,SosEnattos}}(f)$. Further investigations into magnetic noise at Euregio Rhein-Maas and Saxony could help compare the currently proposed sites, but we do not make any statement about which site will be used as the actual location of the ET detector. Site-specific amplifying or reducing ambient magnetic fields are typically a second order effect that can be ignored. However, as shown by measurements at KAGRA, local amplification of ambient magnetic fields may not always be negligible [51, 73]. This amplification has been found to be up to a factor of 10. Recent studies have indicated this amplification is due to a current induced in the 3km long KAGRA beam tube. In close proximity to the beam tube strongly amplified Schumann resonances have been observed [361]. To reduce similar effects Virgo's beam tube is electrically grounded every couple of hundred meters. Also for future detectors one should carefully investigate over which distance scales the beam tube should be grounded.

[2]This is a typical assumption made as there are a large number of 'technical noise sources' not included in the design noise budget.

To get an estimate of fundamental magnetic noise at frequencies above 100Hz, we will use the magnetic CSD observed between magnetometers at LIGO Hanford and LIGO Livingston, as presented in Chapter 7. One should also be aware that the high frequency correlated noise can be larger for detectors near large thunderstorm regions and/or mutual closely located detectors. We assume $P_{\mathrm{mag,ET}}(f) = 2\sqrt{\mathrm{CSD}_{\mathrm{mag,HL}}}$ is a realistic estimation for the ASD of the fundamental environmental magnetic noise at ET. Here $\sqrt{\mathrm{CSD}_{\mathrm{mag,HL}}}$ was shown in Fig. 7.2. Furthermore we include an additional factor of 2 reflecting our uncertainty on the magnetic spectrum.

Finally we also investigate the impact of local magnetic noise. One should study local magnetic noise carefully as this could be a correlated noise source as well because each local corner station for the triangular ET set-up will likely house mirrors for two of the three interferometers (separated by ~ 300m - 500m and in different vacuum tubes [161]). To model local magnetic fields of a GW interferometer, we consider the local magnetic noise measured in the central building at the Virgo site [170]. We use the 90% magnetic percentile of data collected between Feb 10 2020 and Feb 16 2020 - during the second half of the third observing run, O3b. This spectrum is quite similar to the one observed in the Virgo CEB during O2 [121] and it relies on the same data as used in Fig. 8.1.

We assume the local noise at Virgo is a realistic estimation for the local magnetic noise at ET, where we include an additional factor of 2 reflecting our uncertainty on the magnetic spectrum: $P_{\mathrm{mag,ET}}(f) = 2P_{\mathrm{mag,V_{CEB}}}(f)$.

Results

In our analysis, we use two design sensitivities, called $\mathrm{ET-B}$ and $\mathrm{ET-D}$ [200, 201]. These sensitivity curves have become deprecated between publishing these results in [218] and writing this PhD dissertation. The ASD sensitivity curves of the different designs are shown in Fig. 2.7 and their PI sensitivity to a GWB in Fig. 4.1. As mentioned in Chapter 2 the latest sensitivity curves are HFLF-cryo (almost identical to ET-D) and HF-only, which has a considerably worse low frequency sensitivity compared to ET-B. In this chapter we will present the results as they were presented in [218], where in the discussion of the results we will briefly highlight how the results and conclusions change in light of the latest sensitivity curves HFLF-cryo and HF-only. The figures using the updated sensitivities HFLF-cryo and HF-only are presented in Appendix B.

The upper limits presented here assume the reduction of the magnetic coupling is the only pursued method to prevent magnetic fields from coupling significantly to the interferometer. Methods such as the use of Wiener filters [134], as discussed in Chapter 5, could also be used to reduce the effects of correlated magnetic noise. However, the best strategy for ET will be to design the magnetic isolation to be as good as possible.

In Fig. 8.2 we show limits on the coupling imposed by our target sensitivity measures. This also contains limits placed on the magnetic coupling function such that there is no effect on the search for a GWB, $\kappa^{\mathrm{GWB}}_{\mathrm{ET}-D}(f)$. The method to calculate these upper limits, $\kappa^{\mathrm{GWB}}_{\mathrm{ET}-D}(f)$, will be introduced and discussed in Sec. 8.3. The $\kappa^{\mathrm{ASD}}_{\mathrm{ET}-D}(f)$ limits are denoted by the dash-dotted yellow curve. As a comparison we show the average coupling measurements made at Virgo [122, 170], LIGO Hanford and LIGO Livingston [139, 263, 276, 278] during the O3 run, indicated by the large green circles, small orange circles, and magenta stars respectively. Please note that the magnetic coupling measurements only start from 11Hz, 9Hz and 7Hz for respectively the Virgo, LIGO Hanford and LIGO Livingston interferometers. Based on the results

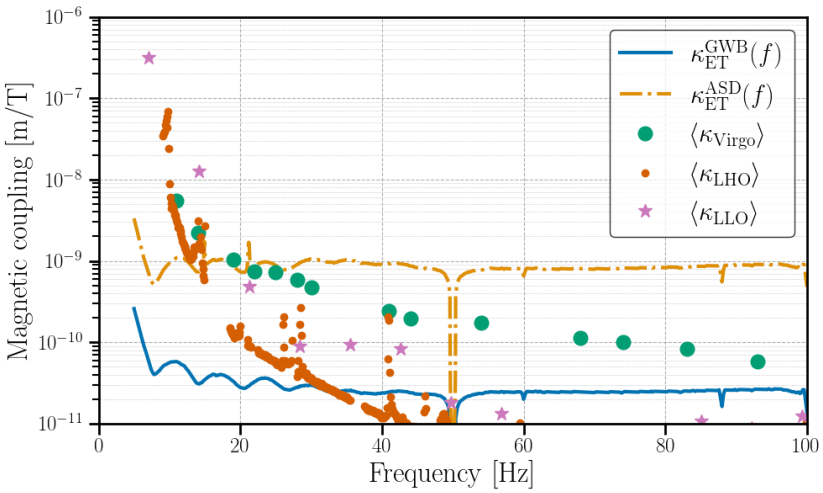

Fig. 8.2.: 'ASD' and 'GWB' magnetic coupling function upper limits for the ET $- D$ design sensitivity. Also included are the average of the weekly measurements of the coupling functions at LIGO Hanford, LIGO Livingston and Virgo during the O3 run for comparison.

in Fig. 8.2 we can conclude that between $\sim$ 15Hz and 20Hz a modest improvement in the magnetic coupling is needed with respect to LLO and Virgo. LHO has already a sufficiently low magnetic coupling in this frequency region. However below $\sim$ 15Hz significant improvements of up to two orders of magnitude and more, are needed to prevent the coupling of fundamental, environmental magnetic noise to have an effect on the ET's instantaneous sensitivity.

We notice that the upper limit on the magnetic coupling at certain frequencies is allowed to be greater than the magnetic coupling at current observatories[3], for example $\gtrsim 30$Hz in the $\kappa^{\rm ASD}_{{\rm ET}-D}(f)$ curve in Fig. 8.2. This means that one can be less concerned about Schumann resonance magnetic noise coupling into ET as compared to LIGO/Virgo detectors. The reason for this result can be seen by considering the difference between the magnetic coupling measured in units of $[{\rm T}^{-1}]$ [4] and in units of $[{\rm m\ T}^{-1}]$. The latter takes into account the arm-length of the interferometer, $L_{\rm arm}$,

$$\kappa[{\rm T}^{-1}] = \frac{\kappa\,[{\rm m\ T}^{-1}]}{L_{\rm arm}[m]}\ . \tag{8.2}$$

Since ET is planned to have a 10 km arm-length, instead of 4 km (LIGO) or 3 km (Virgo), the test masses displacements due to magnetic effects measured in the units $[{\rm m\ T}^{-1}]$ is allowed to be larger compared to existing interferometers. Furthermore, the Schumann resonances are currently not coupling significantly to existing interferometers with the observed magnetic coupling functions.

For the magnetic coupling above 100Hz, we do not show the upper limits calculated using the 'ASD' formalism, Eq. 8.1, since these limits are less stringent than the measured magnetic coupling at present day interferometers. Instead, in Fig. 8.3 we show the improvement needed in the magnetic coupling function when comparing the average magnetic coupling functions for LHO, LLO and Virgo. In the top panel of Fig. 8.3 we present the results ≤ 100Hz, whereas the bottom panel focuses on frequencies ≥ 100Hz. In line with the better low frequency sensitivity for the ET-D design compared to the ET-B configuration, an additional order of magnitude of reduction in the magnetic coupling is needed for ET-D compared to ET-B below $\sim$ 10Hz. That is one to two (two to three) orders of magnitude in improvement are needed to achieve the ET-B (ET-D) design sensitivity below $\sim$ 10Hz. Above $\sim$ 20Hz to 30Hz, no effect from fundamental magnetic noise is expected to impact significantly the ET's ASD, regardless of design. The conclusion concerning ET-D is directly transferable to the HFLF-cryo design due to their almost identical sensitivity. HF-only has a sensitivity which is a factor 3-4 times worse compared to ET-B between 7Hz and 9Hz, which are the lowest frequencies probed in the magnetic coupling function measurements at LLO and LHO. Therefore the needed improvement for HF-only will be less stringent by these factors compared to the ones stated for ET-B in Fig. 8.3. The results presented in Fig. 8.3 also imply that up to $\sim$ 15Hz the

[3] Above 100Hz the weekly measurements of the magnetic coupling are often upper limits rather than an actual measurements. However during some periods of 'extreme' magnetic coupling such high values are actually measured as well [170].

[4] The unit of magnetic coupling function $[{\rm T}^{-1}]$ is often referred to as [strain ${\rm T}^{-1}$].

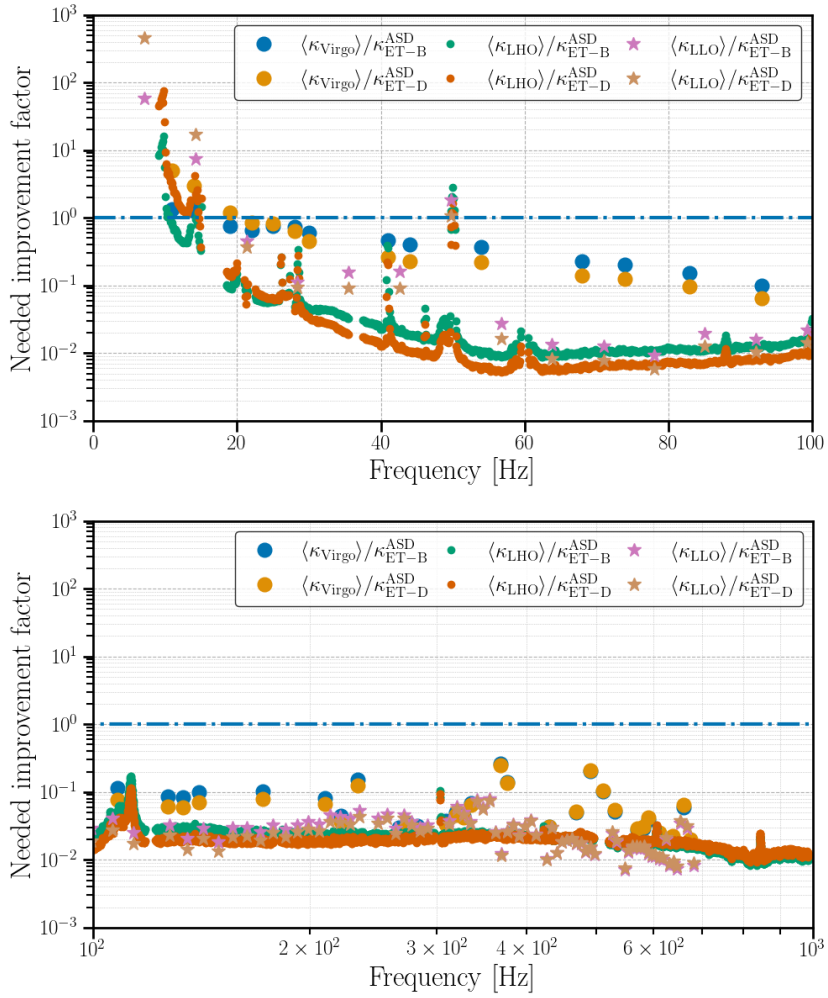

Fig. 8.3.: Needed improvement factor as a function of frequency for the 'ASD' upper limits on the ET magnetic coupling function. The low-frequency (top panel) magnetic coupling poses a greater challenge for the operation of ET compared to the high-frequency (bottom panel) magnetic coupling. In both panels, the dash-dotted blue line indicates the line where no improvement is necessary.

HFLF-cryo design will barely be able to improve upon the HF-only design in case one is unable to deal with the excess in magnetic coupling.

Finally, if one is unable to reduce the effect from local magnetic fields originating from e.g., used infrastructure, local magnetic noise sources will dominate the fundamental magnetic noise discussed above. This leads to the most stringent coupling upper limits, reported in Fig. 8.4. To construct these upper limits the magnetic noise as observed in the Virgo central building is used. This represents a realistic magnetic environment in present-day interferometers, however that does not have to be the case for the ET. Possible methods to reduce the magnetic noise from detector infrastructure could be to use (extremely) low noise devices, place them as far

away as possible from coupling sensitive components or try to shield the potentially offending noise sources.

Below $\sim$ 30Hz, the instantaneous detector sensitivity will be limited by magnetic noise if the coupling is not reduced below the current day magnetic coupling of Hanford, which is already significantly smaller compared to the coupling measured at Livingston and Virgo. These upper limits are about one order of magnitude

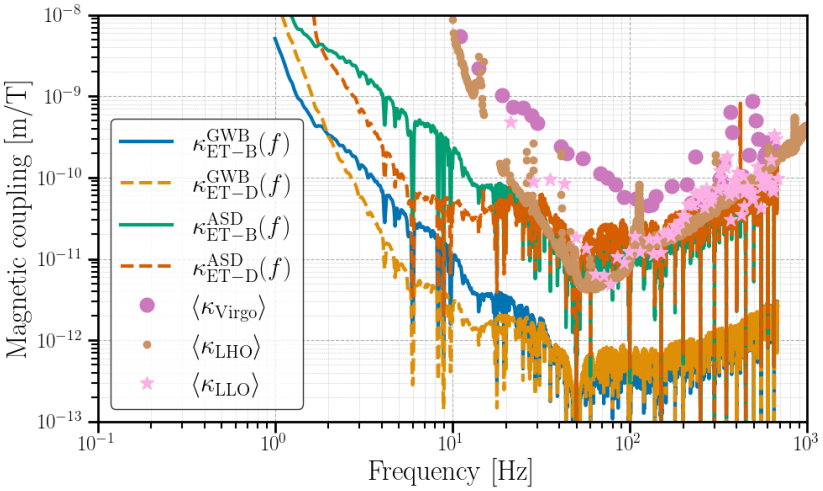

Fig. 8.4.: 'ASD' and 'GWB' magnetic coupling function upper limits of the ET-B and ET-D design sensitivities in the case the local magnetic noise is the same level as the CEB at Virgo during O3. Also included are the average of the measurements of coupling functions at LIGO Hanford, LIGO Livingston and Virgo during the O3 run for comparison.

more stringent compared to the previous upper limits, since the magnetic noise observed in the CEB of Virgo is about a factor ten larger compared to the ambient environmental noise. In this pessimistic noise scenario, the HFLF-cryo design would not improve upon the HF-only design as they both will be dominated by magnetic noise in the low frequency region.

8.1.3 Cosmic explorer

Please note that the results presented in this subsection have not (yet) been published, nor peer reviewed. However the same methodology was used as for the results for the ET presented in Sec. 8.1.2, which were peer-reviewed and published in [218].

Since there was no magnetic contamination in the high frequency region (>100Hz) for the ET, and CE has a similar strain sensitivity, we will only investigate the potential effect of magnetic noise on the low frequency region (<100Hz) for CE.

To this extent we consider the same data as in previous section, i.e. $P_{\mathrm{mag,CE}}(f) = 2P_{\mathrm{mag,SosEnattos}}(f)$, where we use the 10% percentile scaled to the 95% percentile curve for $P_{\mathrm{mag,SosEnattos}}(f)$. As for CE's sensitivity we consider both the (nominal) 40km and 20km design sensitivity [335].

In Fig. 8.5 we show the needed improvement in magnetic coupling such that magnetic noise is a factor 10 lower than CE's design sensitivity, as explained in previous section. First we would like to point out that the difference in magnetic coupling between the 20km and 40km design is minimal as the dominant gain in sensitivity between the two designs is the increase in distance. However, as shown in Eq. 8.2 the magnetic coupling in units of T^{-1} (sometimes also referred to as 'strain T^{-1}') also scales with the arm length. Furthermore, the other designs considered in [335] such as 'post-merger' or 'low frequency' tuned detectors all have similar sensitivities in the frequency range where magnetic noise is important, i.e. below $\sim$ 15Hz. We find that below 10Hz, the magnetic coupling of CE should be one to two orders of magnitude better compared to the magnetic coupling of second generation detectors to prevent an effect of fundamental magnetic noise. A smaller effect is present up to $\sim$ 15Hz.

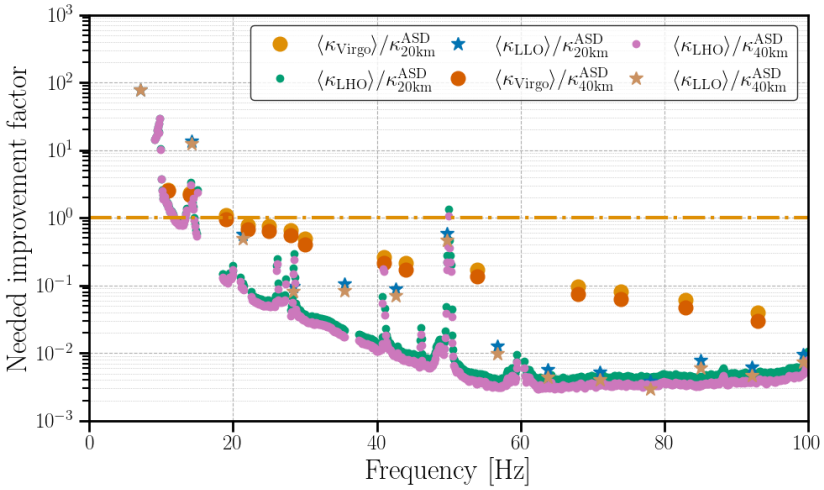

Fig. 8.5.: Needed improvement factor as a function of frequency for the 'ASD' upper limits on the CE magnetic coupling function. The dash-dotted orange line indicates the line where no improvement is necessary. We have used the 40km and 20km design sensitivities as presented in [335] and which are accessible in [233].

For CE we will not present the impact of infrastructural noise. However as indicated in previous section, this makes the upper limits on the magnetic coupling function more stringent by one order of magnitude assuming the observed magnetic noise at Virgo's CEB.

8.2 Formalism to predict impact of correlated noise on the search for an isotropic gravitational-wave background

8.2.1 Noise budget formalism

Equivalent to the cross-correlation statistic (Eq. 4.11) one can construct a magnetic cross-correlation statistic [346, 348]

$$\begin{aligned} \hat{C}_{\mathrm{mag},IJ}(f) &= |\kappa_I(f)||\kappa_J(f)|M_{IJ}, \\ \text{where } \; M_{IJ} &= \frac{\mathrm{CSD}_{\mathrm{mag},IJ}}{\gamma_{IJ}(f)S_0(f)} \; , \end{aligned} \tag{8.3}$$

where $\kappa_I(f)$ is the magnetic coupling function, as introduced in Chapter 7. $\mathrm{CSD}_{\mathrm{mag},IJ}$ is the magnetic cross spectral density between the two sites I and J. In case we would use an equivalent definition as Eq. 4.11, this would imply

$$\mathrm{CSD}_{\mathrm{mag},IJ} = \frac{2}{T}\mathrm{Re}\left[\tilde{m}_I^*(f)\tilde{m}_J(f)\right], \tag{8.4}$$

where $\tilde{m}_I(f)$ is the Fourier transform of the time domain data $m_I(t)$ measured by a magnetometer at site I. T is the duration of the segments used when Fourier transforming the magnetic data. However to yield a conservative estimate we will be taking the modulus of the Fourier transform rather than only the real part. Furthermore we will also take into account the contributions of the different CSD's coming from the two magnetometers at each site which are needed to fully characterize the horizontal magnetic field[5] at a given site. Therefore we will use the quadratic sum of the different pairs, as was introduced in Eq. 7.1. This approach is different from what was done by the LVK collaborations during O3, where they only used the real part of one, the most conservative, sensor pair [30].

When analysing data in search of an isotropic GWB, one typically constructs the magnetic cross-correlation statistic $\hat{C}_{\mathrm{mag},IJ}(f)$ to investigate if the observed magnetic fields might result in correlated noise in the analysis. The magnetic coupling functions $\kappa_I(f)$ are the product of the outside-to-inisde and inside-to-GW channel magnetic coupling functions.

[5] The vertical magnetic field component is negligible for 'distant' lightning strikes as well as for the Schumann resonances.

Similar to the budget presented in [30] the three separate magnetic budgets for each baseline are combined weighting them by the sensitivity of the respective baseline to a GWB:

$$\begin{aligned} \hat{C}_{\mathrm{mag}} &= \sum_{IJ} w_{IJ}(f)\hat{C}_{\mathrm{mag},IJ}(f), \text{ where} \\ w_{IJ}(f) &= (\sigma_{IJ}(f)/\sigma(f))^{-2} \text{ and} \\ \sigma^{-2} &= \sum_{IJ} \sigma_{IJ}^{-2}. \end{aligned} \tag{8.5}$$

This weighting method was first proposed in [267]. Given that the HL-baseline is the most sensitive pair to GWs, its magnetic budget will dominate the total budget which we present in Sec. 8.3, except around the zeros of its GW overlap reduction function.

8.2.2 Error propagation for the noise budget

In the budget we want to combine the multiple different baselines by weighting them with respect to their importance for the GWB search as introduced in Eq. 8.5. The sum runs over the different baseline pairs and the definition of $C_{\mathrm{Mag},IJ}(f)$ was introduced in Eq. 8.3. We know that the coupling function can be divided in two components as follow,

$$\kappa_I(f) = \kappa_{I,\mathrm{OTI}}(f) \cdot \kappa_{I,\mathrm{ITGW}}(f), \tag{8.6}$$

where we have used the abbreviations OTI and ITGW for outside-to-inside and inside-to-GW channel respectively, as introduced in Chapter 7.

For the calculation of the errors we will assume all quantities are exactly known apart from the coupling functions, i.e. $s_{\mathrm{CSD}_{IJ}} = 0$, $s_{\gamma_{IJ}} = 0$, $s_{S_0} = 0$ and $s_{w_{IJ}} = 0$. The outside-to-inside coupling has only one uncertainty, whereas the inside-to-GW channel has an uncertainty due to the measurement and location of witness sensors ($s_{\mathrm{intrinsic}}$) as well as due to the weekly variation (s_{weekly}).

$$s_{\kappa_{I,\mathrm{ITGW}}}(f) = \sqrt{s_{\mathrm{weekly,I}}(f)^2 + s_{\mathrm{intrinsic,I}}(f)^2} \tag{8.7}$$

The error on the total coupling function becomes

$$\begin{aligned} s_{\kappa_I}(f) = \Big[& s^2_{\kappa_{I,\mathrm{OTI}}}(f) \cdot \kappa^2_{I,\mathrm{ITGW}}(f) + \\ & s^2_{\kappa_{I,\mathrm{ITGW}}}(f) \cdot \kappa^2_{I,\mathrm{OTI}}(f) \Big]^{1/2} \end{aligned} \tag{8.8}$$

The error on $\hat{C}_{\mathrm{mag},IJ}(f)$ is given by,

$$s_{\hat{C}_{\mathrm{mag},IJ}}(f) = \left[s^2_{\boldsymbol{\kappa}_I}(f) \left(\frac{\hat{C}_{\mathrm{mag},IJ}(f)}{\boldsymbol{\kappa}_I(f)} \right)^2 + s^2_{\boldsymbol{\kappa}_J}(f) \left(\frac{\hat{C}_{\mathrm{mag},IJ}(f)}{\boldsymbol{\kappa}_J(f)} \right)^2 \right]^{1/2} \tag{8.9}$$

Finally for the combined budget including all baselines we get the following error

$$s_{\hat{C}_{\mathrm{mag}}}(f) = \sqrt{\sum_{I,J} w^2_{IJ}(f) \cdot s^2_{C_{\mathrm{Mag},IJ}}(f)}, \tag{8.10}$$

The weekly measurements of the inside-to-GW channel magnetic coupling functions at the central building of LIGO Hanford, LIGO Livingston and Virgo were used to compute the geometric standard deviation. This standard deviation is a good measure of the uncertainty introduced by the time variability of the coupling functions. As a figure of merit we present the geometric standard deviation for each baseline, averaged across the entire frequency range,

$$\begin{aligned} \langle s_{\mathrm{weekly},H} \rangle &= 1.4 \cdot \boldsymbol{\kappa}_{H,\mathrm{ITGW}}(f) \\ \langle s_{\mathrm{weekly},L} \rangle &= 1.3 \cdot \boldsymbol{\kappa}_{L,\mathrm{ITGW}}(f) \\ \langle s_{\mathrm{weekly},V} \rangle &= 1.6 \cdot \boldsymbol{\kappa}_{V,\mathrm{ITGW}}(f). \end{aligned} \tag{8.11}$$

However since there is a non negligible amount of frequency variability, the frequency dependent error will give the most accurate results.

The other errors that will be used for the noise budget in Sec. 8.3 are

$$\begin{aligned} s_{\mathrm{intrinsic},I}(f) &= 2 \cdot \boldsymbol{\kappa}_I(f), \\ s_{\mathrm{OTI},+} &= 0.4, \\ s_{\mathrm{OTI},-} &= 0.3. \end{aligned} \tag{8.12}$$

8.2.3 Placing upper limits on the magnetic coupling function

Above, we discussed how $\hat{C}_{\mathrm{mag}}$ can be calculated for LIGO and Virgo based on the measurements of the magnetic cross correlation $\mathrm{CSD}_{\mathrm{mag}}$ and the magnetic coupling functions $\boldsymbol{\kappa}_I$, $\boldsymbol{\kappa}_J$. Here we will consider a different approach: given a desired sensitivity, i.e. the design sensitivity of the ET, and a magnetic spectrum $\mathrm{CSD}_{\mathrm{mag}}$, we estimate the maximal allowed magnetic coupling function $\boldsymbol{\kappa}_{\mathrm{ET}}(f)$ such that ET will

not be limited by this magnetic noise, in line with what we did for the ASD upper limits in Sec. 8.1.2

To ensure that magnetic noise does not obstruct the isotropic search for a GWB, we construct an upper limit on the magnetic coupling function that we label 'GWB', in the following way. We use Eq. 8.3 and take the upper limit for the magnetic cross-correlation $\hat{C}_{\mathrm{mag,ET_1ET_2}}(f)$ to be the 1σ-PI sensitivity curve – $\Omega^{\mathrm{PI}}_{\mathrm{ET_1ET_2}}$ – after one year of taking data:

$$\kappa^{\mathrm{GWB}}_{\mathrm{ET}}(f) \equiv \sqrt{\frac{\Omega^{\mathrm{PI}}_{\mathrm{ET_1ET_2}}}{M_{\mathrm{ET_1ET_2}}}} \,. \tag{8.13}$$

To make full use of ET's capabilities when searching for an isotropic GWB, one should use $\kappa^{\mathrm{GWB}}_{\mathrm{ET}}(f)$. On the contrary, to find the level at which magnetic fields might directly impact the instantaneous sensitivity achieved by ET, then $\kappa^{\mathrm{ASD}}_{\mathrm{ET}}(f)$, as introduced in Sec. 8.1 is the relevant measure.
As before, these upper limits are predominantly related to the ITGW magnetic coupling as the OTI magnetic coupling is a second order effect which has a value of $\sim \mathcal{O}(1)$.

8.3 Effect from correlated magnetic noise on searches for an isotropic gravitational-wave background

In this section we will study the impact of the Schumann resonances as well as from the (superposition of) individual lightning strokes on the search for an isotropic GWB. In Sec. 8.3.1 we start by describing the effect on second generation detectors LIGO and Virgo, whereas in Sec. 8.3.2 we describe the effect on the ET.

8.3.1 LIGO and Virgo

The method we will use to construct the magnetic budget, as presented in Sec. 8.2, is different from the budget presented by the LIGO, Virgo and KAGRA collaborations in their search for an isotropic GWB [30]. There are four main differences, the first being the larger frequency range from 20Hz to 675Hz which is the entire frequency range having regular measurements of the inside-to-GW channel magnetic coupling at all three sites. A linear interpolation as a function of frequency is performed. Secondly, the LVK collaborations used the magnetic spectrum obtained from one (the

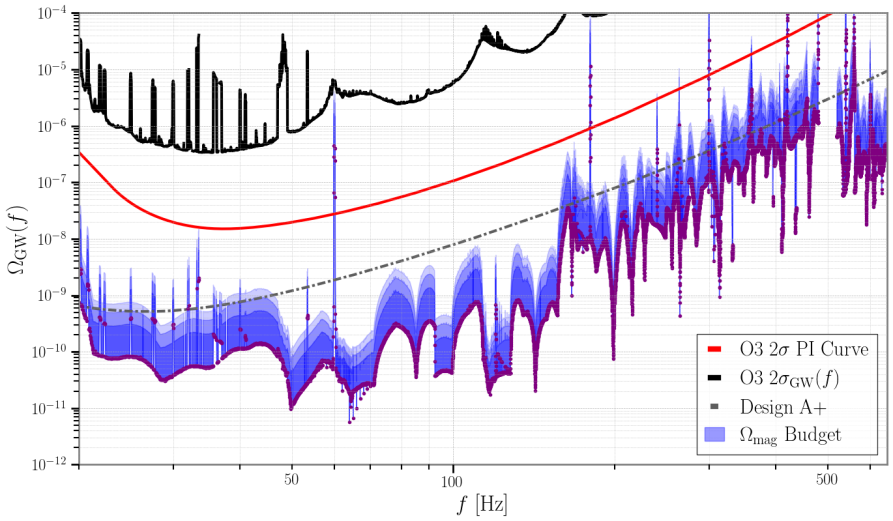

Fig. 8.6.: Magnetic noise budget represented by the blue band. The purple dots represent the budget without any errors included. The dark and lighter blue bands represent the upper 1σ-3σ uncertainty as described in Sec. 8.2.2. No error is included for the weekly variation, however as explained in the text this effect was found to be minimal. The lower errors are not shown in this figure since the error propagation as described in Sec. 8.2.2 leads to negative lower limits. Also represented are the O3 sensitivity for narrowband features for an isotropic GWB, given by its standard deviation $\sigma(f)$; the O3 broadband sensitivity, given by its power-law integrated (PI) curve (red); and the broadband sensitivity expected to be reached with the LIGO A+ and Advanced Virgo Plus network, Design A+ (grey dot-dashed).

worst) pair e.g. $\mathrm{Re}[\tilde{m}^*_{I_2}(f)\tilde{m}_{J_1}(f)]$ [30], whereas here we use the more conservative CSD_{IJ}, combining the modulus for all four CSD-pairs for one baseline. In [30], an additional factor of 2 is included because of their choice of one single direction compared to the total CSD. Thirdly, in [30] they use an approximate outside-to-inside transfer function of 1, based on measurements made using injection coils at LHO. Here we will use the measurement for LLO described in Chapter 7, based on lightning-generated magnetic fields instead of coil-generated fields, with a resulting value of $0.7^{+0.4}_{-0.3}$. For the budget we will assume both LHO and Virgo have the same outside-to-inside coupling function as LLO. In the future dedicated studies at the other sites should give accurate site-dependent measurements. Fourth and finally, in [30] they used the weekly magnetic coupling measurements at each site and computed a budget for every week of O3. Here we will rather use the sitewide coupling functions measured for LHO and LLO since they are more conservative. For Virgo we will use the average of the weekly measurements in the central building, which has the largest coupling. A downside of the sitewide coupling with respect to the weekly measurements is that for LHO the frequency resolution is worse compared to the resolution of the weekly injections.

The purple dots in Fig. 8.6 represent the noise budget, without taking any errors into account. The darkest and lighter blue bands respectively indicate the upper 1σ, 2σ and 3σ uncertainties. No lower errors are shown, since they are found to be negative. In Sec. 8.2.2 the error propagation of the budget is discussed in detail. This includes the uncertainty of the outside-to-inside coupling as well as a factor 2 of uncertainty related to inside-to-GW channel magnetic coupling function, given the limitations of the inside-to-GW channel coupling function measurement [277]. The variation of the weekly measurements was observed at the central building of each site. However the sitewide coupling functions used for LHO and LLO rely on measurements from different physical locations, which were only performed at the start and end of O3. Given there is no guarantee that these other coupling locations have the same weekly variation, no error for the weekly variation was taken into account. The weekly variation was measured, as described in Sec. 8.2.2, and was found to have a minimal effect on the budget presented in Fig. 8.6. Ideally, the weekly variation of the sitewide coupling would also be measured in the future such that this error can be taken into account, even if the impact is small.

We want to point out that much of the topology of the budget is due to the limited frequency resolution of the measured coupling function and the linear interpolation between points. The peaks and dips near 50Hz and above are a clear example. Ideally, future measurements of the inside-to-GW channel magnetic coupling function would have finer frequency resolutions. This is being addressed at LHO, LLO and Virgo by installing much larger injection coils to produce larger fields so that broadband injections can be made, as was discussed in Chapter 7.

We conclude that there was no magnetic contamination in the search for an isotropic GWB during O3, which is consistent with the lack of an observation of any excess in the search for an isotropic GWB [30]. This conclusion was also reached based on the magnetic budget by the LVK collaborations in the frequency range 20Hz - 100Hz [30], i.e. Fig. 5.5. Note that the difference of about an order of magnitude in the predicted effect of magnetic fields is due to an error found in the code used to produce Fig. 5.5, rather than the different approach used for calculating the budget. An erratum to [30] is in preparation.
Also at frequencies between 100Hz - 675Hz, there was no magnetic contamination, neither narrowband, nor broadband. Concerning narrowband magnetic contamination, one should compare the upper range of the magnetic budget and its narrow features with the standard deviation of the search for an isotropic GWB $\sigma(f)$. We note that the loudest peaks (60Hz and harmonics) linked to the US power mains are excluded from the analysis [30]. The blue band of the magnetic budget being below

the powerlaw integrated sensitivity curve (red line) implies there is no broadband magnetic contamination.

If the correlations from the magnetic field fluctuations, both amplitude and frequency behavior, as well as the magnetic coupling (outside-to-inside as well as inside-to-GW channel) remain the same for future observing runs, there is a possibility that magnetic contamination might affect the search for an isotropic GWB when LIGO and Virgo reach the A+ [20] and AdV+ [20] sensitivities respectively. These sensitivities are planned to be reached later this decade. For Fig. 8.6 we used a PI-curve with an observation period of 1 year and a duty cycle of 100% and SNR=2. Up to $\sim$50Hz, the 2σ budget contour touches the PI curve indicating there is a non-negligible risk that magnetic noise might bias or affect the search for an isotropic GWB. From $\sim$160Hz, there is again a non-negligible possibility of significant magnetic contamination. However, we note that the values of the inside-to-GW channel magnetic coupling at these and higher frequencies are often not measured but are rather upper limits.

Based on this budget we believe more work in the upcoming observing run(s) (O4 and O5) is needed. First, we recommend to increase the magnetic injection strength at frequencies above $\sim$160Hz to either measure the inside-to-GW channel magnetic coupling or push down the upper limits by a factor of 2-3 at each interferometer. Second, a reduction in the variability of the outside-to-inside magnetic coupling would be helpful. This might be possible by taking into account the direction to the lightning and the specific location in the building. In order to reduce the coupling variability, it may be necessary to reduce the lightning-induced currents on the beam tube that pass through the buildings (see Appendix A of [214]). Ideally the outside-to-inside magnetic coupling would be measured at each site. Third, it would be helpful to reduce the factor of two uncertainty in the inside-to-GW channel coupling function, although this might prove difficult [277]. The budget would also benefit from a finer frequency resolution of the measurements of the inside-to-GW channel coupling functions, which is made possible with louder magnetic fields injected with the larger coils. Finally, instead of a combined budget for an entire observing run, the time-dependence of the magnetic coupling and its effect on the search for a GWB should be studied in more detail. This ideally would entail performing weekly (nearly) sitewide injections. Many of these suggestions are already being pursued [316, 317], as was also discussed in Chapter 7.

The diurnal and seasonal variations in the amplitude of the magnetic field fluctuations may provide a test to differentiate between correlated noise from lightning and a GWB signal. The current search for a GWB uses year-scale periods of data that are broken into minute-scale segments. As one test for lightning contamination,

the inter-site correlation could be re-computed for only daytime segments and, separately, for nighttime segments. If a correlation were due to lightning, we would expect a greater correlation for the nighttime data than for the daytime data. We would expect no significant day/night difference if the correlation were only due to an isotropic GWB. One could similarly separate the data into seasons for a second test. Furthermore we want to point out that in the past several efforts have been studied to validate the detection of a GWB in the case of correlated noise [106, 133, 134, 217, 267, 346, 348], as discussed in Chapter 5. These works have mainly focused on the Schumann resonances. Even though they have to be further validated for the magnetic correlations above ~ 100Hz from the superposition of individually correlated lightning strikes, there should not be fundamental showstoppers to perform this extrapolation.

8.3.2 Einstein Telescope

To compute the effect of magnetic noise on the ET, we approximate the ET as three interferometers and ignore the details of the xylophone configuration [201]; this does not affect our results. In what follows, we assume the three co-located, 10km long arm interferometers in triangle configuration of ET, namely $\mathrm{ET}_1, \mathrm{ET}_2, \mathrm{ET}_3$, as having identical sensitivity. Furthermore, we neglect the difference in γ_{IJ} between the baseline pairs $IJ = \mathrm{ET}_1\mathrm{ET}_2, \mathrm{ET}_1\mathrm{ET}_3, \mathrm{ET}_2\mathrm{ET}_3$, where we will be using $\gamma_{\mathrm{ET}_1\mathrm{ET}_2}$ from now on. For frequencies under 1 kHz the relative differences are [59]:

$$\frac{|\gamma_{\mathrm{ET}_1\mathrm{ET}_2} - \gamma_{\mathrm{ET}_1\mathrm{ET}_3}|}{\gamma_{\mathrm{ET}_1\mathrm{ET}_2}} < 5 \times 10^{-7},$$

$$\frac{|\gamma_{\mathrm{ET}_1\mathrm{ET}_2} - \gamma_{\mathrm{ET}_2\mathrm{ET}_3}|}{\gamma_{\mathrm{ET}_1\mathrm{ET}_2}} < 2 \times 10^{-7},$$

justifying our choice to neglect the difference between baseline pairs.

Note that, as mentioned in Chapter 4, the normalisation factor $S_0(f)$ has a different numerical value for the ET compared to LIGO, Virgo and KAGRA due to the different opening angle.

Data

We use the same data sets of magnetic data to study the effect on $\kappa_{\mathrm{ET}}^{\mathrm{GWB}}(f)$ as we did for $\kappa_{\mathrm{ET}}^{\mathrm{ASD}}(f)$ in Sec. 8.1.2. Also here we will use a factor 2 uncertainty at the level of the ASD, i.e. a factor 4 at the level of the magnetic CSD. This

implies that for the low frequency ($\geq$ 100Hz) environmental noise projections we have $\mathrm{CSD}_{\mathrm{mag,ET}}(f) = 4\left[P_{\mathrm{mag,SosEnattos}}(f)\right]^2$ and for the high frequency ($\leq$ 100Hz) environmental magnetic noise projection we have $\mathrm{CSD}_{\mathrm{mag,ET}}(f) = 4\mathrm{CSD}_{\mathrm{mag,HL}}(f)$. For our investigations of the infrastructural noise, using the measurements at the CEB of Virgo, we have $\mathrm{CSD}_{\mathrm{mag,ET}}(f) = 4\left[P_{\mathrm{mag,V_{CEB}}}(f)\right]^2$.

Results

In Fig. 8.2 we compared the upper limits on $\kappa_{\mathrm{ET}}^{\mathrm{ASD}}(f)$ and $\kappa_{\mathrm{ET}}^{\mathrm{GWB}}(f)$ for the ET-D design sensitivity. From this figure we can conclude that the requirements on the magnetic coupling are about one order of magnitude more stringent to prevent any effect on the search for an isotropic GWB, compared to the effect on the detector ASD. This implies that the magnetic coupling function for the ET has to be improved with respect to the average magnetic coupling at LIGO Hanford measured during O3 below 30Hz and up to three orders of magnitude or more for frequencies below 15Hz. Compared to the average magnetic coupling of Virgo during O3, a reduction of the magnetic coupling has to be achieved up to 100Hz. As a reminder, the equivalent figures using the latest HFLF-cryo and HF-only sensitivities can be found in Appendix B.

This low-frequency range is where most of the sensitivity is for the ongoing isotropic GWB searches, with the most recent LIGO-Virgo observing run containing 99% sensitivity to a flat Ω_{GW} spectrum below 100Hz [30]. The sensitivity at high frequencies is suppressed since the ORF for the LIGO and Virgo baseline pairs drops significantly with frequency and approaches zero at a few hundreds of Hz. The same, however, may not be true for the ET detectors, whose geometry leads to no suppression at high frequency, and the anticipated ORF remains approximately constant up to 1 kHz, e.g. $\gamma_{\mathrm{ET_1ET_2}}(1\text{ kHz})/\gamma_{\mathrm{ET_1ET_2}}(1\text{Hz}) = 99.48\%$. We therefore also look to place upper limits on the magnetic coupling function at high frequencies.

In Fig. 8.7 and Fig. 8.8 we show low and high-frequency coupling limits, $\kappa_{\mathrm{ET}}^{\mathrm{GWB}}(f)$, respectively for each of the design options (solid blue for ET-B, yellow dashed for ET-D). The average coupling measurements at Virgo, LIGO Hanford, and LIGO Livingston are the same as in Fig. 8.2. We emphasise again that Fig. 8.2 and Fig. 8.7 use data measured at the Sos Enattos candidate site for ET. However, given the similar amplitude of the Schumann resonances around the globe, these results could be transferable to another location and more specifically the other ET candidate sites in the Euregio Rhein-Maas and Saxony.

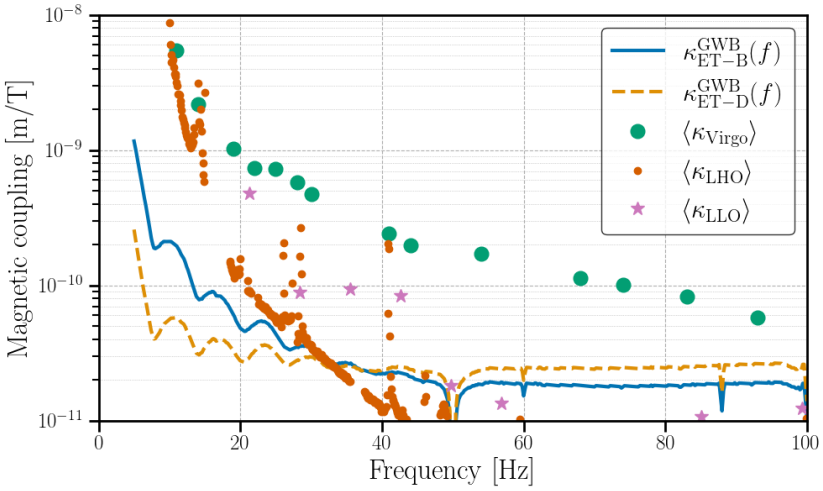

Fig. 8.7.: Variation in the 'GWB' magnetic coupling function upper limits for the different ET designs. Also included are the average of the measurements of coupling functions at LIGO Hanford, LIGO Livingston and Virgo during the O3 run for comparison.

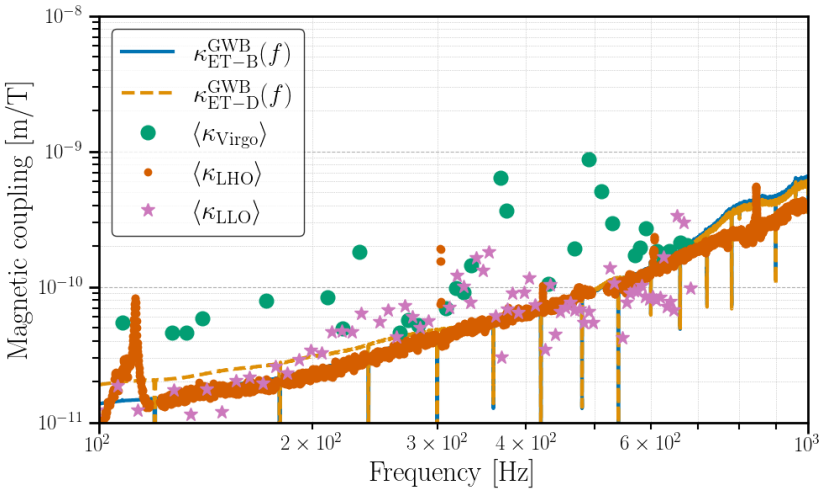

Fig. 8.8.: Upper limits on 'GWB' magnetic coupling function of ET-B and -D at high frequencies. Also included is the average of the measurements of coupling functions at LIGO Hanford, LIGO Livingston and Virgo during the O3 run for comparison.

We illustrate in Fig. 8.8 the effect of magnetic fields at ET above 100Hz. An example of an analysis that could target a signal at these higher frequencies is the study of a GWB from unresolved millisecond pulsars. This search is complementary to the standard continuous-wave search of individual pulsars, and can help constrain ellipticity of rotating neutron stars [24, 26, 340]. Current forecasts predict an improvement of one to two orders of magnitude in the sensitivity to ellipticity going from LIGO-Virgo to ET. However, correlated magnetic noise at high frequencies

could weaken the ellipticity constraints (see, Fig. 6 in [255]), and should thus be treated carefully.

However, since magnetic fields from the sources contributing to this magnetic noise (e.g. individual lightning strikes [80, 214]) are attenuated over long distances, the fundamental magnetic spectrum at ET could be stronger compared to our predictions. Therefore one should be cautious interpreting the upper limits presented in Fig. 8.8.

We summarise these results in Fig. 8.9, where we express the estimated 'GWB' upper limits as a factor of improvement needed in the ET coupling function relative to LIGO Hanford, LIGO Livingston and Virgo coupling functions. We show how this factor varies with frequency, as well as how it changes with the choice of ET design sensitivity. For frequencies below $\sim$ 30Hz, the magnetic coupling would need to be drastically reduced, with factors of improvement of the order $10^2 - 10^4$ needed for the isotropic GWB search, see top panel. High-frequency coupling, on the other hand, would only require up to a factor of 10 reduction in magnetic coupling to run a successful GWB search (bottom panel). As mentioned earlier, the results for HFLF-cryo will be almost identical to the results shown for ET-D. The difference in sensitivity between HF-only and ET-B is more significant for the Broadband PI sensitivity curve, compared to the ASD. Therefore the results for HF-only will have less stringent constraints compared to ET-B by a factor $\sim$3-4 between 7Hz and 10Hz[6]. Above $\sim$15Hz there is less than a factor 2 difference between the HF-only and ET-B sensitivities. This implies the HFLF-cryo design will yield minimal to no improvement for the search for an isotropic GWB compared to the HF-only design if one is unable to reduce the magnetic coupling.

Note that above 30Hz Advanced LIGO's magnetic coupling is dominated by induction of currents in cables [277]. One mitigation strategy that could be followed in this scenario is using, as much as possible, a cabling network of optical fibers. The implementation of a large-scale optical fiber network has been investigated and implemented at CERN [326]. An important factor for the reduced magnetic coupling for Advanced LIGO compared to Advanced Virgo is that LIGO uses electrostatic test mass actuators whereas Virgo uses magnetic actuation [122, 277]. Further reducing the number of magnets attached to the suspensions should reduce magnetic coupling. Additional magnetic shielding can be a complementary method to reduce the magnetic coupling [121]. Ultimately, if methods for magnetic coupling reduction are

[6]Please note that the PI-curve of HF-only is about a factor $\sim$10-20 less sensitive compared to ET-B between 7Hz and 10Hz. However when calculating the maximally allowed magnetic coupling this involves taking the square root, where we assume the coupling functions are identical for both detectors.

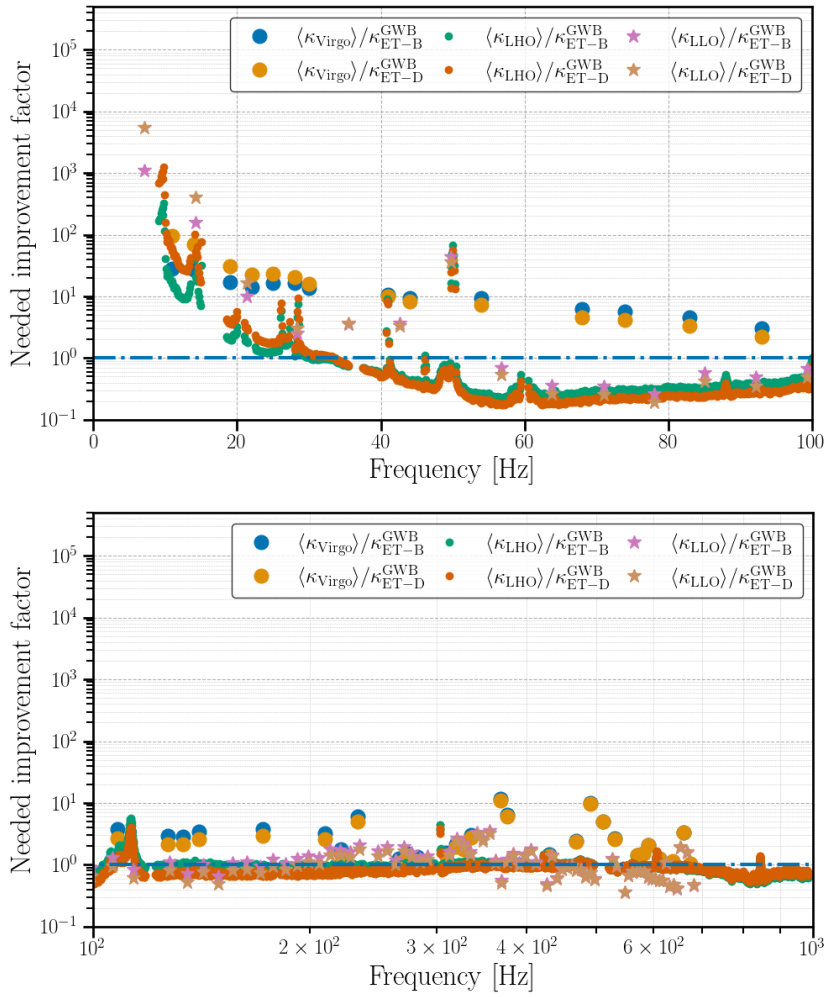

Fig. 8.9.: Needed improvement factor as a function of frequency for the 'GWB' upper limits on the ET magnetic coupling function. The low-frequency (top panel) magnetic coupling poses a greater challenge for the operation of ET compared to the high-frequency (bottom panel) magnetic coupling. In both panels, the dash-dotted blue line indicates the line where no improvement is necessary.

insufficient one could consider the cancellation of magnetic noise, similar to what is considered in the context of Newtonian Noise [75, 196], albeit using magnetometers instead of seismometers.

For Virgo, the direct coupling from magnetic fields to the mirror magnets is dominant for frequencies below $\sim$ 100Hz. This coupling is inversely proportional to the mirror mass [122]. This is important as the ET will have mirrors which are about five times more massive compared to Virgo. However this assumes the same configuration and strength of control magnets, which implies the control of the test masses becomes more difficult. This factor is included in Fig. 8.10 (as it was presented in the top left panel of Fig. 34 of [100]), however it should be considered with caution.

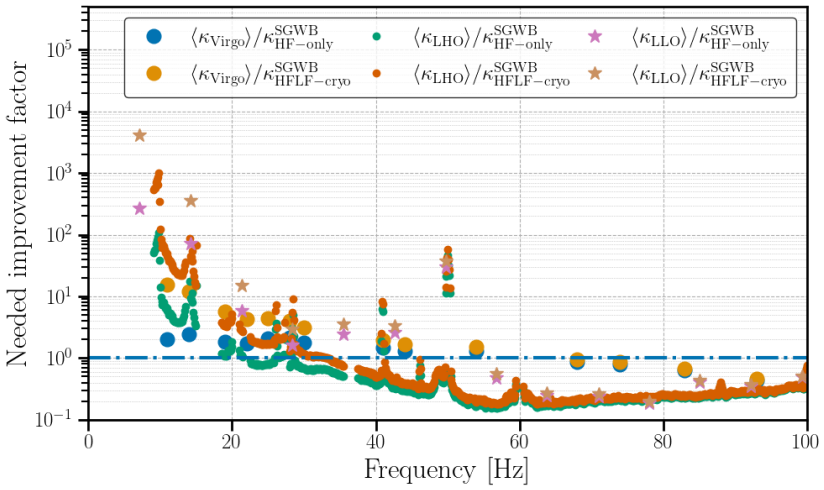

Fig. 8.10.: Needed improvement factor as a function of frequency for the '(S)GWB' upper limits on the ET magnetic coupling function with respect to the HFLF-cryo and HF-only sensitivities. For Virgo we have included a factor 5 reduction according to the increased mirror mass. The dash-dotted blue line indicates the line where no improvement is necessary.

Furthermore Fig. 8.10 also uses the HFLF-cryo and HF-only sensitivities, rather than ET-D and ET-B when comparing to the top panel of Fig. 8.9.

In Fig. 8.4 the effect of local infrastructural noise was presented. Also upper limits on $\kappa^{\rm GWB}_{\rm ET}(f)$ were shown in this figure. In the case of Virgo this local noise does not pose a serious problem in the GWB search since it is uncorrelated with local magnetic noise at far-away LIGO Hanford and LIGO Livingston detectors. Between co-located ET interferometers, however, the local noise could become correlated. As we will discuss in Chapter 9, the shortest distance between a mirror of one interferometer and the mirror of another interferometer is planned to be between 300m and 500m. This can lead to drastically more stringent upper limits on the magnetic coupling. If one wants to fully utilize the data for GWB searches, the magnetic coupling should be well below the magnetic coupling measured at LIGO Hanford, LIGO Livingston and Virgo, see Fig. 8.4. This implies that the search for an isotropic GWB would be entirely dominated by magnetic noise, in case the infrastructural magnetic noise is fully correlated between the different interferometers and no improvement in magnetic coupling is achieved with respect to second generation detectors.

8.4 Conclusion

We have shown that second generation detectors are expected to be only marginally affected by magnetic fields at their design sensitivities. Virgo's ASD sensitivity is projected to become limited by magnetic noise during O5, for only a fraction of the time in a small set of frequency bands. This projection furthermore assumes that both the magnetic coupling as well as the infrastructural magnetic noise used for this budget remain similar. The search for an isotropic GWB with LIGO Hanford, LIGO Livingston and Virgo will potentially be limited by correlations in magnetic field fluctuations at design sensitivity between 20Hz and 45Hz. More concretely the 2σ and 3σ noise projections surpass the expected broadband sensitivity of the detector network to an isotropic GWB. Also above $\sim$160Hz contamination from correlated magnetic noise is possible, however at these frequencies the values of the magnetic coupling function are mainly upper limits of the two LIGO detectors, which form the principle contribution to the budget presented. Therefore more detailed investigations and measurements of the magnetic coupling functions should be performed during upcoming observing runs.

ET is a powerful and promising instrument for detecting gravitational waves, with an unprecedented low-frequency sensitivity compared to LIGO and Virgo [255]. However achieving these low frequency sensitivity goals will prove challenging. In this chapter we have shown how ET's ASD will be degraded by fundamental magnetic noise below $\sim$10Hz if the magnetic coupling of the ET is similar to the coupling observed at second generation detectors. More specifically, several orders of magnitude in improvement of the magnetic coupling at low frequencies are needed to achieve the design sensitivity. Furthermore, this implies the HFLF-cryo design will barely improve upon the HF-only sensitivity below 15Hz, as both of them are affected by the magnetic noise. In case of a pessimistic scenario with high levels of infrastructural noise, as observed in Virgo during O3, ET will be limited by magnetic noise below $\sim$ 30Hz. This makes any potential benefit in science goals, as discussed in Chapter 3 and [100], of the HFLF-cryo design almost negligible.

CE promises to be a similarly powerful instrument as the ET, with the main difference a slightly worse sensitivity at the low frequency end. Nevertheless, also CE's ASD will be affected by fundamental magnetic noise up to $\sim$15Hz assuming similar magnetic coupling as second generation detectors. Below 10Hz an improvement of one to two orders of magnitude is needed. The needed improvement in magnetic coupling is almost irrespective of the different design sensitivities, i.e. 20km and 40km, and also differently tuned detectors, as they have similar design sensitivities below $\sim$15Hz.

With one year of GW data, ET-D/HFLF-cryo could be sensitive at the SNR=1 level to a cosmological ($\alpha = 0$) GWB $\Omega_{\rm GW}(f) \sim 10^{-12}$, but this depends critically on the low-frequency performance of ET. The ability to detect a GWB through correlation methods between multiple detectors assumes the absence of correlated noise [118], however globally coherent magnetic fields have been identified as a potentially limiting noise source for the present GW detector network [267, 346, 348]. As we have shown, this is also the case for ET. More precisely, we have shown that the magnetic coupling functions for ET must be better than those of LIGO and Virgo by a factor of $10^2 - 10^4$ for frequencies below 30Hz in order to avoid correlated noise from Schumann resonances affecting GWB searches. Furthermore we have shown that the HFLF-cryo design yields minimal improvements in sensitivity compared to the HF-only design if the magnetic coupling function of ET is similar to the magnetic couplings observed at second generation detectors. Finally, in the pessimistic case that ET has similar levels of infrastructural magnetic noise as Virgo and this noise is correlated between interferometers, it will be virtually impossible to perform the search for an isotropic GWB, regardless of the design. Over the entire frequency band ET's magnetic coupling should be improved by at least an order of magnitude compared to second generation to remove contamination from this infrastructural magnetic noise. However we want to stress that more research is needed to investigate such a scenario. Furthermore, whereas the effect of the fundamental magnetic noise is relevant regardless of the detector configuration, the infrastructural noise would effectively be dealt with when opting for a 2L configuration rather than the triangular configuration.

Reducing the magnetic coupling to prevent a significant impact on the interferometers, and also to ensure that local magnetic noise is as small as possible, is the best strategy for ET. This could be achieved by reducing the number of magnets attached to the suspensions [277], additional shielding [121], and using optical fibers as much as possible for signal transmission [277]. There could also be a synergy with noise subtraction methods, such as Wiener filters [134]. Such methods have been investigated to cancel Newtonian noise [75, 196], see also Chapter 9. However, such noise subtraction methods could also be used to reduce the effects of correlated magnetic noise and loosen the requirements on the magnetic coupling, as presented here.

Not reaching the reported upper limits on the magnetic coupling functions could have a direct impact on the search for a GWB with ET, as well as on all science goals of the ET. The importance of correlated magnetic noise coupling will need to be considered as ET is designed and constructed.

Due to the unknown location and respective orientations of the two CE detectors, as well as their orientations and locations with respect to the ET, no studies have investigated the impact of correlated magnetic noise on the search for an isotropic GWB with these detectors. However, future work should investigate this question in a parametric approach, which could become important input for decisions regarding the chosen detector sites and their respective orientations.

9 Correlations in seismic and Newtonian noise and its impact on the Einstein Telescope

The last two chapters (Chapter 7-8) were devoted to describing Earth-scale distance correlations between magnetic field fluctuations and how they couple to GW detectors and more specifically a search for an isotropic GWB. In this chapter we will look at the possibility of correlations in seismic and Newtonian noise, introduced in Chapter 5. In contrast to the magnetic fields, seismic fields are typically correlated over shorter distance scales. The seismic waves caused by earthquakes are able to travel large distances, but the typical ambient seismic field in the frequency region of interest for Earth-based interferometric detectors (above several Hz) are mainly correlated on the order of several hundreds of metres to several kilometers. Therefore they are not considered to affect stochastic searches with second generation interferometric detectors which all have large mutual distances. However, as introduced in Chapter 2 the proposed design for the third generation detector Einstein Telescope relies on a triangular configuration of three (almost) co-located interferometers. We will start this chapter by further explaining the relevance of correlations in the seismic and Newtonian noise and how it might affect the ET (Sec. 9.1). We also include a short discussion on the relevance for atom interferometers. Afterwards we will discuss a study identifying the level of seismic correlations on the distance scale of several hundreds of meters (Sec. 9.2). In Sec. 9.3 we will use the information about the correlations in the data to predict upper limits on the seismic transfer function, describing the coupling of seismic waves to the detectors. Afterwards the seismic correlations will be used in Sec. 9.4 to make an estimate of the level of correlated NN. In Sec. 9.5 we will create a budget to study the impact of NN on stochastic searches with the ET.

Since earlier work has studied the effect from seismic and Newtonian noise on the instantaneous sensitivity $P_{\mathrm{ET}}(f)$ [56, 77, 195], we will only focus on the impact on the search for an isotropic GWB in this chapter. It was found that seismic noise could

be dominant up to several Hz [56]. To achieve the desired sensitivity, the effect of NN on the other hand has to be reduced by about a factor of 3, which is considered to be feasible in case enough seismometers are deployed to apply effective (offline) noise mitigation relying on e.g. Wiener filtering [56, 75].

Please note that in this chapter we will only focus on fundamental ambient seismic noise while we do not investigate the effect of infrastructure which might have a larger impact.

9.1 Relevance of correlated seismic and Newtonian noise for Earth-based GW detectors

The difficulty in conducting a search for a GWB with co-located detectors was displayed by LIGO with its H1 and H2 detectors in its fifth science run; correlated noise prevented the search for an isotropic GWB for frequencies below 460Hz [2].

9.1.1 The Einstein Telescope

As introduced in Chapter 2, the ET is proposed to be made up of six interferometers with opening angle of $\pi/3$ and arm lengths of 10km, arranged in an equilateral triangle. In this chapter, we ignore the details of the xylophone configuration [201] and treat ET as consisting of three interferometers; this will have no effect on our studies.

The effect of seismic and Newtonian noise on GW interferometers and the possibility to apply (offline) noise subtraction has been studied extensively both for the second [76, 127, 128, 130, 148, 196, 352] and third generation [61, 75, 77, 142, 143, 228] interferometric GW detectors. Ambient seismic fields rapidly lose coherence over large distances at the frequency range of interest of Earth-based GW interferometers (above several Hz) [127, 129, 274, 336]. However, since the three interferometers of the ET triangular configuration will be (nearly) co-located, it is interesting to have a more detailed study of correlated seismic noise, the resulting NN and their impact on the ET.

To first order, one can typically assume that seismic fields over the scale of 10km will be no longer correlated above a couple of Hertz [129]. In future studies, one might need to test this hypothesis in the case of an underground environment,

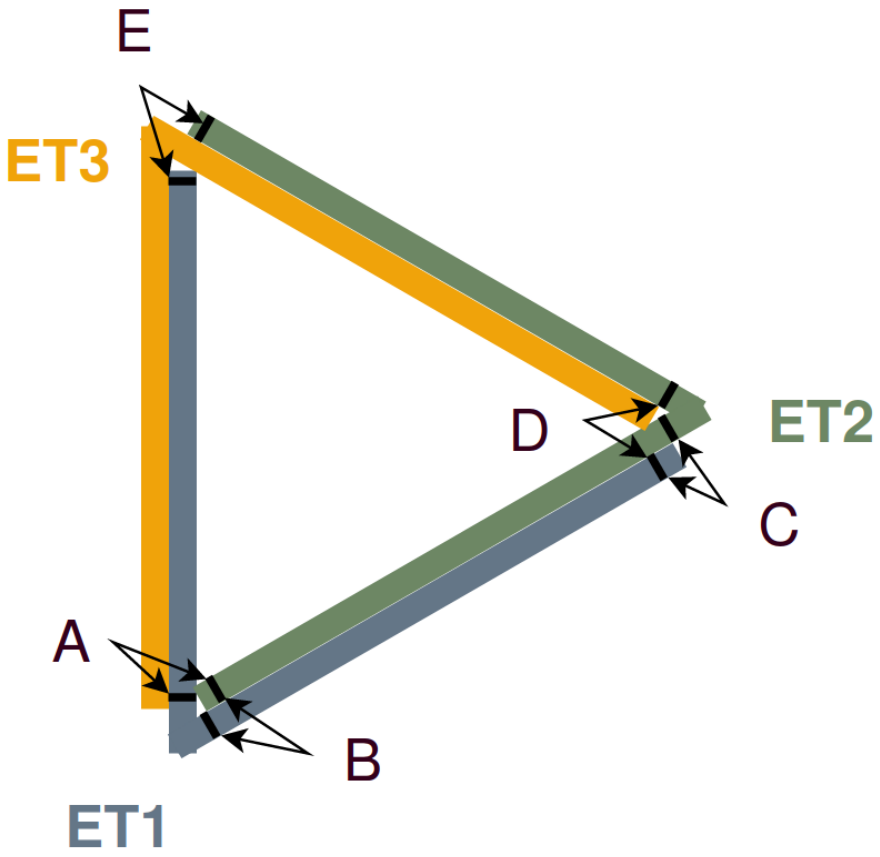

Fig. 9.1.: Scheme of the ET configuration, the low- and the high-frequency detectors are not shown separately. Considering the ET1-ET2-baseline, we can identify 5 possible coupling locations where noise can correlate: A to E. B and C involve the coupling of two aligned mirrors, while A,D and E involve mirrors which are rotated by 60°with respect to each other. The distances between the mirrors of such pairs is about 300m to 560m.

preferable including the detector infrastructure. However, the end mirror of one of the ET-interferometers will be at a distance of several hundreds of meters from the input mirror of another ET-interferometer, e.g. 300m to 500m [161]. In this chapter we will expand on previous studies of seismic correlated noise [127, 129] where we will focus on distance scales of 200m to 810m using both surface and underground sensors in a frequency range of 0.05Hz - 50Hz. Furthermore, we will use these seismic correlations to discuss the amplitude of correlated NN on a length scale of several hundreds of meters. Please note that this chapter does not contain a site comparison and the seismic spectra that will be used were selected based on the grid spacing of the installed sensors. The statements on the impact of correlated seismic and NN fields on the ET, will be of general nature, regardless of the exact location of the ET.

The horizontal separation for aligned mirror pairs (B and C) is about 300m - 500m, whereas one can calculate the distance for the other pairs (A, D and E) to be about 330m - 560m [161], see Fig. 9.1. However as the design and those distances are not yet fixed these investigations have two main goals. First of all we want to investigate whether we observe significant correlations of seismic and Newtonian noise on distance scales of 300m to 600m. If yes, we aim to quantify their impact on the ET and its science goals. Finally, we plan to investigate whether an increased distance between the mirror pairs could help to reduce the observed effect.

9.1.2 Atom interferometers

Earth-based atom interferometers plan to be sensitive to GWs, approximately in the frequency range 0.1Hz to 10Hz. One of their dominant noise sources is NN, both from seismic as well as atmospheric origin. One of the methods to reduce the effect of NN on future atom interferometric GW detectors is to have multiple atom gradiometer baselines which can be used to average out the effect of seismic NN [115]. In [115] they propose to have 80, 16.3km baseline atom gradiometers with a separation of 200m between the atom interferometers of subsequent gradiometers. However one of the assumptions made in [115] is that the NN at two atom interferometers of a single atom gradiometer with a baseline of 16.3km is uncorrelated. Furthermore, they only consider NN from Rayleigh waves. Therefore it is important to understand the correlation levels of NN[1] on distance scales of hundreds of meters up to tens of kilometers for both Rayleigh and body waves. Based on the observed correlations on such distances one can investigate to which extent they might limit the sensitivity and NN reduction with future atom interferometric GW detectors, as well as searches for a GWB with those detectors.

9.2 Seismic correlations

To study the correlations of seismic noise at distances between 200m and 810m we use two different sensor networks. The first is an array of surface geophones measuring the vertical seismic velocity, which was deployed near Terziet (Netherlands) [323]. This array covers (a part of) the region of the ET candidate site at the Euregio Rhein-Maas. The advantage of this seismic network is its large scale, and the presence of many sensors with horizontal separation of interest to us. However, there

[1] Here we will only consider NN of seismic origin.

are also several downsides, namely the large level of anthropogenic activity in the region, the absence of an extensive underground network and the limited operation time of the network ($\propto$ month(s)). We also use underground sensors deployed in the former Homestake mine (USA) [257]. Although the amount of sensors is more modest compared to the Terziet array, there are underground seismic measurements at several depths as well as horizontal separations of interest to our study. Furthermore, the Homestake mine is a seismically (relatively) quiet environment and data are available for almost two years. Note that whereas geophones measure velocity, seismometers are able to measure velocity or acceleration depending on the sensor model. The seismometers used in this analyses recorded seismic velocity.

Surface data from the Terziet geophone array

To characterize the seismic environment at the ET candidate site Euregio Rhein-Maas, hundreds of sensors (geophones, seismometers, ...) were deployed at the beginning of 2020 [323]. From this network we use a handful of geophones which where deployed in the region for one to several months. The sensor pairs used in the analysis are summarized in Tab. 9.1. They were solely selected on their horizontal separation and no further investigations were performed concerning their geological location and/or their seismic environment. However, another study [227] has shown the observed seismic spectrum varies significantly depending on the location of the sensors. It shows that the sensors which form our 300m , 400m and 500m pairs are intrinsically more quiet compared to the other sensors used in our analysis of the Terziet sensors.

As mentioned earlier, the distance between the central station of one interferometer at the ET and the terminal station of another interferometer is proposed to be around 300m-500m. Therefore we decided to present coherence and cross-power spectral density (CSD) results for the data taken from the geophones with a horizontal separation of 400m ('XPPNA-XIPOA'-pair). Other distances will be presented in comparison with the 400m pair.

Fig. 9.2 presents the coherence for the vertical geophones, whereas Fig. 9.3 shows the CSD of the seismic spectrum in units of velocity. Given the limited data (10:15:01 UTC 07 Nov. 2020 - 12:13:59 UTC 5 Dec. 2020 for XPPNA-XIPOA) we use a frequency resolution of 0.1Hz after which we average the data over stretches of 4 hours. This implies we are unable to get detailed results of the microseism peak near 0.2Hz. However, in this chapter we are mainly interested in frequencies above 1Hz since the ET will be insensitive to GWs with lower frequencies. Furthermore, we

Location	Sensor Type	Name sensor 1	Name sensor 2	Horizontal distance	Depth	Direction
Terziet	Geophone	YKNVA	YONYA	~ 200m	0m	Vertical
Terziet	Geophone	YCQGA	YIQEA	~ 300m	0m	Vertical
Terziet	Geophone	XPPNA	XIPOA	~ 400m	0m	Vertical
Terziet	Geophone	XPPNA	XYPWA	~ 500m	0m	Vertical
Terziet	Geophone	YLOWA	YCPBA	~ 600m	0m	Vertical
Terziet	Geophone	YKNVA	YSOJA	~ 700m	0m	Vertical
Homestake	Seismometer	A2000	B2000	~ 255m	610m	3-axial
Homestake	Seismometer	D2000	E2000	~ 405m	610m	3-axial
Homestake	Seismometer	A2000	D2000	~ 580m	610m	3-axial
Homestake	Seismometer	B2000	D2000	~ 810m	610m	3-axial

Tab. 9.1.: Table summarizing the sensor pairs that are used in the correlation analysis in this chapter. Please note that a depth of 0m implies the sensor is located at the surface, however this does not imply the different sensors are at the same height above sea-level. The given distance is accurate up to 5 m.

also show the 10% and 90% percentiles of the coherence as well as CSDs, measured during the local night time, represented as an orange band, when we expect lower levels of antropgenic noise. For the local night time we have chosen 21:15 to 7:15 local time[2]. The color scale in Fig. 9.2 and Fig. 9.3 represents the density of the ($\mathcal{O}(100)$) 4h-segments of the analyzed data.

Based on Fig. 9.2 we state that during 50% of the time there is significant[3] coherence up to $\sim$ 10Hz and at least 10% of the time the coherence is significant up to 50Hz. The seismic spectrum observed at these frequencies are approximately 10^{-9} ms$^{-1}/\sqrt{\text{Hz}}$ to 10^{-8} ms$^{-1}/\sqrt{\text{Hz}}$, see Fig. 9.3.

The local night time should give an indication of a quiet time when the effect of anthropoghenic noise is lower. Whereas the levels of observed coherence are comparable or marginally higher during the night, the observed CSD is (marginally) lower during the night. This behaviour can be expected since during the night-time fewer local anthropogenic sources might disturb the coherence from the typically smaller ambient seismic fields. We note that for some other pairs of geophones the difference was more pronounced.

Around 0.2Hz we clearly observe the second microseism peak, which is caused by ocean waves, and the observed cross-correlation spectrum lies within the seismic low noise and high noise models of Peterson [210]. Note however, that these noise models were constructed for the amplitude/power spectral density of one seismic sensor and not the cross spectral density of two seismic sensors separated by several hundreds of meters.

In Fig. 9.4 and Fig. 9.5 we present the 50% percentile of the coherences and of the CSDs measured for different geophone separations. Fig. 9.4 shows that the seismic coherence for distances between 200m and 700m is significant up to $\sim$ 10Hz for 50% of the time. Both Fig. 9.4 and Fig. 9.5 show that there is no clear relation between the observed coherences (or the CSDs) and the horizontal separations between the geophones. If the seismic field were perfectly isotropic and homogeneous, we should have observed high coherence up to around 0.1Hz with a faster decrease for larger geophone separations (Equation (1) of [368]). We do not see this behaviour in the data, on the contrary, we observe more coherence for separations of 400m, 500m and 600m and reduced coherence for 200m, 300m and 700m. A possible explanation can be the large amount of anthropogenic noise

[2]We start 15 minutes after the hour rather than at the top of the hour since the sensor started operating at 10:15 UTC and we analyse the data in stretches of one hour.

[3]We consider the coherence to be significant if the coherence is greater than 1/N, where N is the number of time segments over which was averaged. This 1/N is namely the approximate level of coherence expected from Gaussian data, as introduced in Chapter 6.

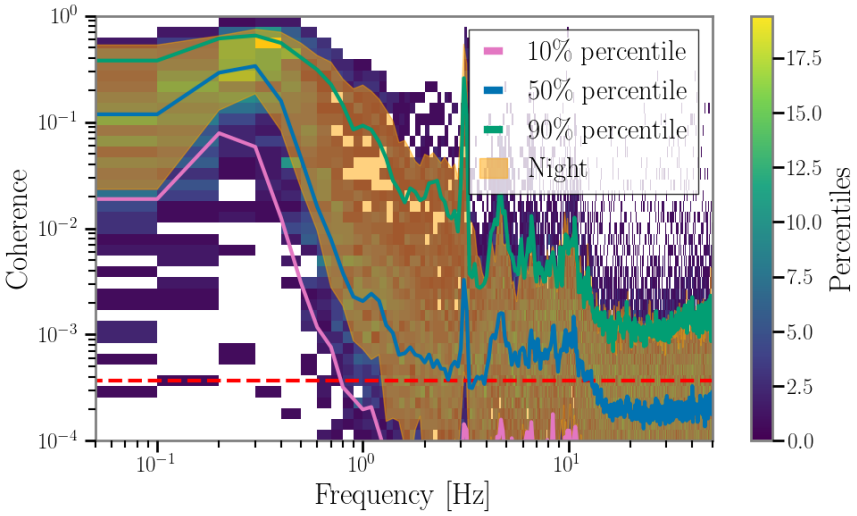

Fig. 9.2.: The coherence between the surface geophones XPPNA and XIPOA with an approximate distance of 400m. The data (10:15:01 UTC 07 Nov. 2020 - 12:13:59 UTC 5 Dec. 2020) are analysed using 10 second long segments which are averaged per 4h-window. The 10^{th}, 50^{th} and 90^{th} percentiles are shown in pink, blue and green, respectively. The percentiles as well as the counts are based on combined day and night data whereas the orange band represents the 10^{th} to 90^{th} percentiles during nighttime. The red dashed line represents the level of coherence expected from Gaussian data which goes approximately as 1/N, where N is the number of time segments over which the coherence was averaged.

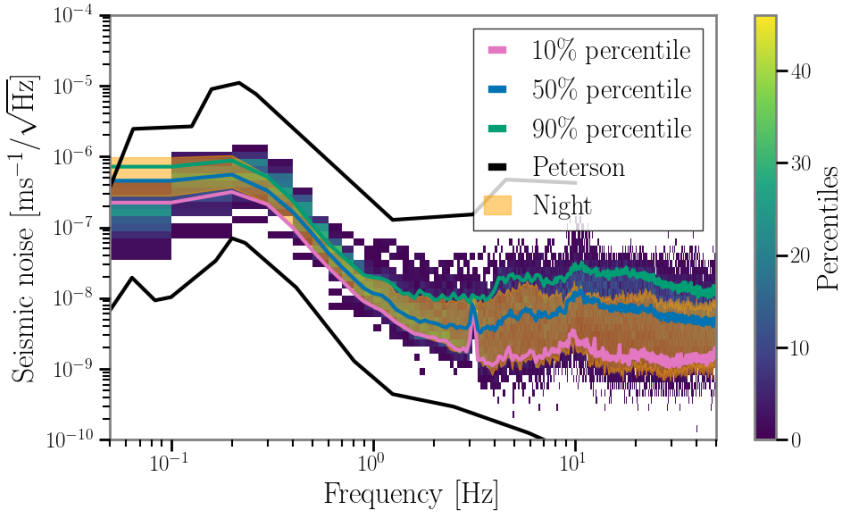

Fig. 9.3.: The $\text{CSD}^{1/2}$ of the surface geophones XPPNA and XIPOA with an approximate distance of 400m. The data (10:15:01 UTC 07 Nov. 2020 - 12:13:59 UTC 5 Dec. 2020) are analysed using 10 second long segments which are averaged per 4h-window. The 10^{th}, 50^{th} and 90^{th} percentiles are shown in pink, blue and green, respectively. The percentiles as well as the counts are based on combined day and night data whereas the orange band represents the 10^{th} to 90^{th} percentiles during nighttime. The black curves represent the low and high noise models by Peterson [210].

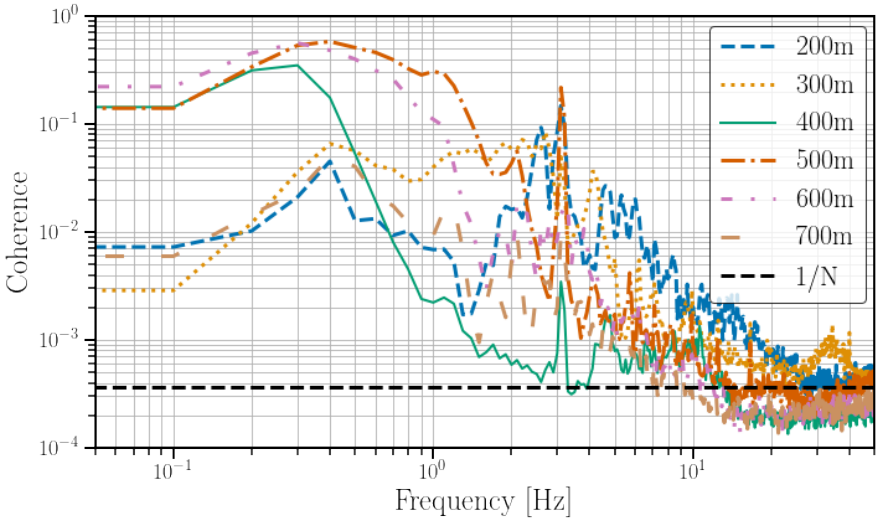

Fig. 9.4.: The median coherence of the surface geophones as a function of distance. The data are analysed using 10 second long segments which are averaged per 4h-window. Please note that the data at different distances is taken during different times as well as varying period (22 days to 28 days).

sources in the region. This can lead to anisotropies in the seismic field. Furthermore, the geophone pairs are located in positions with different levels of ambient seismic fields [227]. Also, the directions of the seismic waves can affect the coherences. The aim of this chapter is to get an order of magnitude estimate of the correlated seismic spectrum between sensors separated by several hundreds of meters and use these to make an estimate of the subsequent NN and their effect on the search for a GWB. However, the variation of both the coherence and seismic spectrum (in units of speed), presented in respectively Fig. 9.4 and Fig 9.5 indicates more precise (site-specific) studies are needed to fully understand the effect of local geology and anisotropies in the seismic field.

Underground data from the Homestake seismometer array

For studying the underground correlations we will use underground seismometers located at the 2000ft-level of the former Homestake mine [257] of which earlier seismic studies are reported in [127, 129, 191, 266]. The ET is proposed to be located at a depth of around 200m-300m underground [161], this is much less than our choice of 2000ft $\approx$ 610m. However, the choice of this depth was driven by the presence of multiple seismometers deployed with horizontal separations between $\sim$125m and $\sim$1200m. Moreover, at this depth, the effect of surface waves will be

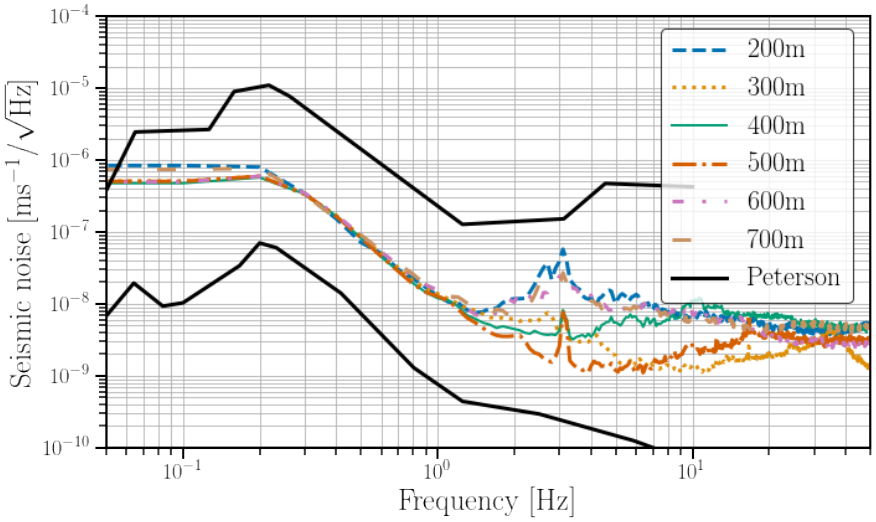

Fig. 9.5.: The median CSD$^{1/2}$ of the surface geophones as a function of distance. The data are analysed using 10 second long segments which are averaged per 4h-window. Please note that the data at different distances is taken during different times as well as varying period (22 days to 28 days). As a comparison, the Peterson low and high noise models [210] are shown in black.

even more suppressed and the correlations will provide realistic insights regarding correlations of seismic body waves at horizontal distances of interest for ET.

The seismometer pairs of which we will present the results are introduced in Tab. 9.1. Similar to what was done with the data of the Terziet array presented earlier, we will use data measured at a distance of 405m, that is between the 'D2000' and 'E2000' stations, as an example. Afterwards we will compare it with data from other distances. Whereas the Terziet geophones were measuring only the vertical seismic velocity, the Homestake seismometers can measure it in the vertical as well as in the horizontal directions (North-South and East-West).

Fig. 9.6 represents the coherence for the vertical seismometers, while Fig. 9.7 shows the accompanying CSD. Similar to the results for Terziet, we show a percentile plot together with the 10$^{\text{th}}$, 50$^{\text{th}}$ and 90$^{\text{th}}$ percentiles. Given the larger amount of data available for Homestake we used a frequency resolution of 0.01Hz and averaged over 24h. The data represented here uses 600 days recorded between March 2015 and December 2016. Furthermore we also show the 10% and 90% percentiles of the coherence as well as CSDs, measured during the local night time, represented as an orange band. We define local night time between 04:00 UTC and 14:00 UTC. This matches 21:00-07:00 local time during the 'standard time' (that is during the winter period).

Above $\sim$ 40Hz the response of the seismometers in the set-up at the Homestake mine decreases rapidly and the results should not be trusted. Fig. 9.6 shows that 90% of the time there is significant coherence up to 20Hz and more than 50% of the days even up to 40Hz. The seismic spectrum observed at these frequencies are approximately 10^{-10} ms$^{-1}/\sqrt{\text{Hz}}$ to 10^{-8} ms$^{-1}/\sqrt{\text{Hz}}$. We notice that, definitely at frequencies above a couple of Hz, the seismic CSD at Homestake is considerable lower than the CSDs observed at Terziet.

Around the microseism peak ($\sim$0.2Hz) one typically expects high levels of coherence, which is not the case for the 10% percentile in Fig. 9.6. Further investigation of the data showed that some of the seismometers observed loud excess on certain days, likely linked to loud anthropogenic and close-by events. These specific anthropogenic and loud disturbances might be unique to Homestake but also at ET many local activities will take place. To this extent the results might give a realistic – or at most conservative – prediction of possible levels of correlated seismic noise at the ET. An ideal scenario is represented by the night time measurements which are not affected by these loud events.

The spread of the coherence and the CSD is lower during night times and above 10Hz the CSD is considerably lower compared to those measured during day and night combined (Fig 9.6 and 9.7). This is what one might expect to observe since at these frequencies many noise sources are anthropogenic which are expected to be lower during local night time. Even though the CSD observed during the night time is considerably lower, the effect on the 10% percentile is modest, i.e. a factor of $\sim$2-3. The 90% percentile during the night is at a comparable level as the 50% percentile measured during the day.

Similarly we investigated whether a reduction in correlated seismic noise could be observed during the weekends compared to the entire data-set. However, in this case no significant effect was observed, which led us to conclude local night times are the most quiet periods due to lower anthropogenic noise.

In Fig. 9.8 and Fig. 9.9 we present the 50$^{\text{th}}$ percentile of the coherences and CSDs respectively measured for different seismometer channels (i.e. vertical and horizontal), all with a horizontal separation of $\sim$ 405m. At low frequencies the coherences between perpendicular channels (NS-EW and EW-NS) are lower than those between parallel channels; this is not true anymore above 6-7Hz, where the coherences starts to be dominated by anthropogenic noise, which we can expect containing many incoherent sources. The difference in CSD for perpendicular and parallel seismometers is negligible above 2-3Hz.

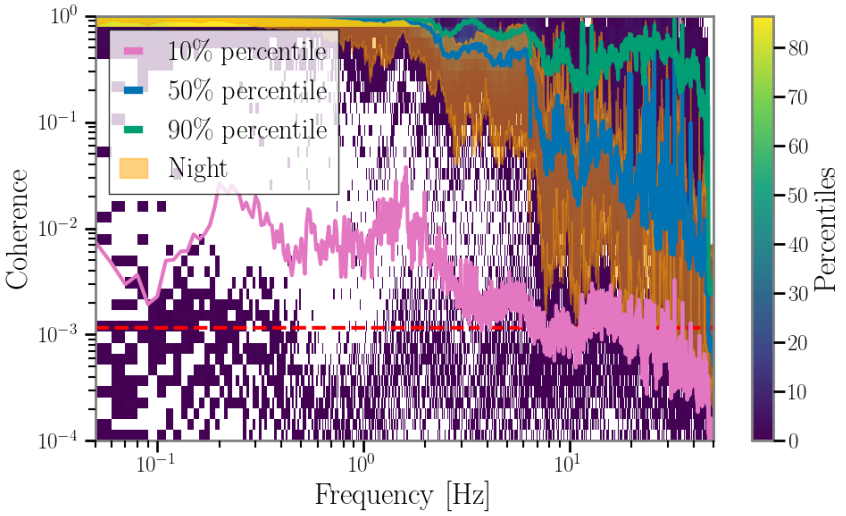

Fig. 9.6.: The coherence between the underground (depth ≈ 610m) seismometers (vertical component) D2000 and E2000 with an approximate horizontal distance of 405m. The data (March 2015 to Dec 2016) are analysed using 100 second long segments which are averaged per 24h-window. The 10^{th}, 50^{th} and 90^{th} percentiles are shown in respectively pink, blue and green. The percentiles as well as the counts are based on combined day and night data whereas the orange band represents the 10^{th} to 90^{th} percentiles during nighttime. The red dashed line represents the level of coherence expected from Gaussian data which goes approximately as 1/N, where N is the number of time segments over which the coherence was averaged.

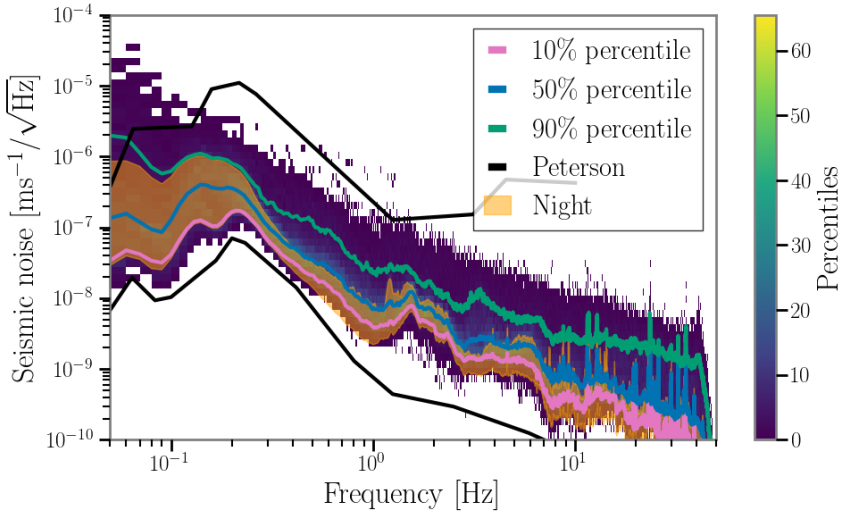

Fig. 9.7.: The $\text{CSD}^{1/2}$ between the underground (depth ≈ 610m) seismometers (vertical component) D2000 and E2000 with an approximate horizontal separation of 405m. The data (March 2015 to Dec 2016) are analysed using 100 second long segments which are averaged per 24h-window. The 10^{th}, 50^{th} and 90^{th} percentiles are shown in respectively pink, blue and green. The percentiles as well as the counts are based on combined day and night data whereas the orange band represents the 10^{th} to 90^{th} percentiles during nighttime. The black curves represent the low and high noise models by Peterson [210].

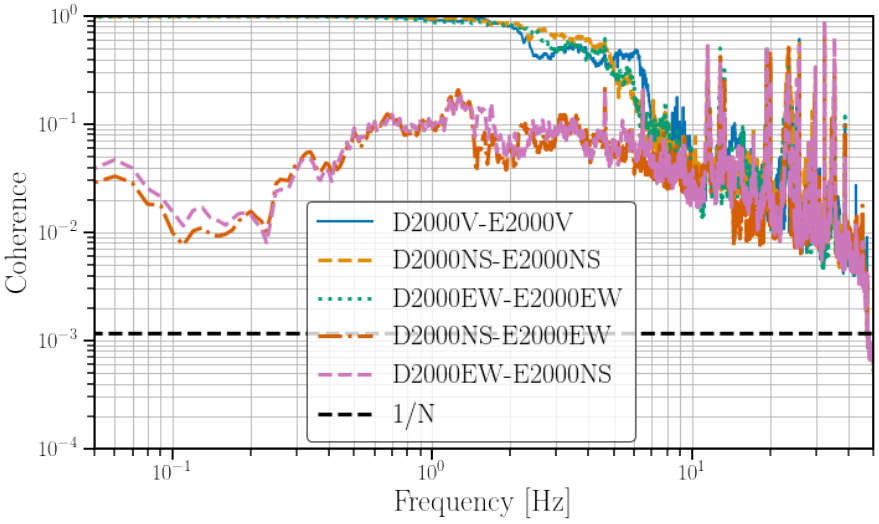

Fig. 9.8.: The median coherence of the underground (depth ≈ 610m) seismometers as a function of the different orientations, at a horizontal separation of 405m. The data (March 2015 to Dec 2016) are analysed using 100 second long segments which are averaged per 24h-window. The black dashed line represents the level of coherence expected from Gaussian data which goes approximately as 1/N, where N is the number of time segments over which the coherence was averaged.

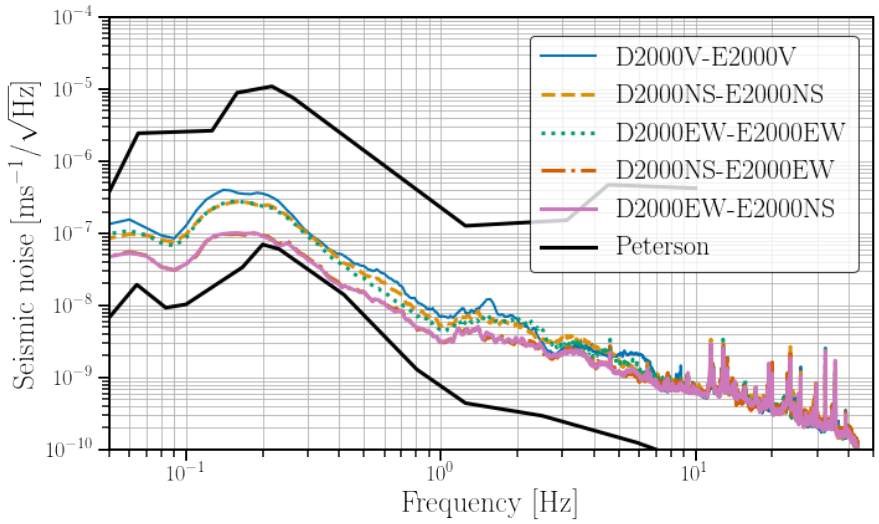

Fig. 9.9.: The median CSD$^{1/2}$ of the underground (depth ≈ 610m) seismometers as a function of the different orientations, at a horizontal separation of 405m. The data (March 2015 to Dec 2016) are analysed using 100 second long segments which are averaged per 24h-window. As a comparison, the Peterson low and high noise models [210] are shown in black.

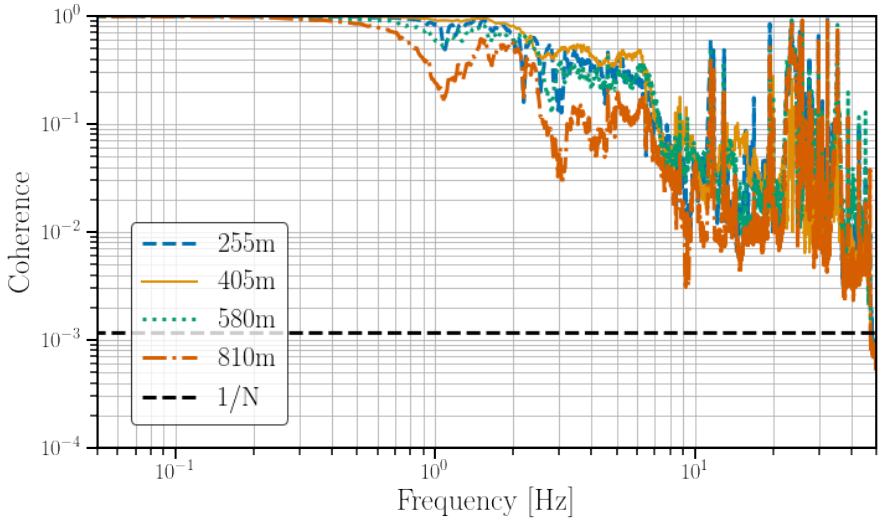

Fig. 9.10.: The median coherence of the underground (depth ≈ 610m) seismometers (vertical component) as a function of the horizontal distance. The data (March 2015 to Dec 2016) are analysed using 100 second long segments which are averaged per 24h-window. The black dashed line represents the level of coherence expected from Gaussian data which goes approximately as 1/N, where N is the number of time segments over which the coherence was averaged.

In Fig. 9.10 and Fig. 9.11 we present the 50$^{\text{th}}$ percentiles of the coherences and CSDs respectvely measured at different seismometer separations. We can notice that the coherences diminish for larger seismometer separations, except for the 405m separation. This could potentially be explained by a partial anisotropy in the seismic field. Furthermore, the CSDs are very similar regardless of the horizontal distance between the seismometers.

9.3 Placing upper limits on the seismic coupling function

In line with the method used to quantify the impact of correlated magnetic noise on the ET in Chapter 8 we will construct a seismic cross-correlation statistic. Furthermore, we refer to the three different ET interferometers as $\mathrm{ET}_1, \mathrm{ET}_2, \mathrm{ET}_3$, which we assume to have identical sensitivity. We neglect the difference in γ_{IJ} between the baseline pairs $IJ = \mathrm{ET}_1\mathrm{ET}_2; \mathrm{ET}_1\mathrm{ET}_3; \mathrm{ET}_2\mathrm{ET}_3$, since the relative difference between the overlap reduction functions of the different arms is smaller than 5×10^{-7} for frequencies under 1 kHz. In the remainder of the chapter we will use the $\mathrm{ET}_1\mathrm{ET}_2$-baseline as our default observing baseline.

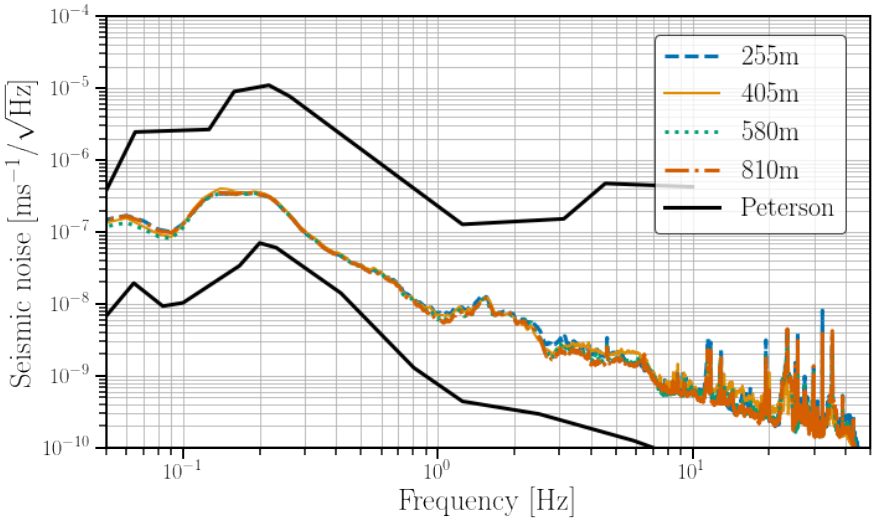

Fig. 9.11.: The median CSD$^{1/2}$ of the underground (depth $\approx$ 610m) seismometers as a function of the horizontal distance. The data (March 2015 to Dec 2016) are analysed using 100 second long segments which are averaged per 24h-window. As a comparison, the Peterson low and high noise models [210] are shown in black.

Similar to the magnetic cross-correlation described in earlier work [218, 346, 348], we can construct equivalent cross-correlation statistics for the correlated seismic noise:

$$\begin{aligned}
&\hat{C}_{\text{seismic,ET}_1\text{ET}_2}(f) = \\
&\quad |\kappa_{\text{seismic},vth,ET}(f)|^2 N_{\text{seismic},v,ET_1\text{ET}_2} \\
&+|\kappa_{\text{seismic},hth,ET}(f)|^2 N_{\text{seismic},h,ET_1\text{ET}_2} \\
&+|\kappa_{\text{seismic},tth,ET}(f)|^2 N_{\text{seismic},t,ET_1\text{ET}_2}, \\
\text{where}\quad N_{\text{seismic},v,ET_1\text{ET}_2} &= \frac{|\text{CSD}_{\text{seismic},vertical}|}{\gamma_{\text{ET}_1\text{ET}_2}(f) S_0(f)} \\
\text{and}\quad N_{\text{seismic},h,ET_1\text{ET}_2} &= \frac{|\text{CSD}_{\text{seismic},horizontal}|}{\gamma_{\text{ET}_1\text{ET}_2}(f) S_0(f)} \\
\text{and}\quad N_{\text{seismic},t,ET_1\text{ET}_2} &= \frac{|\text{CSD}_{\text{seismic},tilt}|}{\gamma_{\text{ET}_1\text{ET}_2}(f) S_0(f)} \\
&\text{and}
\end{aligned} \tag{9.1}$$

Here $\kappa_{\text{seismic},vth,ET}(f)$, $\kappa_{\text{seismic},hth,ET}(f)$ and $\kappa_{\text{seismic},tth,ET}(f)$ are the three different seismic coupling functions. They describe the coupling of vertical seismic motions to a horizontal motion of the test mass (vth), horizontal seismic motion to a horizontal motion of the test mass (hth) and a tilt seismic motion to a horizontal motion of the test mass (tth), respectively. Please note that in this chapter we will assume these three terms are independent. Whereas this is a good assumption, this assumption should be validated in future work.

In this chapter we have only measurements of the correlated vertical and horizontal fields and therefore we neglect all effects coming from the tilt. Furthermore we assume identical seismic coupling for the three different interferometers $\mathrm{ET}_1, \mathrm{ET}_2, \mathrm{ET}_3$. Eq. 9.2 provides the formalism to calculate upper limits on the seismic coupling function of which we present the results here.

The correlated seismic noise in the form of a cross spectral density are the quantities we presented in Sec. 9.2. Here we use the absolute value of the CSD to be conservative. Furthermore, for the horizontal seismic CSD we calculate the 'omni-directional' seismic CSD, where we take into account all possible cross-correlation combinations between the seismometer pairs, similar to the earlier study of magnetic fields in Chapter 8. Moreover, when calculating the upper limits for the seismic coupling function we will also introduce a factor of 5, where we assume incoherent sum of the possible coupling locations A-E as explained in Sec. 9.1 and Fig. 9.1.

Here we equate the broadband sensitivity for an isotropic GWB, $\Omega^{\mathrm{PI}}_{\mathrm{ET}_1\mathrm{ET}_2}(f)$, to the seismic cross-correlation statistic introduced in Eq. 9.1 to compute the upper limits on the seismic coupling functions $\kappa_{\mathrm{seismic},vth,ET}(f)$ and $\kappa_{\mathrm{seismic},hth,ET}(f)$. We will construct these upper limits independently for vertical and horizontal seismic fields:

$$\begin{aligned}\kappa_{\mathrm{seismic},vth,ET}(f) &\equiv \sqrt{\frac{\Omega^{\mathrm{PI}}_{\mathrm{ET}_1\mathrm{ET}_2}}{N_{\mathrm{seismic},v,ET_1\mathrm{ET}_2}}} \\ \kappa_{\mathrm{seismic},hth,ET}(f) &\equiv \sqrt{\frac{\Omega^{\mathrm{PI}}_{\mathrm{ET}_1\mathrm{ET}_2}}{N_{\mathrm{seismic},h,ET_1\mathrm{ET}_2}}},\end{aligned} \tag{9.2}$$

where N_{seismic} was introduced in Eq. 9.1. Fig. 9.12 represents the upper limits on the seismic coupling functions $\kappa_{\mathrm{seismic},vth,ET}(f)$ and $\kappa_{\mathrm{seismic},hth,ET}(f)$ such that seismic noise does not affect the broadband sensitivity $\Omega^{\mathrm{PI}}_{ET}(f)$ for the search for an isotropic GWB using one year of data. Here we have assumed the by now deprecated ET-D design sensitivity, however as mentioned earlier this is almost identical to the latest HFLF-cryo design sensitivity. These upper limits were constructed using the seismic correlations measured underground at the former Homestake mine. The design of the suspensions, and therefore the seismic coupling function for the ET are still under investigation. The upper limits derived here can help making informed decisions on the necessary suspension requirements.

As a comparison, one can look at the 17m suspension design in [161], where Fig. 6.12 represents the seismic coupling for the hth component. Although this design will not be used in the final design of the ET, it gives an order of magnitude estimate

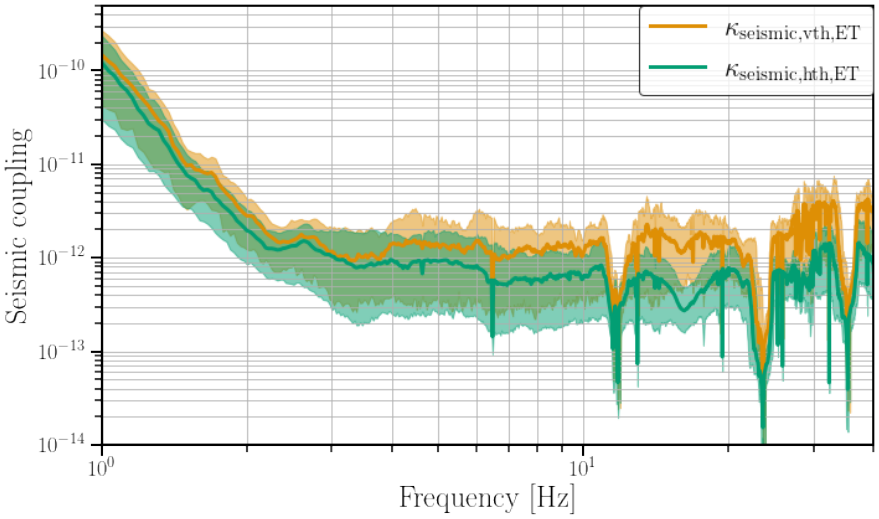

Fig. 9.12.: Upper limits on the seismic coupling functions $\kappa_{\mathrm{seismic},vth,ET}(f)$ and $\kappa_{\mathrm{seismic},hth,ET}(f)$. These upper limits are based on the 1-year power law integrated sensitivity $\Omega_{\mathrm{ET}}^{\mathrm{PI}}$.

of what can be expected. This indicates the seismic coupling might be too large up to a couple of Hz, but between 3Hz and 4Hz the hth component of the seismic coupling function presented in [161] reaches the desired level hth seismic suppression as represented by the green curve and band. This corresponds to an approximate value of $\kappa_{\mathrm{seismic},hth,ET} \sim 10^{-12}$ above several Hz.

Please note that by treating vertical and horizontal seismic correlated noise independently (and neglecting tilt) there is some room for residual contamination. For future designs of the ET suspensions, dedicated follow-up studies should indicate whether they sufficiently reduce seismic (correlated) noise or not.

9.4 Correlations in Newtonian noise

As introduced in Chapter 5, NN is a disturbance by local fluctuations in the gravitational field [192, 208, 314]. In this chapter we will only focus on seismic NN and ignore any possible effect from atmospheric NN.

The formulas to calculate the levels of NN coming from Rayleigh or body waves were introduced in Chapter 5, respectively in Eq. 5.2 and Eq. 5.6. In those formulas $S_\xi(f)$ represented the PSD of the seismic displacement. Here we will rather use the CSDs as discussed in the previous section to get an estimate of the levels of correlated NN. The aim is to provide an estimate of the correlated NN at a horizontal distance

separation of $\sim$ 400m. We will assume a homogeneous and isotropic bulk as well as a flat surface topology.

NN from Rayleigh-waves

For the the calculation of the NN from Rayleigh waves using the measurements of the vertical seismic field with geophones at Terziet we use the following parameters: the surface density $\rho_{0,\text{Surface}} = 2\,800\text{kg}\,\text{m}^{-3}$ [195] and $\gamma = 0.8$ (see Fig 10 of [192]). Furthermore we use $v_R(f) = 2000\ \text{m}\,\text{s}^{-1} e^{-f/4\text{Hz}} + 300\ \text{m}\,\text{s}^{-1}$ as the Rayleigh wave velocity in the frequency range 1Hz - 100Hz [97]. For the velocity of P and S waves we use the estimates of Bader *et al.* [77], since we will be using the surface measurements of Terziet for the calculation of the NN from Rayleigh waves. We use $v_P(f) = 4.05$ km s^{-1} and $v_S(f) = 2.4$ km s^{-1} estimated for a depth $h > 58.2$m [77].

The term $1/L^2(2\pi f)^4$ in Eq. 5.2 accounts for the conversion factor from acceleration to strain, where one test mass was considered. In this study instead, we are interested in the effect of correlated noise on the baseline formed by two interferometers, e.g. ET1 and ET2. As illustrated in Fig. 9.1, there are five possible locations where correlated noise can be introduced in the ET1-ET2-baseline. Therefore, we will multiply the NN contribution by a factor of 5, assuming conservatively the incoherent sum of the correlated NN between all the mirror pairs[4]. In reality, some of them could show correlated behaviour which would lead to a factor lower than 5. Please also note that some pairs involve aligned mirror pairs whereas others are misaligned by 60°. To estimate the NN from Rayleigh waves we used the analytical model taken from [56] rather than performing a numerical analysis as done in [77]. This approach is site independent and gives an idea on the orders of magnitude involved. A site-specific study could be envisioned in the future and will yield more accurate results. This is however beyond the scope of the study performed as part of this PhD dissertation.

The resulting effective strain from NN due to Rayleigh-waves are shown in 9.13, where the CSD of the XPPNA and XIPOA pair was used. In case ET would be built in a similar seismic environment at the surface, the NN from Rayleigh waves would impact the detectors ASD up to $\sim$20Hz-30Hz. However if one considers building the detector underground at a depth of 300m, the levels of correlated NN from Rayleigh-waves affecting the ASD are minimal up to 3Hz and non-existing at higher

[4] This additional factor 5 in Eq. 5.2 is at the level of the PSD, i.e. at the level of the strain ASD it is a factor $\sqrt{5}$.

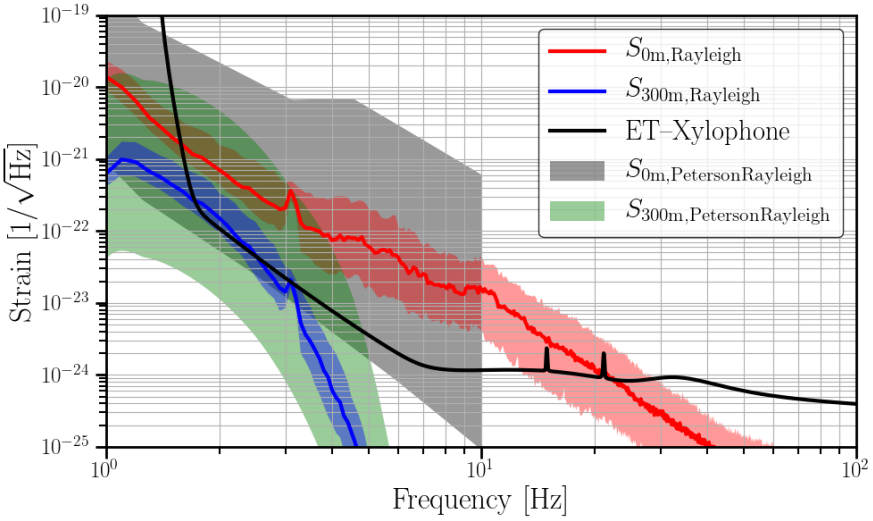

Fig. 9.13.: Strain of the NN with CSD of the surface geophone XPPNA and XIPOA (see Fig. 9.3) with a horizontal distance of 400 m at the surface (red curve) and at 300 m depth (blue curve). In the two cases considered, the solid line corresponds to the NN strain from the 50 % percentile, whereas the associated surface is delimited by the 10^{th} and 90^{th} percentiles of the CSD. The respective gray and green surface, delimited by the low and high limits of Peterson measurement [210], are the Rayleigh NN strain of the surface and 300 m depth. The black line is the ET-Xylophone (ET-D) design sensitivity. Figure produced by G. Boileau of the University of Antwerp.

frequencies. Again, we can easily see that building the ET underground can lead to a reduction of the Rayleigh NN.

NN from body-waves

For the calculation of the contribution of the NN from body waves we use a bulk density of $\rho_{0,\mathrm{Bulk}} = 2800\mathrm{kg\,m^{-3}}$. Furthermore we assume a value of $1/3$ for the mixing ratio of P- and S-waves, p, which accounts for an equal energy distribution between P-waves and S-waves [192], since the latter has two polarizations.

The resulting effective strain from NN due to body-waves is shown in Fig. 9.14, where the mean CSD of the two directions NS-NS and EW-EW was taken for the D2000 and E2000 seismometer pair. This figure shows that correlated NN form body-waves could affect the ET's ASD, from before 2Hz up to 10Hz, assuming a similar seismic environment as the Homestake mine.

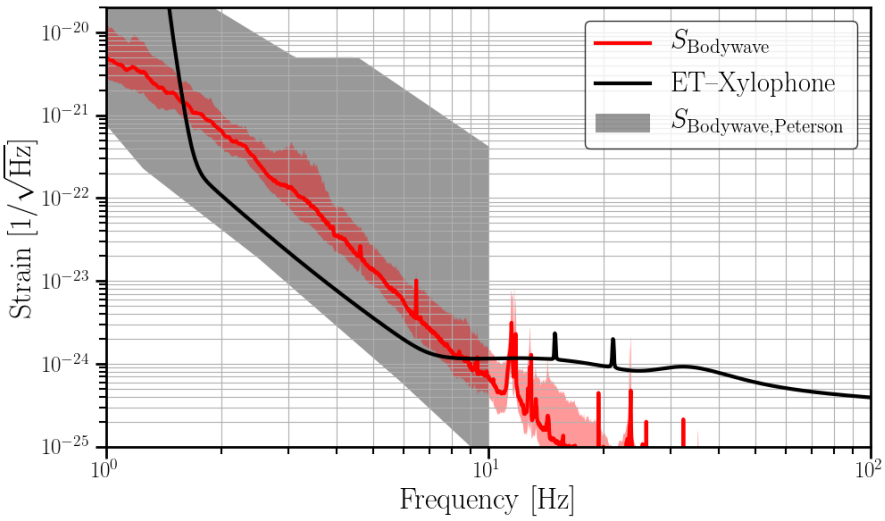

Fig. 9.14.: Strain of the NN with CSD of the Homestakes underground seismometers D2000 and E2000 horizontal displacement measurement (see Fig. 9.9) with a horizontal distance of 405m at a depth of $\sim$ 610 m (red curve). The solid line is the body wave NN strain from the 50 % percentile and the surface associated is delimited by the 10$^{\text{th}}$ and 90$^{\text{th}}$ percentiles CSD. The gray surface, delimited by the low and high limits of Peterson measurement [210], are the body wave NN strain at 610 m depth. The black line is the ET-Xylophone (ET-D) design sensitivity. Figure produced by G. Boileau of the University of Antwerp.

9.5 Impact of correlated Newtonian noise on the search for an isotropic gravitational-wave background

Since the search for a GWB is very sensitive, if not the most, to correlated noise sources we will investigate the impact of the correlated noise described in Sec. 9.4. In this section we will describe the relevant formalism and discuss the obtained results. We want to highlight that in this entire section we have used the ET-D design sensitivity, which is almost identical to the HFLF-cryo sensitivity.

Since the calculated NN is the direct effect of gravity fluctuations on the strain there is no additional coupling function '$\kappa_{\text{NN,ET}}(f)$' to take into account. The NN in Eq. 9.3 can either come from Rayleigh waves or body waves, for which S_{NN} was presented in Chapter 5, respectively Eq. 5.2 and Eq. 5.6.

$$\begin{aligned} \hat{C}_{\text{NN,ET}_1\text{ET}_2}(f) &= N_{\text{NN},ET_1\text{ET}_2}, \\ \text{where} \quad N_{\text{NN},ET_1\text{ET}_2} &= \frac{\text{S}_{\text{NN}}}{\gamma_{\text{ET}_1\text{ET}_2}(f) S_0(f)}. \end{aligned} \tag{9.3}$$

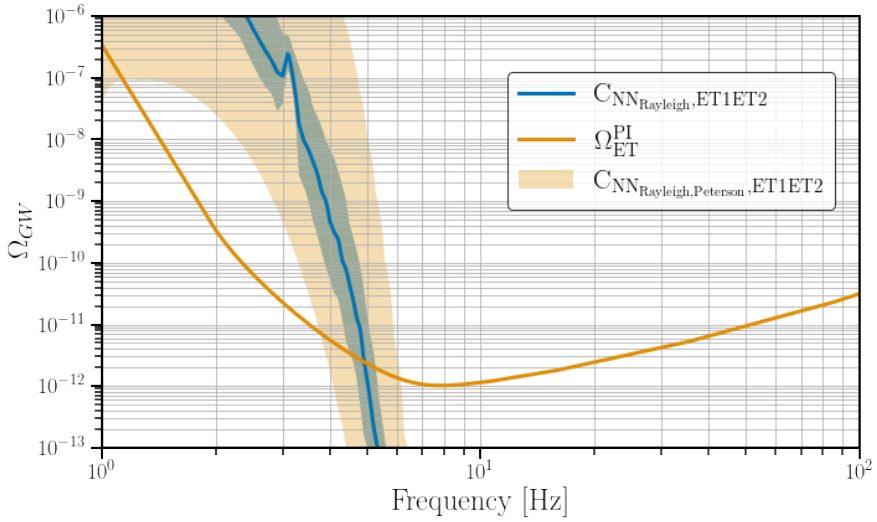

Fig. 9.15.: The projected impact from correlated NN from Rayleigh waves. The blue line represents the median value and the associated surface is delimited by the 10% and 90 % percentiles. We only show the projection for the NN which includes the attenuation gained by placing the ET 300m below the surface. As a comparison we also make the same projection using the Peterson low noise and high noise models. For the broadband (Ω_{ET}^{PI}) sensitivity to a GWB we assumed one year of observation time (100% duty cycle).

Fig. 9.15 projects the impact of NN from Rayleigh waves using the Terziet seismic data assuming a depth of 300m below the surface. Whereas the impact on the instantaneous sensitivity is shown to be problematic up to $\sim$ 3Hz in Fig. 9.13, the effect on the search for an isotropic GWB is affected up to $\sim$ 5Hz. At higher frequencies the depth of 300m ensures enough suppression of the NN from Rayleigh waves to prevent significant impact. For comparison also the NN from Rayleigh waves is shown using the Peterson low and high noise models.

We indicated earlier more dedicated (site-specific) studies are needed to take the local geology and anisotropies in the seismic field into account such that a more accurate noise projection can be achieved. However, the Peterson high noise model predicts NN from Rayleigh waves can contaminate the search for an isotropic GWB up to $\sim$ 6Hz, whereas this scenario represents the very worst case possibility: a very noisy environment as well as 100% correlated data. This indicates that regardless of the outcome of more precise site-specific studies investigating the correlations of seismic spectra at the surface, their impact through NN from Raleigh waves on the search for an isotropic GWB is expected to not exceed $\sim$ 6Hz, if the ET is located 300m below the surface.

Fig. 9.16 on the other hand, displays a worrisome level of correlated NN from body waves which affects the search for an isotropic GWB up to at least 40Hz, the highest

frequency with reliable data from the Homestake mine. Whereas the effect from Rayleigh waves decreases with the depth, there is no such reduction present for the NN from body waves. This leads to levels of correlated noise which are up to $\sim 8 \times 10^6$ (90% percentile), $\sim 6 \times 10^5$ (50% percentile) times larger than the desired sensitivity at $\sim$ 3Hz. Even when one would consider the seismic correlated noise observed during the night at Homestake, this does not alter significantly the impact displayed in Fig. 9.16. As mentioned in Sec. 9.2 the 90% percentile observed during the night is similar to the 50% percentile observed during the day and the correlated NN from body-waves still affects the isotropic search for a GWB up to 40Hz.

Here we would like to point out that the local seismic environment of the ET candidate sites might give different results than the ones obtained using the data from the Homestake mine. To this extent site-specific studies of underground correlation measurements over the scale of several hundreds of meters could give more insights. Evidently in case the ET candidate site would have lower levels of correlated seismic noise than observed at Homestake, this will lead to less stringent constraints. However we also want to note that infrastructure for the ET installed in the underground environment will create local seismic fields that could be louder and/or more strongly correlated at the mirrors of the different interferometers. To this extent it is also crucial to look into the possible disturbances of infrastructure and methods to reduce their effect. Also, it should be understood whether the effect from infrastructure or rather ambient seismic environment is the dominant factor.

Noise subtraction for NN is being investigated [61, 75–77, 127, 128, 130, 142, 148, 196, 228, 352], however with a focus to reduce the impact needed to reach the desired ASD sensitivity. The amount of reduction needed for the search for an isotropic GWB is many orders of magnitude larger. However, the budget shown in Fig. 9.16 is at the level of the baseline, such that the improvement of 5-7 orders of magnitude at $\sim$ 3 Hz corresponds to an improvement of about 3 orders of magnitude at every interferometer. Reducing the impact of NN on the ET with such levels is nevertheless considered to be out of reach. A more realistic (and already optimistic) level of reduction is a factor of 10 at each interferometer [75], that is a factor of 100 for the baseline. Even with this amount of NN subtraction, NN from body waves could be expected to contaminate the search for an isotropic GWB up to $\sim$ 30Hz. This would not only imply we lose the most sensitive region of the analysis but also that in the low-frequency region negligible improvement is gained compared to the expected sensitivity reachable by the LIGO and Virgo instruments after their A+ upgrades [20]. This will have a dramatic impact on the search for an isotropic GWB, regardless of the excepted source. As an example for the GWB coming from

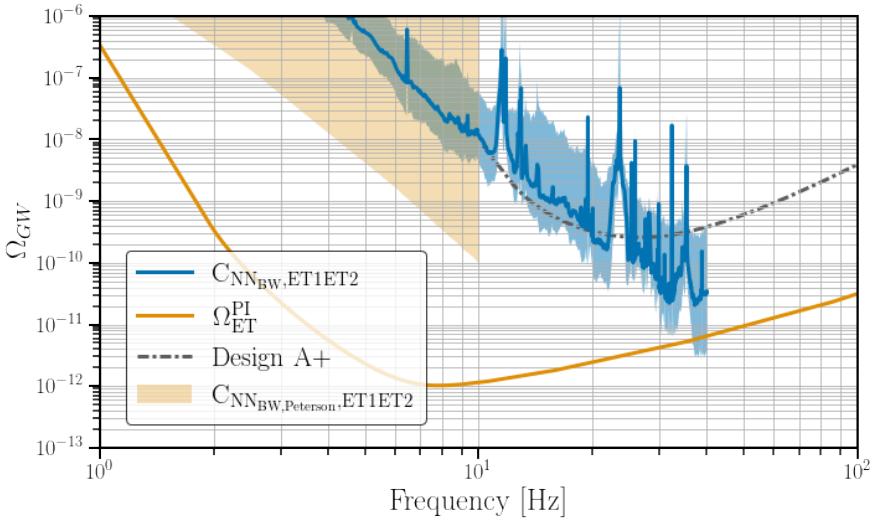

Fig. 9.16.: The projected impact from correlated NN from body-waves. The blue line represents the median value and the associated surface is delimited by the 10% and 90 % percentiles. As a comparison we also make the same projection using the Peterson low noise and high noise models. For the broadband ($\Omega_{\mathrm{ET}}^{\mathrm{PI}}$) sensitivity to a GWB we assumed one year of observation time (100% duty cycle). The one year PI curve of the A+ design for the LIGO Hanford, LIGO Livingston and Virgo detectors is represented by the dot-dashed curve. This curve was obtained using the open data provided by the LVK collaborations [243] and was first presented in [30]. Please note: in this chapter we present the 1σ PI-curve, whereas in [30] and in Fig. 8.6 the 2σ PI-curve is shown.

unresolved CBC events, more than 95% of the SNR is expected to be below 30Hz for the Xylophone ET design considered here [298].

As part of the work presented in [100], several more optimistic assumptions where made concerning the effect of NN from body waves, as shown in Fig. 9.17. The construction of these optimistic scenarios are broken down as follows. We start from the yellow curve, which displays the affect of NN from body waves assuming a seismic spectrum identical to the Peterson low noise model [210] and 100% coherence. We then assume a NN cancellation by a factor of 3 (i.e. a factor of 9 on the search for a GWB), which is considered as a realistic target (green curve). The dark orange curve is generated from the assumption that the coherence equals the median coherence observed in Homestake, as reported in Fig. 9.6. Finally the pink curve represents the Peterson low noise model multiplied by the coherence observed at Homestake, as well as a factor of 3 NN cancellation for each detector. This pink curve represents the most optimistic scenario that one can achieve. In this case, GWB searches will still be affected by correlated NN up to $\sim$10Hz.
Here, we would like to note that the factor 3 of NN cancellation typically assumes the construction of a Wiener filter. However, to be able to construct such a Wiener

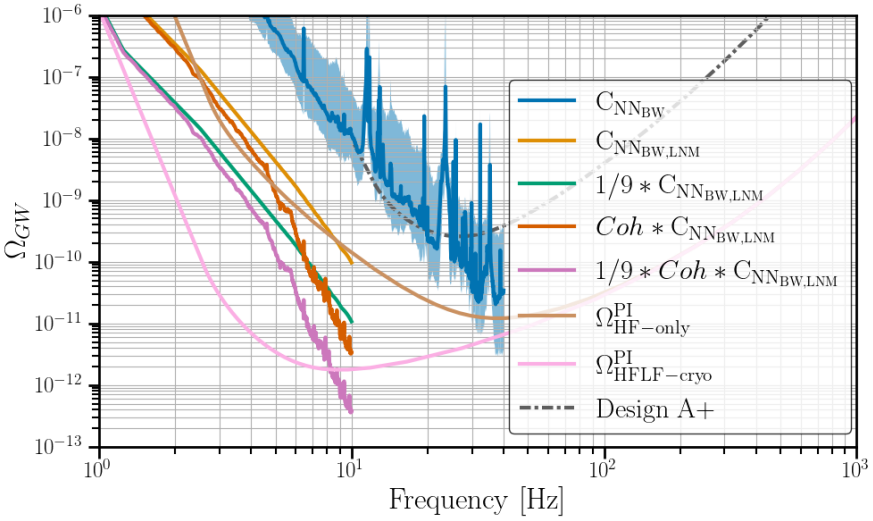

Fig. 9.17.: The projected impact from correlated NN from body-waves. Apart from the prediction based on the measurements at Homestake, also presented in Fig. 9.16. Furthermore, several other curves with more optimistic assumptions are shown as well. Finally the one year PI sensitivity curves are shown for ET's HFLF-cryo (light pink) and HF-only (light brown) sensitivity as well as for LIGO's A+ design (grey, dot-dashed).

filter the noise source has to couple significantly to the detectors strain ASD. As the NN in a non-negligible part of the frequency band will be sub-threshold for the strain ASD on timescales the Wiener filters are calculated, the achieved levels of NN cancellation could be even lower.

9.6 Conclusion

The ET promises to be a powerful instrument to observe GWs in the coming decades, outperforming LIGO and Virgo. The ET is also planned to have an unprecedented sensitivity to GWs in the 'low-frequency' region of several Hz to several tens of Hz [255]. This could significantly improve the capability of the ET to observe a GWB of either astrophysical or cosmological origin. To illustrate, more than 95% of ET's sensitivity to a GWB coming from unresolved CBC events is from below 30Hz [298].

However this low frequency region is also susceptible to several correlated noise sources. In Chapter 8 we showed that correlated magnetic fields could affect GWB searches up to $\sim$ 30Hz and magnetic coupling functions should be reduced by several orders of magnitude compared to the observed magnetic coupling at LIGO and Virgo.

In the same context we have investigated the possible impact from correlated seismic and Newtonian noise on the ET and its search for a GWB.

We analysed correlations between vertical seismic spectra measured between sensors of the Terziet surface array [323], with a horizontal separation of several hundreds of meters. Furthermore, both vertical and horizontal seismic spectra were analysed for data taken $\sim$ 610m below the surface at the former Homestake mine [257]. At both locations significant seismic coherence was observed up to 10Hz, 50% of the time or more. Also, between 10Hz and 50Hz significant coherence was observed. Although the observed correlated seismic spectra above $\sim$ 10Hz are lower during the nights due to less human activity, no decrease in seismic coherence is observed during the weekend.

By comparing correlated seismic spectra observed at different horizontal sensor separation, ranging from $\sim$ 200m to $\sim$ 810m, we have tried to identify the possible impact from the distance between the test masses from two different ET interferometers. Currently, this distance is foreseen to be about 300m to 500m. The observed correlated seismic spectra using data from the Terziet surface array do vary significantly above 1 Hz. However, no pattern related with the distance between sensors is observed, leading to the conclusion that the variation is most likely due to local variations in the number and location of the noise sources compared to the sensor locations. Site-specific studies using the entire array of deployed sensors should give further insights. However, the data presented here is able to give us an order of magnitude estimate of the correlated noise and its impact on the ET. The observed seismic spectra from the more quiet Homestake mine, show no dependence on horizontal separation between the sensors. The correlated seismic spectra at Homestake in the vertical direction are also very similar to the horizontal seismic spectra if one looks at aligned sensors. The correlated seismic spectra between two perpendicular seismometers is lower up to $\sim$ 2Hz-3Hz when compared to two aligned seismometers. At higher frequencies no difference is observed.

The measurements at the surface (Terziet) are used to predict the levels of correlated Newtonian noise from Rayleigh waves. If the ET were built at the surface, the NN would have been roughly one order of magnitude above ET's design sensitivity in the region of 2Hz - 10Hz. Please note that in these calculations we used a simplified model not taking into account the entire geological complexity, as was done in [77]. By building the ET 300m underground a marginal effect on the ET's ASD is present up to 3Hz. Similarly we used the underground measurements (Homestake) to calculate the level of correlated NN from body waves, of which the median is 3-5 times larger than the ET's design sensitivity between 2Hz and 10Hz.

The key result of this chapter is the propagation of these correlated seismic and Newtonian noise estimates onto the sensitivity for the search for an isotropic GWB. First of all, we presented upper limits on the seismic coupling function which has to be of the order of $\kappa_{\mathrm{seismic},hth,ET} \sim 10^{-12}$ or lower above 2Hz. Secondly, the effect from correlated NN from Rayleigh waves is found to impact the GWB sensitivity up to ∼5Hz, in the scenario the ET facility is located 300m below the surface. Finally, correlated NN from body waves are found to affect the GWB sensitivity up to 40Hz, with a maximal effect of $\sim 8 \times 10^6$ (90% percentile), $\sim 6 \times 10^5$ (50% percentile) at 3Hz. Even with a NN mitigation factor of 10 in each interferometer, the GWB search would be contaminated by correlated noise from body waves below 30Hz. Also when considering the seismic correlations during the local night, when minimal anthropogenic activities take place the impact on the stochastic search remains of the same order of magnitude, i.e. $\sim 10^5 - 10^6$ at 3Hz and a non-negligible impact up to 40Hz.
These results show that in the case of the correlated noise measurements at Homestake, the ET would, regardless of design, barely improve upon LIGO's and Virgo's design sensitivity for observing an isotropic GWB. When considering several more optimistic scenarios the effect of correlated NN from seismic body waves could be lower. However, even in the most optimistic case of a seismically quiet site and applied NN cancellation, ET's HFLF-cryo design will still be affected up to 10Hz for the search for an isotropic GWB. In the most optimistic scenario ET's HF-only design would not be affected. This indicates the potential science gain of the HFLF-cryo design over the HF-only would become more limited in such a scenario.

The presented results for the effect of correlated NN indicate a negative impact on the scientific goals for the ET. This subject must be further studied, and subsequent work has to include simulations for a more accurate prediction of the NN. These studies could also be envisioned to include site-specific studies to get a more accurate understanding of the effect at the candidate sites. However, not only the correlated ambient seismic fields at the sites should be understood, but also the noise from the infrastructure. This could lead to additional local (and possibly correlated) seismic noise. One should try to understand whether this effect is dominant over the sites ambient seismic correlations and if so to which extent clever design and placement of the infrastructure could decrease this impact. Other studies should try to understand the interplay between the correlated NN and the ET interferometric system. An accurate simulation of seismic fields interacting with the ET system should be performed to understand the possible interplay of the multiple coupling locations of seismic and Newtonian noise as introduced in Fig. 9.1 Finally, one can also investigate the possibility of using the null channel as a tool to estimate

correlated noise. In Chapter 11 we propose a formalism to estimate the ET's noise PSD which also gives insight in the cross-correlated noise terms. However, more work has to be done to understand its efficiency in scenarios with realistic correlated noise sources, such as the seismic and Newtonian noise as presented here.

10 Gravitational-wave geodesy

Throughout this entire work there has been a large focus on correlated noise and its interference with the search for a GWB (Chapters 5-9). In this chapter we will discuss a method that aims to provide statistical statements on the likelihood of the data being consistent with a GW signal or instead a correlated noise source. The concept of this tool called 'gravitational-wave geodesy' was already briefly introduced in Chapter 5. However, in Sec. 10.1 we will give a more detailed introduction. Sec. 10.2 introduces Gaussian Processes, which afterwards, in Sec. 10.3, will be used in an attempt to construct a false alarm rate for correlated noise. In Sec. 10.4 we will conclude this work and highlight the assumptions that were made as well as possible use cases for the future. This method goes beyond the budgets provided in Chapters 8 and 9 by providing statistical statements. The budgets should be seen as a method to get a sense of the order of magnitude, indicating possible impact. This should then be further studied with for instance a tool such as GW geodesy or Bayesian parameter estimation, as introduced in Chapter 5. As a reminder, in Chapter 5 an overview is made of the different methods and techniques that could be used to characterize and/or handle correlated noise.

10.1 Gravitational-wave geodesy: philosophy

In Chapter 4, we introduced the cross-correlation statistic $\hat{C}_{IJ}(f)$ (Eq. 4.11) as an estimator for the GWB energy density $\Omega_{\rm GW}(f)$. In the context of GW geodesy it makes more sense to not include the ORF, $\gamma(f)$, in the definition of $\hat{C}_{IJ}(f)$, since we want to infer the observed ORF. This results in the following definition of the cross-correlation statistic

$$\hat{C}_{IJ}(f) = \frac{2}{T}\frac{\mathrm{Re}[\tilde{s}_I^*(f)\tilde{s}_J(f)]}{S_0(f)}, \tag{10.1}$$

with its expectation value given by [55]

$$\langle \hat{C}_{IJ}(f) \rangle = \gamma(f)\Omega_{\rm GW}(f). \tag{10.2}$$

Given the detection of a GWB, we could seek to infer $\Omega_{\rm ref}$ and α, as introduced in Eq. 4.13. Additionally, however, the dependence of our measured cross-correlation spectrum $\hat{C}(f)$ on the ORF means that the GWB could be used to infer the geometry of our detector network itself. This fact forms the basis of GW geodesy: a true GWB should yield an inferred geometry consistent with the true geometry of our detector network. An isotropic astrophysical or cosmological GWB must be consistent with the expected functional form of our baseline's ORF. Correlated terrestrial noise sources, on the other hand, do not necessarily need to follow the behaviour of the ORF. Thus, there is no reason why non-GW correlated noise sources would prefer the true geometry over any random geometry [106]. We formalize this test by defining the following two hypotheses:

- Hypothesis $\mathcal{H}_\gamma$: The measured cross-correlation is consistent with the *true* baseline geometry and ORF.
- Hypothesis $\mathcal{H}_{\rm Free}$: The measured cross-correlation spectrum is consistent with an *unphysical* baseline geometry. Under this hypothesis, we treat our detector positions and orientations as free variables to be inferred from the data, allowing them to range (unphysically) across the surface of the Earth.

To compare the hypotheses $\mathcal{H}_\gamma$ and $\mathcal{H}_{\rm Free}$, one can construct a Bayes factor $\mathcal{B}$ between these hypotheses to establish which model is favored by the cross-correlated data[1] $\hat{C}$,

$$\mathcal{B} = \frac{p(\hat{C}|\mathcal{H}_\gamma)}{p(\hat{C}|\mathcal{H}_{\rm Free})}, \tag{10.3}$$

where $p(\hat{C}|\mathcal{H}_\gamma)$ and $p(\hat{C}|\mathcal{H}_{\rm Free})$ are the probabilities of finding the observed cross-correlation – as defined in Eq. 10.1 – given hypothesis $\mathcal{H}_\gamma$ and $\mathcal{H}_{\rm Free}$, respectively[2]. Because $\mathcal{H}_{\rm Free}$ is a more complex model, it will be penalized by the Bayesian 'Occam's factor'. Therefore, an isotropic astrophysical signal will be consistent with both $\mathcal{H}_\gamma$ and $\mathcal{H}_{\rm Free}$, but will favor $\mathcal{H}_\gamma$ since it is the simpler hypothesis. Non-GW correlated noise sources have a priori no preference for $\mathcal{H}_\gamma$ and therefore will be better fitted by the additional degrees of freedom provided by non-physical geometries, leading to favouring the $\mathcal{H}_{\rm Free}$ hypothesis.

We would like to stress that whereas time-shifted analysis can provide a null distribution for detection confidence, this is only true if the detector noise has no correlated noise component. The correlated noise component would namely also

[1] Note that we have dropped the explicit dependence of $\hat{C}$ on the observing detectors I, J. We will do this for the rest of this chapter.

[2] Note that this identical equation was already introduced earlier in Eq. 5.7. However, for clarity we also include the equation here.

be 'washed out' by the applied time-shift. This is exactly where GW geodesy can provide additional value and make statements about detection confidence of a GWB with respect to correlated noise sources.

10.2 Gaussian processes

If, in the future, we compute a geodesy Bayes factor $\mathcal{B}$ associated with a candidate GWB, we do not yet know exactly how we should quantitatively interpret this result. In order to fully understand the statistical significance of a particular Bayes factor, we need to know how often it arises simply by chance. However, this poses a dilemma. To quantify a false alarm probability, we would need to know all possible terrestrial signals, which we do not. So instead, we can ask a similar question: how often do particular Bayes factors arise from the generic space of smooth functions in the frequency domain? This latter question can be answered using Gaussian processes.

Gaussian processes are very flexible and are frequently used for model fitting or model predictions based on a data set [291]. In this work, we use the Gaussian processes to produce a distribution of functions with a given mean and variance. We consider each draw from this distribution to be a possible realisation of a correlated terrestrial signal. The two main inputs of the Gaussian process are a covariance matrix, often called the 'kernel', and its mean. In this work, we use the Gaussian processes to generate possible realizations of $\langle \hat{C}(f) \rangle$. The probability density function for the draws is given in Eq. 10.4. This is the probability to draw a certain cross-correlation spectrum **C**(f), from the function space governed by the co-variance matrix Σ [291]

$$p(\mathbf{C}(f)|\mu,\Sigma) = \frac{1}{(2\pi)^{n/2}|\Sigma|^{1/2}} \cdot \exp\left(-\frac{1}{2}(\mathbf{C}(f)-\mu)^T\Sigma^{-1}(\mathbf{C}(f)-\mu)\right), \tag{10.4}$$

where n is the dimension of the co-variance matrix Σ.

We generate distributions of cross-correlation spectra with zero mean and consider one of the most commonly used co-variance matrices, the so called 'squared expo-

nential (SE)'. In this case, the covariance between cross-correlation values measured at frequencies f_i and f_j is given by [291]

$$\Sigma_{\mathrm{SE},ij}(\sigma, l) = \sigma^2 \exp\left(-\frac{(f_i - f_j)^2}{2l^2}\right). \tag{10.5}$$

σ^2 is the variance at a single frequency, and while this parameter can be used to scale the signal strength with respect to observations, it will have no impact on the spectral shape of the draws from the distribution. l is the characteristic length-scale over which our $\mathbf{C}(\mathrm{f})$ measurements are correlated across frequencies. We would like to point out that this correlation across frequencies is purely 'artificial' and is a means for us to create a smooth signal curve with certain properties. This is unrelated to the fact that stationary data has independent frequency bins (see Chapter 4).

In order to utilize Eqs. 10.4 and 10.5, we still need to choose a length-scale parameter l. We will tune this parameter by deliberately targeting the most conservative scenario, in which the Gaussian process yields cross-correlation spectra that most resemble – on average – a proper astrophysical/cosmological signal. In doing so, we will always obtain conservative estimates of the false alarm probability for a given geodesy Bayes factor.

To select the most conservative value of the length-scale parameter, we will maximize the probability for our target astrophysical signal itself to be drawn from the Gaussian process. The cross-correlation spectrum we expect from a GWB is $\mathbf{C}(f) = \gamma_{\mathrm{HL}}(f) \cdot \Omega_{\mathrm{ref}} \left(\frac{f}{f_{\mathrm{ref}}}\right)^{\alpha} := \mathbf{C}_{\alpha}(\mathrm{f})$, with $\alpha = 0$, 2/3 or 3, where we approximate the mean to be zero. These are the power-laws typically searched for by the LIGO, Virgo and KAGRA collaborations [30]. Note that we have chosen the Hanford-Livingston baseline as our observing baseline. This baseline is the most sensitive for observing an isotropic GWB, due to their better sensitivity compared to Virgo but more importantly because their ORF is considerably larger. The log-likelihood of this signal under our Gaussian process is

$$\begin{aligned} \ln(\mathcal{L}) &= \ln p(\mathbf{C}_{\alpha}(\mathrm{f}) | \mu = 0, \Sigma) \\ &= -\frac{1}{2}\ln(|\Sigma|) - \frac{1}{2}\mathbf{C}_{\alpha}(\mathrm{f})^T \Sigma^{-1} \mathbf{C}_{\alpha}(\mathrm{f}) + \text{constants}. \end{aligned} \tag{10.6}$$

As we will later freely adjust the overall amplitude of our Gaussian process draws in order to vary their SNRs, we will optimize only the length parameter l, fixing the overall covariance to $\sigma^2 = 1$. Accordingly, for consistency we normalize our target astrophysical signal via

$$\tilde{\mathbf{C}}_{\alpha}(f) = \frac{\mathbf{C}_{\alpha}(f)}{\sqrt{\mathrm{Var}\,\mathbf{C}_{\alpha}(f)}}, \tag{10.7}$$

choosing the l that maximizes $\ln p(\tilde{\mathbf{C}}_\alpha(f)|\mu = 0, \Sigma)$.

In practice, the inversion of Σ is unstable, with a determinant that is nearly zero. To increase stability, we add a diagonal term to the co-variance matrix: $\Sigma \to \Sigma + \epsilon\, I$, with I the identity matrix and ϵ a small dimensionless constant, here chosen to be 10^{-3}. This diagonal term can be interpreted as a noisy observation of our function $\mathbf{C}_\alpha(\mathrm{f})$.

We optimize the kernel parameter l using the formalism described above, in the following parameter range: $l \in [10^{-4}\,\mathrm{Hz}, 10^{4}\,\mathrm{Hz}]$. The optimal length-scale parameter to mimic a power-law with slope $\alpha = 0$, 2/3 and 3 are respectively: $l = 47.65\,\mathrm{Hz}$, $33.18\,\mathrm{Hz}$ and $29.20\,\mathrm{Hz}$, determined using a 0.01Hz frequency resolution for l.

In Fig. 10.1, we show several random draws from the Gaussian process described by the SE-kernel, optimized to most closely match an $\alpha = 2/3$ astrophysical signal, as well as the signals we expect to observe from unresolved binary mergers and terrestrial Schumann resonances. Here we have chosen $\alpha = 2/3$ since this GWB is the signal expected to be first observable by advanced LIGO and advanced Virgo.

The Schumann resonance spectrum used here is identical to the spectrum used in the first description of GW Geodesy [106]. This spectrum is obtained by replacing the strain data s_1 and s_2 in Eq. 10.1 by data from magnetometers measuring the Schumann resonances in a magnetically quiet location, the Hylaty station in Poland as reported in [134]. We furthermore assume that the coupling function linking environmental magnetic fields to GW interferometers is a power-law that declines as $\propto f^{-2}$ in frequency [106]. An important assumption about our correlated magnetic spectrum is that it is positive since the frequency dependent sign of the cross-power between the two LIGO sites is unknown. More detailed studies in the future could investigate the effect when relaxing this assumption. In this context two models have been developed modeling a Schumann resonance; first a simple analytical model [204] and secondly a more complex model taking the anisotropic character of lighting strikes sourcing the Schumann resonances into account [203]. These analytical models give a mathematical framework to investigate the departure of the assumption of a fully positive magnetic cross-spectrum as a function of the magnetic phase angle between the two sites [204] or the global lightning density map [203].

Fig. 10.1 illustrates that the SE-kernel with optimized parameters is able to produce cross-correlation curves which are, on average, functionally similar to the true-signal curve. As discussed above, this behavior is deliberately conservative, maximizing the probability that our Gaussian process will spuriously yield cross-correlation

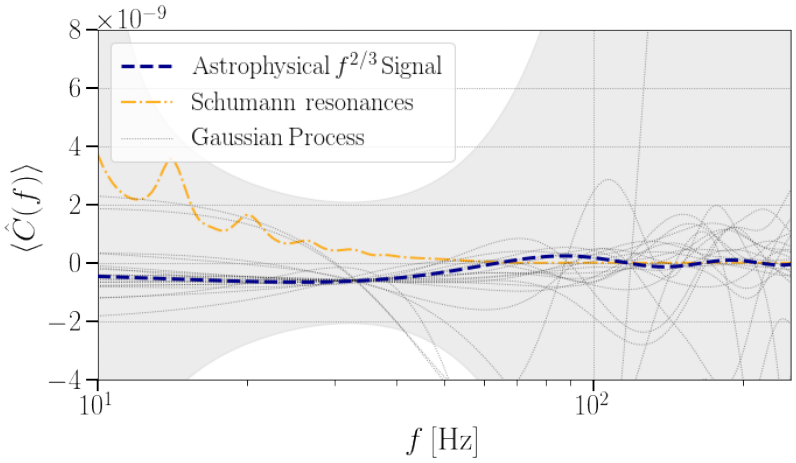

Fig. 10.1.: The expected cross-correlation for an astrophysical background from unresolved binary systems (blue/bold), Schumann resonances (orange) and 20 random draws from the SE kernel (gray). The kernel-parameter used for the Gaussian process instantiations is the optimal value for mimicking an 2/3-power-law signal, as described in the text. The injected signal strength yields $\mathrm{SNR} = 3$ after a 3-year long observation at LIGO's design sensitivity.

measurements with favorable geodesy Bayes factors. As already was stated in the initial implementation of the GW Geodesy framework, having similar zero-crossings might play a crucial role in mimicking a signal [106]. Everywhere in this analysis we investigate the GW Geodesy framework in the frequency range of 10–250 Hz with a frequency resolution of 0.24 Hz. The lower limit is based on the lowest frequency that can be observed by current ground-based interferometers. Because of the combined effects of the ORF and the reduced sensitivity at higher frequencies, there is a negligible gain when going to higher frequencies compared to the computational costs. For example, when looking for an isotropic power-law signal using the HL-baseline with a power-law slope of α =0, 2/3 and 3, 99% of the sensitivity during the latest O3 run was respectively contained below 76.1 Hz, 90.2 Hz and 282.8 Hz [30].

In the rest of this chapter, when we mention a Gaussian process signal, we are referring to a Gaussian process with a SE kernel and a length-scale parameter optimized for the relevant power-law slope α. Also, when mentioning 'unknown correlated noise sources', we refer to this Gaussian process signal, which in this study serves as a conservative proxy for these unknown correlated noise sources.

10.3 False alarm probabilities and detection confidence

10.3.1 Simulations

Using our Gaussian process machinery, we will explore the false alarm probabilities and statistical significance associated with geodesy Bayes factors. We will make use of three different sources of cross-correlation: a power-law signal with slope α, magnetic Schumann resonances and a proxy for unknown terrestrial cross-correlation mimicking an α-power-law signal using Gaussian processes. As a proof of concept we will start by investigating Bayes factors given by signals with SNR=3 after three years of observation at LIGO's design sensitivity [20]. This specific signal-to-nose-ratio is chosen as this is the fiducial value when one might first claim (a hint of) evidence for a detected GWB.

The signal-to-noise ratio of our model signal $\mathbf{C}_\alpha(f)$ is given by

$$\begin{aligned} \mathrm{SNR}_\alpha &= \frac{\int_f \hat{C}(f)\mathbf{C}_\alpha(f) \times \sigma_\alpha^2/\sigma^2}{\sigma_\alpha}, \\ &\text{with} \\ \sigma_\alpha^2 &= \left(\int_f \frac{{\mathbf{C}_\alpha}^2(f)}{\sigma^2} \right)^{-1}. \end{aligned} \tag{10.8}$$

In what follows we will drop the subscript α and refer to the signal to noise ratio SNR_α as just SNR. One can compute the *expected* SNR or the *observed* SNR. In the former case $\hat{C}(f)$ is the injected signal, whereas in the latter case Gaussian-distributed noise consistent with Eq. 4.12 has been added to each frequency bin of $\hat{C}(f)$.

When performing an injection for a certain power-law with slope $\alpha = 0, 2/3, 3$, the signal is injected with an expected SNR_α of the desired strength. Note that in case of the Schumann signal as well as the Gaussian process signal, sometimes a power-law with a different slope might be recovered with a higher SNR as their spectral shape can align better with a different power-law: $\mathrm{SNR}_{\tilde{\alpha}} > \mathrm{SNR}_\alpha$, where $\tilde{\alpha} \neq \alpha$.

Note that the SNR defined in Eq. 10.8 can be positive if the data matches well with our signal model or negative if the data anti-correlates with our signal model. Here our signal model consists of the true HL overlap reduction function with a power-law GW signal. As we are concerned primarily with signals we might mistake as astrophysical, we will only investigate those that yield positive SNRs as observed by the HL baseline. Therefore, if the SNR of a Gaussian process draw is negative

at the target α (0, 2/3 or 3), it is rejected and a new signal is simulated. This happens, on average, 50% of the time. The rejection of this signal is chosen to match a realistic experimental condition. In case of a detection, one would like to apply this tool mainly to a positive SNR detection, whereas a negative SNR detection would immediately be categorized as unphysical. Note that this only applies for an isotropic GWB. As discussed in Chapter 4, a point source could, depending on its sky localisation, yield a negative SNR when searched for using analysis methods for an isotropic GWB.

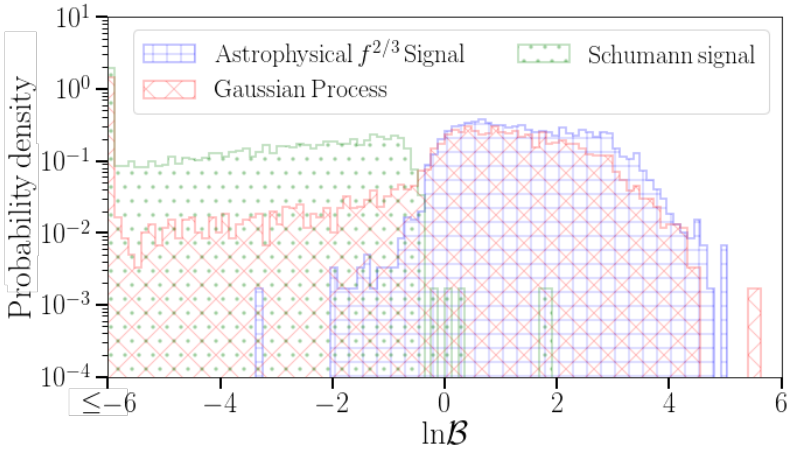

Fig. 10.2.: Probability density of $\ln\mathcal{B}$ for an astrophysical $\alpha = 2/3$ power-law signal, random draws from a Gaussian process using our optimized (most conservative) SE-kernel and a Schumann signal. The lowest bin contains all $\ln\mathcal{B} \leq -6$. For each signal type 5000 injections were performed with an injection strength of SNR=3, when recovered with an $\alpha = 2/3$ signal model. We note that there is a strong separation between a Schumann signal and an astrophysical signal. Even though a significant fraction of the Gaussian process signals have large negative log-Bayes factors, there is also a substantial fraction which is able to very well mimic the astrophysical signal and achieve similar log-Bayes factor. Also, note that the the loudest reported log-Bayes factor in this figure is from the Gaussian process.

For our three signal classes, we simulate and analyze 5000 cross-correlation spectra. In the case of the astrophysical power-law and Schumann resonances, this involves generating 5000 distinct Gaussian noise realizations that are added to the fixed underlying models. Under our Gaussian process, meanwhile, each trial involves a random draw from our Gaussian process (restricted to positive SNR) and a randomly generated noise spectrum. For every injection, we use `PyMultiNest` to compute Bayesian evidences [104], using 2000 live-points. `PyMultiNest` is a python interface for `MultiNest` [166, 167], which is an implementation of the nested sampling algorithm [328, 329].

The model corresponding to our hypothesis $\mathcal{H}_\gamma$ has two free parameters, the reference amplitude $\Omega_{\rm ref}$ of the signal at $f_{\rm ref} = 25$Hz and the power-law slope α. We use a log uniform prior for the reference amplitude between 10^{-12} and 10^{-6}. For α we use a Gaussian prior with zero mean and a standard deviation of 3.5. Our alternative hypothesis $\mathcal{H}_{\rm Free}$ has three additional free parameters, the distance between the two interferometers Δx and the rotation angles of your interferometers ϕ_1 and ϕ_2 [106]. We use uniform priors on ϕ_1 and ϕ_2 (0,2π). Furthermore we use a uniform prior on cosθ, where $\Delta x = 2R_{\rm Earth} \sin\theta/2$. This corresponds to a prior on the distance between the detectors: $p(\Delta x) \propto \Delta x$. These priors are chosen to be consistent with earlier work [106].

Figure 10.2 represents the log-Bayes distribution for the different signal models, assuming SNR=3 and $\alpha = 2/3$. The lower bin in the histograms also includes all simulations with a recovered log-Bayes factor smaller than -6. The smallest log-Bayes factor for an injection with a Schumann signal is approximately -23, whereas this is approximately -6×10^7 in case of the Gaussian process signal.

First, we notice the overlap of the histograms of the Gaussian process and the power-law signals is significantly larger than the overlap between the Schumann signal and the power-law signal. This shows the selection of the Gaussian process parameters in section 10.2 is successful and indeed yields a conservative condition, where the Gaussian process is able to mimic the power-law signal. However, it also shows what possibly is one of the weaknesses of current implementation of the tool: our Gaussian process might be overly conservative as it is able to very well mimic the $\alpha = 2/3$-power-law, and therefore to a large extent yielding similar log-Bayes factors.

On the other hand, whereas power-law signals yield a handful of mildly negative log-Bayes values, the Gaussian processes give an extended tail towards negative log-Bayes factors, which will further grow as we increase the SNR of our injections. This illustrates the intrinsic random nature of the Gaussian process. Despite the process being able to produce signals mimicking the power-law signal, at the same time, other types of signals are produced which are not properly described by a power-law.

Assuming that the Gaussian process is a (very) conservative, estimate of a terrestrial contamination for isotropic GWB searches, we can construct an upper bound on the false alarm probability and detection probability associated with our geodesy Bayes factors. The false alarm probability (FAP) is the probability with which our terrestrial signal (for which the Gaussian process is our proxy) gives a geodesy Bayes factor as high or higher than the Bayes factor we recover from our actual

data. The detection probability gives the probability to detect the signal at a certain FAP/log-Bayes factors. The detection probability and false dismissal probability (FDP) are linked to each other by: $\mathrm{FDP} = 1 - \mathrm{det.prob.}$; where the FDP is a figure of merit of the probability to wrongly reject the signal model.

For future observations, we would like to have the FAP to be as small as possible (i.e. unlikely to be a false signal) and a large detection probability (i.e. likely to be true signal). Generally, before analysing the data, one chooses a FAP considered to be the largest allowed value, for example 5% or 1%. Given a signal injected with a SNR=3 the log-Bayes factors and detection probability are listed in Table 10.1 for a FAP of 5% and 1%. We also show the results when looking for a power-law signal with slope $\alpha = 0$ or 3. We see, for example, that given an apparent detection of the GWB with $\mathrm{SNR} = 3$ under an $\alpha = 2/3$ model, there is no more than a 5% chance that a log-Bayes factor $\ln \mathcal{B} = 2.94$ would arise from a non-astrophysical signal.

We notice that for a given FAP, the detection probability becomes higher for power-law signals with a steeper slope (larger α). However all reported detection probabilities are very small. This is linked to our Gaussian process being (overly) conservative and is very good in mimicking the GW power-law signals. This was already clear from Figure 10.2 for $\alpha = 2/3$.

Table 10.2 shows the same for an injected signal with SNR=5 when looking for a power-law with slope $\alpha = 0$, 2/3 or 3. The detection probability for a flat and 2/3-power-law remains very small. Note that for a flat power-law the detection probability even decreases slightly when going from SNR=3 to SNR=5. For an $\alpha = 3$ power-law there is on the other hand a drastic increase in detection probability when going from SNR=3 to SNR=5.

Table 10.3, for comparison, lists log-Bayes factors and detection probabilities when one compares the power-law signals with a Schumann signal with an injection strength of SNR=3. For a fixed FAP of 1%, the detection probability is >99% meaning the GW Geodesy tool is very effective in differentiating a Schumann signal from a power-law signal. Here we have to take the assumptions into account used to generate the Schumann resonance signal. Future work should investigate whether the results presented here still hold when using different assumptions when generating the Schumann resonance signal, as well as which scenario is most likely the true situation.

As searches for the GWB accumulate SNR slowly over the course of months to years, the above scenario in which a candidate signal has a moderate $\mathrm{SNR} = 3$ represents a realistic situation in which we will first need to use the geodesy test. It is

	$\alpha = 0$		$\alpha = 2/3$		$\alpha = 3$	
FAP	ln$\mathcal{B}$	det. prob.	ln$\mathcal{B}$	det. prob.	ln$\mathcal{B}$	det. prob.
5.0%	2.95	6.92%	2.94	10.56%	3.42	15.44%
1.0%	3.68	0.76%	3.72	1.78%	4.04	8.10%

Tab. 10.1.: The log-Bayes factor and detection probabilities matching a FAP of 1% and 5% comparing a α-power-law GW signal and a Gaussian process signal. For each signal type 5000 injections were performed with an injection strength of SNR=3.

	$\alpha = 0$		$\alpha = 2/3$		$\alpha = 3$	
FAP	ln$\mathcal{B}$	det. prob.	ln$\mathcal{B}$	det. prob.	ln$\mathcal{B}$	det. prob.
5.0%	3.54	6.78%	3.67	15.54%	3.91	67.08%
1.0%	4.12	0.62%	4.30	1.80%	4.71	41.40%

Tab. 10.2.: The log-Bayes factor and detection probabilities matching a FAP of 1% and 5% comparing a α-power-law GW signal and a Gaussian process signal. For each signal type 5000 injections were performed with an injection strength of SNR=5.

		$\alpha = 0$	$\alpha = 2/3$	$\alpha = 3$
ln$\mathcal{B}$	FAP	det. prob.		
-0.82	5.0%	99.72%	99.64%	99.60%
-0.55	1.0%	99.44%	99.28%	99.28%

Tab. 10.3.: The log-Bayes factor and detection probabilities matching a FAP of 1% and 5% comparing a α-power-law GW signal and a Schumann signal. For each signal type 5000 injections were performed with an injection strength of SNR=3.

instructive, however, to more broadly investigate how the distributions of log-Bayes factors evolve as a function of SNR. To do this, we simulate signals with strengths logarithmically spaced between SNR=0.1 and SNR=100. Here we will only be looking at the $\alpha = 2/3$ case, injecting astrophysical $\alpha = 2/3$ power-law signals and drawing random 'terrestrial' signals from our Gaussian process optimized to this same power-law form.

As mentioned above, the free parameters are the reference signal strength $\Omega_{\rm ref}$ at 25Hz and the power-law slope α in case of our hypothesis $\mathcal{H}_\gamma$. For the hypothesis $\mathcal{H}_{\rm Free}$, the set of five free parameters consist of $\Omega_{\rm ref}$, α, Δx, ϕ_1 and ϕ_2. Note that for our astrophysical signal, even though we inject α=2/3 our best fit α may well differ due to different noise instantiations, whereas for the Gaussian process realizations α will adjust to best fit the random signal with a power-law .

In Figure 10.3, the median of the α-posterior is shown with respect to the SNR at which this signal would be observed by the HL-baseline. Note that both α and SNR

are calculated from the posterior consistent with the HL-baseline. Although this might be disfavoured with respect to the posteriors from the Random-Baseline, we are interested on how the HL-baseline would observe such a signal.

For extremely small SNR (< 1), α is closely centered around 0 for both the true power-law GW signal as well as the simulated Gaussian process signal. These signals are so weak that whatever we observe is dominated by the Gaussian background of our search. This Gaussian background has by definition no power-law slope and therefore matches $\alpha = 0$.

When our signal has a strength of order SNR=1, the retrieved values of α are still centered around zero, but the variance increases. The posterior-median α spans a range from large negative to large positive power-law slopes. There starts to be some excess but given the weak strength of the signal the randomness of the Gaussian background can drive the large negative or positive α.

The behaviour for power-law GW signals and the Gaussian process signals starts to differ from SNR $\sim$ 10. In the case of a power-law signal, the variation on α drastically decreases and the center of the retrieved values shifts from 0 to the real value: $2/3$. Whereas in case of the Gaussian process signal, α (slightly) prefers to take a positive value, there is a large variation on its recovered value. The bulk of the recovered α values lies between $\alpha = -2$ and $\alpha = 3$. This seems to indicate that with large enough SNR, we can make a clear distinction between a power-law GW signal and some unknown (terrestrial) correlated noise sources, simulated by the Gaussian processes.

To further strengthen this statement, Figure 10.4 shows the log-Bayes factor between $\mathcal{H}_\gamma$ and $\mathcal{H}_{\rm Free}$ as a function of the observed SNR. Weak signals are on average unable to differentiate between $\mathcal{H}_\gamma$ and $\mathcal{H}_{\rm Free}$, leading to log-Bayes factors $\sim$0. When the observed SNR reaches values $\sim$1, the log-Bayes factor of the power-law $2/3$ signals starts to prefer positive values, with increasing LogBayes for increasing SNR. This is consistent with both our expectations for a true signal as well as the earlier results of the GW Geodesy tool [106].

At the same time, the data from the Gaussian process starts to separate into two categories when the SNR reaches order one. One population of signals starts to prefer negative log-Bayes factors, preferring $\mathcal{H}_{\rm Free}$ over $\mathcal{H}_\gamma$. These are the signals that look nothing like a power-law signal as observed by the HL-baseline. However, there is also a population of signals that starts to prefer positive log-Bayes factors. These are the signals that succeeded in mimicking the HL-baseline $\alpha = 2/3$ power-law signal to a (very) good extent. This behaviour is expected because we purposely chose

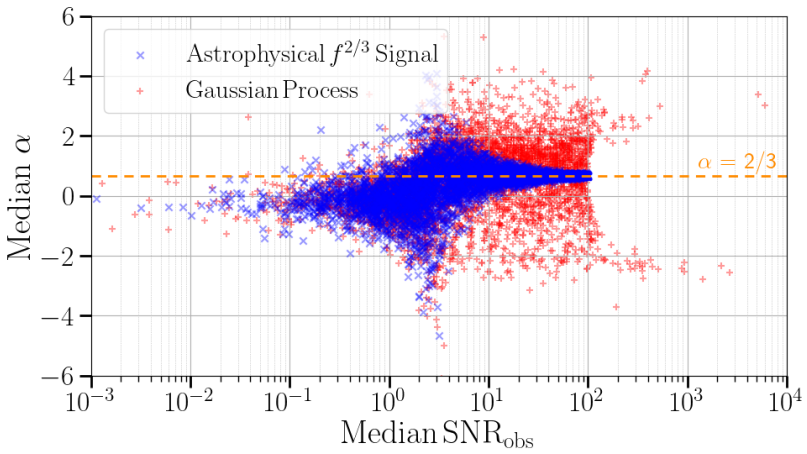

Fig. 10.3.: The median of the posterior of the power-law slope α is represented against the median of the SNR-posterior, assuming the signal has been observed by the HL-baseline. Each point in this scatter plot represents one injected signal. For each signal type 5000 injections were performed with a logarithmically spaced injection strength between SNR=0.1 and SNR=100.

our Gaussian process parameters to have this kind of behaviour, which is the key ingredient in creating conservative estimates for the FAP. However, as the observed SNR keeps on increasing the population of signals with positive log-Bayes factors decreases at the cost of the population with negative log-Bayes factors. Although at high SNR, the probability for a Gaussian process to have high, positive log-Bayes factors is very small it is still non-zero.

Fig. 10.3 and Fig. 10.4 enable us to make statements on the distinctive character of our tool to differentiate a power-law GW signal and some unknown (terrestrial) correlated noise sources, simulated by the Gaussian process.

10.3.2 Detection probability curve

We construct a detection probability curve – for the situation $\alpha = 2/3$ – where we show the behaviour of the detection probability versus the SNR of the signal for several fixed false alarm rates. Injections at five different SNRs were performed: 1.25, 3, 5, 10 and 20. At each SNR, we performed 5000 injections for both the conservative Gaussian process signal as well as an $\alpha = 2/3$ power-law signal. The result is shown in Fig. 10.5.

The results indicate our Gaussian process is very conservative. Given a FAP of 1%, the detection probability at SNR 20 is not even reaching 40%. A detection probability

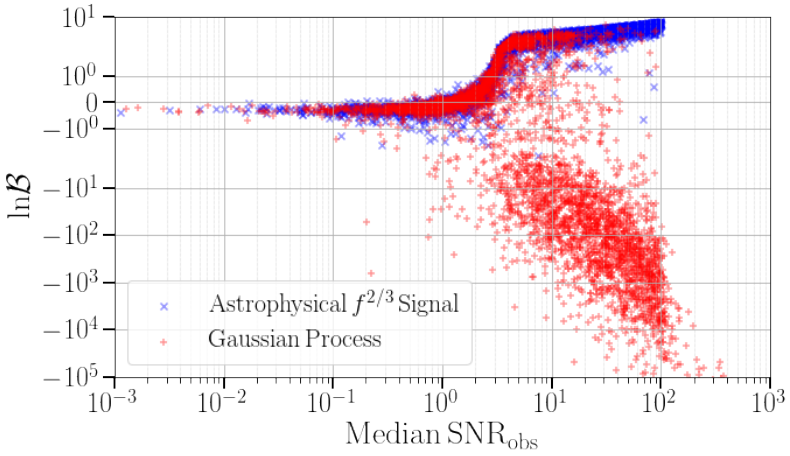

Fig. 10.4.: The Log-Bayes factor comparing a 2/3-power-law signal with a Gaussian process is represented against the median of the SNR-posterior, assuming the signal has been observed by the HL-baseline. There are 40 events with $\ln\mathcal{B} < -10^5$, which are not shown in this figure. The smallest $\ln\mathcal{B} = -5.3 \times 10^7$. Each point in this scatter plot represents one injected signal. For each signal type 5000 injections were performed with a logarithmically spaced injection strength between SNR=0.1 and SNR=100.

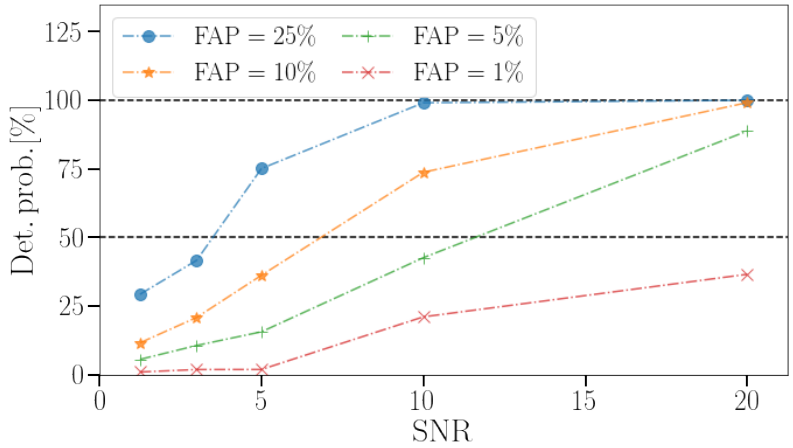

Fig. 10.5.: Detection probability of a 2/3-power-law signal, for false alarm probabilities of 1% (red), 5%(green), 10%(orange) and 25% (blue). The black dashed lines indicate a detection probability of 50% and 100%. Signals were injected at SNR = 1.25, 3, 5, 10 and 20. For each signal type and SNR 5000 injections were performed.

of 50% and 100% is indicated by the black dashed curves. Given a FAP of 5%, a detection probability of 50% is reached above SNR=10. As shown in Table 10.2, in case of a power-law with SNR = 5 and a steeper slope, e.g. $\alpha = 3$, a detection probability of 41% (67%) is reached for a FAP of 1% (5%). This seems to indicate that even with our very conservative Gaussian process signal generation, a GWB signal with steeper power-law slope is more easily distinguishable from correlated terrestrial noise, here modeled by the Gaussian process.

10.3.3 Application to a real life scenario - O2 outlier

When analyzing the results of their second observing run, the LIGO and Virgo collaborations observed an excess with a SNR=1.25 for a power-law model with $\alpha = 2/3$, as well as $\alpha = 3$ [14]. At the time of this observation, it was stated the low SNR excess was very likely due to random fluctuations in the data. This is confirmed by the lack of detection by the subsequent O3 results [30]. With the geodesy tool described in this chapter, we could, at the time of the O2 observation, have answered a complementary question: given that we have observed an excess with SNR=1.25 for a power-law model with $\alpha = 2/3$, what is the probability the observed signal is due to a source of correlated noise instead of GWs. Although the O3 results have confirmed the excess was just a random fluctuation, it is instructive to demonstrate how the geodesy tool could be used in the future. In our demonstration, we will only investigate the excess given a power-law with $\alpha = 2/3$, although one can easily apply the tool to the $\alpha = 3$ case as well.

In what follows we will use the public available cross-correlation spectrum observed by LIGO during O2 [21] to compute the logBayes-factor linked to this observation. To construct the FAP and detection probability, we performed injections of the conservative Gaussian process signal, Schumann resonances, as well as a 2/3-power-law signal with an observed injection strength of SNR=1.25. All injections consist of 5000 samples and result in the distribution of log-Bayes factors shown in Fig. 10.6.

The log-Bayes factor for the observed signal of the O2 run by LIGO and Virgo was computed and found to be 0.063. Given the distributions from the simulations shown in Fig. 10.6, the observed signal is consistent with a FAP of $39.00\% \pm 0.02\%$ and a detection probability of $46.80\% \pm 0.02\%$. The high FAP does not give us enough confidence to prefer a GW signal over a correlated noise source.

However if one compares a GW signal with a correlated signal coming from Schumann resonances a FAP of $1.00\% \pm 0.02\%$ is found, effectively ruling out Schumann

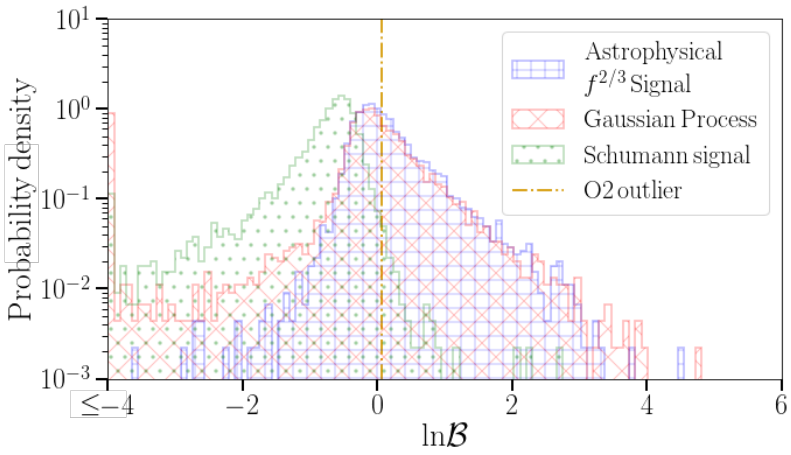

Fig. 10.6.: Probability density of $\ln\mathcal{B}$ for an astrophysical $\alpha = 2/3$ power-law signal, random draws from a Gaussian process using our optimized (most conservative) SE-kernel and a Schumann signal. The lowest bin contains all $\ln\mathcal{B} \leq -4$. For each signal type 5000 injections were performed with an injection strength of SNR=1.25. The choice of $\alpha = 2/3$ and SNR=1.25 matches the parameters of observed outlier of the O2 results for an isotropic GWB [14]. For a low SNR outlier the GW Geodesy tool has very limited power, as can be seen by the high level of overlap between the Gaussian process and the astrophysical signal distributions. However, it can be confidently excluded that the O2-outlier was caused by a Schumann signal.

resonances as possible source with high confidence. This is consistent with projections showing there was no significant magnetic coupling in the analysis for an isotropic GWB using O2 data [14].

10.4 Conclusion and outlook

In this chapter, we presented a tool that requires the observed signal to be consistent with the geometry of the observing detectors. We use Gaussian processes as a conservative proxy for the unknown space of all terrestrial correlated signals that might impact the search for an isotropic GWB. This enables us to make quantitative statistical statements and false alarm probabilities concerning the origin of the observed signal. The framework was applied to a SNR=1.25 excess for an α =2/3-power-law , observed by the LIGO and Virgo collaborations during their second observing run. Based on this analysis there was not enough evidence to prefer a GWB-signal over terrestrial correlated noise. However, Schumann resonances were effectively ruled out as possible source.

In this section we discussed how this GW geodesy tool can be used in the future as well as the assumptions used in the current work and the possibilities for future improvements.

The primary use for this tool is to apply it to the observed cross-correlation spectrum when (a hint of) a power-law isotropic GWB is observed. From analyzing the data three estimated parameters will be needed as input for the GW Geodesy tool we are describing here: the power-law index α, the observed SNR and the log-Bayes factor between $\mathcal{H}_{\mathrm{Free}}$ and $\mathcal{H}_{\gamma}$ for the observed signal. The observed α will be used to re-optimize the kernel parameters to get the most conservative scenario for this specific power-law. The SNR will dictate the injection strength of our data. This will lead to a figure equivalent to Fig. 10.2 in this work and log-Bayes factors linked to a certain FAP as in Tab. 10.1. If the observed log-Bayes factor is larger or equal than the log-Bayes factor linked to the desired $\mathrm{FAP}_{\mathrm{desired}}$ (fixed beforehand) we can state that the correlated noise hypothesis is excluded with the confidence $1\text{-}\mathrm{FAP}_{\mathrm{observation}}$.

Both in its current and previous form [106], the GW Geodesy tool can only be used to validate an isotropic GWB. We are currently working to extend this analysis for use with anisotropic GWB searches.

In this chapter we have only demonstrated the tool for the HL-baseline, since this is currently the most sensitive detector-pair for an isotropic GWB. It is however very easy to apply this technique to any preferred detector pair. At some point the ever increasing detector sensitivities and long observation times may enable the detection of a GWB by more than one detector pair. The current tool is able to make statements on all the baselines separately, but one can imagine extending the tool to get one overall figure of merit to make statements for the entire detector network.

It is important to note that the framework demonstrated in this chapter is only tested when there is either a power-law GW signal present or a globally coherent noise source. The separation between a true GW signal and correlated noise becomes less straightforward if they are both present at the same time with similar strengths. In case of a known noise background a technique as proposed in [267] (see also Chapter 5) could be used to search for both sources at the same time.

When applying this tool to a signal coming from Schumann resonances we assumed the magnetic Schumann spectrum to have a positive cross-power, since the (possibly frequency-dependent) sign is not known for the Hanford-Livingston baseline. In the future the departure from this assumption could be investigated by relying on

analytical models describing Schumann resonances and their global cross-power [203, 204].

Instead of only considering power-law signals, one could also investigate more complex models. In the earlier implementation of the GW Geodesy framework [106] it was shown that the tool is quite robust against modeling a broken power-law with a single power-law. This could mean the framework is mainly sensitive to the zero crossings of the overlap reduction function.

11 The null channel: a tool for power spectral density estimation

In Chapter 8 and Chapter 9 we highlighted how magnetic, seismic, and Newtonian noise could seriously endanger the science potential of the Einstein Telescope. The potential danger of correlated seismic and Newtonian noise is a direct consequence of the design in which three interferometers are organised in a(n) (almost) co-located equilateral triangular configuration. Even though this configuration clearly comes at a cost, it also comes with advantages, which where already briefly mentioned in Chapter 2. In this chapter we will focus on the sky-independent null channel (Sec. 11.1) and how it can be used for PSD estimation in an idealized scenario. In Sec. 11.2 we will formulate a more complicated scenario which takes into account the complexity of correlated and non-identical noise sources in the different detectors. This will be demonstrated using several examples in Sec. 11.3. Finally we will discuss how this formalism can be used in a Bayesian framework to estimate noise PSDs as well as the contributions from correlated noise (Sec. 11.4).

11.1 The sky independent null channel: a gravitational-wave insensitive channel for a triangular configuration of interferometers

11.1.1 Motivation

Given the expected sensitivities for ET, CE and LISA, it is predicted they will observe a large number of overlapping signals [57, 294, 297]. The constant presence of numerous signals will make the estimation of the noise PSD of the these interferometers challenging, while unbiased noise PSD estimation is a key ingredient for all GW detection pipelines. A first method to deal with this is to perform a joint estimation of noise and signal parameters [119, 152]. However, in the case of a triangular

configuration of interferometers one can also use the so-called (sky independent) null channel (also know as null stream or symmetrized Sagnac) [297, 332, 351]. For a network consisting of N detectors one can construct $N-2$ sky location dependent null streams [187, 338, 363–365], i.e. a null channel which depends on the sky position of the GW source it is insensitive to. However, in the case of a triangular configuration of three interferometers, there is a unique null channel which is insensitive to GWs from every direction simultaneously. In the context of the GWB, which targets unresolved sources with an isotropic or extended sky location, one can only use this unique null channel of a triangular configuration of interferometers. In the remainder of this chapter we refer to the sky-location-independent null channel as the 'null channel'.

As explained in Chapter 2, the proposal of the third generation ET interferometric GW detector – as well as the space-based LISA – uses an equilateral triangular composition. For the ET [297], the null channel and its PSD estimation capabilities have been demonstrated in the case of identical and uncorrelated noise for the three different interferometers. A more recent study investigates the effectiveness of the null channel in the presence of noise transients, also known as glitches [182]. Also the authors of [366] describe the benefit of using a null and signal space for parameter estimation in the context of the ET. The consideration of using signal and null space is more extensively discussed in the context of LISA [40, 41, 79, 93–95]. Some of these works investigate the possibility of correlated noise [40, 41, 93–95] and other work, non-identical noise [79]. To a smaller extent the null channel was also discussed in context of the space-based TianQin detector [240]. However, especially in the context of the ET, more work is needed to go from the relatively simple example used in [297] to more complex and realistic situations.

While the null channel might be a necessary tool for PSD estimation, it might also be valuable for data quality and the identification and characterisation of correlated noise sources. Correlated noise is particularly problematic for unmodeled sources of GWs which depend on cross-correlation methods, i.e. the search for a GWB and searches for poorly known transient signals, called GW bursts, such as core collapse supernovae. The basic search method for the GWB relies on cross-correlations between detectors. However, correlated noise can limit the sensitivity of these searches. A large distance between the detectors of the baseline can greatly reduce the amount of correlated noise. Only some global sources as explained in Chapters 5, 7 and 8 remain correlated on the scale of thousands of kilometers. When using (nearly) co-located detectors, cross-correlating data from the detectors no longer suppresses the same amount of noise source, since both detectors are to a large extent affected by the same local noise sources. Such searches were

conducted in the past using the two co-located LIGO Hanford detectors: H1 and H2 [2, 175]. During the analysis of the H1-H2 data from the fifth science run of initial LIGO [2], the frequency band 40Hz to 460Hz was not used in the analysis for an isotropic GWB due to insufficient mitigation of correlated noise. Several methods, such as time shifting the data and computing coherence with environmental noise monitoring channels were used to ensure as best as possible that the other frequency regions were not significantly affected [2, 175]. For the ET there have been several studies investigating correlated noise as described in Chapters 8 and Chapter 9 for correlated magnetic and correlated seismic and Newtonian noise. Based on LISA pathfinder data, some preliminary noise correlation studies have also been performed [92]. Correlated effects from micro-thrusters, the magnetic field and temperature variations on the test-mass system can be expected [92].

This implies the three interferometers of the ET and LISA configurations might have many (local) correlated noise sources, which will lead to a non-negligible impact of these noise sources on the cross-correlation spectrum used in searches for a GWB. For ET, one could use a similar technique as used for the H1-H2 analysis [2, 175] and rely on environmental and instrumental monitors. However, as was the case for the H1-H2 analysis [2, 175], this method might be insufficient to ensure a clean spectrum in the entire sensitive frequency range of the ET detector. Furthermore, noise that couples non-linearly to the detector (e.g. scattered light) would not be taken into account by these methods [2, 175]. While the environmental and instrumental monitoring will be very important, one should aim to do better by using additional techniques.

In this chapter we expand on previous studies by presenting how to perform PSD estimation in the case of correlated and non-identical noise. Whereas earlier work has investigated non identical [40, 41, 93–95, 182] and correlated noise [79] separately, we present one formalism to address both non-identical and correlated noise simultaneously. While such a formalism is needed to achieve unbiased PSD estimations, it also provides further information on the correlated noise sources, which is interesting in its own right, particularly for GWB and burst searches.

11.1.2 Formalism

If one formulates an equilateral triangular formation of three interferometers, their detector response functions, first introduced in Chapter 2 (Eq. 2.3), are given by

$$\begin{aligned}\hat{\mathbf{d}}^{\mathbf{X}} &= \frac{1}{2}(\hat{\mathbf{e}}^{\mathbf{1}} \otimes \hat{\mathbf{e}}^{\mathbf{1}} - \hat{\mathbf{e}}^{\mathbf{2}} \otimes \hat{\mathbf{e}}^{\mathbf{2}}),\\ \hat{\mathbf{d}}^{\mathbf{Y}} &= \frac{1}{2}(\hat{\mathbf{e}}^{\mathbf{2}} \otimes \hat{\mathbf{e}}^{\mathbf{2}} - \hat{\mathbf{e}}^{\mathbf{3}} \otimes \hat{\mathbf{e}}^{\mathbf{3}}),\\ \hat{\mathbf{d}}^{\mathbf{Z}} &= \frac{1}{2}(\hat{\mathbf{e}}^{\mathbf{3}} \otimes \hat{\mathbf{e}}^{\mathbf{3}} - \hat{\mathbf{e}}^{\mathbf{1}} \otimes \hat{\mathbf{e}}^{\mathbf{1}}).\end{aligned} \tag{11.1}$$

The null channel is the sum of the strain output of three interferometers in an equilateral triangle, which we will call X, Y and Z. Each detector measures a strain time series $s^I(t)$, which consists both of noise $n^I(t)$ as well as a GW component $h^I(t)$,

$$s^I(t) \equiv n^I(t) + h^I(t), \tag{11.2}$$

where I runs over X, Y and Z. The null channel is given by the sum of the output of the three interferometers [93, 297]:

$$\begin{aligned}s_{null}(t) &\equiv \sum_{I=X}^{Z} s^I(t)\\ &= \sum_{I=X}^{Z} n^I(t) + \sum_{I=X}^{Z}\sum_{A} d^I_{ij} e^{ij}_A h^I_A(t)\\ &= \sum_{I=X}^{Z} n^I(t) + \sum_{A}\left(\sum_{I=X}^{Z} d^I_{ij}\right) e^{ij}_A h^I_A(t)\\ &= \sum_{I=X}^{Z} n^I(t),\end{aligned} \tag{11.3}$$

since from Eq. (11.1) follows $\sum_{I=X}^{Z} \hat{\mathbf{d}}^I = \hat{\mathbf{0}}$. Regardless of the waveforms and polarization A of the GWs, the sum of three interferometers which form an equilateral triangle, as is the case for ET and LISA, becomes insensitive to GWs. Since this sum, the null channel, is insensitive to any GW signal, one can use it to estimate the noise sources present in the detectors. However the calculation assumes the arms of the different interferometers are exactly co-located. For the ET, deviations can be expected since the terminal and central stations of two different ET interferometers are separated by about 300–500 m [161]. In this chapter we do not consider any such deviations and assume the interferometers to be exactly co-located, leading to a perfect null channel. Furthermore, the null channel deteriorates for higher frequencies in an interferometric gravitational-wave detector. This is due to finite

arm length effects. There are further imperfections when the arm lengths are not exactly equal, as will be the case for LISA [40]

We introduce the PSD of the strain of interferometer I, S_s^I,

$$\begin{aligned}\langle s^I(f)s^{I,*}(f')\rangle &= \frac{1}{2}\delta(f-f')S_s^I(f)\\ &= \frac{1}{2}\delta(f-f')\left[S_n^I(f)+S_h^I(f)\right],\end{aligned} \tag{11.4}$$

where $S_n^I(f)$ and $S_h^I(f)$ are respectively the noise and GW PSDs for interferometer I. The CSD of the strain of interferometers I and J, $S_s^{IJ}(f)$, is given by

$$\begin{aligned}\langle s^I(f)s^{J,*}(f')\rangle &= \frac{1}{2}\delta(f-f')S_s^{IJ}(f)\\ &= \frac{1}{2}\delta(f-f')\left[S_n^{IJ}(f)+S_h^{IJ}(f)\right],\end{aligned} \tag{11.5}$$

where $S_n^{IJ}(f)$ and $S_h^{IJ}(f)$ are respectively the noise and GW CSDs for interferometers I and J.

The quantities $S_h^I(f)$ and $S_h^{IJ}(f)$ depend on the response of the interferometer(s) I and I and J respectively, whereas one typically is interested in $S_h(f)$ of the source regardless of the observing interferometer. In this chapter, we focus on an isotropic GWB with equal levels of tensor cross- and plus- polarization. However, the formalism we will present in Sec. 11.2 can be used to estimate noise PSDs in the presence of any other GW signal. In Appendix A of [215] the following equalities are derived for an isotropic GWB with equal levels of tensor cross- and plus- polarization,

$$\begin{aligned}S_h^I(f) &= \frac{3}{10}S_h(f)\\ S_h^{IJ}(f) &= -\frac{3}{20}S_h(f).\end{aligned} \tag{11.6}$$

Note these calculations rely on the detector response of the ET as well as a fully isotropic GW signal. In Appendix B of [215] the equivalent terms in case of the presence of an isotropic GWB with scalar or vector polarizations are also derived, which are predicted by several extensions of general relativity [107].

One can already use the null channel for getting information on the detector noise, but even more information can be extracted using a set of three channels A, E and T. These three channels are often used in the context of LISA and are defined as the

following linear combinations of the three X, Y and Z interferometers [332, 351]:

$$\begin{aligned} A &= \frac{1}{\sqrt{2}}(Z - X) \\ E &= \frac{1}{\sqrt{6}}(X - 2Y + Z) \\ T &= \frac{1}{\sqrt{3}}(X + Y + Z). \end{aligned} \tag{11.7}$$

The T channel is a normalized version of the null channel as first defined in Eq. 11.3 and is insensitive to GWs, whereas the A and E channels contain the GW signal [332]. Under the assumption of identical noise sources in X, Y and Z, the A, E and T channels are orthogonal with respect to one another, implying that their noise PSDs are uncorrelated.

Note that the use of the A, E and T channels as used by the LISA community is equivalent to the description of the null and signal space in the context of the ET [366]. The signal space considered in [366] consists of two channels which correspond to $-A$ and $-E$ in this work and the null space corresponds to T.

11.2 Null channel in a complex environment

In this section, we introduce a formalism to expand on the null channel by using the A, E and T channels. First, we discuss the presence of identical correlated noise, which already has been studied in the context of LISA [287]. Afterwards, we relax this assumption and describe the most general case describing non-identical and correlated noise sources.

11.2.1 Formalism in the presence of identical correlated noise

In the presence of correlated noise, identical in all interferometers – $S_n^{XY}(f) = S_n^{XZ}(f) = S_n^{YZ}(f) \equiv S_n^{IJ}(f)$ – as well as assuming identical noise PSDs – $S_n^X(f) = S_n^Y(f) = S_n^Z(f) \equiv S_n^I(f)$ – the following equalities hold for the A, E and T channels

$$\begin{aligned}
\langle T(f)T^*(f')\rangle &= \frac{1}{2}\delta(f-f')\left[S_n^I(f) + 2S_n^{IJ}(f)\right] \\
\langle A(f)A^*(f')\rangle &= \frac{1}{2}\delta(f-f')\left[S_n^I(f) - S_n^{IJ}(f) + \mathcal{O}\left(S_h(f)\right)\right] \\
\langle E(f)E^*(f')\rangle &= \frac{1}{2}\delta(f-f')\left[S_n^I(f) - S_n^{IJ}(f) + \mathcal{O}\left(S_h(f)\right)\right] \qquad (11.8) \\
\langle T(f)A^*(f')\rangle &= \langle A(f)T^*(f')\rangle = 0 \\
\langle T(f)E^*(f')\rangle &= \langle E(f)T^*(f')\rangle = 0 \\
\langle E(f)A^*(f')\rangle &= \langle A(f)E^*(f')\rangle = \mathcal{O}\left(S_h(f)\right).
\end{aligned}$$

The normalized null channel, i.e. the T channel, can be used for noise PSD estimation since it is independent of the GW signal.

We note there is no correlation between the A and T as well as E and T channels, since the channels were constructed to form independent signal and null space [332, 351, 366]. The exact value of the GW term $\mathcal{O}\left(S_h(f)\right)$ for an isotropic GWB is derived in Appendix A and Appendix B of [215] for respectively Tensor and Scalar-Vector polarized GWs. However, here we only focus on the noise terms as they are our primary interest in this study.

11.2.2 Formalism in the presence of non-identical and correlated noise

In the more general scenario where the correlated noise as well as the noise PSDs are unique for each interferometer, Eq. 11.8 changes to,

$$
\begin{aligned}
\langle T(f)T^*(f')\rangle &= \frac{1}{2}\delta(f-f')\left[\frac{1}{3}(S_n^X(f)+S_n^Y(f)+S_n^Z(f))\right.\\
&\qquad \left.+\frac{2}{3}(S_n^{XY}(f)+S_n^{XZ}(f)+S_n^{YZ}(f))\right]\\
\langle A(f)A^*(f')\rangle &= \frac{1}{2}\delta(f-f')\left[\frac{1}{2}(S_n^X(f)+S_n^Z(f))-S_n^{XZ}(f)+\mathcal{O}\left(S_h(f)\right)\right]\\
\langle E(f)E^*(f')\rangle &= \frac{1}{2}\delta(f-f')\left[\frac{1}{6}(S_n^X(f)+4S_n^Y(f)+S_n^Z(f))+\frac{1}{3}S_n^{XZ}(f)\right.\\
&\qquad \left.-\frac{2}{3}(S_n^{XY}(f)+S_n^{YZ}(f))+\mathcal{O}\left(S_h(f)\right)\right]\\
\langle T(f)A^*(f')\rangle = \langle A(f)T^*(f')\rangle &= \frac{1}{2}\delta(f-f')\left[\frac{1}{\sqrt{6}}(S_n^Z(f)-S_n^X(f)+S_n^{YZ}(f)-S_n^{XY}(f))\right]\\
\langle T(f)E^*(f')\rangle = \langle E(f)T^*(f')\rangle &= \frac{1}{2}\delta(f-f')\left[\frac{1}{3\sqrt{2}}(S_n^X(f)-2S_n^Y(f)+S_n^Z(f)\right.\\
&\qquad \left.-S_n^{XY}(f)+2S_n^{XZ}(f)-S_n^{YZ}(f))\right]\\
\langle E(f)A^*(f')\rangle = \langle A(f)E^*(f')\rangle &= \frac{1}{2}\delta(f-f')\left[\frac{1}{2\sqrt{3}}(-S_n^X(f)+S_n^Z(f)-2S_n^{YZ}(f)\right.\\
&\qquad \left.+2S_n^{XY}(f))+\mathcal{O}\left(S_h(f)\right)\right],
\end{aligned}
\tag{11.9}
$$

whereas just as in Eq. 11.8 the exact contribution of the GW term $\mathcal{O}\left(S_h(f)\right)$ is derived in Appendix A and B of [215] for an isotropic GWB with different polarisation's. Eq. 11.9 presents six independent equations for seven unknowns ($S_n^X(f)$, $S_n^Y(f)$, $S_n^Z(f)$), $S_n^{XY}(f)$, $S_n^{XZ}(f)$, $S_n^{YZ}(f)$ and $S_h(f)$). We want to point out that the frequency behaviour of each of these unknowns is typically parameterized by multiple parameters and therefore the total number of parameters can become very large.

Of these six equations only three are independent of any GW signal and can yield a noise PSD estimate without the need to rely on the knowledge of the present GW signals. That is, $\langle T(f)T^*(f')\rangle$, $\langle T(f)A^*(f')\rangle$ and $\langle T(f)E^*(f')\rangle$. This shows the advantage of using the A, E, T channels over using only the T-channel, namely the gain of two additional independent equations which are free of any GW signal.

Alternatively, one can use another set of three independent equations, free of GWs, given by,

$$\begin{aligned}
\langle T(f)X^*(f')\rangle &= \langle X(f)T^*(f')\rangle = \frac{1}{2}\delta(f-f')\left[\frac{1}{\sqrt{3}}(S_n^X(f)+S_n^{XY}(f)+S_n^{XZ}(f))\right] \\
\langle T(f)Y^*(f')\rangle &= \langle Y(f)T^*(f')\rangle = \frac{1}{2}\delta(f-f')\left[\frac{1}{\sqrt{3}}(S_n^Y(f)+S_n^{YX}(f)+S_n^{YZ}(f))\right] \\
\langle T(f)Z^*(f')\rangle &= \langle Z(f)T^*(f')\rangle = \frac{1}{2}\delta(f-f')\left[\frac{1}{\sqrt{3}}(S_n^Z(f)+S_n^{ZX}(f)+S_n^{ZY}(f))\right].
\end{aligned} \tag{11.10}$$

The use of $\langle T(f)X^*(f')\rangle$, $\langle T(f)Y^*(f')\rangle$ and $\langle T(f)Z^*(f')\rangle$ was proposed in [182], mainly in the context of glitch mitigation in compact binary coalescence (CBC) searches and assuming non-correlated noise. In Eq. 11.10 we show how one can correctly include correlated noise terms such that an unbiased estimate of the X, Y and Z interferometers' PSDs can be achieved.

The equations describing $\langle T(f)X^*(f')\rangle$, $\langle T(f)Y^*(f')\rangle$ and $\langle T(f)Z^*(f')\rangle$ are not independent of the equations describing $\langle T(f)T^*(f')\rangle$, $\langle T(f)A^*(f')\rangle$ and $\langle T(f)E^*(f')\rangle$, since the A, E and T channels are linear combinations of the X, Y and Z channels. However, the two different sets of equations present a different representation of the same problem and depending on the situation, one or the other might be more or less useful. As an example, Eq. 11.9 gives a set of six independent equations that can be used to jointly estimate signal and noise terms. Furthermore, the coherence between the T and A and/or E channels can be used as a simple diagnostic tool. In case the coherence is consistent with Gaussian noise this indicates the noise is identical between the X, Y and Z interferometers. By correlating the T and A and/or E channels over long timescales, one might also gain additional information on non-identical correlated noise sources which do not directly affect the detectors noise PSD, but might be affecting correlation based searches, such as the search for a GWB. On the other hand, Eq. 11.10, might be easier to use if one is just interested in the noise quantities of the X, Y and Z interferometers.

In Sec. 11.3 we illustrate the formalism using two examples of noise for the ET, whereas in Sec. 11.4 we outline the next steps needed to use this formalism in a Bayesian estimation framework.

11.3 Examples in the context of the Einstein Telescope

In this section, we show how Eq. 11.9 and Eq. 11.10 are used to provide unbiased PSD estimates considering two examples of noise in the Einstein Telescope. Both examples contain a GWB signal coming from the superposition of CBC events. The first example additionally contains correlated noise sources having a Gaussian spectrum at three different frequencies. Furthermore, to simulate the case of non identical noise spectra in X, Y and Z, each of the 3 Gaussian noise sources is injected in only two interferometers. The second example presents a more realistic scenario where the same GWB is present as well as correlated magnetic and Newtonian noise. The data sets used are described in Sec. 11.3.1.

The two examples also demonstrate that, although it is insensitive to GWs, the T channel PSD S_n^T [1], as well as the cross-correlated power between the null channel and each interferometer S_n^{TX}, S_n^{TY} and S_n^{TZ} yield biased estimates of S_n^X, S_n^Y and S_n^Z in the case of non-identical and correlated noise as stated in [182]. We demonstrate how the formalism described in this chapter can be used to properly take the non-identical and correlated noise into account, such that unbiased estimates can be defined.

We would like to note that whereas $S_n^T = S_n^X$ in case of identical and non correlated noise in the three interferometers, this is not the case for S_n^{TX}, S_n^{TY} and S_n^{TZ} due to the used normalisation. Therefore we use in the remainder of the chapter ${S'}_n^{TX} = \sqrt{3} S_n^{TX}$ and equivalent for the other channels.

11.3.1 Data sets

Model of a GWB

As signal, we use a background formed by the superposition of a population of BNS distributed isotropically in the sky and up to a redshift of $z = 10$. For the generation of this GWB, we rely on Monte Carlo techniques using the MDC_Generation code [297] that randomly selects the set of parameters for each individual BNS (coalescence time, position in the sky, merger redshift, component masses and spins, orientation) and produces the corresponding gravitational-wave polarizations $h_+(t)$ and $h_\times(t)$. The interferometer response $h^J(t) = h_+(t)F_+^J(t) + h_\times(t)F_\times^J(t)$ is added to the time-domain strain amplitude of the three ET detectors in a frequency band

[1] Note that we have chosen to also give a lower index n to the spectral density of the T channel to explicitly indicate it only depends on noise terms and is insensitive to GWs.

5 Hz - 2048 Hz. For simplicity we assume identical component masses of 1.4 $M_\odot$ and no spin. We also assume that sources are on average separated by a short time interval of Δt=1.5 s. Although unrealistic, this short interval has the advantage to give a continuous and Gaussian background that is detectable within a short observation period.

The energy density $\Omega_{\rm GW}(f)$ of the GWB, as introduced in Eq. 4.4, coming from unresolved CBC events is predicted to behave as a power-law, with a slope of $\alpha = 2/3$, at lower frequencies where all the sources contribute in their inspiral phase [295, 296]. We assume the GW signal consists of equal parts tensorial plus- and cross-polarization, as expected by general relativity. Given the normalization constant $S_0(f)$ contains a factor f^{-3}, this implies $\mathrm{Re}[\tilde{s}_I^*(f)\tilde{s}_J(f)] \propto f^{-7/3}$.

The strain PSD amplitude of the injected signal at the reference frequency $f_{\rm ref}$=25 Hz is $\sim 2.14 \times 10^{-49}$ 1/Hz. This corresponds to $\Omega_{\rm GW} \sim 2.03 \times 10^{-8}$. This amplitude is about two orders of magnitude larger than the value predicted by the LVK colaboration based on the results of their third observing run $2.1^{+2.9}_{-1.6} \times 10^{-10}$ [30]. The amplitude is chosen such that the signal is clearly visible in a limited amount of data for illustrative purposes.

Gaussian peaks

Gaussian peaks in the frequency domain are used to simulate correlated noise sources. The Gaussian peaks are defined with the following PSD

$$S_n^{\rm GP}(f) = \left(\frac{A}{\sqrt{2\pi}} e^{\frac{-(f-\mu)^2}{2\sigma^2}} \right)^2 , \tag{11.11}$$

where the amplitude A, the peak frequency μ and its variance σ are the free parameters. In our first example we use three peaks which have a peak frequency of μ=10Hz, μ=50Hz and μ=90Hz. Their respective amplitudes are $A^{\rm GP,10} = 4 \times 10^{-24}$, $A^{\rm GP,50} = 2 \times 10^{-24}$ and $A^{\rm GP,90} = 1.5 \times 10^{-24}$. For all three frequencies we use $\sigma = 1$.

Correlated magnetic noise

We use the magnetic noise spectrum described in Fig. 7.3 of Chapter 7. This low-frequency spectrum (< 100Hz) is based on measurements at the ET candidate site in the Sos Enattos mine in Sardegna, Italy [56, 275, 305]. The measurements

focus mainly on the Schumann resonances [318, 319]. 10% of the measured magnetic spectrum at Sos Ennatos are used to get a clean measurement of the Schumann resonances. The amplitude of the fundamental mode is then rescaled to the amplitude of the 95% percentile to get a conservative estimate.

Due to the long distance correlations of the Schumann resonances it is safe to assume all interferometers of the ET are affected by this noise coherently. We thus assume this noise source to be identical, and fully correlated, among the three interferometers.

A final aspect one needs to understand is to which extent these ambient magnetic fields couple to the ET interferometers. In Chapter 8 we placed upper limits on the maximal allowed coupling such that correlated magnetic noise would not impact GWB searches. Here we assume a coupling function which is proportional to f^{-2}, as is measured at Virgo during the third observing run for frequencies below $\sim$ 100Hz [170]. The amplitude is chosen to match the weekly-average of the magnetic coupling measured at Virgo [170, 218]. This yields an amplitude of 0.4×10^{-10}m/T at 100Hz.

The power spectral density of this noise source will be referred to as S_n^{Mag} in the rest of this chapter.

Correlated Newtonian noise from body waves

For the correlated NN from body waves, we rely on the results discussed in Chapter 9. In this chapter we assume the correlated NN from body waves is only present in one vertex, which consists of the central station of the X interferometer and the end station of the Y interferometer. This implies that whereas in Chapter 9 a factor of 5 for the number of independent couplings is considered, we assume a factor of 2. This reduces the noise spectrum used in this chapter by a factor of 2/5 with respect to the results presented in Fig. 9.16 in Chapter 9 from which we used the median estimates.

The power spectral density of this noise source will be referred to as S_n^{NN} in the rest of the chapter.

Total data set

For the first example we use 2000s of data containing Gaussian noise colored with the design sensitivity of the ET-D xylophone configuration[2]. In the rest of the chapter we refer to this colored Gaussian noise as 'ET noise' and use S_n^{ET} [3] for its PSD. Note that despite the fact that we use identical noise, the X, Y and Z data are different Gaussian noise realisations. On top of the detector noise we inject in the time domain an artificially enhanced GWB coming from CBC events, as introduced earlier in this section. Furthermore, two Gaussian peaks are injected in the time domain data of each interferometer. The injected peaks are correlated, such that every pair of interferometers has one correlated peak. More specifically we inject a Gaussian peak at 10Hz and 50Hz in the X interferometer, at 10Hz and 90Hz in the Y interferometer and at 50Hz and 90Hz in the Z interferometer.

If we refer to the PSD of the Gaussian peak at 10Hz by $S_n^{\mathrm{GP},10}$, and equivalent for the other Gaussian peaks, we can write the PSD and CSD of the X, Y and Z interferometers as follow

$$\begin{aligned} S_n^X(f) &= S_n^{\mathrm{ET}}(f) + S_n^{\mathrm{GP},10}(f) + S_n^{\mathrm{GP},50}(f) \\ S_n^Y(f) &= S_n^{\mathrm{ET}}(f) + S_n^{\mathrm{GP},10}(f) + S_n^{\mathrm{GP},90}(f) \\ S_n^Z(f) &= S_n^{\mathrm{ET}}(f) + S_n^{\mathrm{GP},50}(f) + S_n^{\mathrm{GP},90}(f) \\ S_n^{XY}(f) &= S_n^{\mathrm{GP},10}(f) \\ S_n^{XZ}(f) &= S_n^{\mathrm{GP},50}(f) \\ S_n^{YZ}(f) &= S_n^{\mathrm{GP},90}(f). \end{aligned} \tag{11.12}$$

For the second example, we use 2000s of ET noise data on top of which we inject the same GWB as in previous example. We also add the correlated magnetic and Newtonian noise as introduced earlier in this section. The magnetic noise is correlated and identical among the X, Y and Z interferometers. The Newtonian noise is also correlated but only present in the X and Y interferometers, leading to non-identical noise sources in the three different ET interferometers.

With the introduced notations for the different spectral densities we can write the spectral densities as follow:

[2] As discussed in Chapter 2 this sensitivity is by now deprecated. However it is very similar to the latest HFLF-cryo sensitivity as shown in Fig. 2.7.

[3] The PSD of the ET noise S_n^{ET} is not to be confused with the CSD of correlating the T and E channels, i.e. S_n^{TE}.

$$
\begin{aligned}
S_n^X(f) &= S_n^{\mathrm{ET}}(f) + S_n^{\mathrm{Mag}}(f) + S_n^{\mathrm{NN}}(f) \\
S_n^Y(f) &= S_n^{\mathrm{ET}}(f) + S_n^{\mathrm{Mag}}(f) + S_n^{\mathrm{NN}}(f) \\
S_n^Z(f) &= S_n^{\mathrm{ET}}(f) + S_n^{\mathrm{Mag}}(f) \\
S_n^{XY}(f) &= S_n^{\mathrm{Mag}}(f) + S_n^{\mathrm{NN}}(f) \\
S_n^{XZ}(f) &= S_n^{\mathrm{Mag}}(f) \\
S_n^{YZ}(f) &= S_n^{\mathrm{Mag}}(f).
\end{aligned}
\tag{11.13}
$$

11.3.2 Demonstration

Toy example with correlated Gaussian peaks

Fig. 11.1 shows the PSD for the X, Y and Z interferometers. All the separate components are also shown as to compare their relative contributions. Due to the continuous presence of CBC signals it is impossible to directly estimate the noise spectral density from the observed spectrum.

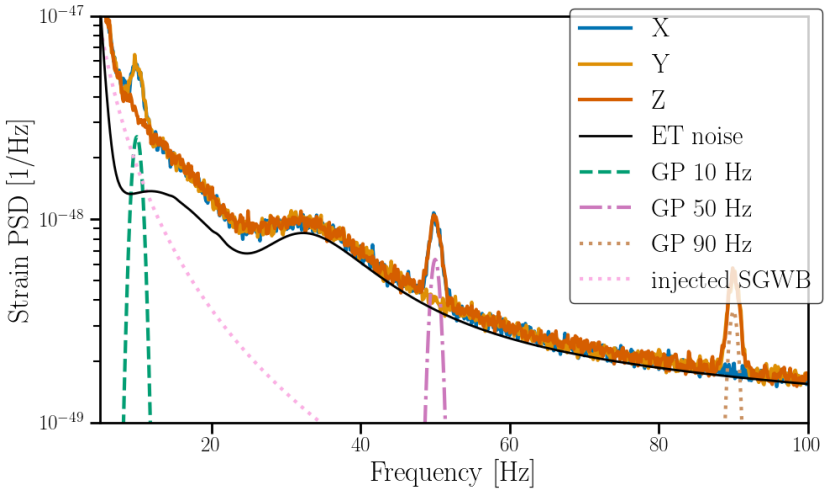

Fig. 11.1.: The PSDs of the X, Y, Z channels, the ET noise and the injected correlated noise $S_n^{\mathrm{GP},10}$, $S_n^{\mathrm{GP},50}$ and $S_n^{\mathrm{GP},90}$(see text for a more detailed description). The contribution of the injected GWB S_h^{GWB} is also shown. We point out that at high frequencies the X, Y and Z PSDs seem to not match the ET noise curve. This is due to the small but non-negligble contribution of the GW signal, as can be seen by the perfect match for the T channel PSD in Fig. 11.2.

The top panel of Fig. 11.2 shows the spectral densities of the A, E and T channels. This figure illustrates that the null channel is indeed free of GWs. Therefore, as pointed out by [182], one could hope to use S_n^T as an estimate for the noise PSD of

e.g. the X interferometer S_n^X, or alternatively, use ${S'_n}^{TX}$ in case non-identical noise in the different X, Y and Z interferometers is suspected. However, as shown by the bottom panel of Fig. 11.2, both S_n^T and ${S'_n}^{TX}$ are biased for our dataset. To be more specific two biases are present.

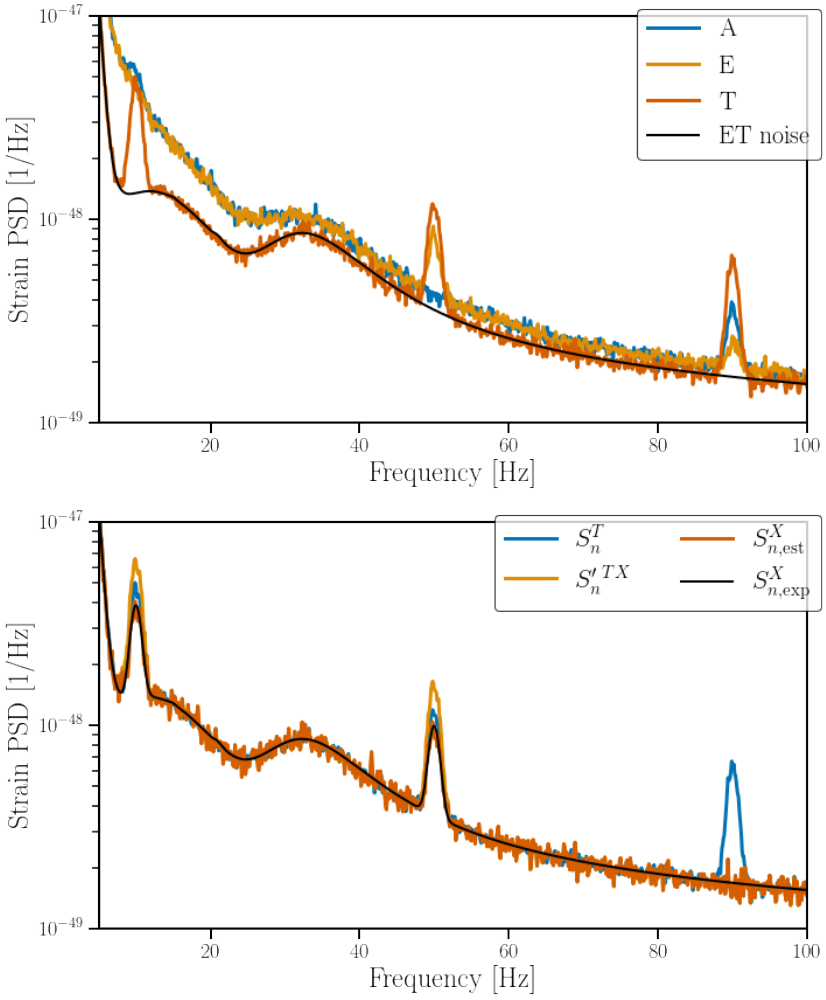

Fig. 11.2.: Top: The PSDs of the A, E, T channels and the ET noise. Bottom: The PSD of the null channel T, the CSD of the T and X channels, normalised such that it can serve as an estimate of S_n^X. The expected PSD of X as shown in Eq. 11.12 and the estimated PSD as calculated in Eq. 11.14 and Eq. 11.15 are shown in dark orange and black respectively. The equivalent figures for the Y and Z channels are shown in Appendix C, Fig. C.1.

First, the PSD of the T channel includes all noise features present in any of the 3 interferometers. Whereas the X interferometer only contains the Gaussian peaks at 10Hz and 50Hz, S_n^T includes all three Gaussian peaks. S_n^T is thus a biased estimate of the X interferometer. A similar statement is applicable to the two other

interferometers, where respectively the 50Hz and 10Hz peak are not present in the Y and Z interferometers, but they are in S_n^T.

This bias can be addressed by using the cross-correlation between the null channel and the interferometer of interest, i.e. ${S'_n}^{TX}$, as it has been first proposed in [182]. However, this also yields a biased estimate since it does not take into account the fact that some of the noise sources are correlated. This is reflected in a general overestimate due to not properly taking the correlation into account. As shown in Eq. 11.9 and Eq. 11.10, these non zero correlations imply that the cross-correlation between e.g. the T and X channel differs from the noise PSD S_n^X. Only by taking both elements, i.e. non-identical and correlated noise, into account can one build an unbiased PSD estimator for the different interferometers as explained below.

We now build an unbiased PSD estimator $S^X_{n,est}$ using Eq. 11.10 as follows

$$\begin{aligned} {S'_n}^{TX} &= \sqrt{(3)} * S_n^{TX} \\ &= S_n^X + S_n^{XY} + S_n^{XZ} \\ &= S^X_{n,\mathrm{est}} + S_n^{\mathrm{GP},10} + S_n^{\mathrm{GP},50} \\ &\Downarrow \\ S^X_{n,\mathrm{est}} &= {S'_n}^{TX} - S_n^{\mathrm{GP},10} - S_n^{\mathrm{GP},50}. \end{aligned} \tag{11.14}$$

Equivalently we find

$$\begin{aligned} S^Y_{n,\mathrm{est}} &= {S'_n}^{TY} - S_n^{\mathrm{GP},10} - S_n^{\mathrm{GP},90} \\ S^Z_{n,\mathrm{est}} &= {S'_n}^{TZ} - S_n^{\mathrm{GP},50} - S_n^{\mathrm{GP},90}. \end{aligned} \tag{11.15}$$

The spectral densities ${S'_n}^{TX}$, ${S'_n}^{TY}$ and ${S'_n}^{TZ}$ can be extracted from the data. For this, we use the entire stretch of 2000s of data, split it in 10s long segments over which FFT's are calculated using 50% overlapping Hann-windows. We average over the different segments. We assume to know perfectly $S_n^{\mathrm{GP},10}$, $S_n^{\mathrm{GP},50}$ and $S_n^{\mathrm{GP},90}$ that are subtracted from ${S'_n}^{TX}$, ${S'_n}^{TX}$ and ${S'_n}^{TZ}$. In Sec. 11.4 we discuss how this assumption can be dropped by developing a Bayesian estimation framework.

The bottom panel of Fig 11.2 compare the estimated PSDs to the expected ones for the X interferometer. The expected PSD $S_{n,\mathrm{exp}}$ is given by Eq. 11.12 where we have used the simulated data. The agreement is excellent and much better than with the other estimators S_n^T or ${S'_n}^{TX}$. The equivalent figures for the Y and Z channels are shown in Appendix C, Fig. C.1.

As mentioned in Sec. 11.2, the cross-correlation between the T and A, E channels (S_n^{TA} and S_n^{TE}) contains additional information on the non-identical character of the correlated noise. The left panel of Fig. 11.3 shows the coherence between the T channel and the A and E channels. This coherence is consistent with a Gaussian noise origin[4] apart from the Gaussian peaks. This indicates, correctly, that the only parts of the noise in the X, Y and Z channels which is not identical, are the Gaussian peaks. The bottom panel of Fig. 11.3 shows the modulus of the cross spectral densities estimated from the data on top of the expected quantities which are given by,

$$
\begin{aligned}
|S^{TA}_{n,\mathrm{exp}}| =& \frac{1}{\sqrt{6}}|S_n^Z(f) - S_n^X(f) + S_n^{YZ}(f) - S_n^{XY}(f)| \\
&\Downarrow \text{Eq. 11.12} \\
=& \frac{1}{\sqrt{6}}|S_n^{\mathrm{ET}} + S_n^{\mathrm{GP,50}} + S_n^{\mathrm{GP,90}} - (S_n^{\mathrm{ET}} + S_n^{\mathrm{GP,10}} + S_n^{\mathrm{GP,50}}) + S_n^{\mathrm{GP,90}} - S_n^{\mathrm{GP,10}}| \\
=& \frac{2}{\sqrt{6}}|-S_n^{\mathrm{GP,10}} + S_n^{\mathrm{GP,90}}| \\
=& \frac{2}{\sqrt{6}}\sqrt{\mathcal{R}e\left(-S_n^{\mathrm{GP,10}} + S_n^{\mathrm{GP,90}}\right)^2 + \mathcal{I}m\left(-S_n^{\mathrm{GP,10}} + S_n^{\mathrm{GP,90}}\right)^2} \\
&\Downarrow \text{All the quantities involved are real; } (A-B)^2 = (A+B)^2 - 4AB \\
=& \frac{2}{\sqrt{6}}\sqrt{\left(S_n^{\mathrm{GP,10}} + S_n^{\mathrm{GP,90}}\right)^2 - 4S_n^{\mathrm{GP,10}}S_n^{\mathrm{GP,90}}} \\
&\Downarrow S_n^{\mathrm{GP,i}}S_n^{\mathrm{GP,j}} \ll \left(S_n^{\mathrm{GP,k}}\right)^2, \text{ where } i \neq j \text{ and } i,j,k \in \text{['10','50','90']} \\
\approx& \frac{2}{\sqrt{6}}\left(S_n^{\mathrm{GP,10}} + S_n^{\mathrm{GP,90}}\right)
\end{aligned}
\tag{11.16}
$$

[4]The expected coherence for uncorrelated data goes approximately as 1/N, where N is the number of time segments over which the coherence is averaged, as discussed in Chapter 6.

$$
\begin{aligned}
|S^{TE}_{n,\mathrm{exp}}| =& \frac{1}{3\sqrt{2}}|S^X_n(f) - 2S^Y_n(f) + S^Z_n(f) - S^{XY}_n(f) + 2S^{XZ}_n(f) - S^{YZ}_n(f)| \\
=& \frac{1}{3\sqrt{2}}|S^{\mathrm{ET}}_n + S^{\mathrm{GP,10}}_n + S^{\mathrm{GP,50}}_n - 2(S^{\mathrm{ET}}_n + S^{\mathrm{GP,10}}_n + S^{\mathrm{GP,90}}_n) \\
& + S^{\mathrm{ET}}_n + S^{\mathrm{GP,50}}_n + S^{\mathrm{GP,90}}_n - S^{\mathrm{GP,10}}_n + 2S^{\mathrm{GP,50}}_n - S^{\mathrm{GP,90}}_n| \\
=& \frac{2}{3\sqrt{2}}| - S^{\mathrm{GP,10}}_n + 2S^{\mathrm{GP,50}}_n - S^{\mathrm{GP,90}}_n| \\
=& \frac{2}{3\sqrt{2}}\sqrt{\mathcal{R}e\left(-S^{\mathrm{GP,10}}_n + 2S^{\mathrm{GP,50}}_n - S^{\mathrm{GP,90}}_n\right)^2 + \mathcal{I}m\left(-S^{\mathrm{GP,10}}_n + 2S^{\mathrm{GP,50}}_n - S^{\mathrm{GP,90}}_n\right)^2} \\
& \Downarrow \text{All the quantities involved are real; } (A-B)^2 = (A+B)^2 - 4AB \\
=& \frac{2}{3\sqrt{2}}\sqrt{\left(S^{\mathrm{GP,10}}_n + 2S^{\mathrm{GP,50}}_n + S^{\mathrm{GP,90}}_n\right)^2 - 8S^{\mathrm{GP,50}}_n\left(S^{\mathrm{GP,10}}_n + S^{\mathrm{GP,90}}_n\right)} \\
& \Downarrow S^{\mathrm{GP,i}}_n S^{\mathrm{GP,j}}_n \ll \left(S^{\mathrm{GP,k}}_n\right)^2, \text{ where } i \neq j \text{ and } i,j,k \in \text{['10','50','90']} \\
=& \frac{2}{3\sqrt{2}}(S^{\mathrm{GP,10}}_n + 2S^{\mathrm{GP,50}}_n + S^{\mathrm{GP,90}}_n),
\end{aligned}
\tag{11.17}
$$

As one can see in the bottom panel of Fig. 11.3 the expected quantities calculated in Eq. 11.16 and Eq. 11.17 are consistent with the CSD estimated from the data.

Superposition of GWB, correlated magnetic and correlated Newtonian noise

Fig. 11.4 shows the power spectral density spectrum for the X, Y and Z interferometers with the second data-set composed of Gaussian noise on top of which correlated magnetic, Newtonian noise and GWB signal have been added. All the separate components are shown as to compare their relative contributions.

The top panel of Fig. 11.5 shows the spectral densities of the A, E and T channels. Compared to the previous example it is slightly more difficult to immediately see the T channel is indeed free of GW due to the presences of the magnetic and Newtonian noise. However, based on Fig. 11.4 one could expect a negligible effect from either the magnetic or Newtonian noise above 20Hz, apart from the magnetic resonance at 50Hz.

In the previous example we showed how S^T_n as well as S'^{TX}_n yielded a biased estimate for the noise PSD of the X interferometer S^X_n, due to the presence of non-identical and correlated noise. Afterwards we showed that one can build unbiased estimators of the interferometers' PSD using Eq. 11.9 and Eq. 11.10. We now

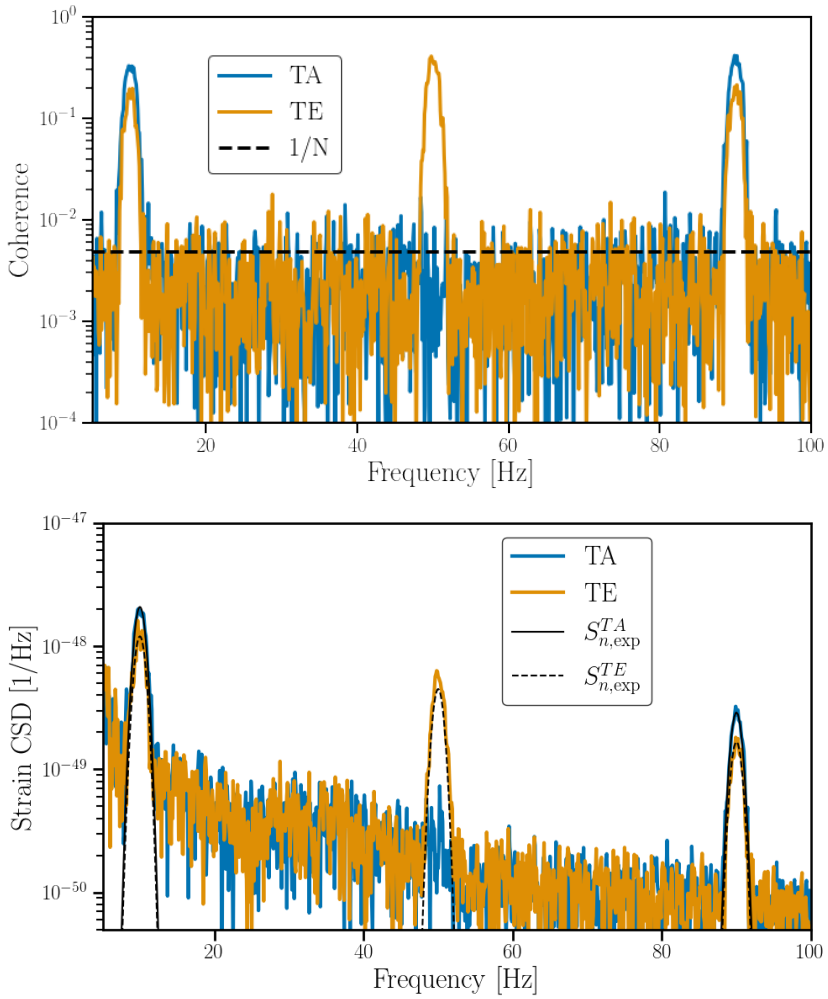

Fig. 11.3.: Top: the coherence between the T and A, E channels. The black dashed line represents the level of coherence expected from independent Gaussian data, which goes approximately as $1/N$, where N is the number of time segments over which was averaged. Bottom: the modulus of the CSD between the T and A, E channels. The expected cross spectral densities associated with the T and A channels, and T and E channels given by Eq. 11.16 and Eq. 11.17 for the toy model example are shown in black. The expected CSD is in agreement with the observed CSD.

provide another demonstration with a more realistic scenario where correlated magnetic and Newtonian noise are present.

Similar to the previous example we compare our estimators with the expected quantities given by Eq. 11.13. The estimated PSDs for this example are given by:

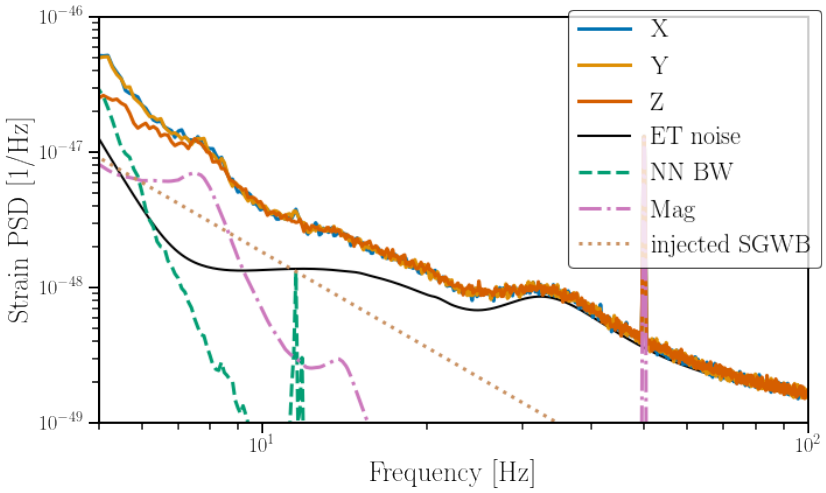

Fig. 11.4.: The PSDs of the X, Y, Z channels, the ET noise and the injected correlated Newtonian noise from body waves (NN BW) and magnetic noise (Mag). The contribution of the injected GWB $S_h^{\rm GWB}$ is also shown.

$$\begin{aligned} S^X_{n,\rm est} &= S'^{TX}_n - 2 * S^{\rm Mag}_n - S^{\rm NN}_n \\ S^Y_{n,\rm est} &= S'^{TY}_n - 2 * S^{\rm Mag}_n - S^{\rm NN}_n \\ S^Z_{n,\rm est} &= S'^{TZ}_n - 2 * S^{\rm Mag}_n. \end{aligned} \tag{11.18}$$

$S^{\rm Mag}_n$ and $S^{\rm NN}_n$ can be measured for instance using witness sensors. In a more realistic scenario the knowledge of each individual noise sources might be inaccurate because of inefficiencies introduced by the witness sensors. This source of inaccuracy should be more thoroughly investigated in future work.

The bottom panel of Fig 11.5 shows a good agreement between $S_{n,\rm exp}$ and $S_{n,\rm est}$ for respectively the X interferometer. The equivalent figures for the Y and Z channels are shown in Appendix C, Fig. C.2.

The previous two examples have shown how one can build unbiased PSD estimators based on the T channel and an estimate of the correlated noise present in the data. In the next section we discuss the following steps to develop a PSD estimation framework.

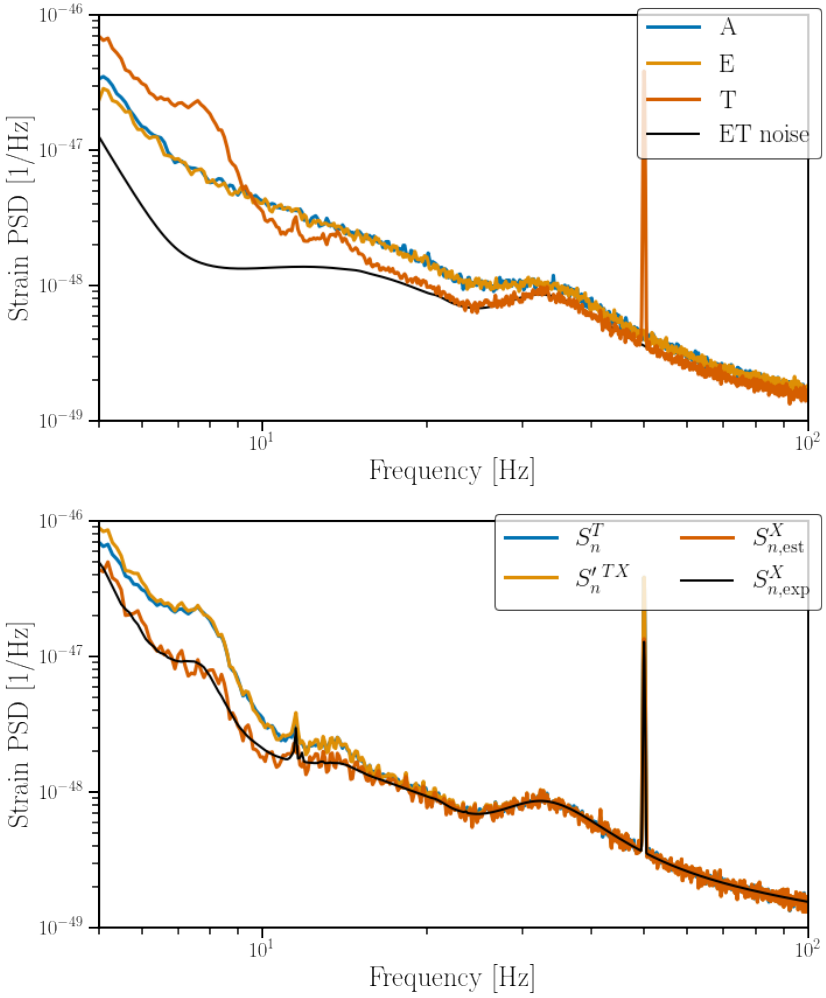

Fig. 11.5.: Top: The PSDs of the A, E, T channels and the ET noise. Bottem: The PSD of the null channel T, the CSD of the T and X channels, normalised such that it can serve as an estimate of S_n^X. The expected PSD of X, as shown in Eq. 11.13 and the estimated PSD as calculated in Eq. 11.18. As explained in the text, S_n^T and ${S'_n}^{TX}/{S'_n}^{TY}/{S'_n}^{TZ}$ yield a biased PSD estimate and one needs to use $S^X_{n,\mathrm{est}}/S^Y_{n,\mathrm{est}}/S^Z_{n,\mathrm{est}}$, derived in Eq. 11.18 using Eq. 11.10. The equivalent figures for the Y and Z channels are shown in Appendix C, Fig. C.2.

11.4 Recipe to transform the null channel formalism into a power spectral density estimation framework

In previous sections, we have shown how one can construct the sky-location-independent null channel for an equilateral triangular GW interferometer configuration in a situation where there is correlated noise unique to each detector pair, as well as where all the interferometers have different noise levels. However, the examples assumed one has perfect knowledge of the correlated and individual noise sources. In the example one could get an estimation of $S_n^{\rm Mag}$ ($S_n^{\rm NN}$) from e.g. witness sensors measuring the magnetic (seismic) fields, combined with a measurement of the magnetic coupling function (formula to predict NN based on seismic fields). In a real scenario for the ET, this knowledge will never be perfect. Furthermore, it is very likely that some part of the noise is not properly understood. In this section, we propose further investigations so that one can estimate the noise PSDs as well as correlated noise levels for ET (or LISA) to observe GWs.

After the proof of concept of the A, E and T channels for the ET in earlier sections, one should develop a Bayesian framework to enable parameter estimation [119, 152] of the noise PSDs as well as correlated noise PSDs, that is S_n^I and S_n^{IJ} or in the more general scenario S_n^X, S_n^Y, S_n^Z, S_n^{XY}, S_n^{XZ} and S_n^{YZ}. Here one should consider multiple scenarios such as identical noise sources, unique noise sources for each X, Y and Z interferometer, absence/presence of correlated noise. In the case of non-identical noise sources for the different interferometers it is beneficial to use the cross-correlation of the null channel T with the X, Y and Z channels ($S_n^{TX}(f)$, $S_n^{TY}(f)$ and $S_n^{TZ}(f)$) rather than using the PSD of T ($S_n^T(f)$) to estimate the noise sources in the different interferometers. Alternatively one can also extract this information on the non-identical noise components in the X, Y and Z channels by using the cross spectral density of the null channel with the A and E channels ($S_n^{TA}(f)$ and $S_n^{TE}(f)$), together with the null channel (S_n^T). Furthermore, one should understand the effect of knowledge of (un)correlated noise sources, from possible witness sensors observing the noise sources (e.g. magnetometers, seismometeres, etc.), and how this can improve the final parameter estimation of the noise PSDs. Given the high dimensional problem, estimations of all the parameters with the desired accuracy might prove difficult in the most general scenario and more work is needed to achieve such a goal. To this extent, one should also take the non-stationary character of real data into account. This implies that it is not trivial to just extend the duration of the data used to compute the different noise contributions using the null channel formalism, presented in this chapter.

Third and finally, the knowledge of correlated noise sources and their properties should be understood and studied further if one wants to simulate a realistic scenario for the above techniques. In the context of the search for a GWB using Earth-based interferometers there have already been significant investigations concerning the effects of correlated magnetic fields, e.g. Schumann resonances [133, 134, 203, 204, 267, 346, 348], also in the context of ET as discussed in Chapter 8. As discussed in Chapter 9, correlated seismic and Newtonian noise over distances of several hundreds of meters can impact GWB searches using the ET. These results form the ideal starting point for studying correlated noise in the formalism described in this chapter but more dedicated follow-up studies could look into the effect from earthquakes, the possibility of correlated seismic fields on the scale of 10km and the interplay between different coupling locations, and to which extent there is constructive or destructive interference between e.g. correlated magnetic fields coupling to both input and end mirrors of the interferometers.

For LISA, noise correlation studies resulting from the spatial environment can benefit from more detailed noise characterisation. These noises include for example the effect of micro-thrusters, the magnetic field and the temperature variations on the test-mass system [92].

These research topics pose fundamental questions for understanding the data analysis environment at the ET and LISA, and should be studied in significantly more detail over the course of the coming years before the instruments become operational to ensure they can fulfill their scientific goals. This is especially true for correlated noise, which would seriously affect the search for a GWB.

11.5 Conclusion

Future GW interferometers such as ET, CE and LISA will have sensitivities allowing them to resolve many transient sources to such an extent that they are expected to observe a large amount of overlapping signals [57, 294, 297]. This makes it difficult to estimate the noise PSD of the interferometers needed to perform GW searches.

A first method is to simultaneously model noise and signals using for instance a joint Bayesian parameter estimation framework [119, 152]. This chapter is investigating a different approach relying on the sky-location-independent null channel which can be constructed for triangular configurations of interferometers, such as the ET and LISA. This sky-location-independent null channel is insensitive to GWs from any direction.

We introduce a formalism which is able to not only address correlated noise between the different interferometers, but also allow for non-identical noise both correlated and uncorrelated. The formalism goes beyond using the sky-location-independent null channel and relies on three linear combinations A, E and T of the three interferometers X, Y and Z, which have been used in LISA before [332, 351]. The advantage of relying on the A, E and T channels, of which the T channel is a normalized version of the null channel, is that their cross-correlation spectra contain additional information in the case of non-identical noise sources. Alternatively one can correlate the null channel with the X, Y and Z channels which allows for the estimation of the noise PSDs and CSDs in the case of non-identical noise. The later was also investigated in [182], however, although mentioning the possible bias coming from correlated noise, the authors did not take it into account.

We illustrate the formalism considering simplified but realistic noise realisations for the ET on top of which a GWB signal is added. We have shown that the T channel is indeed insensitive to GWs. Furthermore, we show that our formalism enables an unbiased estimation of the noise spectral densities of the X, Y and Z channels, even in the presence of correlated and non-identical noise. These examples use knowledge of the noise sources to prove the mathematical consistency of this formalism, which in future research should be used as an ingredient for a Bayesian estimation framework, as discussed in Sec. 11.4.

12 Conclusion and outlook

In this thesis I have investigated the data quality for the search for an isotropic gravitational-wave background (GWB), with Earth-based interferometric detectors. We started in Chapter 1 with the introduction of Einstein's theory of general relativity and its prediction of the production of gravitational waves (GWs). In Chapter 2 various detection methods for GWs were discussed, which are sensitive to GWs with frequencies ranging from nHz to kHz. Earth-based interferometric detectors were described in more detail, where the Virgo instrument was used as an example. Chapter 3 contains a review of a wide variety of astrophysical objects and cosmological processes that are predicted to produce GWs. I also highlighted some of the recent achievements, such as the first direct observations of GWs from binary black hole, binary neutron star and black hole neutron star systems by the Laser Interferometer Gravitational wave Observatory (LIGO) and Virgo. Another, very recent, achievement in the field of GW observations, is the strong evidence for a nHz GWB signal found by multiple pulsar timing arrays. Chapter 4 reviews the analysis methods used to search for a GWB signal using Earth-based interferometric detectors, with a focus on the search for a Gaussian, stationary and isotropic signal. Finally, in Chapter 5, I present what was the state of the art on noise sources for a GWB at the start of my PhD. This includes a discussion on non-stationary noise features, spectral artefacts and correlated noise. I also discuss previously developed methods that aim to address (some of) these data quality issues.

In Chapter 6 I explained the data quality procedures to identify spectral artefacts. I highlight the work I have performed after O3, both for the search for an isotropic GWB as well as for more general noise lines in the Virgo detector. This chapter also contains a discussion of the implementation of the notch-list and the new version I have implemented as part of '`pygwb`', the new python-based isotropic GWB analysis pipeline. Finally, I describe the more proactive data quality procedure which is being implemented in O4. This involves weekly shifts following up the data quality on time-shifted data and a full analysis every $\sim$ 2 months.

Chapter 7 contains a description of Earth-scale distance correlations in magnetic field fluctuations between 1Hz and 1kHz. Between 5Hz and several tens of Hz these Earth-scale correlations are dominated by the Schumann resonances. They are standing

electromagnetic waves in the cavity formed by the Earth's surface and the ionosphere and are sourced by lightning strikes. Above 100Hz the correlations are dominated by the incoherent superposition of individual lightning strikes, i.e. a 'stochastic background of lightning strikes'. Afterwards, I introduce the measurement of the magnetic coupling function, which describes the extent to which magnetic fields couple to our strain measurements in the GW detectors. For this, magnetic fields are created or 'injected' in the experimental buildings and enable us to understand the magnetic coupling for our instruments. Apart from measurements during O3, I highlight my contributions for deploying larger, better performing injection coils at Virgo to allow for louder and more broadband magnetic injections in the future. Finally, I present the proposal to perform magnetic injections correlated across GW detectors. These injections will enable us to gain further understanding in how correlations in magnetic field fluctuations affect GW detectors. I also present preliminary results of the first attempt of a correlated injection between LIGO Hanford and LIGO Livingston. The injection was successful and with this proof of concept we can plan the final injection which will have a colored magnetic spectrum similar to the Schumann resonances, however with a larger magnitude.

The observed Earth-scale correlations in magnetic field fluctuations and the magnetic coupling function from the previous chapter are the key ingredients used to construct the magnetic noise budget discussed in Chapter 8. The magnetic budget provides an order of magnitude estimate of the level at which (correlated) magnetic noise will limit GW searches. I show that ambient magnetic fields will have only a limited effect on Virgo's design strain sensitivity. However, if the next generation detector, the Einstein Telescope (ET), has similar magnetic coupling as current detectors, the ET will be dominated by magnetic noise below $\sim$ 15Hz. The coupling of magnetic fields to the ET below 15Hz has to be lower by up to two to three orders of magnitude to achieve ET's design strain sensitivity. Given the (slightly) less ambitious low-frequency sensitivity aimed for by Comic Explorer (CE), the constraints are less stringent. However, CE also still needs to have reduced magnetic coupling by up to two orders of magnitude. In the second part of this chapter, I present the impact of correlated magnetic noise for the search for an isotropic GWB. This includes the first budget for Advanced LIGO and Advanced Virgo looking at the effect of correlated magnetic noise above 100Hz. Below 50Hz, the search for an isotropic GWB with LIGO and Virgo at design sensitivity could be affected by correlated magnetic noise. This is also the case for frequencies above $\sim$ 150Hz, however in this frequency band the magnetic coupling function is dominated by upper limits rather than measured values. More detailed investigations in the future should provide a definite answer. We end this chapter by presenting the impact of correlated magnetic noise on the ET.

I show how the search for an isotropic GWB places even more stringent constraints on the maximally allowed magnetic coupling function by about an additional order of magnitude compared to the earlier results focusing on the strain sensitivity. Furthermore, I show that ET's triangular configuration of detectors could also be prone to electromagnetic noise from the detector infrastructure. This should be further investigated, since it could seriously hamper all ET's science goals.

In Chapter 9 I describe observed correlations in seismic noise between sensors with a horizontal separation of several hundreds of meters. I also show the relevance of this distance scale as the test masses of one ET detector are situated on similar distances of the test masses of another ET interferometer. More specifically, we can identify five such pairs, i.e. five possible coupling locations for correlated noise to enter the detectors. Afterwards we use those measurements to project the impact on the search for an isotropic GWB. I show that the effect of seismic noise coupling will be minimal if a seismic isolation is achieved similar to the preliminary design. However, Newtonian noise (NN), and more specifically NN originating from seismic body waves, could seriously hamper the search for an isotropic GWB below $\sim$40Hz by many orders of magnitude. Whereas the effect of magnetic noise could be reduced by decreasing the coupling of magnetic fields to the detector, this is not the case for NN as it exerts a direct force on the test masses, which cannot be shielded. The reduction of this noise source by subtraction methods such as Wiener filters is expected to be limited compared to the magnitude of the noise coupling. However, one could effectively eliminate this source of correlated noise by building the different ET detectors in separate locations rather than having them co-located in a triangular configuration.

In Chapter 10 I discuss my extension on the GW Geodesy tool. In this framework we treat the detector overlap reduction function as a free parameter and infer the separation between the two observing detectors as well as their respective orientation. Whereas a GW signal would favor the true geometry, this is not the case for a fake signal from e.g. correlated noise. Here I present how one can construct a false alarm probability describing the likelihood of the signal to be from GW or rather from correlated noise origin. To form an agnostic model of possible, unknown terrestrial noise sources, I model a conservative scenario using Gaussian processes. However, the tool has limited power due to the conservative approach. When comparing to a signal of Schumann resonances the tool performs well, however some assumptions were made for the simulated Schumann resonance spectrum which should be further validated.

Chapter 11 explains how the sky-localisation independent null channel could be useful for the estimation of detector noise with a triangular configuration of interferometric GW detectors such as the ET and Laser Interferometer Space Antenna (LISA). Due to the large number of overlapping signals, estimation of the detector noise with these next generation instruments will not be as trivial as currently is the case with LIGO, Virgo and KAGRA. I present a new addition to the null channel formalism by allowing for non-identical and correlated noise among the different detectors forming up the triangle. Including these terms is crucial to ensure an unbiased estimate of the detector noise, however they could also further inform us on correlated noise contributions.

Future work

I believe that the work I performed as part of my thesis significantly contributed to the state of the art on data quality for GWB searches with Earth-based GW interferometric detectors. However, at the same time there still seems to be a never-ending list of worthwhile research endeavours to address knowledge gaps in this domain. I will try to address some of them, but this summary is not exhaustive.

During my PhD I strongly focused on the search for an isotropic GWB. More broadly, one finds that potential data quality issues and methods to address these for an anisotropic GWB are less well investigated. A first example is the projection of the effect of correlated noise for the search for an anisotropic GWB. To the best of my knowledge no such studies exist at the time of writing this thesis. Together with S. Venikoudis, J. Suresh and F. Delillo from UCLouvain, Belgium we are in the process of creating an anisotropic magnetic budget similar to the isotropic results presented in Chapter 8. Secondly, the GW Geodesy tool presented in Chapter 10 should also be extended for anisotropic searches. This is something that I was looking into with I. Michaloliakos from the University of Florida and others. Other improvements of the GW geodesy tool could be to: further verify the used Schumann resonance model, extend the usability of the tool to more than two detectors and address the very conservative nature of the false alarm probability when constructed using the Gaussian processes as introduced in Chapter 10.

In the last years, more efficient analysis methods have been developed for a GWB of intermittent nature. These searches are predicted to significantly outperform traditional search methods when looking for a GWB from binary black hole mergers. Whereas these analysis methods are very promising, further validation on non-Gaussian and non-stationary detector noise has to be performed. Also the effect from

correlated noise on these algorithms should be understood. With respect to this, it will be crucial to understand whether the superposition of correlated lightning glitches as presented in Chapter 7 could 'fake' an intermittent GWB signal.

As part of my PhD I investigated the effect of correlated magnetic noise on the search for an isotropic GWB above 100Hz. I also presented how correlated magnetic, seismic and Newtonian noise could seriously hamper the ET. Even though these results, achieved by making noise budgets, are important, there are also a large number of approximations involved. Therefore one should regard these noise budgets as order of magnitude estimates.
A first approximation is that we only use the amplitude of the magnetic coupling function and neglect its potential phase component. Furthermore, we assume the injections used to determine the magnetic coupling function are a fully homogeneous, far-field noise injection, which we know is not the case. Earlier work has demonstrated that this introduces an intrinsic uncertainty of a factor two. To address some of these concerns I did propose to coherently inject magnetic noise in multiple GW detectors. This proposal and some of the preliminary results are introduced in Chapter 7. The results of the final injection and the planned follow-up studies of this should provide us a more fundamental insight in how correlations in magnetic field fluctuations could affect Earth-based GW interferometers. This correlated injection could also help verify the Schumann resonance model used in the GW Geodesy tool. More broadly, additional investigations are needed to understand the effect of (correlated) magnetic noise on third generation detectors such as the ET and CE. My thesis contains predictions with respect to ET, as well as some (unpublished) additional work for CE, but further research efforts could for instance focus on the following topics: the effect of correlated noise on GWB searches using CE and CE+ET, the effect of the distance to active thunderstorm regions for a candidate detector site, and the effect of magnetic noise caused by infrastructure. The investigation of magnetic noise on GWB searches for a CE-CE or CE-ET detector pair is strongly related to the overlap reduction function for the observing baseline and thus the sensitivity of your baseline to a GWB. I have started some preliminary investigations on probing these relations for a variety of distances as well as orientations of the detectors in collaboration with J. Romano and N. Christensen.

The work focusing on the effect of seismic and Newtonian noise for the ET was limited in its scope by considering only one underground location, which is not one of the ET candidate sites. Furthermore, we did not probe the effect of local seismic transients and how they would impact our results. A paper addressing some of these issues is under preparation. In this work we also aim to include the effect of correlated seismic and Newtonian noise on atom interferometers. The effect of NN

from seismic body waves both correlated and uncorrelated is not yet investigated for atom interferometers and such addition would yield crucial information for future atom interferometers. Additionally, we are also in the process of setting up a dedicated seismic measurement campaign at the Laboratoire Souterrain à Bas Bruit in France. In this set-up we would be able to control for several dependent variables such as sensor depth, sensor distance and orientation between two sensors forming a pair in a much more systematic way compared to existing seismic data.
Finally, one could also look to investigate the effect of correlations in magnetic field fluctuations on atom interferometers. In earlier studies, it was assumed the observed magnetic field fluctuations are uncorrelated over long distances. However, we know this assumption to break down, at least for the Schumann resonances ($\sim$5Hz-60Hz). Therefore more accurate investigations are needed, taking the coherent nature of low frequency, environmental magnetic field fluctuations into account with respect to their impact on atom interferometers.

Apart from searches for a GWB, also searches looking for continuous gravitational waves (CWs) use long stretches of data typically spanning one to multiple year(s). Since these CW signals have a more characteristic and narrowband signal morphology, it is less likely correlated noise sources could 'fake' a CW signal, whereas this could be the case for a GWB. However, one could imagine that high levels of correlated noise among GW detectors could reduce the sensitivity achieved by CW analyses. To the best of my knowledge, this has not yet been studied and might be a worthwhile research project to pursue in the future.

Mental well-being survey

As a concluding remark I would like to comment on the mental well-being survey I have been conducting the last two years. In appendix A, I presented the results of the survey's first edition, which took place in 2021. Some of the interesting findings are that early career or young scientists, as well as people who struggle with job security and people who do not feel properly recognised for their work have worse mental health and are also considering more often to leave academia or the collaborations. On the other hand the majority (62.7%) of participants find their work very meaningful.

When setting up the survey my goal was threefold. First of all, I wanted to normalize talking about mental well-being, in which I believe the survey (at least partially) succeeded, given the numerous presentations I gave at collaboration meetings and conferences as well as the two articles I wrote for the LIGO magazine. Secondly,

the survey enables us to gauge the mental well-being as well as the demographics from our collaborations. This data can provide us insights which are critical for the third goal of this effort: taking action. I believe there are a number of structural flaws in the academic system such as short term contracts leading to job insecurity and unwritten rules 'forcing' early career scientists to move to distant institutes, regardless of the potential impact on their well-being. My idealistic self hopes that in the future we could improve some of these issues and I believe that having data to back certain changes is crucial. Therefore I am excited to keep on pushing forward the mental well-being survey in the domain of GW and High Energy astrophysics and associated fields. This does not only include having a (yearly) recurring survey, but also further optimizing the questions, broadening the pool of possible participants and increasing the participation rate. Finally, we should also try to include relevant control groups such as people in academia outside large, international collaborations and highly educated people outside academia.

Appendix

A

Probing depressive symptoms and the desire to leave academia among scientists in large, international collaborations in STEM

Please note that the results in this appendix have not yet been published, nor peer reviewed. The paper is submitted for peer review and a preprint is available at [219].

In this appendix we will present some of the key results of the first mental well-being survey, distributed in the LVK collaborations during the summer of 2021. We introduce our work with respect to the state of the art in Sec. A.1. Afterwards, in Sec. A.2 we introduce the used methods and the scope of the survey. The results are presented in Sec. A.3 and in Sec. A.4 some of the key findings are discussed. In Sec. A.5 some additional results are supplied.

A.1 Introduction

Many present-day research projects in STEM (Science, Technology, Engineering, and Mathematics) require large investments both concerning funding as well as person power. Therefore it is often no longer feasible for a single institution to conduct such research. Instead, a large number of institutions join effort in a scientific collaboration to which they contribute with financial resources and/or person power [98]. In addition to their large membership size, members of these collaborations are typically scattered across multiple continents and time zones. This creates unique working conditions in terms of working hours, work-related pressure, and recognition for individual efforts. Some of these factors could potentially contribute to additional stress on mental health. For instance, in large collaborations, published papers are often attributed to the entire collaboration, involving hundreds or even thousands of authors, without specifically identifying individual contributions. This

may impact members' sense of recognition for their individual efforts within the collaboration. Additionally, due to the global nature of these collaborations, online meetings often fall outside regular office hours. Furthermore, these international collaborations can encompass a culturally diverse group of members, presenting challenges in creating a safe, culturally sensitive, and inclusive work environment [249]. On the other hand, these collaborations can also foster an active network where individuals closely work with a large number of colleagues. For instance, in the scientific collaborations examined in this study, social events for early-career researchers are actively organized during large internal meetings held twice a year. These networks of collaborators can foster a sense of solidarity among scientists in these collaborations, which may not be available to scientists who are not part of such collaborative projects.

To the best of our knowledge, no study has examined the well-being and desire to leave academia among members of large, international scientific collaborations. However, previous studies have indicated that certain groups within the scientific community are prone to experiencing mental health challenges. For instance, earlier research has shown that PhD students often face poor mental health [158, 163, 179]. Evans et al. [163] reported high levels of depressive and anxiety symptoms among graduate students (both doctoral and master's students) in STEM and other academic domains. The unfavorable work-life balance and compromised mental well-being can result in young researchers leaving the academic environment shortly after completing their PhD, as demonstrated by various previous studies [125, 190, 264]. The significant outflow of young researchers could potentially impact the quality of future research.

Another study examined how the research culture affects the mental health of STEM researchers and highlighted the detrimental effects of job insecurity and the competitive academic environment [247]. Moss et al. [272] investigated the relationship between mental health literacy, help-seeking behavior, and levels of psychological distress among postgraduate researchers at two UK universities. They found that lower levels of well-being were associated with higher levels of distress and decreased help-seeking [272].

Furthermore, there is evidence suggesting that the psychological well-being of researchers is worse than that of the general population or other highly educated populations. Researchers commonly experience higher levels of burnout compared to the general population, aligning more closely with 'high-risk' employees such as healthcare workers [188]. Moreover, the study found that a greater proportion of researchers self-report mental health problems compared to the general population.

A study conducted in the United Kingdom found that doctoral researchers reported significantly higher levels of depressive and anxiety symptoms compared to similarly highly educated individuals in non-academic positions, even after controlling for various confounding factors [197]. Additionally, Leveque et al. [239] demonstrated that PhD students in Belgium exhibit a higher prevalence of mental health problems compared to comparable groups of highly educated individuals.

Furthermore, the COVID-19 pandemic disrupted the daily lives of many individuals and had a significant impact on their mental well-being [158, 164, 280, 290, 325]. The pandemic may have exacerbated the existing inequalities observed in academia. Emerging evidence indicates that the pandemic had a negative impact on the productivity of early-career and female researchers across various disciplines, including STEM [91, 199, 334].

In this study, our objective is to investigate the reported levels of depressive symptoms and the desire to leave academia among researchers involved in large, international collaborations in the STEM field. To achieve this, we conducted an online survey during the summer of 2021, which can be considered as the post-COVID-19 pandemic period in many member countries, including the United States. However, for certain countries in the collaboration, notably Japan, COVID-related restrictions were not fully relaxed until May 2023, making them still in the midst of the ongoing pandemic during the survey. Specifically, our survey targeted scientists in the field of gravitational-wave astrophysics who are members of the LIGO (Laser Interferometer Gravitational-Wave Observatory), Virgo, and KAGRA (Kamioka Gravitational Wave Detector) collaborations. These collaborations operate gravitational-wave detectors located in the United States, Europe, and Japan, respectively. The respective sizes of the different collaborations are: LIGO $\sim$ 1450 members, Virgo $\sim$ 470 members and KAGRA $\sim$ 450 members. Although the collaborations represent three separate entities, each with their own gravitational-wave detector(s), they have come together through a memorandum of agreement due to their shared scientific goals and challenges, namely, the detection of gravitational waves. The exploration of the scientific data is therefore conducted jointly.

By conducting this first well-being survey focused on large and international collaborations in the STEM field, our aim is to explore the prevalence of depressive symptoms and the intention to leave academia or the collaboration among its members. In particular, we investigate whether early-career scientists, who often face uncertain job prospects, experience different levels of depressive symptoms and exhibit a greater inclination to leave academia compared to senior, tenured faculty members who enjoy relatively secure positions and possibly greater work flexibility.

Additionally, this project examines whether members who identify themselves as belonging to minoritized groups, either within the collaboration or the country of their residence, experience distinct levels of psychological well-being and a differing willingness to leave academia or collaborative efforts compared to their peers who do not identify as belonging to minoritized groups. Lastly, we aim to understand the relationship between the high levels of job insecurity that might be experienced by early-career scientists and their mental health, as well as their desire to leave the academic field.

A.2 Methods

A.2.1 Recruitment and participants

Data collection for the survey started on 23rd August 2021 and concluded on 30th September 2021. An initial email to announce the survey was sent at the start of data collection to all members of the collaborations through the general email lists of the LIGO, Virgo, and KAGRA collaborations, to which all active members are expected to be subscribed. Additionally, the survey was announced during two collaboration meetings: a KAGRA internal meeting (27 - 29 August 2021) and a joint LIGO-Virgo-KAGRA collaboration meeting (6 - 10 September 2021). Finally, a reminder email was distributed to the same mailing lists several days before the end of the data collection period.

The survey was conducted online and maintained complete anonymity. This is the first well-being survey conducted by these collaborations. Participation in the survey was voluntary, and no monetary compensation was provided to the participants. To ensure confidentiality and create a safe environment for freely expressing their opinions, it was clearly stated at the beginning of the survey that only the research team would have access to the data. Furthermore, it was explicitly mentioned that participation in the survey would not have any effect on participants' current or future careers. All participants (N = 417) included in the analysis explicitly provided their informed consent. However, five participants were excluded from the subsequent analysis as they had skipped one or more crucial questions necessary for the analysis. An additional 15 participants were excluded because they were not actively engaged in research (e.g. administrative staff, retired professors). As a result, our final sample consisted of 397 participants. Ethical approval for the study was obtained from the ethical review committee of the University of Antwerp (reference number: SHW_21_75).

The survey was initially created in English. To increase participation rates from members in Asia, we also made the survey available in Japanese, Chinese (both traditional and simplified characters), and Korean. The distribution of respondents across the languages is as follows: English: 339 (82.3% of all participants), Japanese: 65 (15.8%), Chinese (Simplified and Traditional combined): 5 (1.2%), and Korean: 3 (0.7%).

Participants indicated their primary affiliation, and the sample sizes for each collaboration were as follows: LIGO: 202 (49.0% of all participants), Virgo: 109 (26.5%), and KAGRA: 89 (21.6%). Some participants' primary affiliations were not one of the three targeted collaborations in this survey, and they were mainly affiliated with different collaborations in related research fields. This group accounted for the remaining 12 (2.9%) participants.

The response rate for each collaboration can be estimated using two different methods. One approach would be to consider the number of individuals subscribed to the mailing lists through which the survey was distributed. However, it should be noted that these lists may include individuals with varying levels of activity within the collaboration, thus providing a lower limit for the participation rate. Another method involves focusing solely on individuals listed as authors within the collaboration, as this represents a more restricted and active group of members. The lower (upper) limits of the participation rates are as follows: LIGO: 14.2% (21.3%), Virgo: 23.2% (24.4%), and KAGRA: 20.2% (41.7%), respectively.

A.2.2 Measures

Depressive symptoms

Depressive symptoms were measured by using the Patient Health Questionaire (PHQ-9), which is a validated 9-item set of questions used for diagnosing depressive symptoms [230]. Participants respond to the questions using a four-point Likert scale ranging from 0 (not at all) to 3 (nearly every day), focusing on their experiences of the last two weeks. The total score is ranged between 0 and 27, where high scores indicate higher levels of depressive symptoms. An often used criteria for people experiencing depressive symptoms is a cut-off score of 10 [230]. The internal consistency between the different questions of PHQ-9 was good with a Cronbach's alpha value of 0.89 (95% confidence interval (CI): [0.87 ; 0.90]).

Leaving academia/collaboration

Participants were asked how often they considered to leave academia/the collaboration in the last 9 months. They could choose one of the following options: (1) Never, (2) Once or twice, (3) Several times per month, (4) Several times per week, (5) Every day, and (6) Prefer not to answer. We created an indicator variable that takes a value of 1 if they indicated that they considered leaving academia/the collaboration more than several times per week (i.e. those who chose (4) and (5)), which captures their desire to leave academia/the collaboration.

Demographics

Self reported age was recorded and divided in four categories. The age 50+ category will be used as the reference group to which different age categories are compared. As for gender identity, respondents could indicate one or multiple of the following categories: (1) male, (2) female, (3) cisgender, (4) transgender, (5) non-binary, (6) non-queer, (7) other, and (8) prefer not to answer. For the subsequent analysis, people indicating (fe)male or (fe)male + cisgender were categorized as '(Fe)male'. Other participants were grouped in the 'Other' category. In the regression analysis, male respondents are used as the reference group, to which female and those whose gender identify is 'other' will be compared.

Career level

Participants were asked to indicate their career level, for which they could choose from: (1) Bachelor (BA)/Master (MA) student, (2) PhD student, (3) post-doc, (4) staff scientist/engineer, (5) tenure track professor, (6) tenured professor, (7) other. As noted above, those who selected 'other' were excluded from the analysis. Tenured professors are set as the reference group in the regression analysis.

Working location

Participants were asked whether they primarily work on-site at the detector or in an office. Given the global measures to fight the spread of the COVID-19 virus, people who were not working at the detector sites are considered to be more likely to have been working from home due to the less crucial character of their 'on-site' presence. In the regression analysis, those who primarily work on-site are set as the reference group.

Uneven workload

We asked 'How often is the workload unevenly distributed so that it piles up?'. Participants could answer: Never (1), Rarely (2), Sometimes (3), Often (4) and Always (5). For the analysis, the first two options are coded as the 'Low' level of uneven workload, the third item ('Sometimes') as 'Medium' and the last two as 'High'. Those who reported a low level of uneven workload are set as the reference group in the regression analysis.

Work-life interference

We asked two questions pertaining work-life balance/interference. 'How often do you feel that the demands of your work interfere with your private or family life?' and 'How often do you feel the irregular meeting times interfere with your private or family life?' The latter question was asked as meeting times often can fall outside the regular office hours due to the global character of the joined research performed in collaboration between LIGO, Virgo and KAGRA. Participants could answer: Never (1), Rarely (2), Sometimes (3), Often (4) and Always (5). Both question were summed to get one overall parameter which serves as an indicator for work-life interference and can take values between 2 (low levels of interference) and 10 (high levels of interference). The two questions had a Cronbach's alpha of 0.76 (95% CI: [0.71 ; 0.83]), indicating a decent internal consistency. For the analysis, a combined score of 2-4 was categorized as the 'Low' level of work-life interference, a score of 5-7 as 'Medium' and a score of 8-10 as 'High'. Those who reported a low level of work-life interference are set as the reference group in the regression analysis.

Job influence

Participants were asked whether they have a large degree of influence on the decisions concerning their work and could answer with one of the following options: (1) Never, (2) Rarely, (3) Sometimes, (4) Often, and (5) Always. Items (1) and (2) were grouped as 'Low', (3) as 'Medium' and (4) and (5) as 'High' levels of job influence in the analysis. Those who reported 'High' level of influence in their work are set as the reference group in the regression analysis.

Recognition for work

Participants were asked whether they think their work as being part of the collaboration is properly recognised. They could respond with one of the following options: (1) Yes, both inside and outside the collaboration, (2) Only inside the collaboration, (3) Only outside the collaboration, (4) Neither inside nor outside the collaboration. We coded (1)-(3) as 'Yes' and (4) as 'No' with respect to recognition, where the former is used as reference group in the subsequent analysis.

Meaningfulness of work

Participants were asked how meaningful they find their work and were able to choose between one of the following options: (1) To a very large extent, (2) To a large extent, (3) Somewhat, (4) To a small extent and (5) To a very small extent. For the analysis, the first two options are coded as the 'High' level of meaningfulness, the third item ('Somewhat') as 'Medium' and the last two as 'Low'. Those who reported a high level of meaningfulness are set as the reference group in the regression analysis.

Job insecurity

Participants were asked whether they felt insecure about the future of their job and could answer with one of the following options: (1) Never, (2) Rarely, (3) Sometimes, (4) Often and (5) Always. Options (1) and (2) were grouped in 'Low', (3) in 'Medium' and (4) and (5) in 'High' levels of job insecurity for the subsequent analysis. The 'Low' group will be used as reference category.

Minoritized groups

Participants were asked whether they considered themselves as part of a minoritized group and could answer (1) Yes, in my country of residence, as well as the collaboration, (2) Yes, in the collaboration, (3) No and (4) Prefer not to answer. People who indicated to consider themselves to be part of a minoritized group were subsequently asked several additional questions, which are discussed in A.5.2. Non-minoritized participants are the reference group in the regression analysis.

A.3 Results

The prevalence of depressive symptoms and the proportion of individuals seriously contemplating leaving academia or the collaboration are presented in Table A.1, alongside the corresponding number of respondents in each category. Among the participants in this survey, the prevalence of depressive symptoms, as indicated by a PHQ-9 cut-off score of 10 or higher (indicating moderate to severe symptoms), was found to be 22.92% (95% CI: 18.88%-27.38%). The mean PHQ-9 score was 6.69 with a standard deviation of 5.86. Furthermore, 18.90% (95% CI: 15.16%-23.09%) of the participants reported considering leaving academia or the collaboration several times a week or more.

The results presented in Table A.1 indicate notable variations in the prevalence of depressive symptoms based on participants' career stages, with early-career scientists exhibiting higher levels of depressive symptoms compared to their more senior counterparts. To explicitly examine this difference, we further analyzed the prevalence of depressive symptoms separately for early-career scientists (BA/MA students, PhD students, and post-docs) and more senior scientists (staff scientists/engineers, tenure-track professors, and tenured professors). The prevalence among early-career scientists was found to be 32.8% (95% CI: 26.45%-39.75%), while among more senior scientists, it was 12.4%(95% CI: 8.13%-17.94%). This difference between the two groups was statistically significant, with t=5.02 (p-value=8.15e-7), as determined by a two-sided Welch's t-test ($\alpha = 0.05$).

Regarding the desire to leave academia or the collaboration, the findings in Table A.1 indicate that individuals who report a lack of recognition, influence, and meaningfulness in their work are more likely to seriously consider leaving. Furthermore, the results also suggest that those who face challenges in achieving a satisfactory work-life balance tend to contemplate exploring alternative career paths.

As previously mentioned, participants had the option to indicate whether they considered leaving only the collaboration, only academia, or both. Among the 62.7% of participants (N=249) who stated that they had considered leaving the collaboration and/or academia at least once, 47.8% expressed thoughts of leaving both academia and the collaboration, 27.7% considered leaving only academia, 20.1% contemplated leaving only the collaboration, and 4.4% preferred not to specify whether they wanted to leave academia or the collaboration.

Participants were also asked to indicate the reason(s) why they wanted to leave academia or the collaboration, with the option to select multiple reasons. The

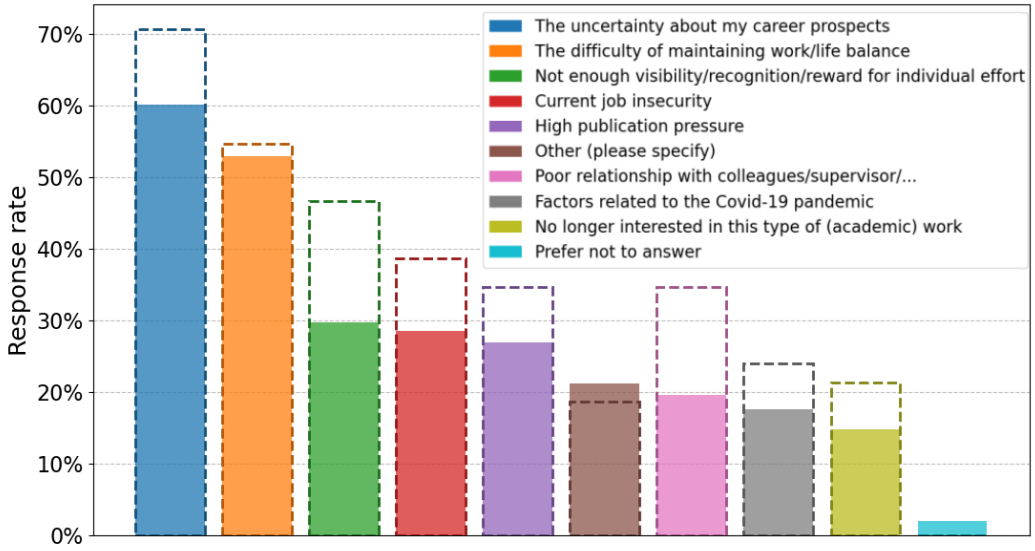

Fig. A.1.: Histogram indicating the different reasons why people consider leaving the collaboration/academia (filled bins). 249 people considered at least once to leave the collaboration/academia. On average each respondent gave about 2.7 reasons, leading to a total of 674 answers to the reasons for leaving shown here. The shown percentages are with respect to the number of people who responded to this question. The dashed bin edges represent the response rates of the 75 participants who consider leaving at least several times a week. These participants gave on average 3.4 reasons for considering to leave academia/the collaboration.

distribution of the 674 indicated reasons is illustrated in Fig. A.1 (filled bins), where the percentages are calculated based on the number of participants considering leaving academia or the collaboration. As participants could choose more than one reason, the sum of the percentages exceeds 100%. As shown in Fig. A.1, the two most common reasons selected were '*The uncertainty of my career prospects*' and '*The difficulty of maintaining work-life balance*', which were cited by over half of the participants who contemplated leaving academia or the collaboration. In Fig. A.1 we also show the response for a subset of participants who consider regularly (at least several times a week) to leave academia/the collaboration (dashed bin edges).

While the results presented in Table A.1 indicate that certain groups are more likely to experience depressive symptoms and contemplate leaving their current position than others, it is important to consider other potential factors that may explain these observed patterns. To account for these factors, we conducted a multivariate linear regression analysis with the PHQ-9 score as the dependent variable to examine the correlates of depressive symptoms. Additionally, we estimated a multivariate logit model with a binary indicator capturing the participants' desire to leave the collaboration/academia as the dependent variable. Both models included the same

set of demographic, career-related, and work-related variables as independent variables. To account for potential heteroskedasticity, we used robust standard errors in all estimations [252].

Table A.2 reports the regression results when the score for PHQ-9 was used as the dependent variable. The estimated coefficients are shown with the 95% CI and the associated p-values. We consider predictor variables to be statistically significant if their p-value is ≤ 0.05, in which case they are shown in bold in Table A.2 and A.3. In Sec. A.5.1, we present the estimation results for a logistic regression model in which the dichotomous dependent variable that captures the existence of depressive symptoms was used as the dependent variable. As in Table A.1, we used a cutoff score of $\geq$10 for the PHQ-9 as an indication of moderate to severe depressive symptoms.

As reported in Table A.2, we find that having high levels of job insecurity and being an early career scientist are strongly associated with higher levels of depressive symptoms. On average, the PHQ-9 score of people who feel insecure about their future job prospects tend to be higher by 3.71 (95% CI: 2.22-5.19) compared to the reference group, even after controlling for other confounding factors. As reported above, the mean PHQ-9 score for all samples was 6.69 and the range of the score is between 0 and 27. In addition, the average PHQ-9 score for BA/MA students (3.67; 95% CI: 0.68-6.65) as well as for PhD students (2.38; 95% CI: 0.26-4.50) and staff scientists/engineers (1.52; 95% CI: 0.06-2.98) are higher than the reference group, and these differences are all statistically significant. Furthermore, people who reported highly uneven workload tend to a have higher scores (3.52, 95% CI: 1.97-5.07) as well as those who reported high levels of work-life interference (2.05, 95% CI: 0.14-3.97), compared to the reference group who did not have any issues related to workload or work-life balance. Moreover, those that feel they lack recognition for their work tend to report higher PHQ-9 score (2.40; 95% CI: 0.52-4.29), indicating stronger depressive symptoms. Finally, participants who indicate to be part of a minoritized group both within their country of residence and the collaboration tend to record higher PHQ-9 scores (1.93, 95% CI: 0.39-3.47). The breakdown of the minoritized status is shown in Sec. A.5.2. At the same time, we did not find any evidence that female members and those who identify themselves as 'other' gender exhibit higher depressive symptoms compared to male counterparts. Further investigation revealed that post-docs and to a lesser extent PhD students and staff scientists, engineers struggle most for recognition, as well as participants from a minoritized group (see Sec. A.5.3).

As for their desire to leave academia/the collaboration, Table A.3 reports the odds ratios (ORs) when we estimated a logit model with an indicator variable for the participants' desire to leave the collaboration/academia as the dependent variable.

Relatively young scientists (age 18-29) and staff scientists/engineers are the most likely to regularly consider leaving academia/the collaboration. Participants who are less than 30 years old are 21.57 times (95% CI: 2.39-194.59) more likely to think weekly or daily about leaving academia/the collaboration, compared to their more senior counterparts. Staff scientists/engineers are 4.02 times (95% CI: 1.22-13.24) more likely to think regularly about leaving the collaboration compared to tenured professors. In addition, scientists who feel high levels of insecurity about their future job prospects (OR=3.87; 95% CI: 1.62-9.26) and those do not feel properly recognized for their work (OR=2.90; 95% CI: 1.33-6.31) are more likely to think about leaving academia/the collaboration. Participants who have little influence on work-related decisions are 2.64 times (95% CI: 1.11-6.26) more likely to consider leaving academia compared to their peers who can exercise a larger influence in their work.

		Prevalence	
	N (%)	Depressed (PHQ-9≥ 10)	Leaving (>several times a week)
Total	397 (100%)	22.92%	18.90%
Age			
18-29	114 (28.7%)	35.09%	28.07%
30-39	109 (27.5%)	23.85%	22.02%
40-49	59 (14.9%)	11.86%	10.17%
50+	55 (13.9%)	12.73%	1.82%
Unknown	60 (15.1%)	18.33%	20.00%
Gender			
Male	273 (68.8%)	21.25%	17.58%
Female	101 (25.4%)	26.73%	21.78%
Other	23 (5.8%)	26.09%	21.74%
Career			
BA/MA student	21 (5.3%)	42.86%	23.81%
PhD	96 (24.2%)	35.42%	22.92%
Post-doc	87 (21.9%)	27.59%	31.03%
Staff scientist, engineer	65 (16.4%)	18.46%	18.46%
Tenure track professor	28 (7.1%)	14.29%	14.29%
Tenured professor	100 (25.2%)	8.00%	5.00%
Working location: onsite			
Yes	65 (16.4%)	16.92%	12.31%
No	332 (83.6%)	24.10%	20.18%
Uneven workload			
Low	60 (15.1%)	10.00%	16.67%
Medium	133 (33.5%)	18.80%	15.79%
High	204 (51.4%)	29.41%	21.57%
Work-life interference			
Low	82 (20.7%)	14.63%	14.63%
Medium	208 (52.4%)	20.67%	14.90%
High	107 (27.0%)	33.64%	29.91%
Job influence			
Low	53 (13.4%)	37.74%	33.96%
Medium	117 (29.5%)	31.62%	25.64%
High	227 (57.2%)	14.98%	11.89%
Recognition			
Yes	345 (86.9%)	18.84%	14.20%
No	52 (13.1%)	50.00%	50.00%
Job meaningfulness			
Low	35 (8.8%)	40.00%	40.00%
Medium	113 (28.5%)	30.97%	25.66%
High	249 (62.7%)	16.87%	12.85%
Job insecurity			
Low	165 (41.6%)	9.09%	7.27%
Medium	85 (21.4%)	16.47%	10.59%
High	147 (37.0%)	42.18%	36.73%
Minority status			
No	271 (68.3%)	22.51%	15.13%
Country & collaboration	66 (16.6%)	28.79%	24.24%
Collaboration	40 (10.1%)	20.00%	30.00%
Unknown	20 (5.0%)	15.00%	30.00%

Tab. A.1.: Prevalence of depressive symptoms as measured by *PHQ-9* (Patient Health Questionnaire-9) and the desire to leave academia by sample characteristics.

	Multivariate regression		
	Coeff	95% CI	p
Age			
18-29	0.40	[-1.80, 2.60]	0.721
30-39	-0.02	[-1.59, 1.55]	0.980
40-49	-0.60	[-2.35, 1.15]	0.502
50+	Ref.	Ref.	Ref.
Unknown	-0.00	[-1.80, 1.79]	0.997
Gender			
Male	Ref.	Ref.	Ref.
Female	-0.06	[-1.26, 1.14]	0.917
Other	1.21	[-1.55, 3.97]	0.390
Career			
BA/MA student	**3.67**	**[0.68, 6.65]**	**0.016**
PhD	**2.38**	**[0.26, 4.50]**	**0.028**
Post-doc	-0.06	[-1.86, 1.74]	0.951
Staff scientist, engineer	**1.52**	**[0.06, 2.98]**	**0.041**
Tenure track professor	0.09	[-2.10, 2.28]	0.937
Tenured professor	Ref.	Ref.	Ref.
Working location: onsite			
Yes	Ref.	Ref.	Ref.
No	**1.10**	**[0.00, 2.20]**	**0.050**
Uneven workload			
Low	Ref.	Ref.	Ref.
Medium	1.34	[-0.15, 2.84]	0.078
High	**3.52**	**[1.97, 5.07]**	**0.000**
Work-life interference			
Low	Ref.	Ref.	Ref.
Medium	1.15	[-0.32, 2.62]	0.125
High	**2.05**	**[0.14, 3.97]**	**0.036**
Job influence			
Low	1.61	[-0.03, 3.26]	0.055
Medium	0.84	[-0.46, 2.15]	0.204
High	Ref.	Ref.	Ref.
Recognition			
Yes	Ref.	Ref.	Ref.
No	**2.40**	**[0.52, 4.29]**	**0.012**
Job meaningfulness			
Low	1.49	[-0.68, 3.65]	0.178
Medium	0.08	[-1.14, 1.30]	0.899
High	Ref.	Ref.	Ref.
Job insecurity			
Low	Ref.	Ref.	Ref.
Medium	0.83	[-0.52, 2.18]	0.231
High	**3.71**	**[2.22, 5.19]**	**0.000**
Minority status			
No	Ref.	Ref.	Ref.
Country & collaboration	**1.93**	**[0.39, 3.47]**	**0.014**
Collaboration	-0.65	[-2.43, 1.13]	0.476
Unknown	-0.74	[-3.61, 2.13]	0.612

Tab. A.2.: Estimated coefficients and the confidence intervals (CIs) when the level of depressive symptoms, as measured by the PHQ-9 score, is used as the dependent variable . Bold values indicates p-values ≤ 0.05.

	Multivariate regression		
	Odds ratio	95% CI	p
Age			
18-29	**21.57**	**[2.39, 194.59]**	**0.006**
30-39	7.83	[0.96, 64.01]	0.055
40-49	5.73	[0.70, 47.24]	0.105
50+	Ref.	Ref.	Ref.
Unknown	8.18	[0.94, 71.40]	0.057
Gender			
Male	Ref.	Ref.	Ref.
Female	0.84	[0.42, 1.68]	0.615
Other	1.14	[0.22, 5.78]	0.876
Career			
BA/MA student	1.01	[0.13, 7.65]	0.994
PhD	0.79	[0.18, 3.43]	0.749
Post-doc	1.42	[0.38, 5.31]	0.602
Staff scientist, engineer	**4.02**	**[1.22, 13.24]**	**0.022**
Tenure track professor	1.49	[0.30, 7.45]	0.627
Tenured professor	Ref.	Ref.	Ref.
Working location: onsite			
Yes	Ref.	Ref.	Ref.
No	2.22	[0.89, 5.57]	0.089
Uneven workload			
Low	Ref.	Ref.	Ref.
Medium	0.65	[0.24, 1.75]	0.393
High	1.00	[0.38, 2.63]	0.995
Work-life interference			
Low	Ref.	Ref.	Ref.
Medium	1.02	[0.42, 2.46]	0.963
High	1.97	[0.74, 5.28]	0.176
Job influence			
Low	**2.64**	**[1.11, 6.26]**	**0.028**
Medium	1.85	[0.95, 3.61]	0.072
High	Ref.	Ref.	Ref.
Recognition			
Yes	Ref.	Ref.	Ref.
No	**2.90**	**[1.33, 6.31]**	**0.007**
Job meaningfulness			
Low	1.38	[0.49, 3.88]	0.539
Medium	1.09	[0.56, 2.15]	0.792
High	Ref.	Ref.	Ref.
Job insecurity			
Low	Ref.	Ref.	Ref.
Medium	1.13	[0.43, 2.99]	0.808
High	**3.87**	**[1.62, 9.26]**	**0.002**
Minority status			
No	Ref.	Ref.	Ref.
Country & collaboration	1.24	[0.53, 2.88]	0.621
Collaboration	1.87	[0.83, 4.20]	0.130
Unknown	1.78	[0.51, 6.17]	0.364

Tab. A.3.: Estimated odds ratios and confidence intervals (CIs) when an indicator variable for high desire to leave academia/collaboration (i.e. consider leaving on a weekly/daily basis) is used as the dependent variable. Bold values indicates p-values ≤ 0.05.

A.4 Discussion

To the best of our knowledge, the present study constitutes the first survey that investigated the prevalence of depressive symptoms as well as the desire to leave academia/the collaboration among scientists in large, international collaborations in STEM fields.

The findings from our multivariate regression analyses indicate that several factors are associated with a higher prevalence of depressive symptoms. Specifically, early-career scientists, individuals belonging to minoritized groups, and those who experience high levels of job insecurity, uneven workload, work-life interference, and lack of recognition are more likely to exhibit higher rates of depressive symptoms compared to their more senior counterparts and those without work-related issues. Additionally, our analysis reveals that younger scientists, individuals who perceive a lack of influence and recognition in their work, and those who experience high job insecurity are more inclined to consider leaving academia or the collaboration on a regular basis. It is worth noting that our model controls for the effect of age, and thus that these results cannot be attributed solely to the fact that young individuals often report poorer mental health, particularly during and following the pandemic period.

The prevalence of depressive symptoms in our sample for BA/MA and PhD students is similar to prevalence reported before the pandemic by Evans et al [163]. The prevalence is slightly lower compared to the one reported for BA/MA during the peak of the pandemic by Essadek et al [158]. However, the results might have been affected by the limited sample sizes for BA/MA students in our sample. The prevalence of depressive symptoms for a sub-population with graduate or higher levels of education in the United States before the pandemic was reported to be significantly lower compared to our sample [283]. Even when we factor in the fact that the age composition of our sample is relatively young compared to the general population, this seems insufficient to explain the observed difference in the prevalence of depressive symptoms. Two possible reasons for the higher prevalence in our sample could be the timing of the survey during the (aftermath of the) COVID-19 pandemic and/or the nature of the academic work environment. However, further research is needed to gain more insights in these aspects.

The results of this study highlight the potential negative implications of the lack of recognition experienced by some members working in 'big science' collaborations, particularly for early-career scientists. This lack of recognition can contribute to a

sense of job insecurity among these researchers, as they may struggle to demonstrate their past achievements when seeking positions outside of the collaboration. Furthermore, due to the large scale of these collaborations, the number of tenure-track faculty positions is typically limited in comparison to the number of post-docs, graduate students, and other scientists involved. As demonstrated earlier, feelings of job insecurity also emerge as a significant determinant of depressive symptoms and the inclination to leave academia or the collaboration.

Furthermore, these large scientific collaborations also have unique features that can have detrimental effects on working conditions and work-life balance. The nature and scale of collaboration networks necessitate extensive coordination among multiple sites and institutions, resulting in a substantial number of meetings. Moreover, these meetings often take place outside regular business hours due to the international and multi-institutional nature of these collaborations, involving scientists from different continents. For instance, during the academic year, typically more than ten meetings are scheduled per week. Although members are not obligated to attend all scheduled meetings, the frequency and inconvenient timing of these meetings are highlighted as concerns in the open-ended responses provided in the survey.

As reported in Fig. A.1, the two dominant reasons that they consider leaving academia/the collaboration are 'uncertain career prospects' and 'the difficulty to maintain work-life balance'. This is true for all participants including those who consider leaving academia/the collaboration only occasionally (filled bins) as well as the subgroup of participants who think about leaving more than several times a week (dashed bin-edges). While the act of contemplating leaving academia/the collaboration is a priori neither positive nor negative, the reasons most often indicated by participants for their inclination to leave academia/the collaboration tend to have a more negative connotation. The response 'No longer interested in this type of (academic) work', which is of a more neutral or positive nature, was selected the least often compared to other reasons.

At the same time, it is also worth noting that a majority of the respondents expressed a sense of meaningfulness in their work (62.7% of all respondents) and reported a high level of influence in their work (57.2%). Additionally, a vast majority (more than 80 percent) of the respondents did not regularly consider leaving academia or the collaboration. These findings suggest that a significant number of scientists involved in the detection of gravitational waves perceive their work as valuable and worthwhile endeavors. Nevertheless, our study results also indicate that specific groups, particularly early-career researchers and those who lack a sense of recog-

nition, could benefit from proactive efforts by the collaborations to address their concerns.

Regarding minoritized groups, our findings reveal that individuals who identify themselves as belonging to minoritized groups in both the collaboration and their country of residence exhibit a higher prevalence of depressive symptoms. However, we did not find statistically significant evidence indicating that scientists who identify themselves as part of minoritized groups solely within the collaboration have a higher prevalence of depressive symptoms. Similarly, there was no evidence suggesting that minoritized groups display a higher propensity to leave academia or the collaboration after controlling for confounding factors. These findings may seem somewhat counter-intuitive, considering past studies that have demonstrated the negative experiences of traditionally underrepresented minorities in STEM fields [113, 286]. Several potential reasons could explain the lack of a strong association between minoritized status and well-being as well as the desire to change career paths. As reported in Sec. A.5.2, a majority of those who identify as part of minoritized groups within these collaborations responded 'No' (65.1%) when asked if they felt excluded because of their minority status. Similarly, 38.7% of these individuals reported that their minority status did not affect their career, and 26.4% stated that their status influenced their career both positively and negatively. Furthermore, our findings indicate that not all respondents who could identify as part of a minoritized group actually consider themselves as such. Considering the underrepresentation of women in STEM fields, including physics, it is highly likely that the majority of our female respondents can be considered part of a minoritized group, at least within the collaboration. However, only about one third of participants identifying with the 'Female' and 'Other' gender categories perceive themselves as part of a 'Gender minority'. This suggests that some individuals within these gender categories may not necessarily feel minoritized based on their gender. Thus, within the specific collaborations examined in this study, individuals belonging to certain minoritized groups may not have had universally overwhelmingly negative experiences associated with their minority status.

This study has several limitations. First, it is important to note that this was the first well-being survey conducted by the collaborations, resulting in a relatively low response rate among collaboration members. Furthermore, participation in the survey was voluntary, which introduces the potential for self-selection bias in our sample. It is possible that individuals with work-related issues or mental health conditions were more inclined to participate, leading to an overrepresentation of such individuals in our sample. As a result, our small sample may not be fully representative of all members within the three collaborations examined in this study.

Second, the lack of a comparison group limits our ability to assess how the conditions experienced by the scientists in this study compare to those of comparable groups. Ideally, we would have included scientists in academia who are not part of large international collaborations, as well as highly educated individuals outside academia, for meaningful comparisons. However, sampling these populations may present challenges as they may not have the same internal structures and connections as the large collaborations, such as LIGO, Virgo, and KAGRA. Third, all survey items, including depressive symptoms, relied on self-report measures, and thus might be subject to measurement errors. Additionally, the concept of minoritized status reflects the subjective perception of participants, which might differ from the traditional conceptualization of minority status, as discussed above. Nevertheless, we believe that understanding participants' subjective perception of belonging to a minoritized group is valuable in predicting its associations with our outcome variables that are also subjective in nature. Finally, it is important to note that this study is cross-sectional, limiting our ability to establish causal relationships between variables.

Despite these limitations, this study offers a significant and valuable contribution to the existing literature by shedding light on the challenges and opportunities associated with working in large and international collaborations. We have conducted a follow-up well-being survey in 2022, extending the invitation to scientists in eleven additional collaborations within the field of High Energy and gravitational-wave astrophysics, in addition to the three collaborations examined in this study. By monitoring the well-being of scientists engaged in these 'big science' projects on an annual basis, we aim to accumulate a more comprehensive understanding of their experiences. Furthermore, future surveys will help us assess the extent to which the results of the present study may have been influenced by the COVID-19 pandemic, as some countries were still under COVID-related restrictions during the survey period, potentially impacting the psychological well-being of certain participants. In conclusion, our findings underscore the importance of improving recognition and providing clearer job prospects, not only in reducing reported depressive symptoms but also in mitigating the likelihood of a substantial proportion of the next generation of scientists leaving academia or collaborative endeavors.

A.5 Additional results

In Sec. A.5.1, Sec. A.5.2 and Sec. A.5.3 we discuss some additional results which were presented as an appendix in [219]. Sec. A.5.4 contains data which is not included in any earlier work.

A.5.1 Logistic regression for depressive symptoms

BA/MA students and participants with high levels of insecurity about future job prospects are the strongest associated with the prevalence of people with depressive symptoms (PHQ-9 $\geq$ 10). BA/MA students are 11.98 times (95% CI: 2.37-60.53) more likely to have depressive symptoms compared to tenured professors. Also PhD students are more likely to experience depressive symptoms (OR= 4.49; 95% CI: 1.23-16.45). Feeling insecure about future job prospects increases the odds on depressive symptoms by 5.33 times (95% CI: 2.35-12.08). Also high levels of uneven workload distribution (OR= 4.05; 95% CI: 1.13-14.52) and lack of recognition (OR= 2.40; 95% CI: 1.08-5.34) are linked to higher odds of depressive symptoms.

Whereas staff scientists/engineers, people not working onsite, participants with high levels of work-life interference and minoritized people (Country & collaboration) did have significantly higher PHQ-9 scores in the multivariate linear regression in Sec. A.3, we do not find they have increased odds at having depressive symptoms (PHQ-9 $\geq$ 10).

A.5.2 Minority status

To gain further insight in the status of minoritized participants, they were asked to which minoritized group they were belonging, which is represented in Fig. A.2. In total 196 responses were collected for 106 participants whom indicated to belong to a minoritized group. The answers from the 66 participants who belong to minoritized groups both in their country of residence as well as the collaboration or indicated by the dashed bin edges in Fig. A.2. Furthermore they were asked whether they felt that being part of a minoritized group altered their career opportunities to which they could answer (1) Yes, (mainly) negatively (29.2% of minoritized participants),(2) Yes, (mainly) positively (1.9%),(3) Yes, sometimes negatively, sometimes positively (26.4%), (4) No (38.7%) and (5) Prefer not to answer (3.8%). Finally they were asked whether they felt excluded within the collaboration where people could

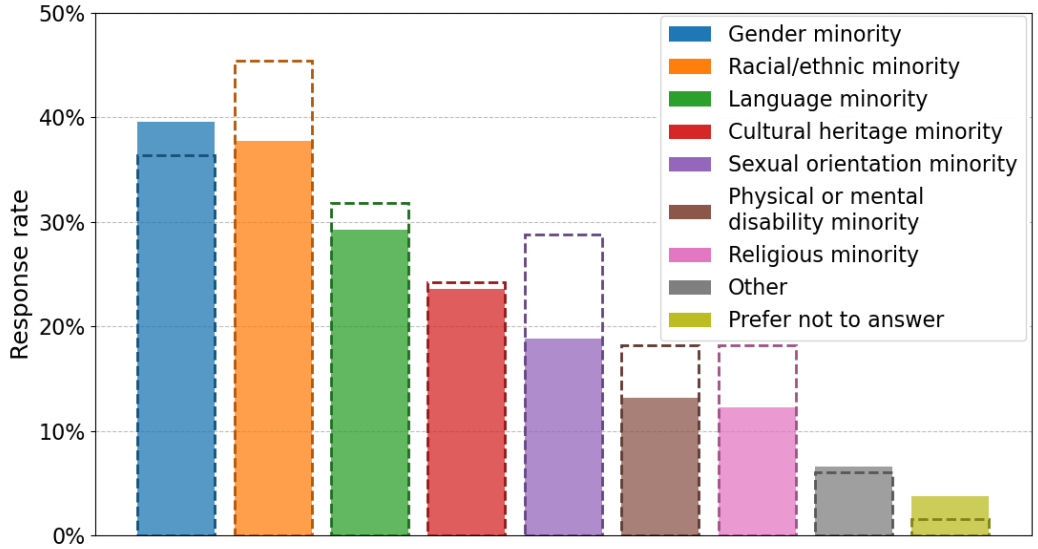

Fig. A.2.: Histogram indicating the different minoritized groups people consider to be part of. On average people belonging to minoritized groups belong to 1.8 minoritized groups. The shown percentages are with respect to the number of people who responded to this question. The dashed bin edges represent the response rates of the 66 participants who consider themselves to be part of a minoritized groups both in their country of residence as well as the collaboration. These participants indicate to belong on average to 2.1 minoritized groups.

indicate multiple answers from the following options (1) Yes, work related (21.7% of minoritized participants), (2) Yes, at social events at collaboration meetings or with colleagues (17.0%), (3) No (65.1%) (4) Prefer not to answer (4.7%). Note that the total percentage is larger than 100% since 9 participants responded with both option (1) as well as (2).

A.5.3 Recognition

In Tab. A.5 we present the uncorrected fractions of participants who reported a lack of recognition both inside as well as outside the collaboration by sample characteristics. The fraction across all respondents is 13.10% (95% CI: 9.94%-16.82%).

A.5.4 Loneliness and harassment

As part of the survey presented in this appendix a number of other questions were asked. In this section we will highlight some of these additional results which were not included in [219].

Loneliness

A sense of loneliness was probed by using the UCLA loneliness scale with a set of 3 questions [308]. Each question has a three-point scale with 1=Hardly Ever; 2=Some of the Time; 3=Often. A total score of 3-5 is often considered as being 'not lonely'and a score for 6-9 as 'lonely'. Therefore a total score of 6 can be used as a cut-off score for being lonely. The mean UCLA-3 score was 5.19 with a standard deviation of 1.78.

Harassment

Participants were asked whether they experienced sexual or any other type of harassment and could answer with one or more of the following options: (1) Yes work-related, (2) Yes, at social events at collaboration meetings or with colleagues, (3) No and (4) Prefer not to answer. In total 27 (73) participants indicated to have experienced sexual (other) harassment. Of the respondents experiencing harassment, 28.6%(19.2%) answered both option (1) as well as option (2) with respect to sexual (other) harassment, whereas the other participants responded either (1) or (2). 15 participants indicated they experienced both sexual as well as other types of harassment.

Sense of inclusiveness

Three questions were asked to gain insight into the inclusiveness of the collaboration. First of all participants were asked whether they 'ever felt uncomfortable due to remarks targeting minorities in the collaboration?'. Participants could answer with (1) Often (2.7% of all respondents), (2) Sometimes (23.5%), (3) Never (70.1%) and (4) Prefer not to answer (3.6%). Secondly they were asked 'Do you have the feeling that the collaborations try to be as inclusive as possible?', to which they could respond with: (1) Yes, they do a (very) good job (36.9% of all participants), (2) Yes, but not enough (44.2%), (3) No, they need to try harder (8.0%), (4) No,

not at all (3.4%), (5) Prefer not to answer (7.5%). Finally they were asked 'Have you ever felt pressured to partake in activities you did not want to (e.g. go to the pub, consume alcohol, take recreational drugs, pursue risky behavior, ...) with your collaborators/superiors?', to which they could respond with: (1) Yes (4.4% of all respondents), (2) No (94.2%), (3) Prefer not to answer (1.5%).

Discussion

In Tab. A.6 we present the prevalence for loneliness (UCLA-3 $\geq$6) and the fraction of participants who reported to have experienced harassment with respect to the sample characteristics. For the harassment we did not make the distinction between sexual or other types of harassment despite the different nature of both. This choice was made as limited statistics are available, especially in the case of sexual harassment. Providing too detailed information could jeopardize the anonymity of the participants. As mentioned earlier, there are 15 participants who experienced both sexual as well as other types of harassment, i.e. 85 participants (21.41%; 95% CI: 17.48%-25.78%) have experienced at least one type of harassment on at least one occasion as part of the collaboration.

The overall prevalence of loneliness is 45.09% (95% CI: 40.12%-50.13%). In a review study including loneliness data for 113 countries or territories [337] it was found that the prevalence of loneliness is somewhere between 10% and 20% depending on country, age and other factors. There are a number of differences that could impact the significantly different loneliness prevalence in our survey compared to this review study [337]. First of all, our survey was conducted in the aftermath of the COVID-19 pandemic. Secondly, the surveys used in [337] did not focus on people in academia, nor highly educated people in general. People part of these large collaborations often change country or even continent for successive academic positions. This could also lead to higher levels of reported loneliness due to higher isolation from their social network. Further investigations would be needed to understand which of these (or other) factors is the dominant reason to understand the stark difference in loneliness prevalence. Finally, one should also try to understand whether the observed prevalence in our sample is affected by self selection bias.

When looking at the uncorrected prevalences in Tab. A.6, we find that some of the more important predictors are: age, career, uneven workload, work-life interference, job influence, recognition, job meaningfulness, job insecurity and some of the minoritized groups. We do not observe large difference across gender and working location.

With respect to harassment we find that important predictors for the uncorrected prevalences in Tab. A.6 are: age, gender, career, uneven workload, work-life interference, recognition, job insecurity and some of the minoritized groups. We do not observe large difference across working location, job influence and job meaningfulness. Interesting to note is that early career/young scientists report lower (uncorrected) prevalences with respect to being harassed. More work is needed to further understand the levels of harassment reported in this survey and the relation to people's mental well-being.

Finally we want to conclude this section with stating that even though the vast majority of participants (81.1%) find the collaboration tries to be as inclusive as possible, a smaller majority (55.6%) believes they could do more.

	Multivariate regression		
	Odds ratio	95% CI	p
Age			
18-29	0.78	[0.17, 3.65]	0.754
30-39	0.60	[0.16, 2.20]	0.441
40-49	0.72	[0.19, 2.75]	0.627
50+	Ref.	Ref.	Ref.
Unknown	0.61	[0.15, 2.54]	0.501
Gender			
Male	Ref.	Ref.	Ref.
Female	1.33	[0.69, 2.56]	0.401
Other	2.12	[0.54, 8.37]	0.285
Career			
BA/MA student	**11.98**	**[2.37, 60.53]**	**0.003**
PhD	**4.49**	**[1.23, 16.45]**	**0.023**
Post-doc	1.39	[0.45, 4.34]	0.569
Staff scientist, engineer	2.28	[0.73, 7.09]	0.155
Tenure track professor	1.38	[0.28, 6.85]	0.694
Tenured professor	Ref.	Ref.	Ref.
Working location: onsite			
Yes	Ref.	Ref.	Ref.
No	1.74	[0.71, 4.22]	0.224
Uneven workload			
Low	Ref.	Ref.	Ref.
Medium	2.01	[0.62, 6.53]	0.246
High	**4.05**	**[1.13, 14.52]**	**0.032**
Work-life interference			
Low	Ref.	Ref.	Ref.
Medium	1.33	[0.51, 3.44]	0.557
High	2.37	[0.78, 7.21]	0.130
Job influence			
Low	2.28	[1.00, 5.22]	0.051
Medium	1.56	[0.78, 3.10]	0.206
High	Ref.	Ref.	Ref.
Recognition			
Yes	Ref.	Ref.	Ref.
No	**2.40**	**[1.08, 5.34]**	**0.032**
Job meaningfulness			
Low	0.77	[0.23, 2.50]	0.658
Medium	0.87	[0.45, 1.67]	0.672
High	Ref.	Ref.	Ref.
Job insecurity			
Low	Ref.	Ref.	Ref.
Medium	1.33	[0.52, 3.43]	0.550
High	**5.33**	**[2.35, 12.08]**	**0.000**
Minority status			
No	Ref.	Ref.	Ref.
Country & collaboration	1.01	[0.50, 2.02]	0.977
Collaboration	0.56	[0.22, 1.46]	0.238
Unknown	0.31	[0.06, 1.69]	0.175

Tab. A.4.: Estimated odds ratios and confidence intervals (CIs) when an indicator variable for the presence of depressive symptoms (PHQ-9 $\geq$ 10) is used as the dependent variable. Bold values indicates p-values $\leq$ 0.05.

	Prevalence
	Lack of recognition (inside and outside collaboration)
Total	13.10%
Age	
18-29	14.91%
30-39	15.60%
40-49	11.86%
50+	5.45%
Unknown	13.33%
Gender	
Male	13.19%
Female	13.86%
Other	8.70%
Career	
BA/MA student	9.52%
PhD	15.62%
Post-doc	20.69%
Staff scientist, engineer	15.38%
Tenure track professor	10.71%
Tenured professor	4.00%
Working location: onsite	
Yes	12.31%
No	13.25%
Uneven workload	
Low	5.00%
Medium	12.03%
High	16.18%
Work-life interference	
Low	6.10%
Medium	10.10%
High	24.30%
Job influence	
Low	16.98%
Medium	19.66%
High	8.81%
Recognition	
Yes	-
No	-
Job meaningfulness	
Low	45.71%
Medium	19.47%
High	5.62%
Job insecurity	
Low	5.45%
Medium	8.24%
High	24.49%
Minority status	
No	9.96%
Country & collaboration	22.73%
Collaboration	15.00%
Unknown	20.00%

Tab. A.5.: Fraction of respondents reporting a lack of recognition both inside as well as outside the collaboration.

		Prevalence	
	N (%)	Lonely (UCLA-3$\geq$ 6)	Harassed (Sexual, other or both)
Total	397 (100%)	45.09%	21.41%
Age			
18-29	114 (28.7%)	48.25%	7.89%
30-39	109 (27.5%)	54.13%	32.11%
40-49	59 (14.9%)	35.59%	23.73%
50+	55 (13.9%)	38.18%	14.55%
Unknown	60 (15.1%)	38.33%	31.67%
Gender			
Male	273 (68.8%)	45.05%	17.95%
Female	101 (25.4%)	44.55%	26.73%
Other	23 (5.8%)	47.83%	39.13%
Career			
BA/MA student	21 (5.3%)	47.62%	9.52%
PhD	96 (24.2%)	45.83 %	6.25%
Post-doc	87 (21.9%)	59.77 %	29.89%
Staff scientist, engineer	65 (16.4%)	38.46%	27.69%
Tenure track professor	28 (7.1%)	57.14%	32.14%
Tenured professor	100 (25.2%)	32.00%	24.00%
Working location: onsite			
Yes	65 (16.4%)	40.00%	24.62%
No	332 (83.6%)	46.08%	20.78%
Uneven workload			
Low	60 (15.1%)	38.33%	15.00%
Medium	133 (33.5%)	41.35%	17.29%
High	204 (51.4%)	49.51%	25.98%
Work-life interference			
Low	82 (20.7%)	28.05%	4.88%
Medium	208 (52.4%)	43.75%	22.60%
High	107 (27.0%)	60.75%	31.78%
Job influence			
Low	53 (13.4%)	54.72%	16.98%
Medium	117 (29.5%)	53.85%	22.22%
High	227 (57.2%)	38.33%	22.03%
Recognition			
Yes	345 (86.9%)	40.58%	20.00%
No	52 (13.1%)	75.00%	30.77%
Job meaningfulness			
Low	35 (8.8%)	65.71%	22.86%
Medium	113 (28.5%)	52.21%	21.24%
High	249 (62.7%)	38.96%	21.29%
Job insecurity			
Low	165 (41.6%)	28.48%	19.39%
Medium	85 (21.4%)	41.18%	12.94%
High	147 (37.0%)	65.99%	28.57%
Minority status			
No	271 (68.3%)	40.59%	17.34%
Country & collaboration	66 (16.6%)	60.61%	24.24%
Collaboration	40 (10.1%)	50.00%	42.50%
Unknown	20 (5.0%)	45.00%	25.00%

Tab. A.6.: Prevalence of loneliness symptoms as measured by *UCLA-3* and prevalence of being harassed (either sexual, other or both) by sample characteristics.

B

Impact of magnetic noise on the Einstein Telescope with the HFLF-cryo and HF-only sensitivities

In this appendix we present the impact of magnetic noise on the ET using its latest sensitivity curves HFLF-cryo and HF-only. These figures complement the figures and discussion made in Chapter 8, where older design sensitivities ET-D and ET-B were used. For further discussion on the implications of the results we refer to Chapter 8. Note that in this appendix we do not consider the possible reduction in magnetic coupling for heavier mirrors. This was only applied in Fig. 8.10, see Chapter 8 for more details.

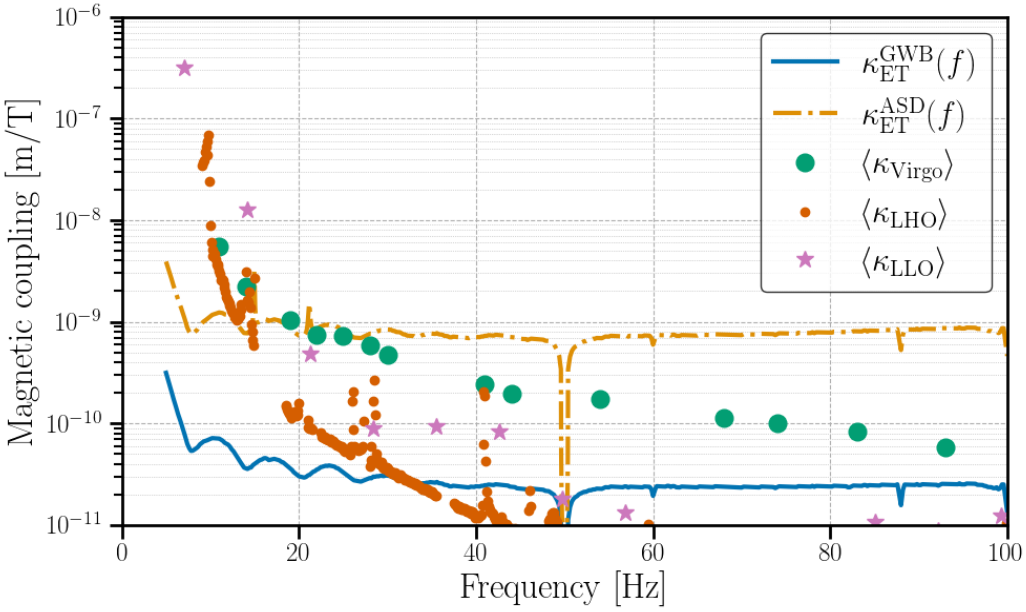

Fig. B.1.: 'ASD' and 'GWB' magnetic coupling function upper limits for the ET's HFLF-cryo design sensitivity. Also included are the average of the measurements of the coupling functions at LIGO Hanford, LIGO Livingston and Virgo during the O3 run for comparison. This figure is the updated version of Fig. 8.2, where the ET-D design sensitivity is replaced by the more recent HFLF-cryo sensitivity.

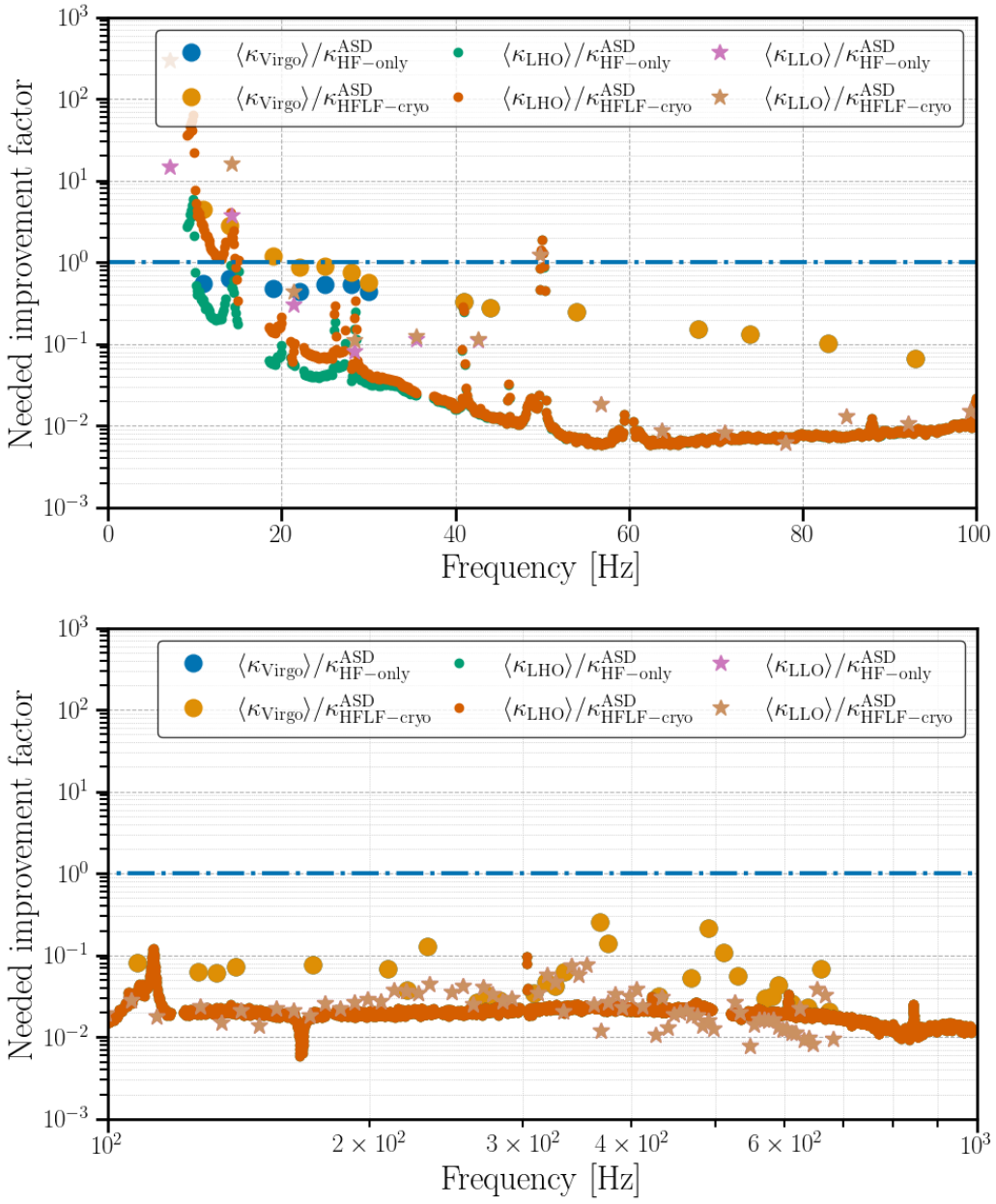

Fig. B.2.: Needed improvement factor as a function of frequency for the 'ASD' upper limits on the ET magnetic coupling function. The low-frequency (top panel) magnetic coupling poses a greater challenge for the operation of ET compared to the high-frequency (bottom panel) magnetic coupling. In both panels, the dash-dotted blue line indicates the line where no improvement is necessary. This figure is the updated version of Fig. 8.3, where the ET-B (ET-D) design sensitivity is replaced by the more recent HF-only (HFLF-cryo) sensitivity.

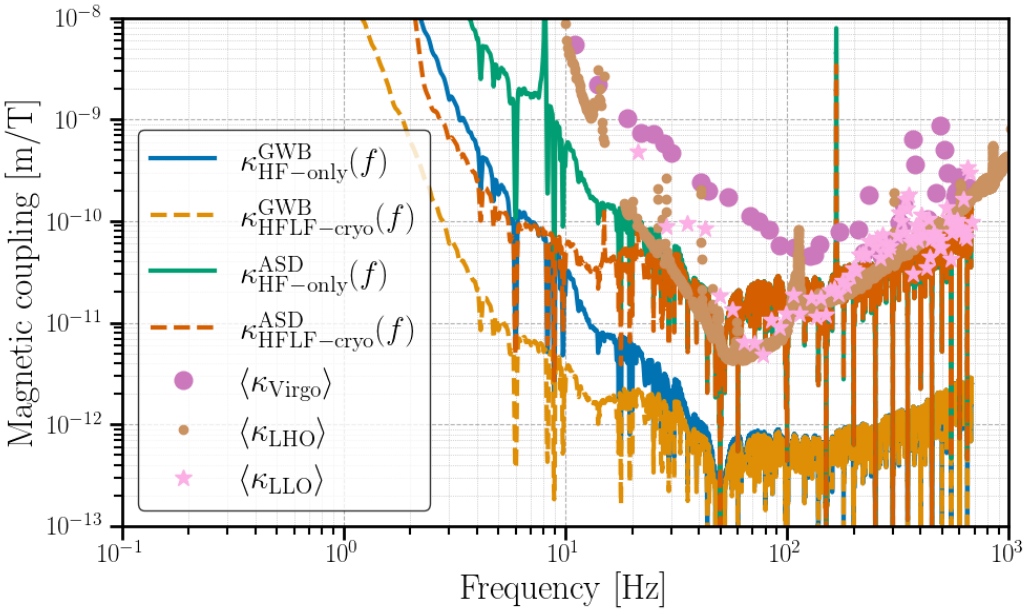

Fig. B.3.: 'ASD' and 'GWB' magnetic coupling function upper limits of the HF-only and HFLF-cryo design sensitivities in the case the local magnetic noise is the same level as the CEB at Virgo during O3. Also included are the average of the measurements of coupling functions at LIGO Hanford, LIGO Livingston and Virgo during the O3 run for comparison. This figure is the updated version of Fig. 8.4, where the ET-B (ET-D) design sensitivity is replaced by the more recent HF-only (HFLF-cryo) sensitivity.

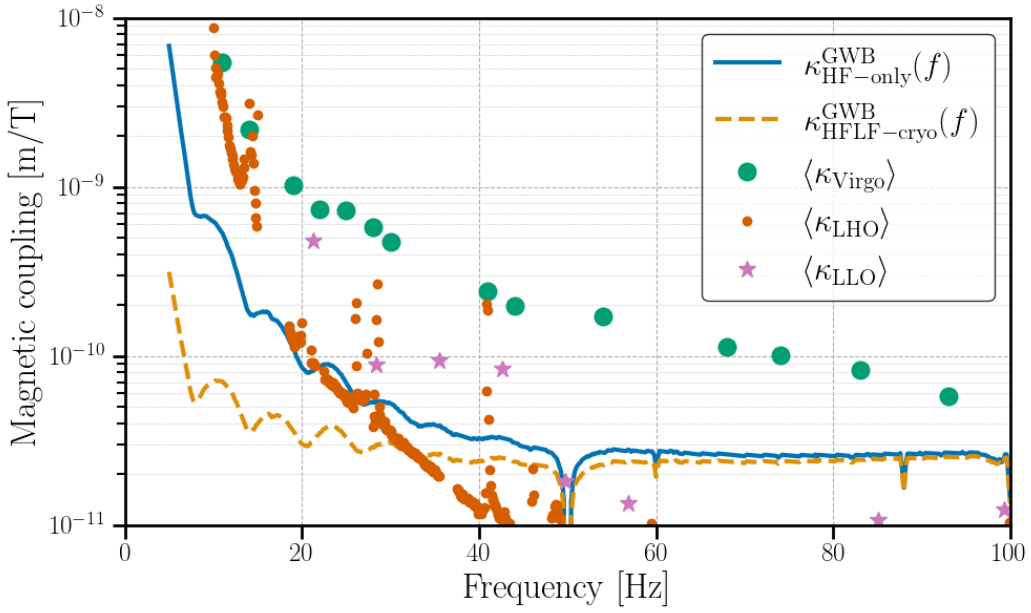

Fig. B.4.: Variation in the 'GWB' magnetic coupling function upper limits for the different ET designs. Also included are the average of the measurements of coupling functions at LIGO Hanford, LIGO Livingston and Virgo during the O3 run for comparison. This figure is the updated version of Fig. 8.7, where the ET-B (ET-D) design sensitivity is replaced by the more recent HF-only (HFLF-cryo) sensitivity.

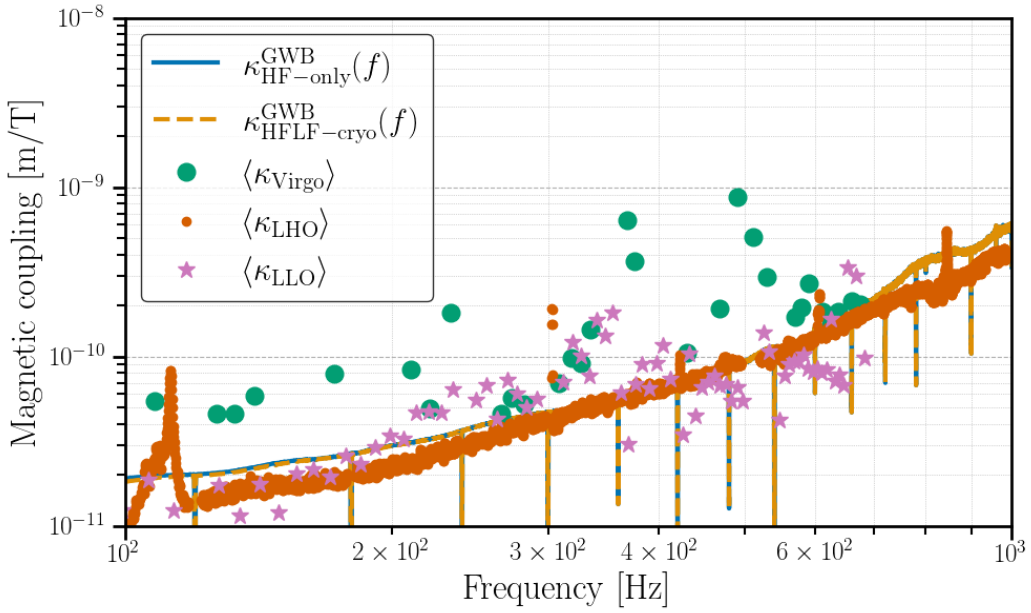

Fig. B.5.: Upper limits on 'GWB' magnetic coupling function of the HF-only and HFLF-cryo designs at high frequencies. Both designs have identical sensitivity in this frequency range. Also included is the average of the measurements of coupling functions at LIGO Hanford, LIGO Livingston and Virgo during the O3 run for comparison. This figure is the updated version of Fig. 8.8, where the ET-B (ET-D) design sensitivity is replaced by the more recent HF-only (HFLF-cryo) sensitivity.

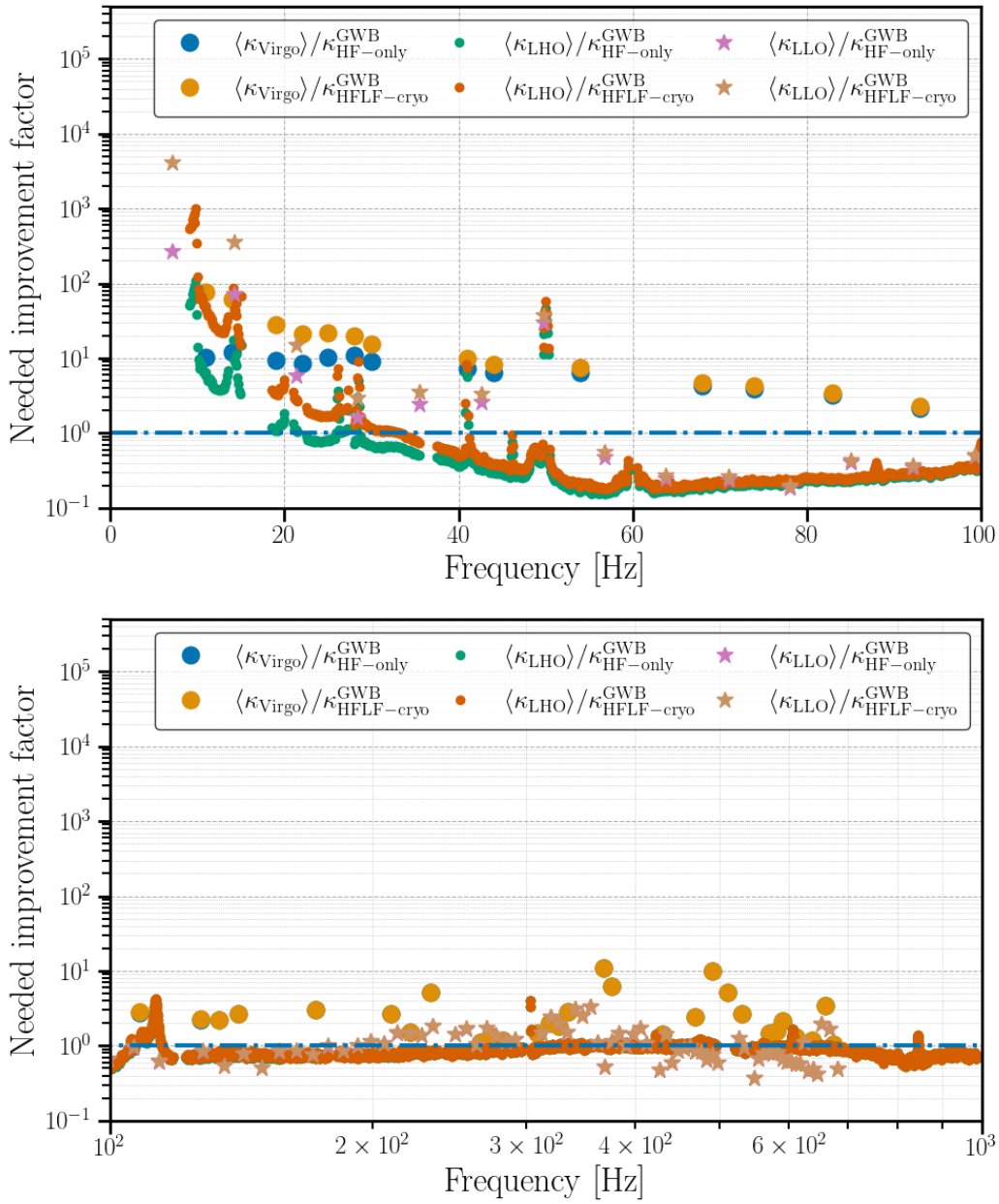

Fig. B.6.: Needed improvement factor as a function of frequency for the 'GWB' upper limits on the ET magnetic coupling function. The low-frequency (top panel) magnetic coupling poses a greater challenge for the operation of ET compared to the high-frequency (bottom panel) magnetic coupling. In both panels, the dash-dotted blue line indicates the line where no improvement is necessary. This figure is the updated version of Fig. 8.9, where the ET-B (ET-D) design sensitivity is replaced by the more recent HF-only (HFLF-cryo) sensitivity.
Note, the top panel of this figure differs from Fig. 8.10 as there a factor 5 reduction for Virgo was included, related to the heavier mass of the mirror. See Chapter 8 for a further discussion on this subject.

C

Complementary figures to Chapter 11

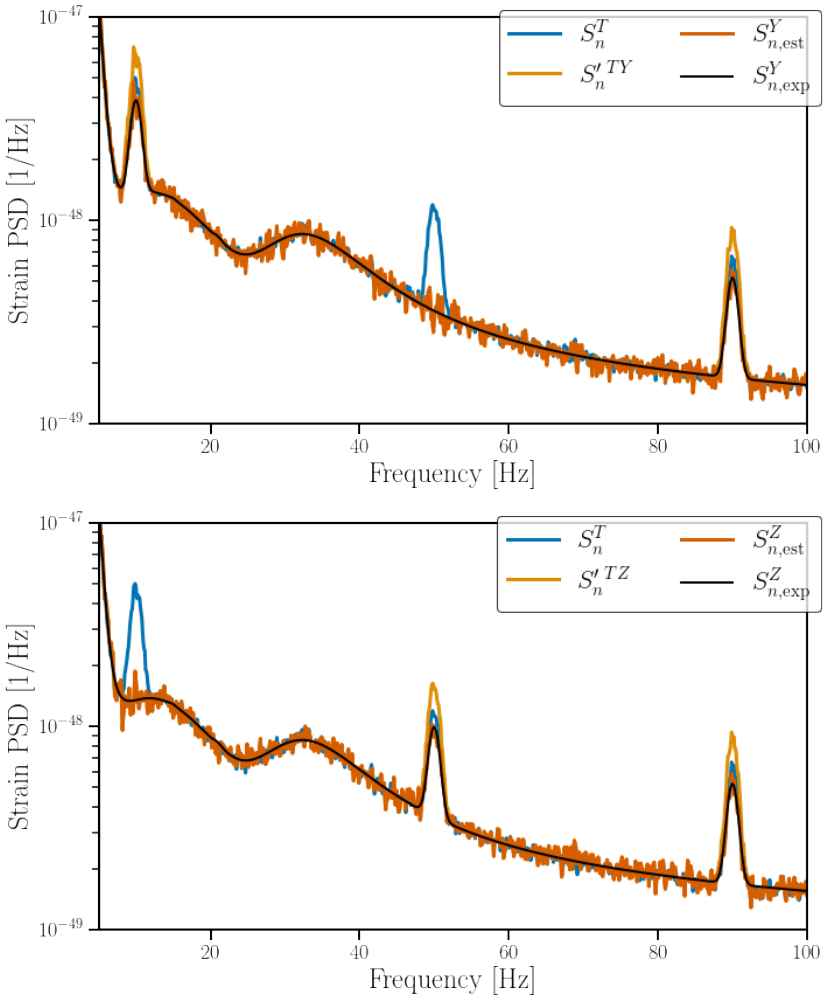

Fig. C.1.: Top (bottom): The PSD of the null channel T, the CSD of the T and $X/Y/Z$ channels, normalised such that it can serve as an estimate of $S_n^X/S_n^Y/S_n^Z$. The expected PSD of $X/Y/Z$, as shown in Eq. 11.12 and the estimated PSD as calculated in Eq. 11.14 and Eq. 11.15. This figure complements Fig. 11.2 in the main text.

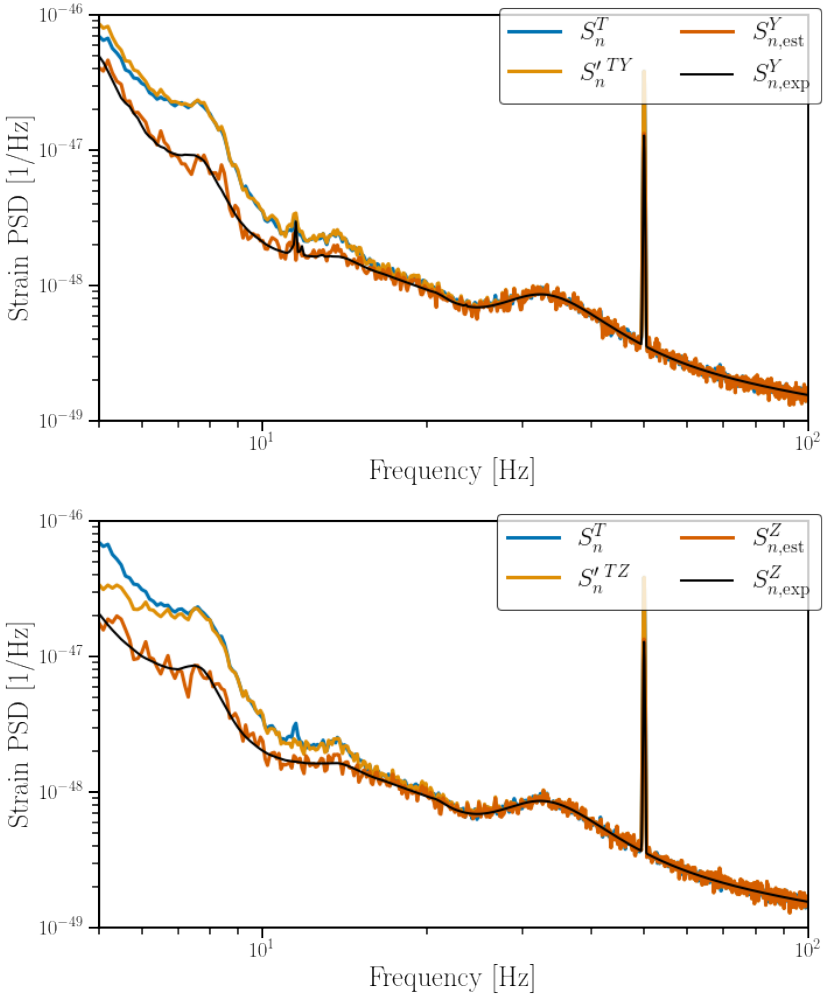

Fig. C.2.: Top (bottom): The PSD of the null channel T, the CSD of the T and Y (Z) channels, normalised such that it can serve as an estimate of S_n^Y (S_n^Z). The expected PSD of Y (Z), as shown in Eq. 11.13 and the estimated PSD as calculated in Eq. 11.18. As explained in the text, S_n^T and $S_n'^{TX}/S_n'^{TY}/S_n'^{TZ}$ yield a biased PSD estimate and one needs to use $S_{n,\mathrm{est}}^X/S_{n,\mathrm{est}}^Y/S_{n,\mathrm{est}}^Z$, derived in Eq. 11.18 using Eq. 11.10. This figure complements Fig. 11.5 in the main text.

List of Figures

List of Tables

Author's contributions

During my PhD I was an active member of the Virgo collaboration as well as the Einstein Telescope collaboration. My involvement concerned a number of working groups such as the stochastic GWB LVK research group, the LIGO and Virgo detector characterisation groups and several data analysis groups in the Einstein Telescope. This high level of involvement on several fronts did translate in a significant amount of scientific output.
Below I list my different publications and presentations both at conferences as well as internal collaboration meetings. The latter shows my high level of involvement in the different collaborations. Furthermore, I was co-chair of the Virgo Early Career Scientists group for one year and half. Since 2022 I am co-chair of the 'Stochastic detector characterisation' subgroup. In this capacity I have been coordinating and pushing forward the current efforts with respect to data quality for the search for a GWB with data from LIGO, Virgo and KAGRA's fourth observing run. Finally, since 2021 I am an active member of the Virgo diversity group. I have created and conducted two successful editions of a mental well-being survey in the field of gravitational-wave and high energy astrophysics over the past years.

Publications

First author

- Janssens K, Boileau G, Bizouard M-A, Christensen N, et al, *'Formulation of an extended null channel formalism for a triangular gravitational wave interferometer configuration in the case of non-identical and correlated noise'*, Eur. Phys. J. Plus 138, 352 `https://doi.org/10.1140/epjp/s13360-023-03948-9`
- Janssens K, Ball M, Schofield RMS, Christensen N, et al, *'Correlated 1-1000 Hz magnetic field fluctuations from lightning over earth-scale distances and their impact on gravitational wave searches'*, Phys. Rev. D 107, 022004 `https://doi.org/10.1103/PhysRevD.107.022004`

- Janssens K, Boileau G, Christensen N, Badaracco F and van Remortel N, *'Impact of correlated seismic and correlated Newtonian noise on the Einstein Telescope.'* Phys. Rev. D 106, 042008 https://doi.org/10.1103/PhysRevD.106.042008
- Janssens K, Callister T A, Christensen N, Coughlin MW, et al, *'Gravitational-wave geodesy: Defining false alarm probabilities with respect to correlated noise.'* Phys. Rev. D 105, 082001 https://doi.org/10.1103/PhysRevD.105.082001
- Janssens K, Martinovic K, Christensen N, Meyers PM and Sakellariadou M, *'Impact of Schumann resonances on the Einstein Telescope and projections for the magnetic coupling function.'* Phys. Rev. D 104, 122006 https://doi.org/10.1103/PhysRevD.104.122006

Contributing author

- van Remortel N, Janssens K, Turbang K, *'Stochastic gravitational wave background: methods and Implications'*, Progress in Particle and Nuclear Physics, 104003 (2022), https://doi.org/10.1016/j.ppnp.2022.104003.
- Acernese F et al., Virgo collaboration, *'Virgo Detector Characterization and Data Quality: results from the O3 run'*, Class. Quantum Grav. 40 185006, https://dx.doi.org/10.1088/1361-6382/acd92d
- Renzini A, et al, *'pygwb: Python-based library for gravitational-wave background searches'*, The Astrophysical Journal, 952 25 (2023), https://doi.org/10.3847/1538-4357/acd775
- Branchesi M, et al, *'Science with the Einstein Telescope: a comparison of different designs'*, https://arxiv.org/abs/2303.15923, JCAP07(2023)068), https://doi.org/10.1088/1475-7516/2023/07/068
- Fiori I, Paoletti F, Tringali MC, Janssens K, et al, *'The Hunt for Environmental Noise in Virgo during the Third Observing Run.'* Galaxies. 2020; 8(4):82. https://doi.org/10.3390/galaxies8040082
- D. Davis, et al, *'LIGO detector characterization in the second and third observing runs'* Classical and Quantum Gravity 2021; 38, 135014, http://dx.doi.org/10.1088/1361-6382/abfd85
- R. Abbott et al., LIGO scientific, Virgo and KAGRA collaboration, *'Upper Limits on the Isotropic Gravitational-Wave Background from Advanced LIGO's and Advanced*

Virgo's Third Observing Run', Phys. Rev. D 104, 022004, https://doi.org/10.1103/PhysRevD.104.022004

Preprints

- Janssens K and Ueda M, *'Probing depressive symptoms and the desire to leave academia among scientists in large, international collaborations in STEM'*, preprint available at https://arxiv.org/abs/2308.05107 and on ResearchGate, submitted to Scientific Reports

Non-scientific

- Janssens K, *'Mental health and the LVK - A crucial part of our wellbeing'*, LIGO Magazine issue 21, https://www.ligo.org/magazine/LIGO-magazine-issue21.pdf#page=30
- Janssens K, *'Mental health and supervision - Building Towards Healthy Supervision'*, LIGO Magazine issue 18, https://www.ligo.org/magazine/LIGO-magazine-issue18.pdf#page=26

Presentations

Conferences

- Recontres de Moriond 18-25 Mar 2023 (La Thuile, Italy)
  - Speaker, *'Prospects for an isotropic gravitational wave background detection with Earth-based interferometric detectors and the threat of correlated noise'*. Proceedings available at https://arxiv.org/abs/2305.02694
- Gravitational Wave Physics and Astronomy Workshop Dec 5-9 2022 (Melbourne, Australia)
  - Speaker, *'Probing mental health in academia in the field of multi-messenger astrophysics'*
- Belgian Dutch gravitational-wave meeting 13-14 Oct 2022 (Ghent, Belgium)

  - Speaker, *'Impact of correlated seismic and correlated Newtonian noise on the Einstein Telescope'*

- La sixième assemblée générale du GdR Ondes Gravitationnelles 10-12 Oct 2022 (Toulouse, France)
  - Speaker, *'Impact of correlated seismic and correlated Newtonian noise on the Einstein Telescope'*

- Gravitational wave orchestra 8-9 Sep 2022 (Louvain-La-Neuve, Belgium)
  - Invited speaker, *'Correlated noise and how it can disturb us listening to the symphony of the universe'*

- TAUP Sep 3 2021 (Virtual)
  - Invited member on panel discussion on *'Diversity and Inclusion in Astroparticle Physics'*

- Amaldi14 July 20 2021 (Virtual)
  - K. Janssens on behalf of the LIGO scientific, Virgo and KAGRA collaborations, *'Upper Limits on the Isotropic Gravitational-Wave Background from Advanced LIGO's and Advanced Virgo's First Three Observing Runs'*

Collaboration meetings

- Einstein Telescope Symposium 15-17 November 2022
  - K Janssens, *'Correlated noise in ET: a comparison between configurations'*

- LVK collaboration meeting 12-15 Sep 2022 (Cardiff, United Kingdom)
  - K. Janssens and P Charleton, *'Stochastic Face-to-Face: Stochastic detchar plans for O4'*
  - K. Janssens, *'Mental health survey - Final results and next steps'*
  - K. Janssens, poster on *'Impact of Schumann resonances on the Einstein Telescope and projections for the magnetic coupling function'*
  - K. Janssens, poster on *'Correlated 1-1000 Hz magnetic field fluctuations from lightning over earth-scale distances and their impact on gravitational wave searches'*

- Virgo collaboration meeting 4-7 July 2022 (Virtual)

  - K Janssens, et al, *'Impact of correlated seismic and correlated Newtonian noise on the Einstein Telescope'*

- LVK collaboration meeting 14-23 Mar 2022 (Virtual)
  - K. Janssens, *'Mental health survey - Gauging the mental health within LVK - Part 3'*

- Virgo collaboration meeting nov 2021 (Virtual)
  - Moderator of panel discussion on 'The ABC of journals and conferences' with Nelson Christensen, Archisman Ghosh and Joris van Heijningen

- LVK collaboration meeting 6-10 Sep 2021 (Virtual)
  - K. Janssens, *'Mental health survey - Gauging the mental health within LVK - Part 2'*

- LVK collaboration meeting 15-18 March 2021 (Virtual)
  - K. Janssens, T. Callister, N. Christensen, et al, *'Extending GW-Geodesy: A tool for validating the detection of a Gravitational Wave Background'*
  - K. Janssens, A. Miller, T. Regimbau and K. Turbang, *'Mental health survey - Gauging the mental health within LVK'*
  - K. Janssens and L. Haegel, *'Introduction to Virgo Early Career Scientsit Group (VECS)'*
  - Moderator of panel *'Navigating in the GW job landscape'* with M. Hennig, J. Slutsky, E. Capocassa and M. Fays.

- Virgo collaboration meeting 25-28 January 2021 (Virtual)
  - K. Janssens and L. Haegel on behalf of the VECS group, *'Virgo Early Career Scientists (VECS)'*

- Virgo collaboration meeting 2-5 November 2020 (Virtual)
  - K. Janssens, *'Hazing rituals and their impact on mental well-being in academia'*

- Virgo collaboration meeting 27-30 January 2020 (Pisa, Italy)
  - K. Janssens, I. Fiori, F. Paoletti, M. Tringali, R. Romero and G. Ballardin, *'Environmental noise: external magnetometers'*

Science communication

I have been one of the speakers of an online webinar presenting the results for the search for a GWB Advanced LIGO and Virgo's third observing run. Available online at: https://youtu.be/lmGTuNP-1uk?t=427. Furthermore, I have written the science summary on the same results in English as well as Dutch. In a science summary we explain the results of our latest papers in an easy to understand language and leave behind many technicalities and jargon. Available online at: https://www.ligo.org/science/Publication-O3StochIso/index.php. Finally, I was part of the 'Cool physics day' at the 2019 EPS conference in Ghent, where I explained the Virgo experiment to the general public.

Bibliography

[1] J. Aasi, J. Abadie, B. P. Abbott, et al., "The characterization of Virgo data and its impact on gravitational-wave searches", Classical and Quantum Gravity **29**, 155002 (2012) (cit. on p. 77).

[2] J. Aasi, J. Abadie, B. P. Abbott, et al. (LIGO Scientific Collaboration and Virgo Collaboration), "Searching for stochastic gravitational waves using data from the two colocated LIGO Hanford detectors", Phys. Rev. D **91**, 022003 (2015) (cit. on pp. 60, 64, 170, 217).

[3] J. Aasi and others., "Advanced LIGO", Classical and Quantum Gravity **32**, 074001 (2015) (cit. on pp. 24, 35, 38, 40, 136).

[4] J. Abadie et al. (LIGO Scientific Collaboration and Virgo Collaboration), "Upper limits on a stochastic gravitational-wave background using LIGO and Virgo interferometers at 600–1000 Hz", Phys. Rev. D **85**, 122001 (2012) (cit. on p. 60).

[5] B. P. Abbott, R. Abbott, T. D. Abbott, et al. (LIGO Scientific Collaboration and Virgo Collaboration), "Effects of data quality vetoes on a search for compact binary coalescences in advanced LIGO's first observing run", Classical and Quantum Gravity **35**, 065010 (2018) (cit. on p. 73).

[6] B. Abbott et al. (LIGO Scientific Collaboration and ALLEGRO Collaboration), "First cross-correlation analysis of interferometric and resonant-bar gravitational-wave data for stochastic backgrounds", Phys. Rev. D **76**, 022001 (2007) (cit. on p. 60).

[7] B. Abbott et al. (LIGO Scientific Collaboration), "Searching for a Stochastic Background of Gravitational Waves with LIGO", Astrophys. J. **659**, 918–930 (2007) (cit. on p. 74).

[8] B. Abbott, R. Abbott, R. Adhikari, et al. (LIGO Scientific Collaboration), "Upper limit map of a background of gravitational waves", Phys. Rev. D **76**, 082003 (2007) (cit. on p. 71).

[9] B. P. Abbott et al. (LIGO Scientific, Virgo Collaborations), "Binary Black Hole Population Properties Inferred from the First and Second Observing Runs of Advanced LIGO and Advanced Virgo", Astrophys. J. Lett. **882**, L24 (2019) (cit. on p. 67).

[10] B. P. Abbott et al. (The LIGO Scientific Collaboration and the Virgo Collaboration), "Directional limits on persistent gravitational waves using data from Advanced LIGO's first two observing runs", Phys. Rev. D **100**, 062001 (2019) (cit. on p. 115).

[11] B. P. Abbott et al. (LIGO Scientific Collaboration and Virgo Collaboration), "First low-frequency Einstein@Home all-sky search for continuous gravitational waves in Advanced LIGO data", Phys. Rev. D **96**, 122004 (2017) (cit. on p. 115).

[12] B. P. Abbott et al. (LIGO Scientific Collaboration, Virgo Collaboration and KAGRA Collaboration), "GW190425: observation of a compact binary coalescence with total mass ~ 3.4 $M_\odot$", The Astrophysical Journal Letters **892**, L3 (2020) (cit. on p. 57).

[13]B. P. Abbott et al. (LIGO Scientific Collaboration and Virgo Collaboration), "GWTC-1: a gravitational-wave transient catalog of compact binary mergers observed by LIGO and Virgo during the first and second observing runs", Phys. Rev. X **9**, 031040 (2019) (cit. on p. 57).

[14]B. P. Abbott et al. (LIGO Scientific and Virgo Collaborations), "Search for the isotropic stochastic background using data from Advanced LIGO's second observing run", Phys. Rev. D **100**, 061101 (2019) (cit. on pp. 211, 212).

[15]B. P. Abbott, R. Abbott, T. D. Abbott, et al., "Gravitational waves and gamma-rays from a binary neutron star merger: GW170817 and GRB 170817A", The Astrophysical Journal **848**, L13 (2017) (cit. on p. 56).

[16]B. P. Abbott, R. Abbott, T. D. Abbott, et al. (LIGO Scientific Collaboration and Virgo Collaboration), "GW150914: implications for the stochastic gravitational-wave background from binary black holes", Phys. Rev. Lett. **116**, 131102 (2016) (cit. on p. 65).

[17]B. P. Abbott, R. Abbott, T. D. Abbott, et al. (LIGO Scientific Collaboration and Virgo Collaboration), "GW170817: Observation of Gravitational Waves from a Binary Neutron Star Inspiral", Phys. Rev. Lett. **119**, 161101 (2017) (cit. on pp. 56, 57).

[18]B. P. Abbott, R. Abbott, T. D. Abbott, et al., "Multi-messenger observations of a binary neutron star merger", The Astrophysical Journal **848**, L12 (2017) (cit. on pp. 56, 57).

[19]B. P. Abbott, R. Abbott, T. D. Abbott, et al. (LIGO Scientific Collaboration and Virgo Collaboration), "Observation of gravitational waves from a binary black hole merger", Phys. Rev. Lett. **116**, 061102 (2016) (cit. on pp. 48, 55, 56).

[20]B. P. Abbott, R. Abbott, T. D. Abbott, et al., "Prospects for observing and localizing gravitational-wave transients with Advanced LIGO, Advanced Virgo and KAGRA", Living Reviews in Relativity **23**, 10.1007/s41114-020-00026-9 (2020) (cit. on pp. 37, 159, 190, 203).

[21]B. P. Abbott and others. (LIGO Scientific Collaboration and Virgo Collaboration), *Data for A search for the isotropic stochastic background using data from Advanced LIGO's second observing run*, tech. rep. LIGO-T1900058-v3 (2019) (cit. on p. 211).

[22]R. Abbott et al. (LIGO Scientific Collaboration, the Virgo Collaboration, and the KAGRA Collaboration), "All-sky, all-frequency directional search for persistent gravitational waves from Advanced LIGO's and Advanced Virgo's first three observing runs", Phys. Rev. D **105**, 122001 (2022) (cit. on p. 71).

[23]R. Abbott et al. (LIGO Scientific, Virgo, KAGRA collaborations), "Constraints on Cosmic Strings Using Data from the Third Advanced LIGO–Virgo Observing Run", Phys. Rev. Lett. **126**, 241102 (2021) (cit. on pp. 53, 65).

[24]R. Abbott et al. (LIGO Scientific and Virgo Collaborations), "Gravitational-wave Constraints on the Equatorial Ellipticity of Millisecond Pulsars", Astrophys. J. Lett. **902**, L21 (2020) (cit. on p. 162).

[25]R. Abbott et al. (The LIGO Scientific Collaboration and the Virgo Collaboration), *GWTC-2.1: deep extended catalog of compact binary coalescences observed by LIGO and Virgo during the first half of the third observing run*, 2021 (cit. on p. 57).

[26]R. Abbott et al. (LIGO Scientific, Virgo, KAGRA collabortions), "Search for continuous gravitational waves from 20 accreting millisecond X-ray pulsars in O3 LIGO data", (2021) (cit. on p. 162).

[27]R. Abbott, T. D. Abbott, S. Abraham, et al. (LIGO Scientific Collaboration and Virgo Collaboration), "GWTC-2: Compact Binary Coalescences Observed by LIGO and Virgo during the First Half of the Third Observing Run", Phys. Rev. X **11**, 021053 (2021) (cit. on p. 57).

[28]R. Abbott, T. D. Abbott, S. Abraham, et al., "Observation of Gravitational Waves from Two Neutron Star–Black Hole Coalescences", The Astrophysical Journal Letters **915**, L5 (2021) (cit. on p. 57).

[29]R. Abbott, T. D. Abbott, S. Abraham, et al. (LIGO Scientific Collaboration, Virgo Collaboration, and KAGRA Collaboration), "Search for anisotropic gravitational-wave backgrounds using data from Advanced LIGO and Advanced Virgo's first three observing runs", Phys. Rev. D **104**, 022005 (2021) (cit. on pp. 76–78, 85, 102, 115).

[30]R. Abbott, T. D. Abbott, S. Abraham, et al. (LIGO Scientific Collaboration, Virgo Collaboration, and KAGRA Collaboration), "Upper limits on the isotropic gravitational-wave background from Advanced LIGO and Advanced Virgo's third observing run", Phys. Rev. D **104**, 022004 (2021) (cit. on pp. 53, 60, 66, 76, 77, 85–87, 97, 103, 104, 118, 121, 129, 135, 153, 154, 156–158, 161, 191, 200, 202, 211, 225).

[31]R. Abbott, T. D. Abbott, F. Acernese, and et al, *The population of merging compact binaries inferred using gravitational waves through GWTC-3*, 2022 (cit. on pp. 57, 67, 68).

[32]R. Abbott, H. Abe, F. Acernese, K. Ackley, et al. (LIGO Scientific Collaboration, Virgo Collaboration, and KAGRA Collaboration), "All-sky search for continuous gravitational waves from isolated neutron stars using Advanced LIGO and Advanced Virgo O3 data", Phys. Rev. D **106**, 102008 (2022) (cit. on p. 52).

[33]M. Abe, P. Adamson, M. Borcean, et al., "Matter-wave Atomic Gradiometer Interferometric Sensor (MAGIS-100)", Quantum Science and Technology **6**, 044003 (2021) (cit. on p. 29).

[34]T. Accadia et al., "The NoEMi (Noise Frequency Event Miner) framework", Journal of Physics: Conference Series **363**, 012037 (2012) (cit. on p. 109).

[35]F. Acernese et al., "Virgo detector characterization and data quality: results from the o3 run", Classical and Quantum Gravity **40**, 185006 (2023) (cit. on p. 77).

[36]F. Acernese and et al, "Virgo upgrade investigations", Journal of Physics: Conference Series **32**, 223 (2006) (cit. on p. 36).

[37]F. Acernese et al. (Virgo Collaboration), "Advanced Virgo: a second-generation interferometric gravitational wave detector", Class. Quant. Grav. **32**, 024001 (2015) (cit. on pp. 24, 30, 34–38).

[38]F. Acernese et al. (Virgo Collaboration), "Calibration of Advanced Virgo and reconstruction of the detector strain h(t) during the observing run O3", Class. Quant. Grav. **39**, 045006 (2022) (cit. on p. 40).

[39]R. Adam and others., "Planck 2015 results. I. Overview of products and scientific results", Astronomy and Astrophysics **594**, A1 (2016) (cit. on p. 59).

[40]M. R. Adams and N. J. Cornish, "Discriminating between a stochastic gravitational wave background and instrument noise", Phys. Rev. D **82**, 022002 (2010) (cit. on pp. 216, 217, 219).

[41]M. R. Adams, "Detecting a stochastic gravitational wave background with space-based interferometers", PhD thesis (Montana State University, United States, Oct. 2014) (cit. on pp. 216, 217).

[42]P. A. R. Ade et al. (Planck Collaboration), "Planck 2015 results. XIII. Cosmological parameters", Astron. Astrophys. **594**, A13 (2016) (cit. on pp. 59, 63).

[43]A. Afzal et al. (The NANOGrav Collaboration), "The NANOGrav 15 yr data set: search for signals from new physics", The Astrophysical Journal Letters **951**, L11 (2023) (cit. on p. 58).

[44]G. Agazie et al. (The NANOGrav Collaboration), "The NANOGrav 15 yr data set: detector characterization and noise budget", The Astrophysical Journal Letters **951**, L10 (2023) (cit. on p. 58).

[45]G. Agazie et al. (The NANOGrav Collaboration), "The NANOGrav 15 yr data set: evidence for a gravitational-wave background", The Astrophysical Journal Letters **951**, L8 (2023) (cit. on pp. 23, 57, 58).

[46]G. Agazie et al. (The NANOGrav Collaboration), "The NANOGrav 15 yr data set: observations and timing of 68 millisecond pulsars", The Astrophysical Journal Letters **951**, L9 (2023) (cit. on p. 58).

[47]G. Agazie et al. (NANOGrav Collaboration), "The NANOGrav 15-year Data Set: Bayesian Limits on Gravitational Waves from Individual Supermassive Black Hole Binaries", (2023) (cit. on p. 58).

[48]G. Agazie et al. (NANOGrav Collaboration), "The NANOGrav 15-year Data Set: Constraints on Supermassive Black Hole Binaries from the Gravitational Wave Background", (2023) (cit. on p. 58).

[49]G. Agazie et al. (NANOGrav Collaboration), "The NANOGrav 15-year Data Set: Search for Anisotropy in the Gravitational-Wave Background", (2023) (cit. on p. 58).

[50]K. Aki and R. P. G., *Quantitative seismology: second edition* (University Science Books, Mill Valley, California, 2009) (cit. on pp. 79–81).

[51]T. Akutsu et al. (KAGRA Collaboration), "Construction of KAGRA: an Underground Gravitational Wave Observatory", PTEP **2018**, 013F01 (2018) (cit. on p. 146).

[52]T. Akutsu, M. Ando, A. Araya, et al., "The status of KAGRA underground cryogenic gravitational wave telescope", Journal of Physics: Conference Series **1342**, 012014 (2020) (cit. on p. 25).

[53]B. Allen, "Variance of the Hellings-Downs correlation", Phys. Rev. D **107**, 043018 (2023) (cit. on p. 21).

[54]B. Allen and A. C. Ottewill, "Detection of anisotropies in the gravitational-wave stochastic background", Phys. Rev. D **56**, 545–563 (1997) (cit. on p. 71).

[55]B. Allen and J. D. Romano, "Detecting a stochastic background of gravitational radiation: signal processing strategies and sensitivities", Phys. Rev. D **59**, 102001 (1999) (cit. on pp. 65, 66, 197).

[56]F. Amann et al., "Site-selection criteria for the Einstein Telescope", Rev. Sci. Instrum. **91**, 9 (2020) (cit. on pp. 25, 44, 81–83, 169, 170, 186, 225).

[57]P. Amaro-Seoane et al. (LISA Collaboration), *Laser Interferometer Space Antenna*, Available at `https://arxiv.org/abs/1702.00786`, Feb. 2017 (cit. on pp. 25–27, 51, 215, 237).

[58]K. L. D. and, "Status of GEO 600", Journal of Physics: Conference Series **610**, 012015 (2015) (cit. on p. 25).

[59]N. Andersson, K. G. Arun, S. Bose, et al., "Einstein Telescope design study: vision document", in (2009) (cit. on p. 160).

[60]M. Andrés-Carcasona, O. Ballester, O. Blanch, et al., "Instrumented baffle for the Advanced Virgo input mode cleaner end mirror", Phys. Rev. D **107**, 062001 (2023) (cit. on p. 39).

[61]T. Andric and J. Harms, "Simulations of gravitoelastic correlations for the Sardinian candidate site of the Einstein Telescope", Journal of Geophysical Research: Solid Earth **125**, e2020JB020401 10.1029/2020JB020401, e2020JB020401 (2020) (cit. on pp. 93, 170, 190).

[62]J. Antoniadis, Z. Arzoumanian, S. Babak, et al., "The International Pulsar Timing Array second data release: Search for an isotropic gravitational wave background", Monthly Notices of the Royal Astronomical Society **510**, 4873–4887 (2022) (cit. on pp. 57, 59).

[63]J. Antoniadis et al., "The second data release from the European Pulsar Timing Array I. The dataset and timing analysis", `10.1051/0004-6361/202346841` (2023) (cit. on p. 58).

[64]J. Antoniadis et al., "The second data release from the European Pulsar Timing Array II. Customised pulsar noise models for spatially correlated gravitational waves", (2023) (cit. on p. 58).

[65]J. Antoniadis et al., "The second data release from the European Pulsar Timing Array III. Search for gravitational wave signals", (2023) (cit. on pp. 23, 57, 58).

[66]J. Antoniadis et al., "The second data release from the European Pulsar Timing Array IV. Search for continuous gravitational wave signals", (2023) (cit. on p. 58).

[67]J. Antoniadis et al., "The second data release from the European Pulsar Timing Array: V. Implications for massive black holes, dark matter and the early Universe", (2023) (cit. on p. 58).

[68]M. A. Arain and G. Mueller, "Design of the Advanced LIGO recycling cavities", Opt. Express **16**, 10018–10032 (2008) (cit. on p. 40).

[69]J. W. Armstrong, "Low-Frequency Gravitational Wave Searches Using Spacecraft Doppler Tracking", Living Reviews in Relativity **9**, 1, 1 (2006) (cit. on p. 19).

[70]Z. Arzoumanian, P. T. Baker, H. Blumer, et al., "The NANOGrav 12.5 yr Data Set: Search for an Isotropic Stochastic Gravitational-wave Background", The Astrophysical Journal Letters **905**, L34 (2020) (cit. on pp. 57, 59).

[71]Y. Aso, Y. Michimura, K. Somiya, et al. (The KAGRA Collaboration), "Interferometer design of the KAGRA gravitational wave detector", Phys. Rev. D **88**, 043007 (2013) (cit. on pp. 24, 25, 40).

[72]P. Astone, M. Bassan, P. Bonifazi, et al., "Crosscorrelation measurement of stochastic gravitational waves with two resonant gravitational wave detectors", Astronomy and Astrophysics **351**, 811–814 (1999) (cit. on p. 60).

[73]S. Atsuta, T. Ogawa, S. Yamaguchi, et al., "Measurement of Schumann Resonance at Kamioka", Journal of Physics: Conference Series **716**, 012020 (2016) (cit. on pp. 79, 146).

[74]I. B and others., *LIGO-India, Proposal of the Consortium for Indian Initiative in Gravitational-wave Observations (IndIGO)*, (2011) `https://dcc.ligo.org/LIGO-M1100296/public` (cit. on p. 25).

[75]F. Badaracco and J. Harms, "Optimization of seismometer arrays for the cancellation of Newtonian noise from seismic body waves", Classical and Quantum Gravity **36**, 145006 (2019) (cit. on pp. 83, 84, 93, 164, 167, 170, 190).

[76]F. Badaracco, J. Harms, A. Bertolini, et al., "Machine learning for gravitational-wave detection: surrogate Wiener filtering for the prediction and optimized cancellation of Newtonian noise at Virgo", Classical and Quantum Gravity **37**, 195016 (2020) (cit. on pp. 93, 170, 190).

[77]M. Bader, S. Koley, J. van den Brand, et al., "Newtonian-noise characterization at Terziet in Limburg—the Euregio Meuse–Rhine candidate site for Einstein Telescope", Classical and Quantum Gravity **39**, 025009 (2022) (cit. on pp. 93, 169, 170, 186, 190, 193).

[78]L. Badurina, E. Bentine, D. Blas, et al., "AION: an atom interferometer observatory and network", Journal of Cosmology and Astroparticle Physics **2020**, 011 (2020) (cit. on p. 29).

[79]Q. Baghi, J. I. Thorpe, J. Slutsky, and J. Baker, "Statistical inference approach to time-delay interferometry for gravitational-wave detection", Phys. Rev. D **103**, 042006 (2021) (cit. on pp. 216, 217).

[80]M. Ball, R. Schofield, and R. Frey, *Intersite Magnetic Signals from Lightning*, tech. rep. T2000634 (LSC, 2020) (cit. on p. 163).

[81]G. Ballardin et al., "Measurement of the transfer function of the steering filter of the Virgo super attenuator suspension", Rev. Sci. Instrum. **72**, [Erratum: Rev.Sci.Instrum. 73, 233 (2002)], 3635–3642 (2001) (cit. on p. 33).

[82]S. W. Ballmer, "A radiometer for stochastic gravitational waves", Classical and Quantum Gravity **23**, S179–S185 (2006) (cit. on pp. 70, 71).

[83]S. W. Ballmer, "A Radiometer for stochastic gravitational waves", Class. Quant. Grav. **23**, edited by N. Mio, S179–S186 (2006) (cit. on p. 66).

[84]B. Battelier, B. Barrett, L. Fouché, et al., "Development of compact cold-atom sensors for inertial navigation", in Quantum optics, Vol. 9900, edited by J. Stuhler and A. J. Shields (International Society for Optics and Photonics, 2016), p. 990004 (cit. on p. 28).

[85]M. Beccaria, M. Bernardini, S. Braccini, et al., "Relevance of Newtonian seismic noise for the Virgo interferometer sensitivity", Classical and Quantum Gravity **15**, 3339 (1998) (cit. on p. 82).

[86]M. G. Beker, J. F. J. van den Brand, E. Hennes, and D. S. Rabeling, "Newtonian noise and ambient ground motion for gravitational wave detectors", Journal of Physics: Conference Series **363**, 012004 (2012) (cit. on p. 82).

[87]M. G. Beker et al., "Improving the sensitivity of future GW observatories in the 1Hz to 10Hz band: Newtonian and seismic noise", Gen. Rel. Grav. **43**, 623–656 (2011) (cit. on p. 82).

[88]D. Bersanetti, B. Patricelli, O. J. Piccinni, et al., "Advanced Virgo: Status of the Detector, Latest Results and Future Prospects", Universe **7**, 322 (2021) (cit. on p. 37).

[89]J. Betzwieser, *aLIGO LLO Logbook*, Available at `https://alog.ligo-la.caltech.edu/aLOG/index.php?callRep=65938`, 2023 (cit. on p. 136).

[90]E. D. Black, "An introduction to Pound–Drever–Hall laser frequency stabilization", American Journal of Physics **69**, 79–87 (2001) (cit. on pp. 32, 33).

[91]V. Böhm and J. Liu, "Impact of the COVID-19 pandemic on publishing in astronomy in the initial two years", Nature Astronomy **7**, 105–112 (2023) (cit. on p. 251).

[92]G. Boileau, N. Christensen, and R. Meyer, "Figures of merit for a stochastic gravitational-wave background measurement by LISA: implications of LISA Pathfinder noise correlations", arXiv e-prints, arXiv:2204.03867, arXiv:2204.03867 (2022) (cit. on pp. 217, 237).

[93]G. Boileau, N. Christensen, R. Meyer, and N. J. Cornish, "Spectral separation of the stochastic gravitational-wave background for LISA: Observing both cosmological and astrophysical backgrounds", Physical Review D **103**, 103529, 103529 (2021) (cit. on pp. 216–218).

[94]G. Boileau, A. C. Jenkins, M. Sakellariadou, R. Meyer, and N. Christensen, "Ability of LISA to detect a gravitational-wave background of cosmological origin: the cosmic string case", Phys. Rev. D **105**, 023510 (2022) (cit. on pp. 216, 217).

[95]G. Boileau, A. Lamberts, N. Christensen, N. J. Cornish, and R. Meyer, "Spectral separation of the stochastic gravitational-wave background for LISA in the context of a modulated Galactic foreground", Monthly Notices of the Royal Astronomical Society **508**, 803–826 (2021) (cit. on pp. 216, 217).

[96]L. G. Book and É. É. Flanagan, "Astrometric effects of a stochastic gravitational wave background", Physical Review D **83**, 024024, 024024 (2011) (cit. on p. 23).

[97]P. Bormann, B. Engdahl, and R. Kind, "New Manual of Seismological Observatory Practice", in (GFZ Potsdam, 2002) Chap. 2 (cit. on p. 186).

[98]K. Börner, F. Silva, and S. Milojević, "Visualizing big science projects", Nat Rev Phys **6**, 753–761 (2021) (cit. on p. 249).

[99]R. Bouchendira, P. Cladé, S. Guellati-Khélifa, F. ç. Nez, and F. ç. Biraben, "New determination of the fine structure constant and test of the quantum electrodynamics", Phys. Rev. Lett. **106**, 080801 (2011) (cit. on p. 28).

[100]M. Branchesi et al., "Science with the Einstein Telescope: a comparison of different designs", JCAP **07**, 068 (2023) (cit. on pp. 42–44, 53, 54, 98, 164, 166, 191).

[101]J. van den Brand, *Einstein Telescope: site and infrastructure session*, Available at `https://indico.in2p3.fr/event/20576/contributions/88527/attachments/61174/83351/Einstein_Telescope_Site_Infrastructure.pdf`, Dec. 2020 (cit. on p. 42).

[102]D. R. Brillinger, *Time series data analysis and theory -expanded edition* (Holden-Day, 1981) (cit. on p. 102).

[103]A. F. Brooks et al. (LIGO Scientific Collaboration), "Point absorbers in Advanced LIGO", Appl. Opt. **60**, 4047–4063 (2021) (cit. on p. 39).

[104]Buchner, J., Georgakakis, A., Nandra, K., et al., "X-ray spectral modelling of the AGN obscuring region in the CDFS: Bayesian model selection and catalogue", A&A **564**, A125 (2014) (cit. on p. 204).

[105]S. Burke-Spolaor et al., "The Astrophysics of Nanohertz Gravitational Waves", Astron. Astrophys. Rev. **27**, 5 (2019) (cit. on pp. 22, 50).

[106]T. A. Callister, M. W. Coughlin, and J. B. Kanner, "Gravitational-wave Geodesy: A New Tool for Validating Detection of the Stochastic Gravitational-wave Background", The Astrophysical Journal **869**, L28 (2018) (cit. on pp. 87–89, 160, 198, 201, 202, 205, 208, 213, 214).

[107]T. Callister, A. S. Biscoveanu, N. Christensen, et al., "Polarization-based Tests of Gravity with the Stochastic Gravitational-Wave Background", Phys. Rev. X **7**, 041058 (2017) (cit. on p. 219).

[108]B. Canuel et al., "ELGAR—a European Laboratory for Gravitation and Atom-interferometric Research", Class. Quant. Grav. **37**, 225017 (2020) (cit. on pp. 28, 29).

[109]B. Canuel et al., "Exploring gravity with the MIGA large scale atom interferometer", Sci. Rep. **8**, 14064 (2018) (cit. on pp. 28, 29).

[110]B. Canuel, "Étude d'un gyromètre à atomes froids", Theses (Université Paris Sud - Paris XI, Mar. 2007) (cit. on p. 143).

[111]C. Caprini and D. G. Figueroa, "Cosmological Backgrounds of Gravitational Waves", Class. Quant. Grav. **35**, 163001 (2018) (cit. on pp. 50–53, 65).

[112]S. Carroll, *Spacetime and geometry - an introduction to general relativity* (Pearson, 2014) (cit. on pp. 9, 14, 18).

[113]E. A. Cech and T. J. Waidzunas, "Systemic inequalities for LGBTQ professionals in STEM", Science Advances **7**, eabe0933 (2021) (cit. on p. 266).

[114]E. Cesarini, M. Lorenzini, A. Amato, et al., "The Virgo coating collaboration: a detailed study on thermoelasticity in crystalline materials and other research lines", in (Sept. 2018), p. 006 (cit. on p. 36).

[115]W. Chaibi, R. Geiger, B. Canuel, et al., "Low frequency gravitational wave detection with ground-based atom interferometer arrays", Phys. Rev. D **93**, 021101 (2016) (cit. on pp. 28, 29, 172).

[116]P. Cheinet, B. Canuel, F. Pereira Dos Santos, et al., "Measurement of the sensitivity function in a time-domain atomic interferometer", IEEE Transactions on Instrumentation and Measurement **57**, 1141–1148 (2008) (cit. on p. 143).

[117]S. Chen, R. N. Caballero, Y. J. Guo, et al., "Common-red-signal analysis with 24-yr high-precision timing of the European Pulsar Timing Array: inferences in the stochastic gravitational-wave background search", Monthly Notices of the Royal Astronomical Society **508**, 4970–4993 (2021) (cit. on pp. 57, 59).

[118]N. Christensen, "Stochastic gravitational wave backgrounds", Reports on Progress in Physics **82**, 016903 (2018) (cit. on pp. 51–53, 167).

[119]N. Christensen and R. Meyer, "Parameter estimation with gravitational waves", Rev. Mod. Phys. **94**, 025001 (2022) (cit. on pp. 215, 236, 237).

[120]M. Cifaldi, E. Cesarini, V. Fafone, et al., "Coping with anomalous power absorptions in the Advanced Virgo core optics", in (Aug. 2022) (cit. on p. 39).

[121]A. Cirone, I. Fiori, F. Paoletti, et al., "Investigation of magnetic noise in Advanced Virgo", Classical and Quantum Gravity **36**, 225004 (2019) (cit. on pp. 86, 126–129, 147, 163, 167).

[122]A. Cirone, A. Chincarini, M. Neri, et al., "Magnetic coupling to the Advanced Virgo payloads and its impact on the low frequency sensitivity", Review of Scientific Instruments **89**, 114501 (2018) (cit. on pp. 86, 126, 148, 163, 164).

[123]K. Collaboration, "Performance of the KAGRA detector during the first joint observation with GEO-600 (O3GK)", Progress of Theoretical and Experimental Physics, ptac093 (2022) (cit. on p. 41).

[124]G. Conforto and R. DeSalvo, "Proposal for lower frequency companions for the Advanced LIGO gravitational wave interferometric detectors", Nucl. Instrum. Meth. A **518**, edited by G. Batignani, F. Cervelli, G. Chiarelli, and A. Scribano, 228–232 (2004) (cit. on p. 42).

[125]B. Cornell, *PhD students and their careers.* Available at `https://www.hepi.ac.uk/2020/07/16/phd-students-and-their-careers/`, 2020 (cit. on p. 250).

[126]N. J. Cornish, "Mapping the gravitational-wave background", Classical and Quantum Gravity **18**, 4277–4291 (2001) (cit. on p. 71).

[127]M. Coughlin, J. Harms, N. Christensen, et al., "Wiener filtering with a seismic underground array at the Sanford Underground Research Facility", Classical and Quantum Gravity **31**, 215003 (2014) (cit. on pp. 81, 93, 170, 171, 177, 190).

[128]M. Coughlin, N. Mukund, J. Harms, et al., "Towards a first design of a Newtonian-noise cancellation system for Advanced LIGO", Classical and Quantum Gravity **33**, 244001 (2016) (cit. on pp. 93, 170, 190).

[129]M. Coughlin, J. Harms, D. C. Bowden, et al., "Coherence-based approaches for estimating the composition of the seismic wavefield", Journal of Geophysical Research: Solid Earth **124**, 2941–2956 (2019) (cit. on pp. 81, 170, 171, 177).

[130]M. W. Coughlin, J. Harms, J. Driggers, et al., "Implications of dedicated seismometer measurements on Newtonian-noise cancellation for Advanced LIGO", Phys. Rev. Lett. **121**, 221104 (2018) (cit. on pp. 93, 170, 190).

[131]M. Coughlin and J. Harms, "Constraining the gravitational wave energy density of the Universe using Earth's ring", Physical Review D **90**, 10.1103/physrevd.90.042005 (2014) (cit. on pp. 19, 20, 59).

[132]M. Coughlin and (. the LIGO Scientific Collaboration and the Virgo Collaboration), "Noise line identification in LIGO S6 and Virgo VSR2", Journal of Physics: Conference Series **243**, 012010 (2010) (cit. on p. 109).

[133]M. W. Coughlin et al., "Subtraction of correlated noise in global networks of gravitational-wave interferometers", Class. Quant. Grav. **33**, 224003 (2016) (cit. on pp. 90, 92, 160, 237).

[134]M. W. Coughlin, A. Cirone, P. Meyers, et al., "Measurement and subtraction of Schumann resonances at gravitational-wave interferometers", Phys. Rev. D **97**, 102007 (2018) (cit. on pp. 80, 90, 92, 148, 160, 167, 201, 237).

[135]P. B. Covas, A. Effler, E. Goetz, P. M. Meyers, et al. (LSC Instrument Authors), "Identification and mitigation of narrow spectral artifacts that degrade searches for persistent gravitational waves in the first two observing runs of Advanced LIGO", Phys. Rev. D **97**, 082002 (2018) (cit. on p. 77).

[136]T. Creighton, "Tumbleweeds and airborne gravitational noise sources for LIGO", Classical and Quantum Gravity **25**, 125011 (2008) (cit. on p. 81).

[137]T. Damour and A. Vilenkin, "Gravitational wave bursts from cusps and kinks on cosmic strings", Phys. Rev. D **64**, 064008 (2001) (cit. on pp. 50, 53).

[138]K. Danzmann and the LISA study team, "LISA: laser interferometer space antenna for gravitational wave measurements", Classical and Quantum Gravity **13**, A247–A250 (1996) (cit. on p. 25).

[139]D. Davis, J. S. Areeda, B. K. Berger, et al., "LIGO detector characterization in the second and third observing runs", Classical and Quantum Gravity **38**, 135014 (2021) (cit. on pp. 77, 102, 148).

[140]N. Demetriades, M. Murphy, and J. Cramer, *Validation of Vaisala's global lightning dataset (GLD360) over the continental United States*, Available at https://www.vaisala.com/sites/default/files/documents/6.Demetriades%2C%20Murphy%2C%20Cramer.pdf, Jan. 2010 (cit. on p. 133).

[141]P. B. Demorest, R. D. Ferdman, M. E. Gonzalez, et al., "Limits on the stochastic gravitational wave background from the North American nanohertz observatory for gravitational waves", The Astrophysical Journal **762**, 94 (2012) (cit. on pp. 21, 50, 51).

[142]M. Di Giovanni, C. Giunchi, G. Saccorotti, et al., "A Seismological Study of the Sos Enattos Area—the Sardinia Candidate Site for the Einstein Telescope", Seismological Research Letters **92**, 352–364 (2020) (cit. on pp. 93, 170, 190).

[143]M. Di Giovanni, S. Koley, J. X. Ensing, et al., "Temporal variations of the ambient seismic field at the Sardinia candidate site of the Einstein Telescope", Geophysical Journal International **234**, 1943–1964 (2023) (cit. on p. 170).

[144]S. Dimopoulos, P. W. Graham, J. M. Hogan, M. A. Kasevich, and S. Rajendran, "Gravitational wave detection with atom interferometry", Physics Letters B **678**, 37–40 (2009) (cit. on pp. 28, 29).

[145]S. Drasco and É. É. Flanagan, "Detection methods for non-Gaussian gravitational wave stochastic backgrounds", Phys. Rev. D **67**, 082003 (2003) (cit. on p. 68).

[146]J. Driggers, *aLIGO LHO Logbook*, Available at `https://alog.ligo-wa.caltech.edu/aLOG/index.php?callRep=70916`, 2023 (cit. on p. 136).

[147]J. C. Driggers, M. Evans, K. Pepper, and R. Adhikari, "Active noise cancellation in a suspended interferometer", Review of Scientific Instruments **83**, 024501 (2012) (cit. on p. 81).

[148]J. C. Driggers, J. Harms, and R. X. Adhikari, "Subtraction of Newtonian noise using optimized sensor arrays", Phys. Rev. D **86**, 102001 (2012) (cit. on pp. 81, 93, 170, 190).

[149]R. Durrer, "The cosmic microwave background: the history of its experimental investigation and its significance for cosmology", Classical and Quantum Gravity **32**, 124007 (2015) (cit. on pp. 20, 51).

[150]S. E. Dwyer, G. L. Mansell, and L. McCuller, "Squeezing in Gravitational Wave Detectors", Galaxies **10**, 46 (2022) (cit. on p. 39).

[151]C. J. D. E. and W. G. Anderson, *Gravitational-wave physics and astronomy: an introduction to theory, experiment and data analysis* (Wiley-VCH, 2011) (cit. on p. 24).

[152]M. C. Edwards, R. Meyer, and N. Christensen, "Bayesian semiparametric power spectral density estimation with applications in gravitational wave data analysis", Phys. Rev. D **92**, 064011 (2015) (cit. on pp. 215, 236, 237).

[153]A. Effler et al., *aLIGO LLO Logbook*, Available at `https://alog.ligo-la.caltech.edu/aLOG/index.php?callRep=47898`, aLog nr 47898 (cit. on p. 130).

[154]A. Einstein, "Die grundlage der allgemeinen relativitätstheorie", Annalen der Physik **354**, 769–822 (1916) (cit. on p. 9).

[155]A. Einstein, "Erklarung der Perihelionbewegung der Merkur aus der allgemeinen Relativitatstheorie", Sitzungsber. preuss.Akad. Wiss **47**, 831–839 (1915) (cit. on p. 9).

[156]A. Einstein, “Näherungsweise Integration der Feldgleichungen der Gravitation”, Sitzungsberichte der Königlich Preußischen Akademie der Wissenschaften (Berlin, 688–696 (1916) (cit. on p. 9).

[157]A. Einstein, “Über Gravitationswellen”, Sitzungsberichte der Königlich Preußischen Akademie der Wissenschaften (Berlin), 154–167 (1918) (cit. on p. 9).

[158]A. Essadek and T. Rabeyron, “Mental health of French students during the COVID-19 pandemic”, Journal of Affective Disorders **277**, 392–393 (2020) (cit. on pp. 250, 251, 264).

[159]ET design team, *ET-B sensitivity curve*, Available at `https://apps.et-gw.eu/tds/?content=3&r=14323`, Apr. 2018 (cit. on p. 43).

[160]ET design team, *ET-D sensitivity curve*, Available at `https://apps.et-gw.eu/tds/?content=3&r=14065`, Feb. 2018 (cit. on p. 43).

[161]ET Steering Committee Editorial Team, “Design Report Update 2020 for the Einstein Telescope”, (2020) (cit. on pp. 25, 38, 41, 147, 171, 172, 177, 184, 185, 218).

[162]M. Evans et al., “A Horizon Study for Cosmic Explorer: Science, Observatories, and Community”, (2021) (cit. on pp. 44, 45).

[163]T. Evans, L. Bira, J. Gastelum, and et al, “Evidence for a mental health crisis in graduate education”, Nat Biotechnol **36**, 282–284 (2018) (cit. on pp. 250, 264).

[164]D. Fancourt, A. Steptoe, and F. Bu, “Trajectories of anxiety and depressive symptoms during enforced isolation due to COVID-19 in England: a longitudinal observational study”, The Lancet Psychiatry **8**, 141–149 (2021) (cit. on p. 251).

[165]M. A. Fedderke, P. W. Graham, and S. Rajendran, “Asteroids for μHz gravitational-wave detection”, Phys. Rev. D **105**, 103018 (2022) (cit. on p. 23).

[166]F. Feroz and M. P. Hobson, “Multimodal nested sampling: an efficient and robust alternative to Markov Chain Monte Carlo methods for astronomical data analyses”, Monthly Notices of the Royal Astronomical Society **384**, 449–463 (2008) (cit. on p. 204).

[167]F. Feroz, M. P. Hobson, and M. Bridges, “MultiNest: an efficient and robust Bayesian inference tool for cosmology and particle physics”, Monthly Notices of the Royal Astronomical Society **398**, 1601–1614 (2009) (cit. on p. 204).

[168]V. Ferrari, S. Matarrese, and R. Schneider, “Gravitational wave background from a cosmological population of core-collapse supernovae”, Monthly Notices of the Royal Astronomical Society **303**, 247–257 (1999) (cit. on p. 65).

[169]I. Fiori et al., *Virgo Logbook*, Available at `https://logbook.virgo-gw.eu/virgo/?r=54512`, aLog nr 54512 (cit. on p. 133).

[170]I. Fiori, F. Paoletti, M. C. Tringali, K. Janssens, et al., “The Hunt for Environmental Noise in Virgo during the Third Observing Run”, Galaxies **8**, `10.3390/galaxies8040082` (2020) (cit. on pp. 86, 98, 126–129, 144, 147–149, 226).

[171]D. Fiorucci, J. Harms, M. Barsuglia, I. Fiori, and F. Paoletti, "Impact of infrasound atmospheric noise on gravity detectors used for astrophysical and geophysical applications", Phys. Rev. D **97**, 062003 (2018) (cit. on p. 82).

[172]J. B. Fixler, G. T. Foster, J. M. McGuirk, and M. A. Kasevich, "Atom interferometer measurement of the newtonian constant of gravity", Science **315**, 74–77 (2007) (cit. on p. 28).

[173]R. Flaminio, "Status and plans of the Virgo gravitational wave detector", Proc. SPIE Int. Soc. Opt. Eng. **11445**, 1144511 (2020) (cit. on p. 36).

[174]R. L. Forward, "Wideband laser-interferometer graviational-radiation experiment", Phys. Rev. D **17**, 379–390 (1978) (cit. on p. 55).

[175]N. V. Fotopoulos and the LIGO Scientific Collaboration, "Searching for stochastic gravitational-wave background with the co-located LIGO interferometers", Journal of Physics: Conference Series **122**, 012032 (2008) (cit. on pp. 64, 217).

[176]A. Freise and K. Strain, "Interferometer Techniques for Gravitational-Wave Detection", Living Rev. Rel. **13**, 1 (2010) (cit. on pp. 31, 32).

[177]P. Fritschel, *Output mode cleaner design*, Available at `https://labcit.ligo.caltech.edu/~pking/omc/docs/notes/omc-design.pdf`, Feb. 2004 (cit. on p. 38).

[178]D.-F. Gao, J. Wang, and M.-S. Zhan, "Atomic interferometric gravitational-wave space observatory (AIGSO)", Communications in Theoretical Physics **69**, 37 (2018) (cit. on p. 29).

[179]A. Garcia-Williams, L. Moffitt, and N. Kaslow, "Mental health and suicidal behavior among graduate students", Acad Psychiatry **38**, 554–560 (2014) (cit. on p. 250).

[180]F. Garufi et al., *Virgo Logbook*, Available at `https://logbook.virgo-gw.eu/virgo/?r=54764`, aLog nr 54764 (cit. on p. 133).

[181]L. Ginsberg, "Extremely low frequency (ELF) propagation measurements along a 4900-km path", IEEE Transactions on Communications **22**, 452–457 (1974) (cit. on p. 79).

[182]B. Goncharov, A. H. Nitz, and J. Harms, "Utilizing the null stream of the Einstein Telescope", Phys. Rev. D **105**, 122007 (2022) (cit. on pp. 216, 217, 223, 224, 228, 230, 238).

[183]B. Goncharov, R. M. Shannon, D. J. Reardon, et al., "On the evidence for a common-spectrum process in the search for the nanohertz gravitational-wave background with the Parkes Pulsar Timing Array", The Astrophysical Journal Letters **917**, L19 (2021) (cit. on pp. 57, 59, 60).

[184]B. Goncharov and E. Thrane, "All-sky radiometer for narrowband gravitational waves using folded data", Phys. Rev. D **98**, 064018 (2018) (cit. on p. 71).

[185]M. Granata, M. Barsuglia, R. Flaminio, et al., "Design of the Advanced Virgo non-degenerate recycling cavities", J. Phys. Conf. Ser. **228**, edited by Z. Marka and S. Marka, 012016 (2010) (cit. on p. 37).

[186]D. J. Griffiths, *Introduction to electrodynamics* (Prentice Hall, 1999) (cit. on p. 130).

[187]Y. Gürsel and M. Tinto, "Near optimal solution to the inverse problem for gravitational-wave bursts", Phys. Rev. D **40**, 3884–3938 (1989) (cit. on p. 216).

[188]S. Guthrie, C. A. Lichten, J. van Belle, et al., *Understanding mental health in the research environment: a rapid evidence assessment*, Santa Monica, CA, 2017 (cit. on p. 250).

[189]E. D. Hall, "Cosmic Explorer: a next-generation ground-based gravitational-wave observatory", Galaxies **10**, 90 (2022) (cit. on p. 41).

[190]S. Hancock, *The employment of phd graduates in the uk: what do we know?*, Available at `https://www.hepi.ac.uk/2020/02/17/the-employment-of-phd-graduates-in-the-uk-what-do-we-know/`, 2020 (cit. on p. 250).

[191]J. Harms, F. Acernese, F. Barone, et al., "Characterization of the seismic environment at the Sanford Underground Laboratory, South Dakota", Classical and Quantum Gravity **27**, 225011 (2010) (cit. on p. 177).

[192]J. Harms, "Terrestrial gravity fluctuations", Living Reviews in Relativity **22**, `10.1007/s41114-019-0022-2` (2019) (cit. on pp. 79, 81–83, 185–187).

[193]J. Harms, F. Ambrosino, L. Angelini, et al., "Lunar Gravitational-wave Antenna", The Astrophysical Journal **910**, 1 (2021) (cit. on pp. 19, 20).

[194]J. Harms and S. Hild, "Passive Newtonian noise suppression for gravitational-wave observatories based on shaping of the local topography", Classical and Quantum Gravity **31**, 185011 (2014) (cit. on p. 81).

[195]J. Harms, L. Naticchioni, E. Calloni, et al., "A lower limit for Newtonian-noise models of the Einstein Telescope", arXiv preprint arXiv:2202.12841 (2022) (cit. on pp. 82, 169, 186).

[196]J. Harms and H. J. Paik, "Newtonian-noise cancellation in full-tensor gravitational-wave detectors", Phys. Rev. D **92**, 022001 (2015) (cit. on pp. 93, 164, 167, 170, 190).

[197]C. Hazell, J. Niven, and L. e. a. Chapman, "Nationwide assessment of the mental health of UK doctoral researchers", Humanit Soc Sci Commun **8**, `https://doi.org/10.1057/s41599-021-00983-8` (2021) (cit. on p. 251).

[198]R. W. Hellings and G. S. Downs, "Upper limits on the isotropic gravitational radiation background from pulsar timing analysis", Astrophys. J., Lett. Ed.; (United States) **265**, `10.1086/183954` (1983) (cit. on p. 21).

[199]S. Heo, P. D. Peralta, L. Jin, C. R. P. Nunes, and M. L. Bell, "Differences in self-perception of productivity and mental health among the STEMM-field scientists during the COVID-19 pandemic by sex and status as a parent: a survey in six languages", PLOS ONE **17**, e0269834 (2022) (cit. on p. 251).

[200]S. Hild, S. Chelkowski, A. Freise, et al., "A xylophone configuration for a third-generation gravitational wave detector", Classical and Quantum Gravity **27**, 015003 (2009) (cit. on pp. 42, 43, 147).

[201]S. Hild et al., "Sensitivity Studies for Third-Generation Gravitational Wave Observatories", Class. Quant. Grav. **28**, 094013 (2011) (cit. on pp. 25, 42, 43, 147, 160, 170).

[202]S. Hild, S. Chelkowski, and A. Freise, *Pushing towards the ET sensitivity using 'conventional' technology*, 2008 (cit. on p. 43).

[203]Y. Himemoto and A. Taruya, "Correlated magnetic noise from anisotropic lightning sources and the detection of stochastic gravitational waves", Phys. Rev. D **100**, 082001 (2019) (cit. on pp. 123, 201, 214, 237).

[204]Y. Himemoto and A. Taruya, "Impact of correlated magnetic noise on the detection of stochastic gravitational waves: Estimation based on a simple analytical model", Phys. Rev. D **96**, 022004 (2017) (cit. on pp. 201, 214, 237).

[205]G. Hobbs, "The Parkes Pulsar Timing Array", Classical and Quantum Gravity **30**, 224007 (2013) (cit. on p. 23).

[206]G. Hobbs, A. Archibald, Z. Arzoumanian, et al., "The International Pulsar Timing Array project: using pulsars as a gravitational wave detector", Classical and Quantum Gravity **27**, 084013 (2010) (cit. on p. 23).

[207]J. M. Hogan, D. M. S. Johnson, S. Dickerson, et al., "An atomic gravitational wave interferometric sensor in low earth orbit (AGIS-LEO)", General Relativity and Gravitation **43**, 1953–2009 (2011) (cit. on p. 29).

[208]S. A. Hughes and K. S. Thorne, "Seismic gravity-gradient noise in interferometric gravitational-wave detectors", Phys. Rev. D **58**, 122002 (1998) (cit. on pp. 81, 82, 185).

[209]R. A. Hulse and J. H. Taylor, "Discovery of a pulsar in a binary system", Astrophys. J. Lett. **195**, L51–L53 (1975) (cit. on p. 55).

[210]J. Peterson, "Observation and modeling of seismic background noise", Open-file report **93-322** (1993) (cit. on pp. 175, 176, 178, 180, 181, 183, 187, 188, 191).

[211]K. Janssens et al., *Virgo Logbook*, Available at `https://logbook.virgo-gw.eu/virgo/?r=49094`, aLog nr 49094 (cit. on p. 130).

[212]K. Janssens et al., *Virgo Logbook*, Available at `https://logbook.virgo-gw.eu/virgo/?r=49141`, aLog nr 49141 (cit. on p. 130).

[213]K. Janssens and P. Charlton, *Plans for correlated magnetic injections in O4*, Available at `https://dcc.ligo.org/LIGO-T2200164`, T2200164 (cit. on p. 135).

[214]K. Janssens, M. Ball, R. M. S. Schofield, et al., "Correlated 1–1000 hz magnetic field fluctuations from lightning over Earth-scale distances and their impact on gravitational wave searches", Phys. Rev. D **107**, 022004 (2023) (cit. on pp. 74, 78, 79, 98, 123, 125, 129, 133, 140, 159, 163).

[215]K. Janssens, G. Boileau, M.-A. Bizouard, et al., "Formalism for power spectral density estimation for non-identical and correlated noise using the null channel in Einstein Telescope", Eur. Phys. J. Plus **138**, 352 (2023) (cit. on pp. 99, 219, 221, 222).

[216]K. Janssens, G. Boileau, N. Christensen, F. Badaracco, and N. van Remortel, "Impact of correlated seismic and correlated Newtonian noise on the Einstein Telescope", Phys. Rev. D **106**, 042008 (2022) (cit. on p. 98).

[217]K. Janssens, T. A. Callister, N. Christensen, et al., "Gravitational-wave geodesy: defining false alarm probabilities with respect to correlated noise", Phys. Rev. D **105**, 082001 (2022) (cit. on pp. 89, 99, 160).

[218]K. Janssens, K. Martinovic, N. Christensen, P. M. Meyers, and M. Sakellariadou, "Impact of Schumann resonances on the Einstein Telescope and projections for the magnetic coupling function", Phys. Rev. D **104**, 122006 (2021) (cit. on pp. 54, 98, 147, 151, 183, 226).

[219]K. Janssens and M. Ueda, *Probing depressive symptoms and the desire to leave academia among scientists in large, international collaborations in stem*, Available at `https://arxiv.org/abs/2308.05107`, 2023 (cit. on pp. 100, 249, 268, 270).

[220]A. D. Johnson et al. (NANOGrav Collaboration), "The NANOGrav 15-year Gravitational-Wave Background Analysis Pipeline", (2023) (cit. on p. 58).

[221]K. Riles and J. Zweizig, *Information on self-gating of h(t) used in O3 continuous-wave and stochastic searches*, `https://dcc.ligo.org/T2000384/public`, 2021 (cit. on p. 76).

[222]S. Kawamura, M. Ando, and others., "Current status of space gravitational wave antenna DECIGO and B-DECIGO", Progress of Theoretical and Experimental Physics **2021**, 05A105, `10.1093/ptep/ptab019` (2021) (cit. on p. 25).

[223]A. Khan, A. Pommier, G. Neumann, and K. Mosegaard, "The lunar moho and the internal structure of the Moon: a geophysical perspective", Tectonophysics **609**, Moho: 100 years after Andrija Mohorovicic, 331–352 (2013) (cit. on p. 20).

[224]T. W. B. Kibble, "Topology of cosmic domains and strings", Journal of Physics A: Mathematical and General **9**, 1387 (1976) (cit. on p. 50).

[225]T. Kissel J. andShaffer and L. Dartez, *aLIGO LHO Logbook*, Available at: `https://alog.ligo-wa.caltech.edu/aLOG/index.php?callRep=71706`, 2023 (cit. on pp. 118, 119).

[226]E. W. Kolb and M. S. Turner, *The Early Universe*, Vol. 69 (1990) (cit. on pp. 20, 59).

[227]S. Koley, *Passive seismic with medium aperture arrays in Limburg*, 2021 (cit. on pp. 173, 177).

[228]S. Koley, M. Bader, J. van den Brand, et al., "Surface and underground seismic characterization at Terziet in Limburg—the Euregio Meuse–Rhine candidate site for Einstein Telescope", Classical and Quantum Gravity **39**, 025008 (2022) (cit. on pp. 93, 170, 190).

[229]Kowalska-Leszczynska, I et al, "Globally coherent short duration magnetic field transients and their effect on ground based gravitational-wave detectors", Classical and Quantum Gravity **34**, 074002 (2017) (cit. on pp. 74, 78).

[230]W. J. Kroenke K Spitzer RL, "The PHQ-9: validity of a brief depression severity measure", J Gen Intern Med, `10.1046/j.1525-1497.2001.016009606.x` (2001) (cit. on p. 253).

[231]J. Kubisz (Krakow ELF group), *WERA project*, Available at `http://www.oa.uj.edu.pl/elf/index/projects3.htm` (cit. on p. 123).

[232]A. Kulak, J. Kubisz, S. Klucjasz, et al., "Extremely low frequency electromagnetic field measurements at the Hylaty station and methodology of signal analysis", Radio Science **49**, 361–370 (2014) (cit. on p. 123).

[233]K. Kuns, E. Hall, V. Srivastava, et al., *Cosmic Explorer Strain Sensitivity*, version v6, (2022) https://dcc.cosmicexplorer.org/cgi-bin/DocDB/ShowDocument?docid=T2000017 (cit. on pp. 44, 152).

[234]P. D. Lasky, C. M. F. Mingarelli, T. L. Smith, et al., "Gravitational-wave cosmology across 29 decades in frequency", Phys. Rev. X **6**, 011035 (2016) (cit. on p. 59).

[235]J. Lawrence, K. Turbang, A. Matas, et al., *A stochastic search for intermittent gravitational-wave backgrounds*, 2023 (cit. on p. 68).

[236]K. J. Lee, "Prospects of Gravitational Wave Detection Using Pulsar Timing Array for Chinese Future Telescopes", in Frontiers in radio astronomy and fast early sciences symposium 2015, Vol. 502, edited by L. Qain and D. Li, Astronomical Society of the Pacific Conference Series (Feb. 2016), p. 19 (cit. on p. 23).

[237]G. Lefèvre, "Développement d'un interféromètre atomique en cavité pour le projet MIGA", Theses (Université de Bordeaux, May 2019) (cit. on p. 143).

[238]L. Lentati, S. R. Taylor, C. M. F. Mingarelli, et al., "European Pulsar Timing Array limits on an isotropic stochastic gravitational-wave background", Monthly Notices of the Royal Astronomical Society **453**, 2577–2599 (2015) (cit. on p. 23).

[239]K. Levecque, F. Anseel, A. De Beuckelaer, J. Van der Heyden, and L. Gisle, "Work organization and mental health problems in PhD students", Research Policy **46**, 868–879 (2017) (cit. on p. 251).

[240]Z.-C. Liang, Y.-M. Hu, Y. Jiang, et al., "Science with the TianQin Observatory: preliminary results on stochastic gravitational-wave background", Phys. Rev. D **105**, 022001 (2022) (cit. on p. 216).

[241]LIGO scientific and Virgo collaborations, *O3 instrumental lines*, (2021) https://www.gw-openscience.org/O3/o3speclines/ (cit. on pp. 77, 85, 109, 111).

[242]LIGO Scientific Collaboration, Virgo Collaboration and KAGRA Collaboration, *The population of merging compact binaries inferred using gravitational waves through GWTC-3 - data release*, version v1 (Zenodo, Nov. 2021) (cit. on p. 68).

[243]LIGO Scientific Collaboration, Virgo Collaboration, KAGRA collaboration, *Data for Upper Limits on the Isotropic Gravitational-Wave Background from Advanced LIGO's and Advanced Virgo's Third Observing Run*, (2021) https://dcc.ligo.org/G2001287/public (cit. on pp. 77, 85, 87, 109, 112, 191).

[244]LIGO Scientific Collaboration, Virgo Collaboration, KAGRA collaboration, *Data products and supplemental information for O3 stochastic directional paper*, (2021) https://dcc.ligo.org/LIGO-G2002165/public (cit. on pp. 77, 85, 102).

[245]LIGO Scientific, Virgo and KAGRA collaborations, *LIGO, Virgo and KAGRA observing run plans*, Available at https://observing.docs.ligo.org/plan/, June 2022 (cit. on pp. 37, 41).

[246]LIGO scientific, Virgo and KAGRA collaborations, *GraceDB - LIGO, Virgo and KAGRA public alerts*, Available at https://gracedb.ligo.org/superevents/public/O4/, Jan. 2010 (cit. on p. 57).

[247]J. Limas, L. Corcoran, A. Baker, A. Cartaya, and Z. Ayres, "The impact of research culture on mental health & diversity in STEM", Chemistry **28**, 10.1002/chem.202102957 (2022) (cit. on p. 250).

[248]A. N. Lommen, "Pulsar timing arrays: the promise of gravitational wave detection", Reports on Progress in Physics **78**, 124901 (2015) (cit. on pp. 21, 22, 50, 51).

[249]S. Lucatello and A. Diamond-Stanic, "Diversity and inclusiveness in large scientific collaborations", Nat Astron **1**, 0161 (2014) (cit. on p. 250).

[250]H. Luck et al., "The upgrade of GEO600", J. Phys. Conf. Ser. **228**, edited by Z. Marka and S. Marka, 012012 (2010) (cit. on p. 24).

[251]J. Luo, L.-S. Chen, H.-Z. Duan, et al., "TianQin: a space-borne gravitational wave detector", Classical and Quantum Gravity **33**, 035010 (2016) (cit. on p. 25).

[252]J. G. MacKinnon and H. White, "Some heteroskedasticity-consistent covariance matrix estimators with improved finite sample properties", Journal of Econometrics **29**, 305–325 (1985) (cit. on p. 259).

[253]A. Macquet, M. Andrés-Carcasona, M. Martínez, et al., "Simulations of light distribution on new instrumented baffles surrounding Virgo end mirrors", Classical and Quantum Gravity **40**, 077001 (2023) (cit. on p. 39).

[254]M. Maggiore, *Gravitational waves - volume 1: theory and experiments* (Oxford university press, 2008) (cit. on pp. 9, 11, 12, 14–18, 31, 32, 36, 65).

[255]M. Maggiore, C. V. D. Broeck, N. Bartolo, et al., "Science case for the Einstein telescope", Journal of Cosmology and Astroparticle Physics **2020**, 050–050 (2020) (cit. on pp. 25, 163, 166, 192).

[256]O. Malaspinas and R. Sturani, "Detecting a stochastic background of gravitational waves by correlating n detectors", Class. Quant. Grav. **23**, 319–328 (2006) (cit. on p. 66).

[257]V. Mandic, V. C. Tsai, G. L. Pavlis, et al., "A 3D Broadband Seismometer Array Experiment at the Homestake Mine", Seismological Research Letters **89**, 2420–2429 (2018) (cit. on pp. 173, 177, 193).

[258]K. Martinovic, P. M. Meyers, M. Sakellariadou, and N. Christensen, "Simultaneous estimation of astrophysical and cosmological stochastic gravitational-wave backgrounds with terrestrial detectors", Phys. Rev. D **103**, 043023 (2021) (cit. on p. 66).

[259]a. Matas, I. Dvorkin, T. Regimbau, and A. Romero, *Applying gating to stochastic searches in O3*, https://dcc.ligo.org/P2000546/public, 2021 (cit. on pp. 75, 76).

[260]M. A. McLaughlin, "The North American Nanohertz Observatory for Gravitational Waves", Class. Quant. Grav. **30**, 224008 (2013) (cit. on p. 23).

[261]M. Mehmet and H. Vahlbruch, "The Squeezed Light Source for the Advanced Virgo Detector in the Observation Run O3", Galaxies **8**, 79 (2020) (cit. on p. 39).

[262]J. Mei, Y.-Z. Bai, J. Bao, et al., "The TianQin project: Current progress on science and technology", Progress of Theoretical and Experimental Physics **2021**, 05A107, 10.1093/ptep/ptaa114 (2020) (cit. on p. 25).

[263]K. Merfeld et al., *aLIGO LHO Logbook*, https://alog.ligo-wa.caltech.edu/aLOG/index.php?callRep=48212, 2019 (cit. on p. 148).

[264]J. Metcalfe, S. Wilson, and K. Levecque, *Exploring wellbeing and mental health and associated support services for postgraduate researchers*, Available at https://www.gla.ac.uk/media/Media_629688_smxx.pdf, 2018 (cit. on p. 250).

[265]P. Meyers, "Cross-correlation searches for persistent gravitational waves with Advanced LIGO and noise studies for current and future ground-based gravitational-wave detectors", Thesis (University of Minnesota, 2018) (cit. on p. 109).

[266]P. Meyers, D. C. Bowden, T. Prestegard, et al., "Direct Observations of Surface-Wave Eigenfunctions at the Homestake 3D Array", Bulletin of the Seismological Society of America **109**, 1194–1202 (2019) (cit. on p. 177).

[267]P. M. Meyers, K. Martinovic, N. Christensen, and M. Sakellariadou, "Detecting a stochastic gravitational-wave background in the presence of correlated magnetic noise", Phys. Rev. D **102**, 102005 (2020) (cit. on pp. 66, 93, 94, 154, 160, 167, 213, 237).

[268]J. Miles, "Aligned and unaligned coherence: a new diagnostic tool", in *44th aiaa aerospace sciences meeting and exhibit* () (cit. on p. 102).

[269]S. Mitra, S. Dhurandhar, T. Souradeep, et al., "Gravitational wave radiometry: Mapping a stochastic gravitational wave background", Phys. Rev. D **77**, 042002 (2008) (cit. on p. 66).

[270]S. Mitra, S. Dhurandhar, T. Souradeep, et al., "Gravitational wave radiometry: mapping a stochastic gravitational wave background", Physical Review D **77**, 10.1103/physrevd.77.042002 (2008) (cit. on p. 71).

[271]S. Miyoki, "Current status of KAGRA", in Ground-based and airborne telescopes VIII, Vol. 11445, edited by H. K. Marshall, J. Spyromilio, and T. Usuda (International Society for Optics and Photonics, 2020), pp. 192–204 (cit. on p. 25).

[272]R. A. Moss, P. Gorczynski, W. Sims-Schouten, K. Heard-Laureote, and J. Creaton, "Mental health and wellbeing of postgraduate researchers: exploring the relationship between mental health literacy, help-seeking behaviour, psychological distress, and wellbeing", Higher Education Research & Development **41**, 1168–1183 (2022) (cit. on p. 250).

[273]K. Naccarato, O. Pinto, S. A. M. Garcia, et al., *Validation of the new GLD 360 dataset in Brazil: First results 1*, Available at https://www.vaisala.com/sites/default/files/documents/7.Naccarato%2C%20Pinto%2C%20Garcia_0.pdf, 2010 (cit. on p. 133).

[274]H. Nakahara, "Formulation of the spatial autocorrelation (SPAC) method in dissipative media", Geophysical Journal International **190**, 1777–1783 (2012) (cit. on p. 170).

[275]L. Naticchioni et al., "Characterization of the Sos Enattos site for the Einstein Telescope", J. Phys. Conf. Ser. **1468**, edited by M. Nakahata, 012242 (2020) (cit. on pp. 125, 225).

[276]P. Nguyen, *aLIGO LHO Logbook*, https://alog.ligo-wa.caltech.edu/aLOG/index.php?callRep=57672, 2021 (cit. on p. 148).

[277]P. Nguyen et al., "Environmental noise in advanced LIGO detectors", Classical and Quantum Gravity **38**, 145001 (2021) (cit. on pp. 86, 126, 127, 129, 158, 159, 163, 167).

[278]P. Nguyen et al., *aLIGO LHO Logbook*, https://alog.ligo-wa.caltech.edu/aLOG/index.php?callRep=49521, 2019 (cit. on pp. 130, 148).

[279]L. Pagano, L. Salvati, and A. Melchiorri, "New constraints on primordial gravitational waves from Planck 2015", Physics Letters B **760**, 823–825 (2016) (cit. on p. 59).

[280]Y. Palgi, A. Shrira, L. Ring, et al., "The loneliness pandemic: loneliness and other concomitants of depression, anxiety and their comorbidity during the COVID-19 outbreak", J Affect Disord **275**, 109–111 (2020) (cit. on p. 251).

[281]Paoletti, F et al, *Test: separating CEB and MCB mains lines, and reducing the unwanted coupling between them (50Hz HVAC sidebands in hrec)*, https://logbook.virgo-gw.eu/virgo/?r=49102, Nov. 2019 (cit. on p. 144).

[282]R. H. Parker, C. Yu, W. Zhong, B. Estey, and H. Müller, "Measurement of the fine-structure constant as a test of the Standard Model", Science **360**, 191–195 (2018) (cit. on p. 28).

[283]J. Patel, Y. Oh, K. Rand, et al., "Measurement invariance of the Patient Health Questionnaire-9 (PHQ-9) depression screener in U.S. adults across sex, race/ethnicity, and education level: NHANES 2005-2016.", Depress Anxiety, 10.1002/da.22940 (2019) (cit. on p. 264).

[284]A. Paul, A. Susobhanan, A. Gopakumar, et al., "The Indian Pulsar Timing Array (InPTA)", in 2019 ursi asia-pacific radio science conference (ap-rasc) (2019), pp. 1–1 (cit. on p. 23).

[285]A. A. Penzias and R. W. Wilson, "A Measurement of Excess Antenna Temperature at 4080 Mc/s.", The Astrophysical Journal **142**, 419–421 (1965) (cit. on pp. 20, 51).

[286]A. M. Porter and R. Ivie, *Women in physics and astronomy, 2019*, Available at https://www.aip.org/statistics/reports/women-physics-and-astronomy-2019, 2019 (cit. on p. 266).

[287]T. A. Prince, M. Tinto, S. L. Larson, and J. W. Armstrong, "LISA optimal sensitivity", Phys. Rev. D **66**, 122002 (2002) (cit. on p. 221).

[288]M. Punturo, M. Abernathy, F. Acernese, et al., "The Einstein Telescope: a third-generation gravitational wave observatory", Classical and Quantum Gravity **27**, 194002 (2010) (cit. on p. 25).

[289]T. Pyne, C. R. Gwinn, M. Birkinshaw, T. M. Eubanks, and D. N. Matsakis, "Gravitational Radiation and Very Long Baseline Interferometry", The Astrophysical Journal **465**, 566 (1996) (cit. on p. 23).

[290]L. Ramiz, B. Contrand, M. Rojas Castro, and et al., "A longitudinal study of mental health before and during COVID-19 lockdown in the French population", Globalization and Health **17**, 10.1186/s12992-021-00682-8 (2021) (cit. on p. 251).

[291]C. E. Rasmussen and C. K. I. Williams, *Gaussian processes for machine learning* (The MIT Press, 2006) (cit. on pp. 199, 200).

[292]D. J. Reardon et al., "The Gravitational-wave Background Null Hypothesis: Characterizing Noise in Millisecond Pulsar Arrival Times with the Parkes Pulsar Timing Array", Astrophys. J. Lett. **951**, L7 (2023) (cit. on p. 58).

[293]D. J. Reardon, A. Zic, R. M. Shannon, et al., "Search for an isotropic gravitational-wave background with the Parkes Pulsar Timing Array", The Astrophysical Journal Letters **951**, L6 (2023) (cit. on pp. 23, 57, 58).

[294]T. Regimbau and S. A. Hughes, "Gravitational-wave confusion background from cosmological compact binaries: implications for future terrestrial detectors", Phys. Rev. D **79**, 062002 (2009) (cit. on pp. 215, 237).

[295]T. Regimbau, "The astrophysical gravitational wave stochastic background", Research in Astronomy and Astrophysics **11**, 369–390 (2011) (cit. on pp. 53, 65, 225).

[296]T. Regimbau, "The quest for the astrophysical gravitational-wave background with terrestrial detectors", Symmetry **14**, 10.3390/sym14020270 (2022) (cit. on p. 225).

[297]T. Regimbau, T. Dent, W. Del Pozzo, et al., "Mock data challenge for the Einstein Gravitational-Wave Telescope", Phys. Rev. D **86**, 122001 (2012) (cit. on pp. 24, 215, 216, 218, 224, 237).

[298]T. Regimbau, D. Meacher, and M. Coughlin, "Second einstein telescope mock science challenge: detection of the gravitational-wave stochastic background from compact binary coalescences", Phys. Rev. D **89**, 084046 (2014) (cit. on pp. 54, 191, 192).

[299]D. Reitze, R. X. Adhikari, S. Ballmer, et al., "Cosmic Explorer: The U.S. Contribution to Gravitational-Wave Astronomy beyond LIGO", Bulletin of the AAS **51**, https://baas.aas.org/pub/2020n7i035 (2019) (cit. on pp. 25, 41).

[300]A. I. Renzini et al., "pygwb: A Python-based Library for Gravitational-wave Background Searches", Astrophys. J. **952**, 25 (2023) (cit. on pp. 74, 97, 112, 113).

[301]A. I. Renzini, B. Goncharov, A. C. Jenkins, and P. M. Meyers, "Stochastic Gravitational-Wave Backgrounds: Current Detection Efforts and Future Prospects", Galaxies **10**, 34 (2022) (cit. on pp. 53, 60).

[302]F. J. Richart, J. J. Hall, and R. Woods, *Vibrations of soils and foundations* (Prentice-Hall Inc., 1970) (cit. on p. 81).

[303]K. Riles, "Gravitational waves: sources, detectors and searches", Progress in Particle and Nuclear Physics **68**, 1–54 (2013) (cit. on pp. 23, 24, 48, 51, 52).

[304]J. D. Romano and N. J. Cornish, "Detection methods for stochastic gravitational-wave backgrounds: a unified treatment", Living Rev. Relativ. **20**, 2 (2017) (cit. on pp. 19, 59, 62, 63, 65, 66, 69, 71, 88).

[305]R. Romero, *Radio waves below 22 khz*, http://www.vlf.it/, (accessed: 01.09.2020) (cit. on pp. 125, 225).

[306]F. Ronga, "Detection of gravitational waves with resonant antennas", Journal of Physics: Conference Series **39**, 18–24 (2006) (cit. on p. 19).

[307]G. Rosi, F. Sorrentino, L. Cacciapuoti, M. Prevedelli, and G. M. Tino, "Precision Measurement of the Newtonian Gravitational Constant Using Cold Atoms", Nature **510**, 518 (2014) (cit. on p. 28).

[308]D. W. Russell, "Ucla loneliness scale (version 3): reliability, validity, and factor structure", Journal of Personality Assessment **66**, PMID: 8576833, 20–40 (1996) (cit. on p. 270).

[309]S. S. and W. M., *An introduction to seismology, earthquakes, and Earth structure* (Blackwell publishing, 2003) (cit. on pp. 79–81).

[310]S. Danilishin and T. Zhang for the Instrument Science Board, *ET sensitivity curves used for CoBA Science Study*, Available at `https://apps.et-gw.eu/tds/?content=3&r=18213`, Mar. 2023 (cit. on p. 43).

[311]R. K. Said, M. B. Cohen, and U. S. Inan, "Highly intense lightning over the oceans: Estimated peak currents from global GLD360 observations", Journal of Geophysical Research: Atmospheres **118**, 6905–6915 (2013) (cit. on p. 133).

[312]M. Saleem, J. Rana, V. Gayathri, et al., *The Science Case for LIGO-India*, Available at `https://arxiv.org/abs/2105.01716`, 2021 (cit. on p. 25).

[313]B. S. Sathyaprakash and B. F. Schutz, "Physics, astrophysics and cosmology with gravitational waves", Living Reviews in Relativity **12**, `10.12942/lrr-2009-2` (2009) (cit. on p. 51).

[314]P. R. Saulson, "Terrestrial gravitational noise on a gravitational wave antenna", Phys. Rev. D **30**, 732–736 (1984) (cit. on pp. 81, 82, 185).

[315]R. Schofield, A. Effler, P. Nguyen, et al., *PEM central*, `pem.ligo.org`, 2021 (cit. on p. 130).

[316]R. Schofield et al., *aLIGO LHO Logbook*, Available at `https://alog.ligo-wa.caltech.edu/aLOG/index.php?callRep=43406`, aLog nr 43406 (cit. on pp. 130, 159).

[317]R. Schofield et al., *August 2019 PEM update and new techniques for localizing scattering*, Available at `https://dcc.ligo.org/LIGO-G1901683/public` (cit. on pp. 130, 159).

[318]W. O. Schumann, "Über die Dämpfung der elektromagnetischen Eigenschwingungen des Systems Erde - Luft - Ionosphäre", Zeitschrift Naturforschung Teil A **7**, 250–252 (1952) (cit. on pp. 78, 226).

[319]W. O. Schumann, "Über die strahlungslosen Eigenschwingungen einer leitenden Kugel, die von einer Luftschicht und einer Ionosphärenhülle umgeben ist", Zeitschrift Naturforschung Teil A **7**, 149–154 (1952) (cit. on pp. 78, 226).

[320]D. D. Sentman and H. Volland, *Handbook of atmospheric electrodynamics - volume 1 - chapter 11: Schumann resonances* (CRC Press, 1995) (cit. on pp. 78, 79).

[321]A. Sesana et al., "Unveiling the gravitational universe at μ-Hz frequencies", Exper. Astron. **51**, 1333–1383 (2021) (cit. on pp. 23, 51).

[322]A. Sesana, F. Haardt, P. Madau, and M. Volonteri, "Low - frequency gravitational radiation from coalescing massive black hole binaries in hierarchical cosmologies", Astrophys. J. **611**, 623–632 (2004) (cit. on p. 51).

[323]Shahar Shani-Kadmiel, Frank Linde, Läslo Evers, and Bjorn Vink, *Einstein Telescope seismic campaigns*, 2020 (cit. on pp. 172, 173, 193).

[324]A. Sharma and J. Harms, "Searching for cosmological gravitational-wave backgrounds with third-generation detectors in the presence of an astrophysical foreground", Phys. Rev. D **102**, 063009 (2020) (cit. on p. 67).

[325]M. Shevlin, O. McBride, J. Murphy, et al., "Anxiety, depression, traumatic stress and COVID-19-related anxiety in the UK general population during the COVID-19 pandemic", BJPsych Open **6**, e125 (2020) (cit. on p. 251).

[326]M. A. Shoaie, S. Meroli, S. Machado, and D. Ricci, "Evolution of optical fibre cabling components at CERN: performance and technology trends analysis", Optical Fiber Technology **42**, 69–74 (2018) (cit. on p. 163).

[327]X. Siemens, V. Mandic, and J. Creighton, "Gravitational-wave stochastic background from cosmic strings", Phys. Rev. Lett. **98**, 111101 (2007) (cit. on p. 65).

[328]J. Skilling, "Nested sampling", AIP Conference Proceedings **735**, 395–405 (2004) (cit. on p. 204).

[329]J. Skilling, "Nested sampling for general Bayesian computation", Bayesian Analysis **1**, 833–859 (2006) (cit. on p. 204).

[330]C. Smarra et al. (European Pulsar Timing Array), "The second data release from the European Pulsar Timing Array: VI. Challenging the ultralight dark matter paradigm", (2023) (cit. on p. 58).

[331]R. Smith and E. Thrane, "Optimal Search for an Astrophysical Gravitational-Wave Background", Phys. Rev. X **8**, 021019 (2018) (cit. on pp. 68, 69).

[332]T. L. Smith and R. R. Caldwell, "LISA for cosmologists: Calculating the signal-to-noise ratio for stochastic and deterministic sources", Phys. Rev. D **100**, 104055 (2019) (cit. on pp. 216, 220, 221, 238).

[333]R. Spiewak, M. Bailes, M. T. Miles, et al., "The MeerTime Pulsar Timing Array: A census of emission properties and timing potential", Publ.Astron.Soc.Austral. **39**, e027, e027 (2022) (cit. on p. 23).

[334]F. Squazzoni, G. Bravo, F. Grimaldo, et al., "Gender gap in journal submissions and peer review during the first wave of the COVID-19 pandemic. a study on 2329 Elsevier journals", PLOS ONE **16**, e0257919 (2021) (cit. on p. 251).

[335]V. Srivastava, D. Davis, K. Kuns, et al., "Science-driven tunable design of Cosmic Explorer detectors", The Astrophysical Journal **931**, 22 (2022) (cit. on pp. 44, 45, 152).

[336]L. Stehly, M. Campillo, and N. M. Shapiro, "A study of the seismic noise from its long-range correlation properties", Journal of Geophysical Research: Solid Earth **111**, `https://doi.org/10.1029/2005JB004237` (2006) (cit. on p. 170).

[337]D. L. Surkalim, M. Luo, R. Eres, et al., "The prevalence of loneliness across 113 countries: systematic review and meta-analysis", BMJ **376**, `10.1136/bmj-2021-067068` (2022) (cit. on p. 271).

[338]P. J. Sutton et al., "X-Pipeline: An Analysis package for autonomous gravitational-wave burst searches", New J. Phys. **12**, 053034 (2010) (cit. on p. 216).

[339]C. Talbot, E. Thrane, S. Biscoveanu, and R. Smith, "Inference with finite time series: observing the gravitational universe through windows", Phys. Rev. Res. **3**, 043049 (2021) (cit. on pp. 68, 69).

[340]D. Talukder, E. Thrane, S. Bose, and T. Regimbau, "Measuring neutron-star ellipticity with measurements of the stochastic gravitational-wave background", Phys. Rev. D **89**, 123008 (2014) (cit. on p. 162).

[341]J. H. Taylor and J. M. Weisberg, "A new test of general relativity - Gravitational radiation and the binary pulsar PSR 1913+16", The Astrophysical Journal **253**, 908–920 (1982) (cit. on p. 55).

[342]*The German center for astrophysics*, Available at `https://www.deutscheszentrumastrophysik.de/en` (cit. on p. 44).

[343]The LIGO Scientific Collaboration, The Virgo Collaboration, and The KAGRA Collaboration, *GWTC-3: compact binary coalescences observed by LIGO and Virgo during the second part of the third observing run*, Available at `https://arxiv.org/abs/2111.03606`, 2021 (cit. on p. 57).

[344]The Virgo collaboration, "Advanced Virgo Technical Design Report", (2012) (cit. on pp. 30, 31, 33–36, 38, 39).

[345]"Thermal noise limit in the Virgo mirror suspension", Nuclear Instruments and Methods in Physics Research Section A: Accelerators, Spectrometers, Detectors and Associated Equipment **461**, 8th Pisa Meeting on Advanced Detectors, 297–299 (2001) (cit. on p. 36).

[346]E. Thrane, N. Christensen, R. M. S. Schofield, and A. Effler, "Correlated noise in networks of gravitational-wave detectors: subtraction and mitigation", Phys. Rev. D **90**, 023013 (2014) (cit. on pp. 90–92, 153, 160, 167, 183, 237).

[347]E. Thrane, S. Ballmer, J. D. Romano, et al., "Probing the anisotropies of a stochastic gravitational-wave background using a network of ground-based laser interferometers", Phys. Rev. D **80**, 122002 (2009) (cit. on p. 71).

[348]E. Thrane, N. Christensen, and R. M. S. Schofield, "Correlated magnetic noise in global networks of gravitational-wave interferometers: observations and implications", Phys. Rev. D **87**, 123009 (2013) (cit. on pp. 90, 92, 122, 153, 160, 167, 183, 237).

[349]E. Thrane, S. Mitra, N. Christensen, V. Mandic, and A. Ain, "All-sky, narrowband, gravitational-wave radiometry with folded data", Phys. Rev. D **91**, 124012 (2015) (cit. on p. 71).

[350]E. Thrane and J. D. Romano, "Sensitivity curves for searches for gravitational-wave backgrounds", Phys. Rev. D **88**, 124032 (2013) (cit. on p. 66).

[351]M. Tinto and S. V. Dhurandhar, "Time-delay interferometry", Living Rev. Rel. **24**, 1 (2021) (cit. on pp. 27, 216, 220, 221, 238).

[352]M. C. Tringali, T. Bulik, J. Harms, et al., "Seismic array measurements at Virgo's west end building for the configuration of a Newtonian-noise cancellation system", Classical and Quantum Gravity **37**, 025005 (2019) (cit. on pp. 93, 170, 190).

[353]University of Waikato, *Seismic waves*, Available at `https://www.sciencelearn.org.nz/resources/340-seismic-waves`, Feb. 2021 (cit. on p. 81).

[354]T. Vachaspati and A. Vilenkin, "Gravitational radiation from cosmic strings", Phys. Rev. D **31**, 3052–3058 (1985) (cit. on pp. 50, 53).

[355]Vaisala, *2021 annual lightning report*, Available at `https://www.vaisala.com/sites/default/files/documents/WEA-MET-2021-Annual-Lightning-Report-B212465EN-A.pdf`, Jan. 2022 (cit. on pp. 123, 133).

[356]N. van Remortel, K. Janssens, and K. Turbang, "Stochastic gravitational wave background: methods and implications", Progress in Particle and Nuclear Physics, 104003 (2022) (cit. on pp. 7, 8, 53).

[357]L. Wainstein and V. Zubakov, *Extraction of signals from noise* (Dover publications, 1971) (cit. on p. 48).

[358]J. R. Wait, *Lectures on wave propagation theory* (Pergamon, 1981) (cit. on p. 79).

[359]Y. Wang, G. Heinzel, and K. Danzmann, "First stage of LISA data processing II: Alternative filtering dynamic models for LISA", Phys. Rev. D **92**, 044037 (2015) (cit. on p. 27).

[360]M. Was, M.-A. Bizouard, V. Brisson, et al., "On the background estimation by time slides in a network of gravitational wave detectors", Class. Quant. Grav. **27**, 015005 (2010) (cit. on p. 103).

[361]Washimi, T. on behlaf of the KAGRA collaboration, "Evaluation of the global magnetic noise for the stochastic gravitational wave background search", Iternational Cosmic Ray Conference (ICR (2023) (cit. on p. 146).

[362]J. Weber, "Detection and Generation of Gravitational Waves", Phys. Rev. **117**, 306–313 (1960) (cit. on pp. 19, 55).

[363]L. Wen, X. Fan, and Y. Chen, "Geometrical expression of the angular resolution of a network of gravitational-wave detectors and improved localization methods", Journal of Physics: Conference Series **122**, 012038 (2008) (cit. on p. 216).

[364]L. Wen and Y. Chen, "Geometrical expression for the angular resolution of a network of gravitational-wave detectors", Phys. Rev. D **81**, 082001 (2010) (cit. on p. 216).

[365]L. Wen and B. F. Schutz, "Coherent network detection of gravitational waves: the redundancy veto", Classical and Quantum Gravity **22**, S1321–S1335 (2005) (cit. on p. 216).

[366]I. C. F. Wong and T. G. F. Li, "Signal space in the triangular network of the Einstein Telescope", Phys. Rev. D **105**, 084002, 084002 (2022) (cit. on pp. 24, 216, 220, 221).

[367]H. Xu, S. Chen, Y. Guo, et al., "Searching for the nano-hertz stochastic gravitational wave background with the Chinese Pulsar Timing Array data release I", Research in Astronomy and Astrophysics **23**, 075024 (2023) (cit. on pp. 23, 57).

[368]T. Yokoi and S. Margaryan, “Consistency of the spatial autocorrelation method with seismic interferometry and its consequence”, Geophysical Prospecting **56**, 435–451 (2008) (cit. on p. 175).

[369]M.-S. Zhan et al., “ZAIGA: Zhaoshan Long-baseline Atom Interferometer Gravitation Antenna”, Int. J. Mod. Phys. D **29**, 1940005 (2019) (cit. on p. 29).

[370]H. Zhou, H. Yu, B. Cao, and X. Qiao, “Diurnal and seasonal variations in the Schumann resonance parameters observed at Chinese observatories”, Journal of Atmospheric and Solar-Terrestrial Physics **98**, 86–96 (2013) (cit. on p. 79).

[371]A. Zic et al., “The Parkes Pulsar Timing Array Third Data Release”, (2023) (cit. on p. 58).

Colophon

This thesis was typeset with LaTeX 2_ε. It uses the *Clean Thesis* style developed by Ricardo Langner. The design of the *Clean Thesis* style is inspired by user guide documents from Apple Inc.

Download the *Clean Thesis* style at `http://cleanthesis.der-ric.de/`.